Experimental and computational investigation of forced convection cooling of rectangular blocks in a duct

Arani, Sassan Abedi

Award date:
1992

Awarding institution:
University of Bath

EXPERIMENTAL AND COMPUTATIONAL INVESTIGATION OF FORCED CONVECTION COOLING OF RECTANGULAR BLOCKS IN A DUCT

Submitted by

Sassan Abedi Arani

for the degree of Doctor of Philosophy

of School of Mechanical Engineering,

University of Bath

1992

COPYRIGHT

ProQuest LLC
789 East Eisenhower Parkway
P.O. Box 1346
Ann Arbor, MI 48106-1346

ACKNOWLEDGEMENTS

There are many people who have helped me in one way or another during the research for this thesis, but unfortunately it is possible only to mention some of them here.

First, I wish to acknowledge with gratitude the guidance, advice and assistance in the research programme provided by my supervisor, Dr. H. Hardisty. His critical assessment at all stages of the work was very valuable in bringing the research to a fruitful conclusion.

I am grateful to Dr. S. MacGregor and Dr. M. Wilson for their freely given help throughout the research programme. Encouragement from Dr. N. Wood was also much appreciated. The support of the departmental technical staff was vital to the research programme: Mr. E. Brain, G. Bonwick were particularly helpful in the experimental part of the work.

For continuous and warm support, many thanks are directed to my family in Iran.

Lastly, many thanks to my wife, whose constant encouragement, understanding, patience and help, especially at the stage of writing up this thesis, were precious.

SUMMARY

This thesis presents a theoretical and experimental study of the problem of conjugate heat transfer for the case of steady, two-dimensional incompressible flow of turbulent air over a regular array of heated blocks mounted on a substrate.

An existing CFD package was further developed to yield a realistic theoretical model of the flow over a series of heated elements in a rectangular duct. The model was then used to investigate the effect of changes in the important parameters such as geometric shape, fluid velocity, energy input, etc, on the nature of the flow, and on the temperatures in both fluid and solid.

In order to provide a basis for direct validation of the numerical results, an experimental study using Laser Doppler Anemometry was carried out. The experimental programme was designed to measure the two components of the mean velocity, the shearing stress and the turbulent intensity of the flow configurations considered computationally.

By quantifying the two components of the mean velocity at each measurement point, the flow acceleration and deflection around the obstacles were described more completely.

Observation of the flow obtained by smoke visualisation was helpful in the interpretation of velocity measurements.

For the two low approach velocities considered, the comparison between predicted velocity profiles and the experimental measurements were in good agreement for different locations in the channel.

It was demonstrated that the temperature rise of the elements downstream of the heated element was due to the thermal wake effect. This was also confirmed from the experimental results.

NOTATION

A	constant in the smooth law of the wall	
A_T	total area	m^2
A_c	cross-sectional area	m^2
A_m	function of Sellars et al	
B	element height	m
C_f	skin friction coefficient	
Cp	specific heat capacity	J/kgC
D	diameter	m
f	friction factor	
f_d	Doppler frequency	
$g(x^+)$	integrating Kernel of Sellars et al	
G	superposition Kernel function	
h	heat transfer coefficient	W/m^2C
H	channel height	m
K_f	thermal conductivity of fluid	W/mC
K	kinetic energy of turbulence	$(m/s)^2$
l	length scale of turbulence	m
l_m	mixing length	m
L	width of element	m
m	mass flow rate	kg/m^3
M_p	cell mass source	
n	normal to a boundary	
N	row number	
p	static pressure	N/m^2
pe	cell peclet number	
Q	heat transfer rate	W
q_i	internal energy generation	W/m^3

q	heat flux	W/m^2
$q_o(\zeta)$	wall heat transfer rate of Sellars et al	W/m^2C
r_o	tube radius of Sellars et al	m
S	element spacing	m
S_ϕ	source term	
S_U^ϕ, S_p^ϕ	source term coefficients	
t	time	s
T	temperature	C
U	streamwise velocity	m/s
$\hat{U}_i$	instantaneous velocity component	m/s
U_i	mean velocity component	m/s
U_w	velocity parallel to the wall	m/s
U_{app}	approach velocity	m/s
V	velocity in normal direction	m/s
u,v	velocity components in x- and y-direction resp	m/s
u'	x-direction velocity fluctuation	m/s
v'	y-direction velocity fluctuation	m/s
$\overline{u'v'}$	time-average of the mixed products of velocity fluctuations	m/s
$\sqrt{\overline{u'^2}}$	u-component of turbulent intensity	m/s
$\sqrt{\overline{v'^2}}$	v-component of turbulent intensity	m/s
u_e	boundary layer edge velocity	m/s
u_τ	friction velocity	m/s

x, y, z	coordinates	m
y_p	normal distance from the wall	m
W	mean velocity component in z-direction	m/s
w	velocity fluctuation in z-direction	m/s

DIMENSIONLESS GROUPS

Re	Reynolds Number	(UH/υ)
Pr	Prandtl Number	$(Cp\mu/K)$
Nu	Nusselt Number	(hH/K)
Bi	Biot Number	(hH/K)
θ	dimensionless adiabatic element temperature	
St	Stanton Number	$(h/\rho UCp)$
x^+	dimensionless distance of Sellars et al	
H/B	channel to block ratio	
S/B	pitch to block ratio	
U^+	dimensionless velocity	(u/u_τ)
Y^+	dimensionless length	(yu_τ/υ)

GREEK LETTERS

τ_w	shear stress at the wall	N/m^2
ρ	fluid density	kg/m^3
υ	kinematic viscosity	m^2/s
μ	dynamic viscosity	Ns/m^2
μ_{eff}	effective viscosity	Ns/m^2
μ_t	turbulence viscosity	Ns/m^2
γ_m	function of sellars et al	
λ	wavelength	

δ_f	fringe spacing	
δ	boundary layer thickness	m
Ψ	correlation coefficient	
κ	Karman constant	
α_ϕ	under-relaxation factor	
Γ_ϕ	exchange coefficient	
Γ_{wall}	exchange coefficient at the wall	
Δx, Δy, Δz,	cell dimensions	
ε	dissipation rate of kinetic energy	
σ_k, σ_ε	turbulence model constants	
ϕ	general variable in transport equation	

SUBSCRIPT

i	local
amb	ambient
in	inlet
ad	adiabatic
h	heated element
s	surface
e	element
b	bulk mean
m	bulk mixed mean
w	value at wall
∞	free stream condition
i, j	components in cartesian tensor notation
ilk	location of point in a rectangular grid
new	current iteration
old	previous iteration
ref	reference value

X_+, X_-, Y_+,	particular nodal points
Y_-, Z_+, Z_-	
x_+, x_-, y_+,	values at the faces of computational cell
y_-, z_+, z_-	
ϕ	variable ϕ

SUPERSCRIPT

U, V, W	velocity components, U, V and W respectively
ϕ	variable ϕ
I, II	first and second TDMA sweeps
*	estimated value
^	instantaneous value
'	corrections to estimated value

TABLE OF CONTENTS

CHAPTER [1]

INTRODUCTION

1.1 HISTORY OF PROBLEM

The reliability of electronic systems is highly dependent on the ability to remove the relatively large amounts of energy which such systems can generate as Joule type heating. If this heat is not removed efficiently overheating of critical components may occur. This of course could lead to ultimate system failure.

The development of microminiaturized electronic components, with their attendant extremely high volumetric heating rates, has made the problem of heat removal an even more critical one.

Recently a great deal of interest has been shown in the investigation of the heat transfer problems associated with the cooling of electronic equipment [1-6].

Figure (1.1) shows the failure rate for electronic system. It has been known for many years that the key to electronic system reliability is keeping integrated-circuit (IC) junction temperatures down Figure (1.2). However, evidently this simple design rule is a lot easier to state than to achieve in practice. The major current trends in electronic design are

increasing operating powers and speed,

more compact systems,

surface-mount technology.

They all combine to make the problem of extracting heat and controlling temperatures more difficult. When these trends are considered alongside the reliability, it is easy to see why thermal management is becoming such a crucial part of overall electronic system design.

When designing a heat removal system for electronic components, the packaging engineer is faced with many choices. These choices may range from relying on simple natural convection, to a very elaborate two phase heat exchanger system. In making his decision, the packaging engineer must consider many factors:

the operating characteristics of the components themselves;

the requirements of the electronic system designer with respect to component layout; the operating environment of the system.

The packaging designer needs a technique which will allow him to predict the thermal performance of electronic system components.

1.2 BACKGROUND OF HEAT-TRANSFER IN THE TECHNOLOGY OF ELECTRONIC SYSTEMS

Microminiaturization of electronic components has steadily advanced for more than a decade. The increase in power density has brought about changes not only in the

functional aspects of computers and other electronic systems but also in the approach to the electronic packaging design.

The heat generated by a single logic gate is small, at most a few milliwatts for most high speed logic such as ECL, much less for other logic families such as CMOS. When tens or hundreds of thousands of logic gates are fabricated on a single VLSI chip, the total power consumption could conceivably reach the kilowatt level if high-performance logic is used. Even if a low-power logic family is used, a complete high performance computer system might have millions of switching elements (eg; transistors) and hence comprise hundreds of chips. If these chips are packed very closely together to minimize propagation delays, the problem of removing tens (or even hundreds) of watts of heat while maintaining normal circuit temperatures (usually less than 120 °C; preferably even lower for enhanced reliability) from a system volume of less than 1 litre becomes difficult.

There are many possibilities for removing energy from a small microelectronic device or array of such devices, as shown in Figure (1.3). These cooling techniques were addressed in the book of Seely and Chu [7] as well as two survey articles, Bergles et al., [2].

It has been claimed that such a heat-removal task may place an ultimate limit on packaging density. One pioneer of system physics has estimated that forced-air cooling of logic chips is limited to power densities of about $1W/cm^2$,

and that liquid cooling is limited to about 20W/cm^2.

The typical modular approach used in construction of large systems results in printed circuit boards carrying rather dense array of small components Figure (1.4) stacked together so that the relatively smooth face of one board confronts the rough surface of its neighbour.

The passages thus defined have one relatively smooth wall through which there is little heat transfer, and one wall which contains an array of discrete heated elements whose heights are significantly large compared with the space between adjacent boards. This is a passage with "large roughness," whose fluid mechanics and heat transfer are complex functions of the arrangement of elements and their individual heat releases.

These boards are typically mounted in card-carriers which are subsequently stacked on one another. One such design is shown in Figure (1.5).

When board spacing is uniform, this arrangement forms long channels periodically interrupted by card guides and supports. Cooling air is forced through these channel passages, either by a fan or blower, or by a free convection mechanism.

Unfortunately, the nature of the design task is such that there are as many attempts at developing this "technique" as there are specific applications, and applications are usually related to specific geometries, Consequently, thermal development of successful electronics modules usually proceeds largely on a trial- and error basis.

1.3 REVIEW OF HEAT-TRANSFER APPLIED TO ELECTRONIC EQUIPMENT

In the development of heat transfer techniques to be applied to electronic equipment, maximum temperatures of components must be limited in order to achieve an acceptable level of reliability.

In addition to limiting the maximum temperature of components, temperature difference between system modules which are electrically connected must be minimized to achieve optimum performance. This latter requirement has become increasingly important as electronic circuit speeds have increased. For example, response times for high performance circuits are now specified in terms of pico-seconds (10E-12 sec).

The heat source in a semiconductor device can be considered to be the emitter-base junction, at which point there is a conversion of electrical to thermal energy that results in an increase of temperature at the junction.

Control of the junction temperature is the objective of heat transfer systems for semiconductor devices. Maximum temperature for germanium and silicon, the most widely used materials for semiconductor devices, are 110°C and 200°C, respectively.

Reliability and response requirements, however, generally dictate that much lower junction temperatures be maintained. In some applications, for example, silicon junction temperatures as low as 50°C have been specified.

The primary function of a cooling system for electronic equipment is to provide a thermal path of low resistance from the heat source to the ultimate energy sink. In most practical cases this sink can be assumed to be the environment in which the electronic system is operating; for example, an air-conditioned room in the case of a digital computer, or outer space, in the case of an orbiting electronic system.

LEVELS OF THERMAL RESISTANCE

There are two levels of thermal resistance associated with electronic equipment. The first level is that of the component and its package, commonly referred to as the internal resistance.

It can be defined as the thermal resistance existing between the device junction and some specified point on the outside surface of the package. In most electronic components, heat must be transmitted through a number of different materials and interfaces, and the total internal resistance is the sum of several conductive thermal resistances in series and in parallel.

In a well-designed component the number of interfaces will be minimized and bonding and sealing operations will be selected to create the least contact resistance.

To perform their function in the electronic system, the components must be arranged in an array on a substrate, printed circuit board card, or chassis. Heat is transferred

from the array by various modes ranging from free convection of gases to nucleate boiling of dielectric liquids. The thermal resistance associated with convection from the surface of the array is called the external resistance. It is defined as the thermal resistance that exists between the surface reference point that terminates the internal resistance and some designated point in the convective stream.

The internal and external resistances are the basic thermal resistances associated with electronic equipment, but another type of resistance, system level resistance is also important.

It is the thermal resistance representing coolant temperature rise and heat exchanger effectiveness that exists between the convective stream and ultimate energy sink.

LIMITATIONS ON HEAT-TRANSFER DESIGNS

In addition to the thermal-hydraulic constraints, there are other limitations that affect heat transfer designs. When a system is designed for commercial applications, cost is the most important overall constraint that will determine whether or not a design will progress beyond the planning stages. Cost factors will not be considered here; however, it is appropriate to discuss reliability and compatibility.

RELIABILITY

Electronic systems are expected to have a long, uninterrupted life because of the inherent reliability of solid-state semiconductor devices, printed circuit elements, and discrete micro-components when operated at low temperatures. This represents a challenge to the heat transfer designer since the cooling equipment can be no less reliable than the system it is supposed to protect. The highest failure rate in heat transfer equipment is usually encountered in air or liquid moving devices, valves, or switches.

To minimize this failure rate, it is necessary to use hardware of appropriate quality and apply a safety factor by derating the operating capacity of all equipment. For hardware with moving parts, reliability can be improved by providing redundancy at the component, or system level.

COMPATIBILITY

There must be compatibility between the heat transfer hardware and the general application of the electronic system. In airborne and space vehicles, for example, the equipment must be small and lightweight; if mobility or portability is important, then electric power requirements must be moderate or small. Toxic, corrosive, and flammable fumes must be controlled, so that personnel or property are not endangered, and all accessible surfaces must be kept at

safe temperature limits.

CHOICE OF MATERIALS

The choice of cooling modes is often limited by packaging requirements and physical characteristics of electronic hardware.

The designer is forced to make compromises with the thermophysical properties of coolant and conductive materials, and then may be forced to mitigate the effect of these compromises by means of augmentative techniques. Bergles [9] surveyed and evaluated the basic techniques for increasing heat coefficients in convective systems.

THERMOPHYSICAL PROPERTIES OF CONDUCTING MEDIA

Electrical requirements for integrated electronics, such as electrical conductivity, resistivity, and dielectric strength, often necessitates the use of materials that have medium or low values of thermal conductivity. A widely used method for effective heat transfer from solid materials of this type is to mount the heat source device on a second material of high thermal conductivity. Consider, for example, a silicon chip mounted on a copper plate. The thermal coefficient of expansion is about six times greater for copper than for silicon, so that a direct bond between the two can result in a fracturing of the silicon during thermal cycling.

The appropriate value of thermal conductivity to be used in an analysis can be uncertain for some materials; a striking example is silicon. Other solids that have wide usage in electronic packages (e.g., copper, aluminium, and molybdenum) show large variations in thermal conductivity between the pure state and the commercially available state, as shown in Figure (1.6). When two metals are joined together to form a thermal circuit, the thermal resistance of their interface is often much greater than that of either of the metals. An effective experimental method for determining interface resistance, based on the guard heater technique for measuring thermal conductivity is reported in [8].

Every attempt should be made to minimize the interface thermal resistance in electronic equipment. Using thermal grease between two materials will decrease the thermal resistance for the given temperature increased.

COOLANT SELECTION

The use of single-phase convection or change-of-phase systems for cooling electronic equipment results in heat transfer coefficient that range over several orders of magnitude, as shown in Figure (1.7). In any particular design, trade-offs will have to be made between the heat transfer coefficient and reliability, serviceability, compatibility, and cost.

Among the appropriate coolants for electronic systems, air

is one of the more desirable; it is abundant, readily available, low in cost, and in most applications it is noncorrosive, nontoxic, nonflammable, and it has good dielectric properties. On the negative side, however, air has the poorest heat transfer properties of any of the standard coolants and it can generate significant amounts of acoustical noise at some velocities.

Improvements can be made in heat transfer coefficients of one to two orders of magnitude if liquids instead of air are used in forced convection systems. Among the non metallic liquids, water has the best thermophysical properties as a coolant.

Excellent water pumps can be obtained commercially and little difficulty is experienced in constructing water-tight ducts and chambers. Water, however, can be highly corrosive and it generally has poor dielectric properties.

Dielectric liquids with fluorinated structures represent a good compromise between air and water. These liquids are nonflammable, nontoxic, chemically nonreactive, they can withstand quite high heat fluxes, and they have excellent dielectric characteristics.

Dielectric liquids are particularly well adapted to pool boiling or flow boiling heat transfer systems for electronic equipment.

The temperature at which they boil under atmospheric (or slightly higher) pressure is quite compatible with the desired junction temperature of electronic devices.

1.4 REVIEW OF STUDIES IN DEVELOPMENT OF ELECTRONIC COOLING TECHNOLOGY

CONDUCTION COOLING

An effective way to remove heat from a semiconductor device is by attaching a cooling stud to it. A material of high thermal conductance, such as copper, should be used for the stud, which protrudes into an air or liquid convective stream.

In some cases a molybdenum or tungsten pad will be required between the device and the stud to allow for unequal thermal expansions.

If the heat flux is particularly high, or if extremely close temperature control is desired, a cooling system, as in Figure (1.8), can be used. The device and a molybdenum pad are joined with the cold junction of a thermoelectric module and the hot junction of the module is joined with the evaporator surface of a heat pipe. A thermal analysis of the design shown in Figure (1.8), requires a knowledge of the thermal resistance of the eutectic bond and the interface between the cold junction and the molybdenum, as well as the interface between the hot junction heat and the heat pipe.

NATURAL CONVECTION

When considerations other than heat transfer become paramount in electronic packaging, then natural convection

may become a desirable mode of heat transfer. In many commercial designs it is necessary to trade-off heat transfer coefficient for savings in space, weight, or cost. Before the advent of semiconductor devices, the most widely used mode of heat transfer was natural convection, and similar types of electrical equipment are cooled in this fashion.

The design of a thermally stable electronic package, made up of several printed circuit boards cooled by natural convection, was considered by Cook [11]. His objective was to limit thermal overloads by appropriate placement of heat sinks and to determine the optimum spacing of boards so that a maximum amount of heat was dissipated in a minimum package size.

A commonly used configuration for free convection cooling of electronic equipment is an array of rectangular fins attached to the components. Such a configuration was tested by Chaddock [12]. The results are given in Figure (1.9) where the Nusselt number is shown as a function of the Grashof and Prandtl numbers, and the array geometry. One must also consider the effects of radiation heat transfer in a design such as this, since the radiation coefficient can be appreciable in comparison with the convective coefficient. Chaddock [12] estimated that for this series of tests, radiation heat transfer ranged between 10% and 20% of the free convection heat transfer.

FORCED CONVECTION

In many instances, a satisfactory heat transfer rate from electronic systems can be achieved by a simple fan and duct system. Heat transfer coefficients are usually sufficiently high due to the turbulence generated as the air is forced over irregular surfaces. Most air-cooled systems exhaust the coolant air to the same environment from which it was obtained. The temperature of the intake air is typically maintained in a particular range by an air conditioning system.

Included among the innovative types of heat exchangers is one described in a brochure published by the Amtech Environmental Corp. This device, called a jet impingement heat exchanger, consists of a chamber and an air moving device, with one or more orifice plates which discharges the air in the form of multiple jets; these jets impinge on a heat transfer surface. The electronic components to be cooled are mounted on the latter surface, as illustrated in Figure (1.10). The advantage of the jet impingement heat exchanger is that it helps to provide a uniform and reliable heat sink that can be adapted to many different uses. The cooling system shown in Figure (1.11) has been used commercially. A combined forced and induced arrangement of centrifugal air-moving devices is used to move air through vertical columns formed by component cards.

Air-to-water heat exchangers are located at different

levels in the gates to remove heat from rising columns of air. The net effect is that a greater amount of heat can be transferred within the constraints of geometry and environment, and device temperature differences throughout the system are minimized.

In many applications it is not necessary to design new heat exchangers for electronic equipment. Since a wide variety of commercial heat exchangers is available, the problem becomes one of selection and modification.

1.5 PROBLEM CONSIDERED: FORCED CONVECTION OF AIR OVER A RECTANGULAR ARRAY OF HEATED MODULES MOUNTED ON A SUBSTRATE

The theoretical and experimental research presented in this thesis is concerned with the conjugate heat transfer problem of steady, incompressible flow of turbulent air over a regular array of heated blocks mounted on a substrate.

The heat transfer problem is conjugate in the sense that both the solid block and the fluid flow lie within the solution domain, and that the thermal boundary conditions have not been specified at the internal solid/fluid interface.

Thus both the temperature distributions throughout the solid/fluid solution domain, and the heat transfer coefficients at the interface, are sought in the solution.

Initially, the principal aim of the investigation was to use computational fluid dynamic methods to make numerical predictions of the flow field. Later, this theoretical research was complemented by a corresponding experimental investigation using laser Doppler techniques.

Practical examples of such heated body flows are generally three-dimensional although symmetry is frequently invoked to simplify the problem to the two-dimensional case. One example of two-dimensional problem is the flow over parallel ribs mounted on the surface of the tubes or plates in order to promote heat transfer, as in the fuel rods of a nuclear reactor.

The increased heat transfer is, of course, obtained only with increased pressure drop, and knowledge of these two characteristics is therefore necessary in selecting the optimum height and spacing of the ribs.

The ability to calculate properties of these flows such as local heat transfer rate, mean flow distribution etc, would clearly be of great values to designers and engineers.

As a step towards these objectives, the studies of the present project were made for a geometrically simple, 2-D flow configuration.

1.5.1 STUDY OF TWO-DIMENSIONAL TURBULENT FLOW

A two-dimensional turbulent flow over a number of cubes mounted on a flat plate, with the front face of the first cube normal to the free stream was studied. The velocity

profile of the flow approaching the cubes was assumed uniform.

Although the configurations examined are geometrically simple, the flow fields they provoke are comparatively complex and exhibit most, if not all, of the main features found in the practical situations mentioned above.

Foremost among these characteristics is separation at the sharp edge or edges of the upstream face, which gives rise to recirculation zones around and downstream of the obstacles, separated from the main flow by highly turbulent shear layers.

These features produced a large drag force and an extensive turbulent wake. The complex nature of these flows poses severe difficulties to investigation by either experimental or theoretical approaches.

Measurement of mean velocity and turbulence structure are comparatively scarce for this configuration, reflecting the unsuitability of many commonly available instruments such as the pitot tube and hot wire anemometer for the regions of high turbulence level and reverse flow which are characteristics of bluff body flows.

The experimental information on these flows is thus rather incomplete. Previous theoretical treatments of turbulent flow have been only partially successful. Potential flow analyses have been applied to the 2-D flow upstream of an obstacle but these fail in the downstream region. Perturbation methods, which have been employed for 2-D flow, have shown moderate success in the prediction of mean

velocity but can be used only in the wake region far downstream of the obstacles. Numerical solution of the full governing equations of motion has been attempted only for laminar flows prior to the present investigation have been less comprehensive than the experimental studies.
Thus numerical solutions were obtained of the finite difference forms of the differential equations describing turbulent, incompressible flow for the situations described at the beginning of the section. In support of the numerical studies, detailed experimental mean velocity, turbulence intensity and temperature measurements were obtained for the flow over a surface mounted cubes.

1.5.2 PRACTICAL AND THEORETICAL RELEVANCE OF THE PRESENT STUDY

The present study has both practical and theoretical relevance. The theoretical relevance of the present study lies principally in its being one of the first attempts to calculate heat transfer coefficients for turbulent flow over an array of 2-D bodies in the whole region of interest, both upstream and downstream of the obstacles. Also the thermal wake effects produced by a heated block on other blocks positioned downstream of it.
Information was also obtained about the accuracy of the 'turbulence model' embodied in the procedure which had been developed and successfully applied for two-dimensional boundary layer flows but which had been comparatively

little used in flows with recirculation.

1.6 PRESENT CONTRIBUTION

The following paragraphs describe the manner in which the investigation was carried out.

1.6.1 EXPERIMENT

The experimental part of the study was concerned with the flow over a number of aluminium blocks for nominally uniform upstream conditions, and the rate of the heat dissipation. Although some earlier experiments had been performed on this configuration, the present aim was to fill the gaps in the available information on the mean velocity field and heat transfer coefficients. The experimental velocity and turbulence intensity were measured by Laser Doppler Anemometry in the regions of interest.

The experimental heat transfer coefficient data were obtained by using a fluxmeter, which was mounted on the surface of the heated block. Details of the fluxmeter and its calibration is explained in Chapter (7).

The local flow temperature measurement was by a hot wire anemometry technique. The hot wires were designed and calibrated by author and this technique is fully explained in Chapter (7).

1.7 THE RESEARCH PROGRAM

1.7.1 OBJECTIVE

Conjugate heat transfer for two-dimensional, developing flow over an array of rectangular blocks, representing finite heat sources is considered.

Incompressible flow over multiple blocks is modelled using the fully elliptic form of the Navier-Stokes equations. A control-volume-based, finite difference procedure, with appropriate averaging for diffusion coefficients, is used to solve the coupling between the solid and fluid regions.

The objective was to use computational fluid dynamic (CFD) methods to develop a theoretical model of the flow over a series of heated elements in a rectangular duct, and then to use this model to investigate the effect of changes in parameters such as geometric shape, fluid velocity, etc, on the nature of the flow (boundary layer development, separation of flow, turbulence levels etc). By using the latest version of PHOENICS, the objective was to overcome the apparent constraint so far encountered with this package, of a limit on the permitted number of boundaries and wall functions.

This objectives can be achieved by using commands within PHOENICS, or alternatively by reformulating the problem in "conjugate" forms.

Originally a rig was constructed for flow visualisation. The flow of air around the so-called blocks placed on a smooth surface has been studied, in a small wind tunnel

using flow visualisation methods. This technique revealed clearly the complexities of the flow.

The velocity measurements were made using the Laser Doppler Anemometer. The temperature measurements was made using Constant Current Hot Wire Anemometer.

One of the principal objectives of the research was to use CFD to evaluate the distribution of the convective heat transfer coefficient over the surface of the modules. Also to reveal the manner in which the flow temperature changes as it flows over a series of modules i.e., to investigate the development of the thermal wake behind the heated blocks.

1.7.2 CONTENTS OF THE THESIS

The thesis is divided into nine Chapters of which five, Chapters (4) to (8), contain the main contributions of the study. The background to the investigation is laid in Chapter (1) and (2), which survey relevant previous work. Chapter (2), section 2.2 outlines the previous efforts to predict laminar and turbulent flow over bluff bodies by approximate analytical or numerical methods.

Chapter (3), which provides the theoretical framework, begins by outlining the time-averaged versions for the momentum conservation equations coupled with energy equations governing turbulent flow, and the associated boundary conditions.

These equations are converted to finite difference form in

section 3.3, and the procedure for solving the latter is described in Appendix (1).

Chapter (4) describes the CFD package PHOENICS. Chapter (5) and (6) represents the theoretical results. The experimental study is described in Chapter (7) and (8). Finally Chapter (9) concludes the present study.

FIGURE 1.1: THE PRIMARY CAUSES OF ELECTRONICS SYSTEM FAILURE

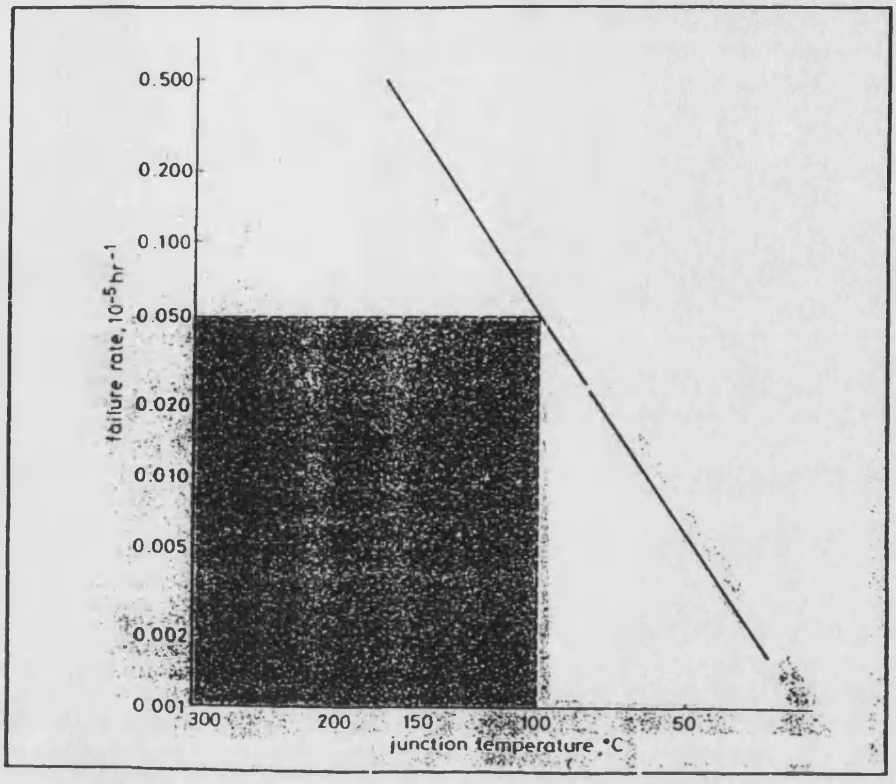

FIGURE 1.2: JUNCTION LIFE STATISTICS

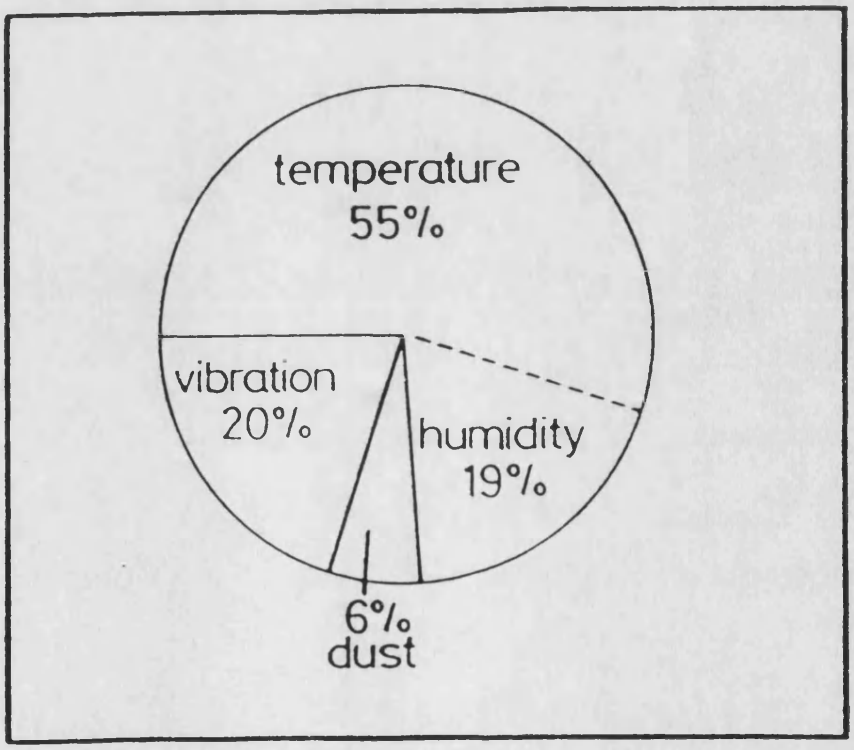

Technique	Scheme	Description
A Conduction Cooling	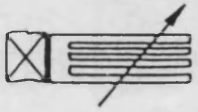	
A1 Fins		Heat transfer by conduction to the fins which are cooled by convection and/or radiation.
A2 Heat Pipe	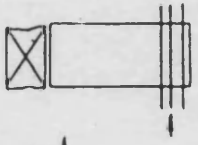	Heat transfer by conduction to the heat pipe (evaporator). The condenser end of the pipe is cooled by convection or radiation.
B Air Cooling		
B1 Natural Convection		Device is cooled by natural convection of air.
B2 Forced Convection		Device is cooled by forced convection of air.
C Liquid Cooling		
C1 Liquid Forced Convection	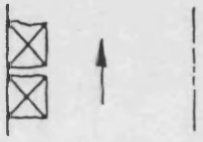	Devices mounted in a channel, in which a liquid is forced to flow. The liquid is then cooled in an air or liquid-cooled heat exchanger.
C2 Vapor Space Condenser	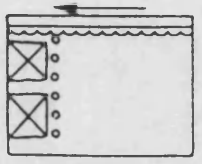	Devices are submerged in a boiling liquid. Heat is rejected to an air or water-cooled condenser. The condenser is usually finned.
C3 Submerged Condenser	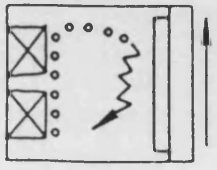	Devices are mounted in an enclosure which is filled with a dielectric fluid, and cooled by an air-cooled or water-cooled heat exchanger. Internal and/or external fins are used.

FIGURE 1.3: ELECTRONIC DEVICE COOLING TECHNIQUES

FIGURE 1.4: SKETCH OF MODERN ELECTRONIC CIRCUIT CARD

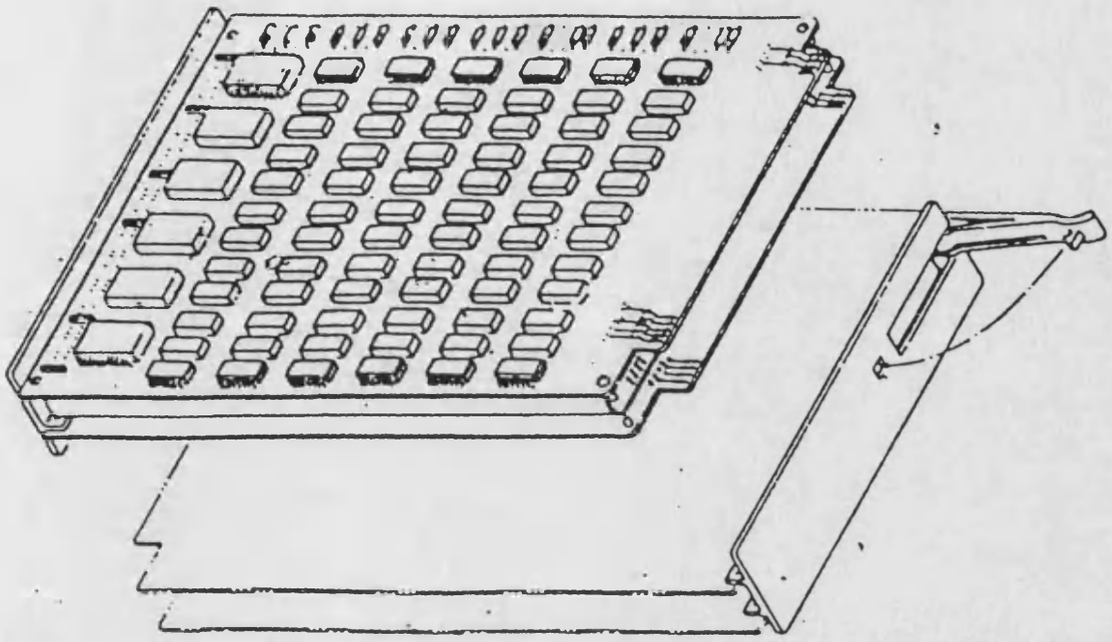

FIGURE 1.5: TYPICAL ELECTRONIC CABINET ILLUSTRATING MODULAR ARRANGEMENT

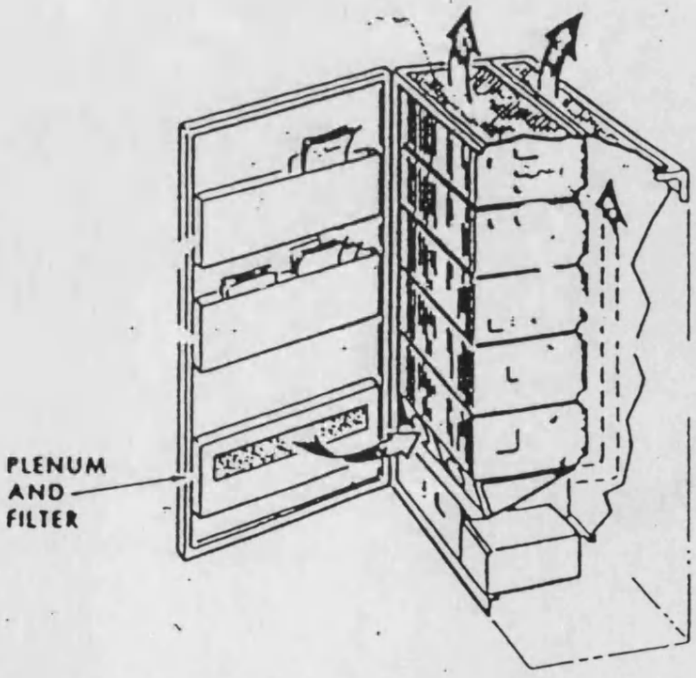

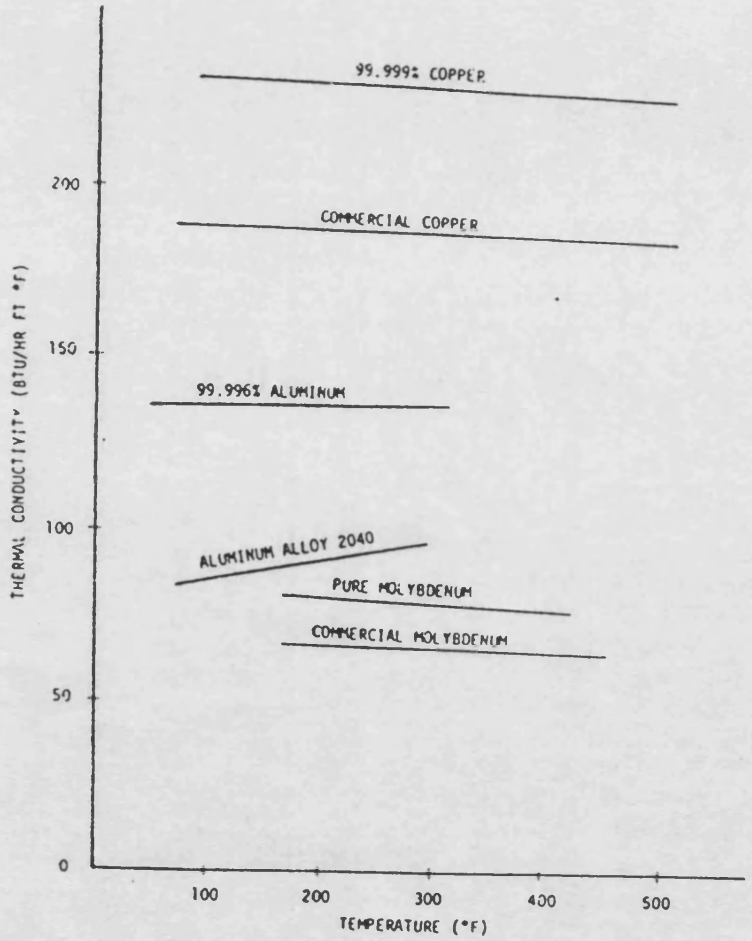

FIGURE 1.6: THERMAL CONDUCTIVITY AS A FUNCTION OF TEMPERATURE FOR PURE AND COMMERCIAL FORMS OF METALS COMMONLY USED IN ELECTRONIC PACKAGING

FIGURE 1.7: TYPICAL HEAT TRANSFER COEFFICIENTS FOR VARIOUS COOLANTS

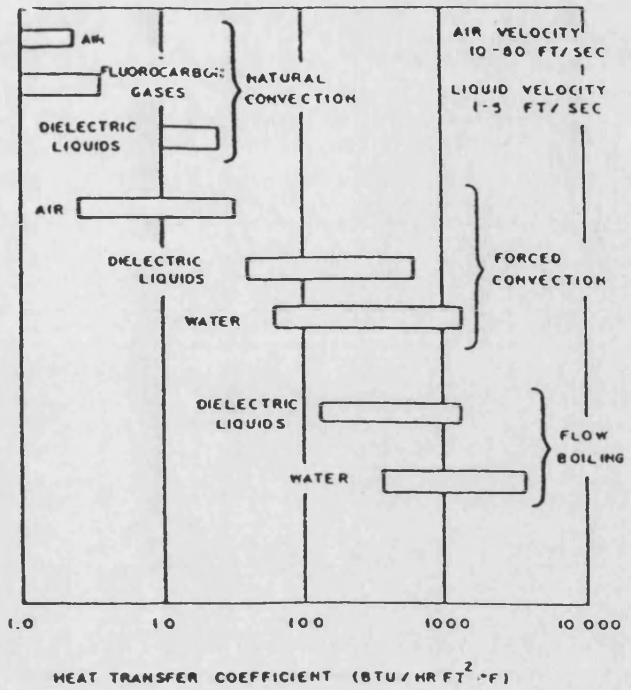

FIGURE 1.8: CONDUCTION COOLING SYSTEM FOR A SEMICONDUCTOR DEVICE

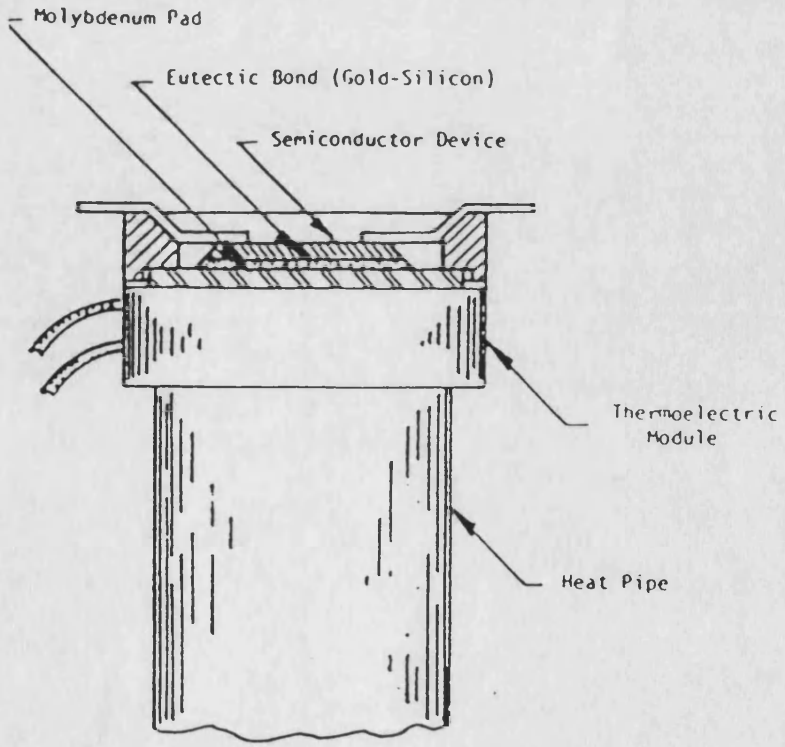

FIGURE 1.9: EXPERIMENTAL RESULTS AND CORRELATION CURVE FOR FREE CONVECTION HEAT TRANSFER FROM VERTICAL RECTANGULAR FIN ARRAYS

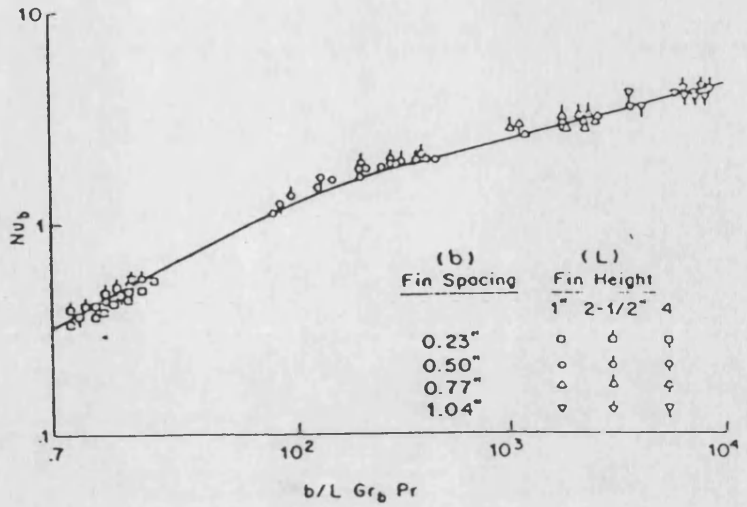

FIGURE 1.10: APPLICATION OF A JET IMPINGEMENT HEAT EXCHANGER AS A COLD PLATE FOR COOLING ELECTRONIC COMPONENTS

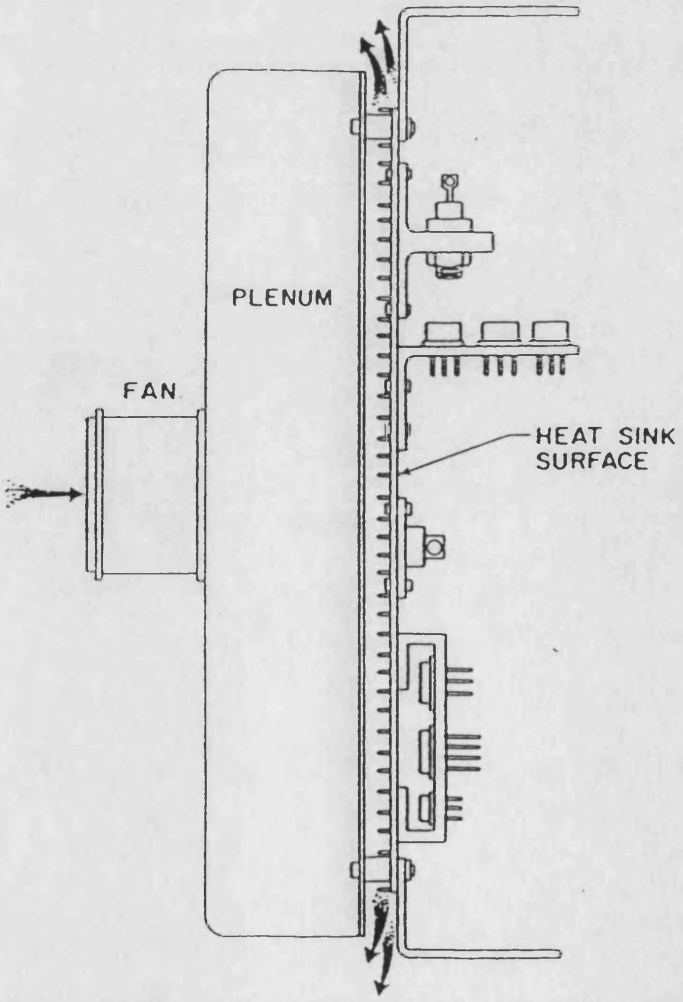

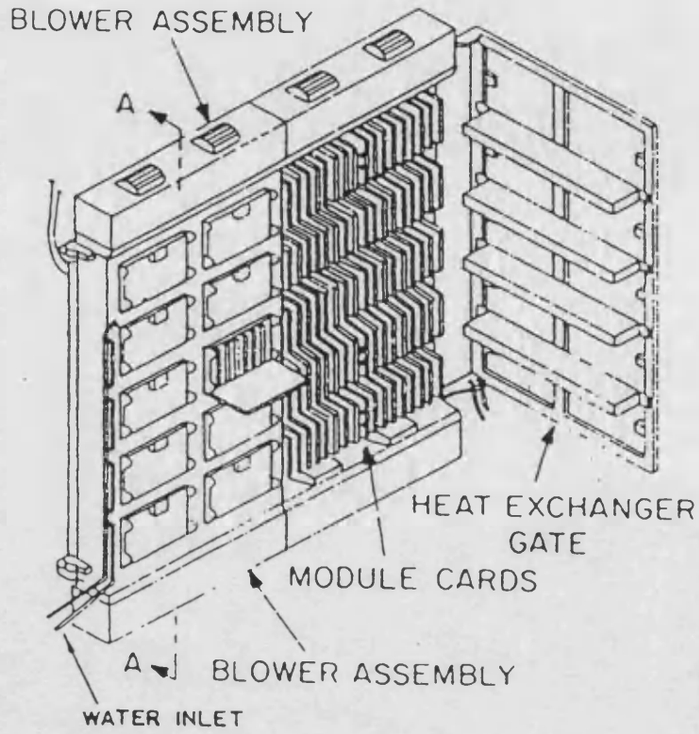

FIGURE 1.11: AIR–LIQUID HYBRID SYSTEM

CHAPTER [2]

REVIEW ON MODELLING AIR FLOW IN ELECTRONIC COMPONENTS

2.1 MODELLING NON-UNIFORM FLOW

Thermal analysis of PCBs involves the solution of heat transfer equations in a complex medium where several heat transfer mechanisms interact. The most important mechanisms are conduction and convection; radiation becomes important only when significant temperature difference occur between the package and its environment or when convection heat transfer coefficients are either low (natural convection) or zero (in a vacuum or when the electronic system is used in outer space applications). Because the wide range of shapes and sizes of components, the board layouts, and variations in the coolant flow path, the analysis of conduction and convection is complex for practical applications.

The most difficult problem associated with PCB thermal analysis, is to determine the surface heat transfer coefficient, **h**. This value quantifies the ability of the electronic component to dissipate heat through convection. Because the heat transfer coefficient is intimately related to complex fluid dynamic transport phenomena occurring on or near a component surface, predicting **h** accurately is crucial for a valid thermal analysis.

However, obtaining **h** via analytical methods is extremely difficult because it requires the use of computational fluid dynamics to determine the value of flow velocity, pressure, and temperatures. Specifically, it would require a solution of the coupled Navier-Stokes and Thermal Energy Equations in three-dimensional space. These complex equations are set out in the following Chapter.

The air velocity distribution over a PCB affects both the ambient air temperature in the vicinity of the components and the heat transfer coefficient associated with the components. To determine the temperature and velocity distribution of air flow within an electronic package enclosure, the thermal analysis tool must deal with the non-uniform flow distribution present in electronic packages. Therefore it is realistic to assume that air velocity is non-uniform across the surface of the PCB because, in typical systems, the inlets and outlets for air are not symmetrically positioned in the enclosure. The air channels are further restricted by components, with the degree of restriction being directly proportional to the components' height.

Air velocity increases in those areas where the channel is narrower due to restrictions of adjacent boards, components, and the outlet. Since the heat transfer coefficient is a function of the velocity, the thermal model of the system must take into account outlet geometry, height of the components, board spacing, and the local density. The theory underlying the solution assumes that

for fluids of low viscosity- in this case, air- the effects of viscosity are appreciable only in a narrow layer at the fluid boundaries. For incompressible flow situations in which the boundary layer remains thin, the ideal fluid results may be applied to the flow of a real fluid with a satisfactory degree of approximation. Based on these assumptions, potential flow analysis can be used to model air flow.

Figure (2.1), shows a series of streamlines showing direction and magnitude of nonuniform air flow. After determining the streamlines, the calculation of local ambient temperatures starts from the inlet, where velocity and temperature are specified.

Then following the streamlines, the energy balance equation, together with the known values of energy dissipation source terms, is used to calculate the cumulative air temperature profiles above the inlet condition. Figure (2.2), shows temperature profiles of ambient air across a PCB. Using the velocities, ambient temperature, components geometries, and heat transfer correlation formulas, the heat transfer coefficient can be determined for each component.

Traditionally, two-dimensional thermal analysis methods have considered the plane of the board while neglecting the critical effects of the components' height, which leads to inaccurate results. Since components have no height, these methods fail to account for external package conduction and conduction/convection from the component to the board.

On the other hand, three dimensional analysis methods require very powerful computers and complex model generation to achieve meaningful results. Flow modelling is a first step toward complete system-level thermal analysis. By employing basic principles, like ideal fluid and potential flow, the designer or analyst can create a representation of the environment influencing the PCB's thermal behaviour. The rapid turnaround makes it possible for designers to evaluate numerous alternatives early in the design process while limiting the cost of change.

2.2 REVIEW OF TWO- AND THREE-DIMENSIONAL FLOWS OVER A BLUFF BODY

The first part of the review is concerned with flow over three-dimensional obstacles and considers the influence of the different, characteristic parameters on the flow, and in particular the case of surface-mounted prismatic obstacles. The second part deals with two-dimensional flows around the obstacles mounted normal to a free stream.

2.2.1 THREE-DIMENSIONAL BLUFF BODY FLOWS

(a) FLOW DESCRIPTION

Practical examples of bluff-body flows are commonly three-dimensional although some can be considered as two-dimensional.

Figure (2.3) shows two-dimensional vs. three-dimensional for the case of rectangular, and Figure (2.4) shows schematic of the cubical array test channel.

Most fundamental studies of three-dimensional flow over bluff bodies have concentrated on wind-tunnel experiments with obstacles of simple geometry. The simplest case is that of a rectangular block with one face normal to the oncoming flow mounted on a plane surface as shown in Figure (2.5), when a nearly uniform flow approaches the front surface of the body, it is deflected by pressure forces and separates from the body at the edges of the windward face (as shown on a simple 2D model, Figure (2.6)). As a result of the deceleration of the fluid, an adverse pressure gradient builds up in front of the body, and flow reversal occurs in the low velocity boundary layer of the approaching flow. Thus, an eddy is formed near the base of the body which wraps around the sides and gives rise to a pair of contra-rotating streamwise vortices at downstream locations.

A positive surface pressure is observed on the front face as a direct consequence of the high pressure immediately upstream of the body. Deceleration of the flow behind the obstacle forms a wake characterised by velocities much smaller than those in the mean flow. Shear along the edge of the wake induces return flow towards the body causing a negative, almost uniform, pressure within this recirculation zone and on the other faces (sides, top and back) of the obstacle.

Three-dimensional turbulent flows over surface-mounted cubes can be predicted by solving the finite-difference forms of the differential equations of motion. Application of finite-difference solutions to 3D problems may in some cases be limited by the computational facilities available because of the long computing time and large grid requirements. Entirely systematic selection of the grid is difficult, because of the almost limitless variety of node distributions.

However, approximately grid-independent solutions can be obtained using fine grids in which the number of nodes does not exceed the storage capacity of a large computer. If 2d and 3d predictions are made on the same computer, the storage for 3d predictions is about 8 times greater, and the computing time over 10 times longer.

(b) INTERFERENCE FROM NEIGHBOURING OBSTACLES

The flow pattern around an obstacle located close to other obstacles which interact with the fluid stream depends on geometrical parameters such as the distance between the obstacles, relative height, shape etc. The interaction has been noted to be particularly acute in the case of two rectangular obstacles of different heights where the tall obstacle lies downstream of the small one (Melbourne and Joubert, 1971; Wise, 1971). Part of the flow passing over the top surface of the upstream block is deflected downwards by the second obstacle, causing flow velocities

in the gap between the blocks which greatly exceed those which would occur immediately upstream of the tall block in isolation.

The data of Castro [58] and Castro and Robins [59] provided information on axial mean velocity and turbulence intensity as well as on surface pressure, for cubes in both uniform flow and a simulated atmospheric boundary layer.

The turbulence information was obtained using pulsed wire anemometry, a technique which has some particular advantages in regions of reverse flow. Peterka and Cermak [15] reported various features of bluff-body flows including mean velocity, turbulence intensity and length scales of turbulence in the wake of the model.

2.2.2 TWO-DIMENSIONAL BLUFF BODY FLOWS

This part of the literature survey is concerned with the two-dimensional (2D) flow over rectangular obstacles. Experimental investigations of the flows over surface-mounted obstacles have been made for several geometries. They include a fence of square cross-section, Tillman [16], a wedge, Plate and Lin [17], a backward facing step, Bradshaw and Wong [18], and sharp-edge fence attached to the leading edge of a flat plate, Sforza and Mons [19]. The characteristics of the flow over a surface-mounted obstacle can conveniently be described by five regions identified by Plate [20] and illustrated in Figure (2.7). In the far upstream region 1, a boundary layer on the plate develops

normally and is uninfluenced by the fence. In the rear-upstream region 2, the flow near the plate is retarded, causing an increase in pressure with a maximum value attained at the upstream face of the fence. At the edge of the fence the flow separates, causing a zone of recirculating flow in the near-downstream region 3 where the pressure is below ambient and almost uniform. The pressure gradient across the separating streamline deflects the main flow towards the plate and it eventually reattaches to the plate.

In the mid-downstream region 4, which starts at the reattachment line, the boundary layer recovers slowly from the disturbance caused by the obstacle, but its properties depend on the geometry of the obstacle and particularly on the ratio $\mathbf{h/\delta}$ (where **h** is the height of the obstacle).

In the far-down stream region 5, the boundary layer reverts to its normal undisturbed behaviour, but it has a greater thickness than a boundary layer which has developed along the plate in the absence of an obstacle. For ease of making experimental measurements, the most accessible parts of the downstream flow are region 4 and 5 where no reverse flow exists.

In these regions reliable measurements of axial mean velocity are possible using a simple pitot tube, and turbulent Reynolds stresses can be measured by hot wire anemometry. In the recovery of the mean flow towards the undisturbed boundary layer profiles, the velocity difference between the undisturbed and disturbed profile

can be treated as a small perturbation, thereby facilitating analysis of the flow.

2.3 REVIEW OF TURBULENCE MODELLING FOR CFD APPLICATIONS

(a) CHARACTERISTICS OF TURBULENT FLOW

As the Reynolds number of a flow is increased, instability occurs due to the influence of random disturbances. These disturbances (in the form of vibration, noise, pressure, or heat) are amplified and become non-linear and three-dimensional. Mutual interaction leads to a tangling and elongation of the vorticity filaments (or vortex lines). Eventually, the motion degenerates into a chaotic random state which can be described only in statistical terms. This is known as turbulent flow.

Turbulent motion is described by Navier-Stokes Equations (applied to the instantaneous properties). Reynolds suggested that these properties could be decomposed into the sum of the mean and fluctuating components. Hence

$$u=\overline{u}+\acute{u}$$

$$p=\overline{p}+\acute{p} \quad etc.$$

Consider the turbulence to be composed of many eddies, all of which are transported with the mean motion. The passage of large eddies leads to low frequency fluctuation while

the small eddies are associated with high frequency fluctuations. There is a continual transfer of energy from the large scale motion (associated with the shear and boundary layers) to smaller and smaller sized eddies. Eventually the energy is dissipated as heat.

The theory explains the wide range of length and time scales within active turbulence: the size of the largest is determined by the mean flow, while the size of the smallest is determined by the fluid viscosity; the intermediate scales interact with the largest and smallest to accomplish the transfer of energy across the range.

Turbulent flows are seen to involve highly complex random processes which can be described only in terms of statistical functions of frequency, time and position.

The determination of these functions, which corresponds to time averaged terms in the governing equations describing the conservation of momentum and energy, presents formidable problems for the experimentalist. Direct numerical simulations (DNS) of turbulent shear flows are beginning to appear. These are based on the full time-dependent Navier-Stokes equations. Such solutions require an enormous investment in computational effort. Recent advances in computer architecture (e.g. parallel computing) make possible considerable increase in the processing rate, and direct solutions are now becoming a practical possibility.

(b) TURBULENT FLOW IN ENGINEERING

The majority of flows through, in or around engineering equipment are turbulent. By "turbulent" we mean that when the flow velocity at a point is continuously sampled the signal is constantly changing in an irregular, non-repeating, chaotic way. Even when the fluid as a whole is constrained to move in a straight line, as in the flow through a long straight pipe, velocity fluctuations arise in all directions. Where the flow has a markedly periodic character, as we find, for example, downstream from a rotating disc of compressor blades, non-periodic velocity perturbations are still to be found superimposed on the cyclic mean signal.

The fluctuations in velocity in a turbulent flow must be accompanied by fluctuations in pressure since only through the interaction of the velocity and pressure fields- expressed mathematically through the Navier-Stokes equations- can the implied accelerations and decelerations of the velocity occur.

When heat transfer takes place across a shear flow in turbulent motion, continual variations in temperature also arise at any point in the flow and in most cases the temperature fluctuations exhibits a character similar to that of the turbulent velocity field, Launder [21].

Records of the instantaneous velocity at a point such as that shown in Figure (2.8) convey a strong impression that turbulence is composed of a very wide range of scales

(whether interpreted in terms of time or distance). Turbulent motion is neither more nor less than an exceedingly complicated viscous flow, time-dependent and three-dimensional in character and describable by the equations of motion known for more than 150 years.
Yet, although the fundamental differential equations are known and numerical methods for solving them well developed, the study of turbulent shear flows, at least those of engineering interest, cannot proceed by direct computer simulation.

(c) FLUID-FLOW COMPUTATION: BASIC DIFFICULTIES

The proliferation of 'off-the-shelf' CAD and structural analysis packages has tended to encourage the view, predominantly in industrial circles, that Computational Fluid Dynamic (CFD) for turbulent engineering flows is closely following this trend and will very soon assume the role of a straightforward, robust and reliable design aid, obviating the need for experimentation and even physical insight. This is a somewhat unrealistic and unlikely scenario, in spite of the availability of some "general and versatile" commercial CFD packages, there exist instances of numerically tolerable grid densities, slow convergence, sensitivity to superficially uninfluential boundary conditions and even a perplexing lack of physical realism in the solutions generated, Leschziner [22].
Most of the above difficulties are rooted in the prominence

of convection in the balance of processes governing the fluid's behaviour and in the interaction between the turbulence model and mean-flow equations. Convection tends to give rise to strongly sheared, often convoluted, regions and steep variations in flow properties. In addition, it introduces strong non-linearities into the equations governing the fluid's motion, and significantly through the appearance of convection-related terms and indirectly through the pressure.

Turbulence, if tackled statistically by means of a model describing the variation of turbulent stresses and/or related turbulence parameters, leads to a further intensification of non-linearity and coupling this time, via the diffusive terms.

If turbulence is modelled through the transport equations, the computational task is further significantly complicated, for these equations are themselves highly non-linear and coupled, and must, in principle, be solved simultaneously with the main-flow equations. Inevitably, this will necessitate an iteration sequence whose stability behaviour responds sensitively to spurious features in the approximation of convection and to precise numerical practices adopted for treating the model's non-linear and coupled 'source' terms.

The manner in which the turbulence-model equations are coupled to those describing the mean flow is a further issue which can play a crucial role in deciding the overall robustness of a computational scheme. Models which provide

the mean-flow equations with an eddy viscosity, tend to display good stability properties, mainly because a property-gradient representation of diffusion gives the mean-flow equations an elliptic character and allows diffusive transport to be treated numerically in an implicit manner, i.e. fully coupled to convection, when the related transport equation is discretized and the resulting algebraic set is solved.

(d) TURBULENT-FLOW SCHEMES: CURRENT NUMERICAL CAPABILITIES

In spite of the difficulties mentioned above, it is fair to say that CFD has reached a stage which (given sufficient care and well defined boundary conditions) permits a realistic description to be obtained of the mean-flow features in a variety of two-dimensional and even three-dimensional turbulent flows of engineering significance. Much of the work contributing to this capability over the past two decades has been done within the finite-volume framework, while serious finite-element computations for turbulent flows have only recently been reported.

With attention restricted to non-reacting, single phase procedures for computing general recirculating flow, a review of recent progress reveals a clear-cut disparity between efforts expanded on numerical/computational issues and those directed towards improving the representation of turbulent transport.

Increasing the geometric adaptability of finite-difference

and finite-volume procedures has been one prominent and very important area of research, its clear objectives begin 'to narrow the gap' between these methods and the finite-element approach, while retaining the simplicity and consequent algorithmic advantages offered by the structured finite-difference meshes.

Finally, a significant amount of work has been done on the development of efficient solution algorithms or the improvement of existing ones, so as to speed up the rate of convergence in iterative schemes designed to yield steady-state solutions.

2.4 APPLICATION OF THE CFD METHOD TO AN ARRAY OF HEATED MODULES

Practical heat transfer problems related to the cooling of electronic equipment are complex. Hence, analysis of these problems using computational fluid dynamic (CFD) methods must proceed by one of the three approaches depending upon the level of detail to be predicted.

These approaches may be called (i) the local analysis, (ii) the system analysis and, (iii) the network analysis.

Local analysis deals with the complete solution of the governing equations for a problem with well defined boundaries and boundary conditions. Typically, however, the domain in such problems represents only a segment of the total electronic cooling system. In contrast, systems analysis deals with the simulation of the entire systems

but with local details modelled via empirical correlations etc.

Network analysis is the simplest, and it deals with the representation of the system as network of current and driving potentials. It is highly desirable that a general purpose CFD code should allow one to perform all three kinds of analyses.

It is believed that the PHOENICS code, which was used to solve all the examples presented herein, possesses such a capability. Figures (2.9, 2.10 and 2.11) shows examples of a flow network for a computer system.

2.5 SOFTWARE FOR FLUID FLOW AND HEAT TRANSFER ANALYSES OF ELECTRONIC COMPONENTS

In the design of enclosures for denser and denser clusters of heat-producing components, new fluid dynamics codes can be used.

Critical conditions within the fluid flow region can be pinpointed using velocity vector plots, streamlines, and temperature contours. Components designed without a thorough consideration of air flow will be uneconomical because of an overly conservative cooling system, or unreliable due to localized hot spots. The margin of error is shrinking as newer packaging becomes denser and use of cooling fans less desirable.

The analyst of the behaviour of air flow has two choices: experiment or simulate with a computer. Experimental

methods, although available, have some disadvantages. The most serious limitation is that an experiment measures performance only at selected locations; it is very difficult to locate critical conditions within the fluid flow regions. Only with luck and intuition based on long experience can a designer pinpoint conditions in the most critical locations. Experiments are also costly and slow, and may not be able to test the full range of operating conditions. Simulation with computers alleviates many of these problems.

Several programs for analysis of fluid dynamics have appeared in the last few years, and over the last two decades developers have learned a lot about solution techniques, pre and post processors, and of course user friendliness.

The benefits of experience are apparent in the more recent fluid codes. The four well-known codes, presently in use are:

Fidap, Flodyn, Phoenics, and Fluent.

These four programs share the same basic purpose of seeking a numerical solution to the general continuum problem described by the Navier-Stokes equations for fluid flow. The Navier-Stokes equation, a nonlinear second-order partial differential equation, is a nightmare to solve. The equation was derived in 1840, but valid general-purpose solution techniques for its practical use have only very recently emerged.

The solution methodology in computational fluid dynamics is

much like that in structural analysis. The continuous region is subdivided with a mesh of discrete computational units, and numerical solutions are obtained at the grid points. In the past, finite difference techniques predominated for these type of problems, but finite element methods are gaining ground. Two of the codes mentioned earlier use the finite element method, two use finite difference.

Regardless of which solution methods is used, the essential goals are calculation of velocity, pressure, and temperature. Solutions are usually represented graphically through velocity vector plots, streamlines, and temperature contours.

Well known thermal simulation codes such as Sinda, or even Ansys, have been used to determine the temperature distribution without requiring air flow patterns, but there are two problems with use of these codes. First, they solve heat conduction equations, which are just not appropriate for strongly convective flow.

Second, one must specify in advance the heat transfer rate between the heated surface, such as a printed circuit board, and the adjacent air. The heat transfer rate, which depends on the air flow pattern over the surface, cannot be accurately predicted.

Reliable values for heat transfer coefficients can be determined through simulation of the air flow and temperature distribution.

These coefficients could then be used with Ansys to

predict, say, the temperature distribution on the printed circuit board itself, where conduction dominates the heat transfer process. Modelling of fluid flow has tremendous potential in the design and analysis of electronic packaging with convection cooling systems. With readily available software one can rapidly solve a host of problems which ordinarily would require expensive laboratory studies.

2.6 CONJUGATE HEAT-TRANSFER IN FORCED CONVECTION COOLING OF ELECTRONIC COMPONENTS

Thermal design of electronic equipment relies upon the solution of the conduction problem in the components. The technique tends now to be substituted or complemented by more refined 2D or 3D finite element discretization. In simple geometries, the effects of conduction can be accounted for analytically, for the case of printed circuit boards (PCBs). In all the above cases, however, thermal conductivity must be supplied as input data at the solid-to-fluid interfaces.

In many electronic applications it is common practice to assemble integrated circuits (ICs) components into densely packed arrays, mounted on closely spaced PCBs. It has been pointed out that the interaction of conduction in the solid, and convection in the cooling fluid, may induce important modifications in the temperature distributions. These may not be accurately predicted by standard heat

transfer correlations, provided that the thermal boundary conditions at the solid-to-fluid interfaces can not be prescribed 'a priori'. Zebib and Wo [23] investigated 2D forced convection cooling of a singular block in a channel formed by two contiguous PCBs. In the analysis, full account was taken of large inhomogeneties in the thermal conductivity of the materials, typical of electronic equipment. A pre-determinate value of the convection coefficient was assumed, to account for heat dispersion from the bottom surface of the PCB, while keeping insulated the upper boundary of the channel.

FIGURE 2.1: STREAMLINES SHOWING DIRECTION AND MAGNITUD
OF NONUNIFORM AIR FLOW

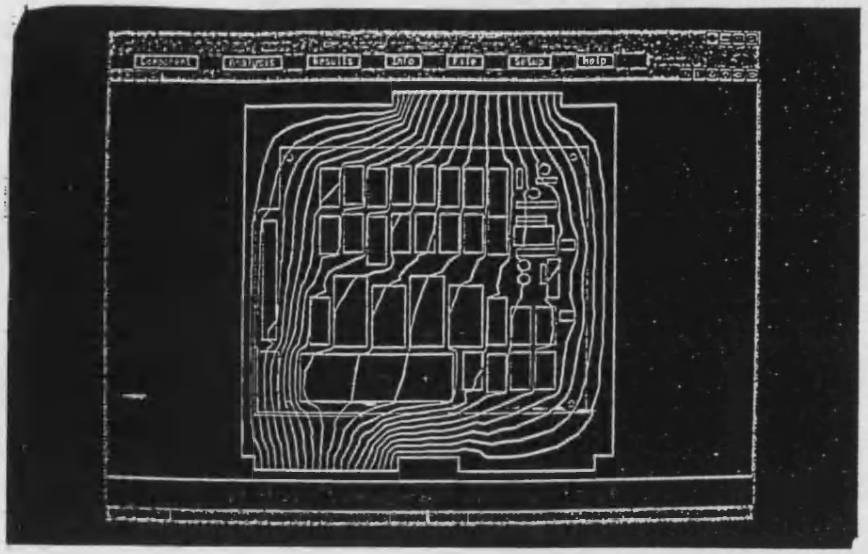

FIGURE 2.2: TEMPERATURE PROFILE OF AMBIENT AIR ACROSS A PC

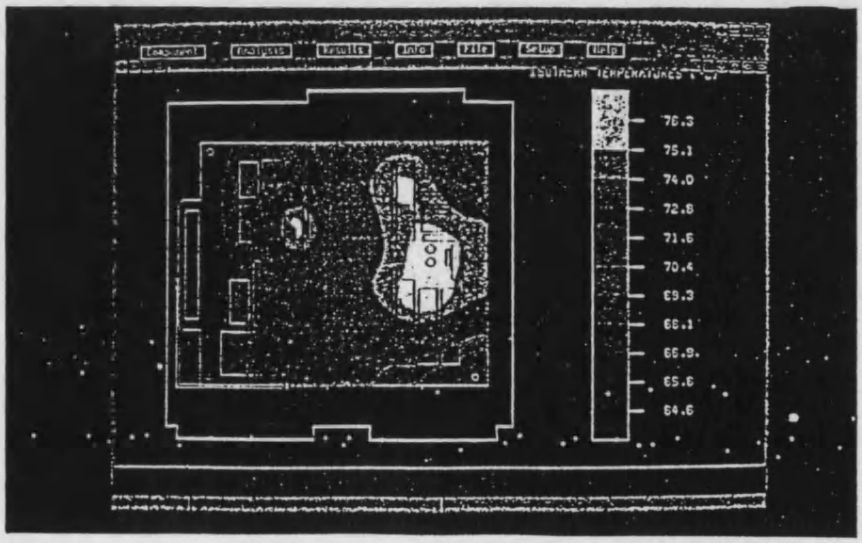

FIGURE 2.3: TWO–DIMENSIONAL VS. THREE–DIMENSIONAL FOR RECTANGULAR GEOMETRY

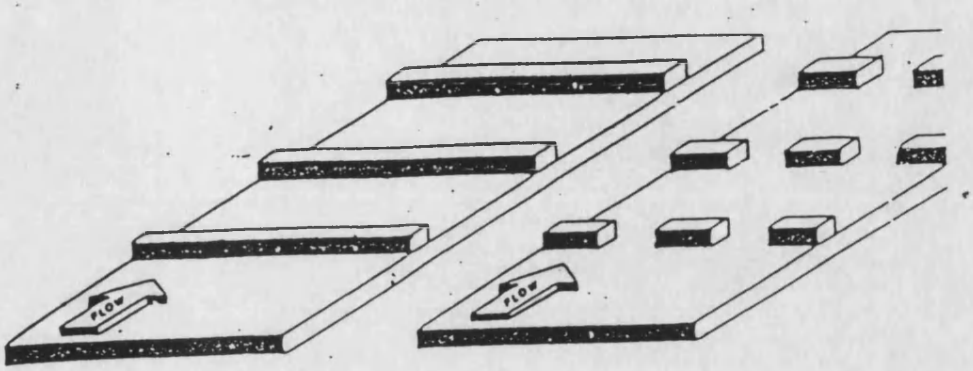

FIGURE 2.4: SCHEMATIC OF THE CUBICAL ARRAY TEST CHANNEL

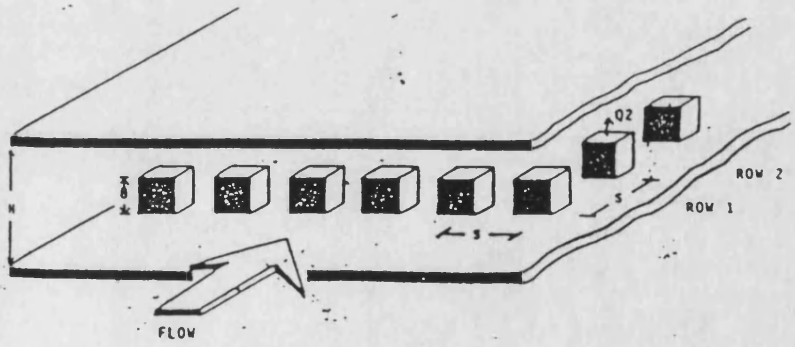

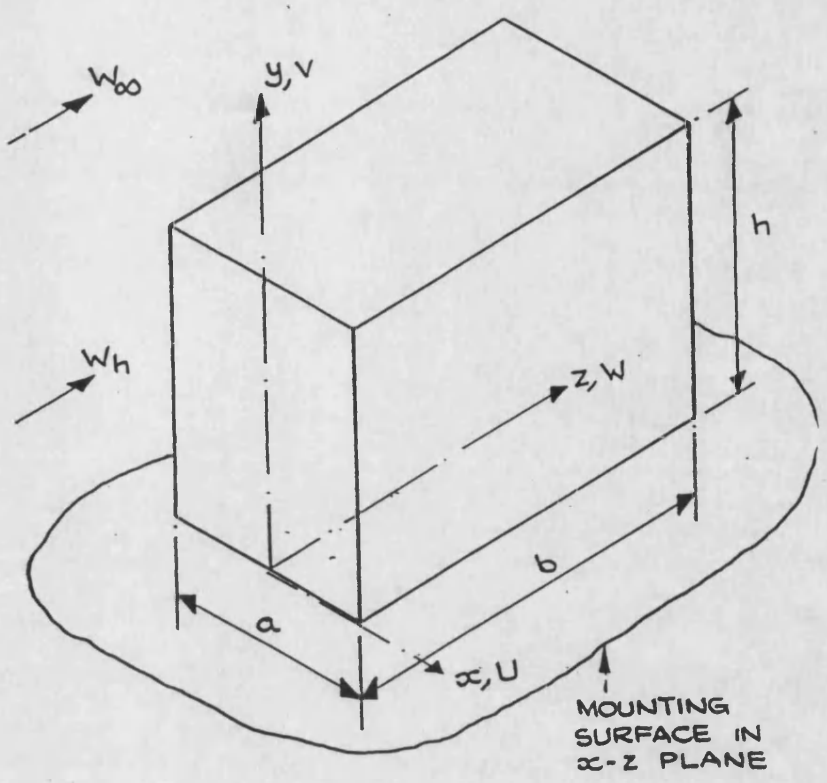

FIGURE 2.5: TYPICAL GEOMETRY OF RECTANGULAR BLUFF BODY

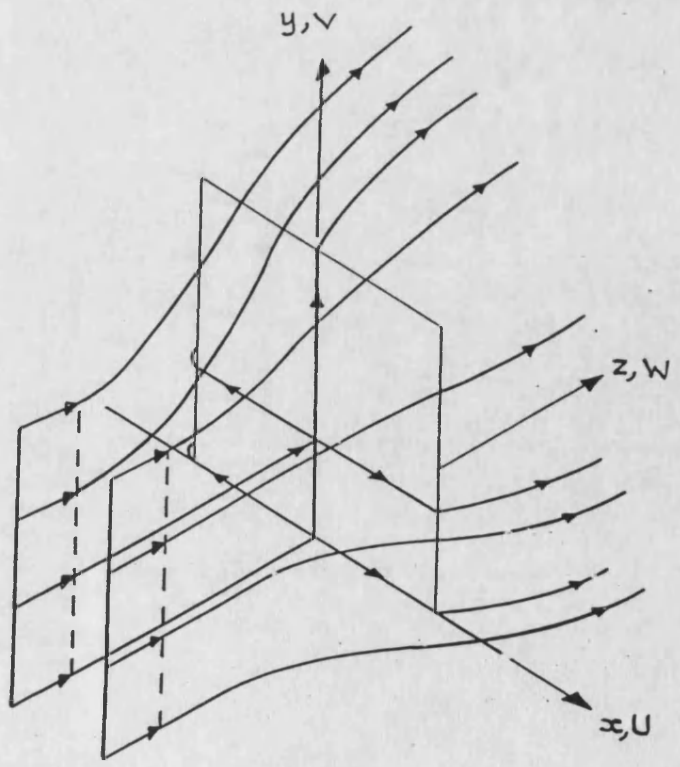

FIGURE 2.6: FLOW PATTERN IN UNIFORM FIELD

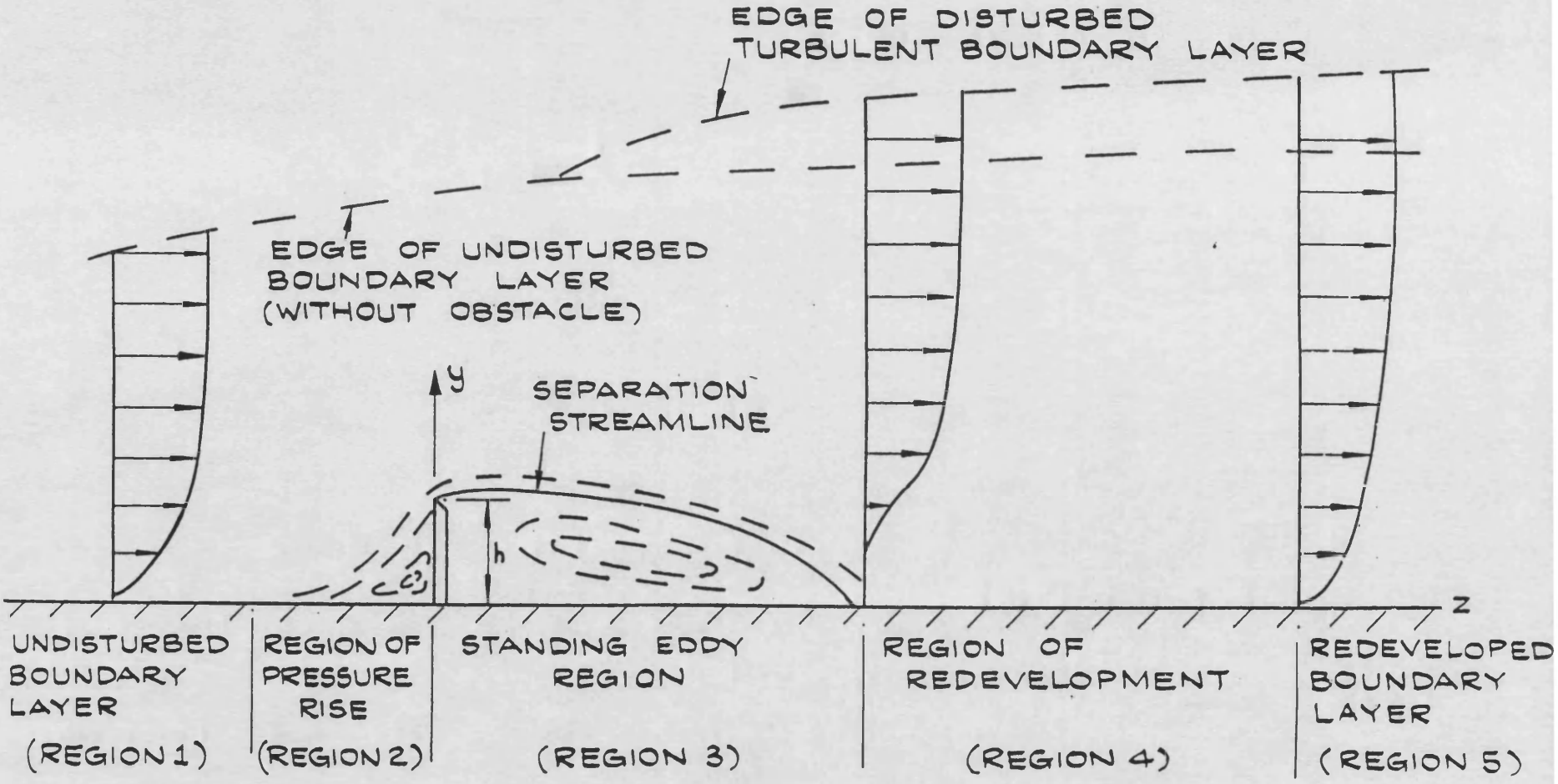

FIGURE 2.7: CHARACTERISTICS OF THE FLOW OVER 2D BLUFF-BODY

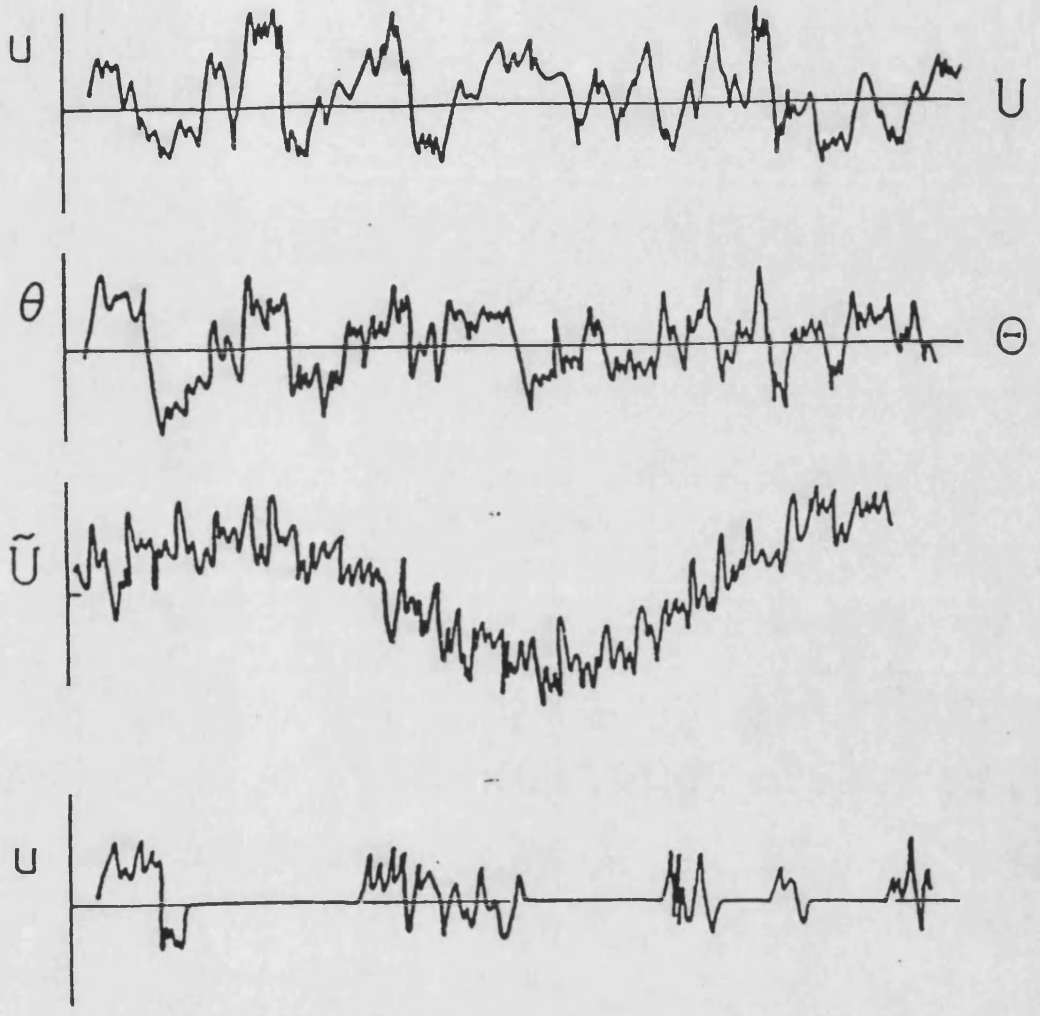

FIGURE 2.8: TIME RECORD IN TURBULENT FLOW

a) VELOCITY FLUCTUATIONS ABOUT MEAN VALUE

b) TEMPERATURE FLUCTUATIONS ABOUT MEAN VALUE

c) INSTANTANEOUS VELOCITY IN PERIODIC FLOW

d) VELOCITY FLUCTUATIONS AT A POINT WHERE FLOW IS INTERMITTENTLY TURBULENT

FIGURE 2.9: A TYPICAL COMPUTER SYSTEM AND THE FLOW NETWORK

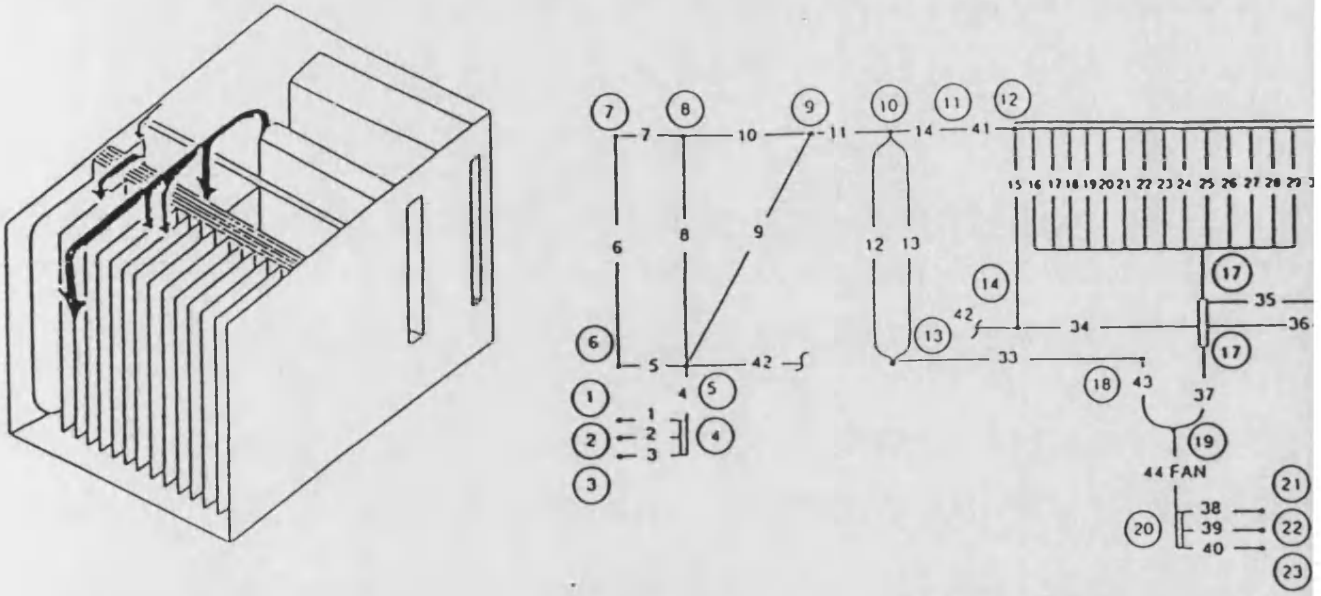

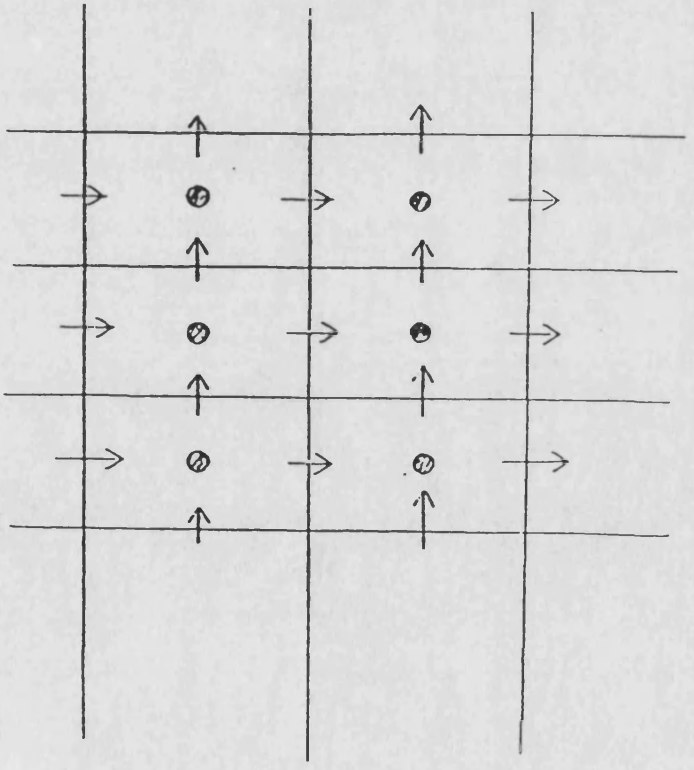

FIGURE 2.10: THE STAGGERED GRID ARRANGEMENT; (·) PRESSURE OR POTENTIAL NODES; (→) AND (↑) VELOCITY OR CURRENT LOCATIONS

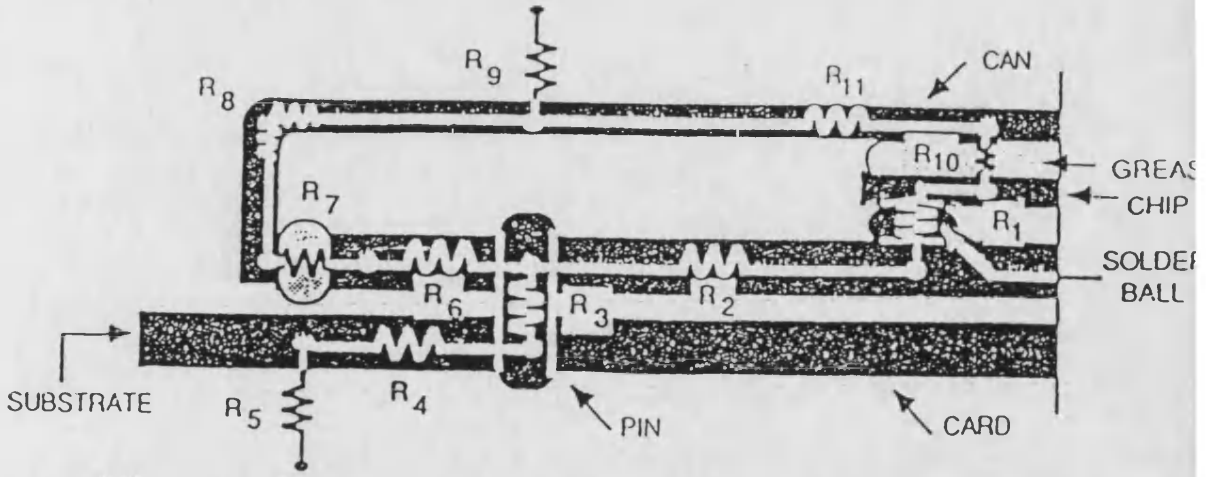

(a)

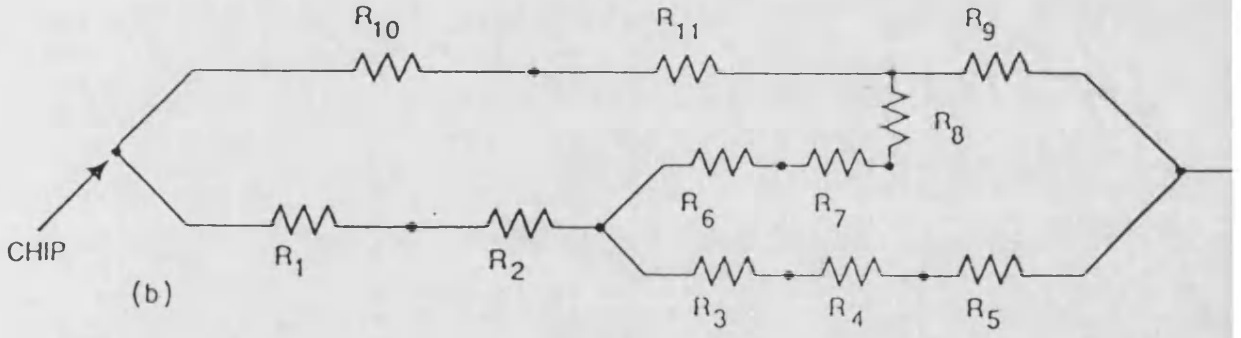

(b)

PHOENICS ANALOG

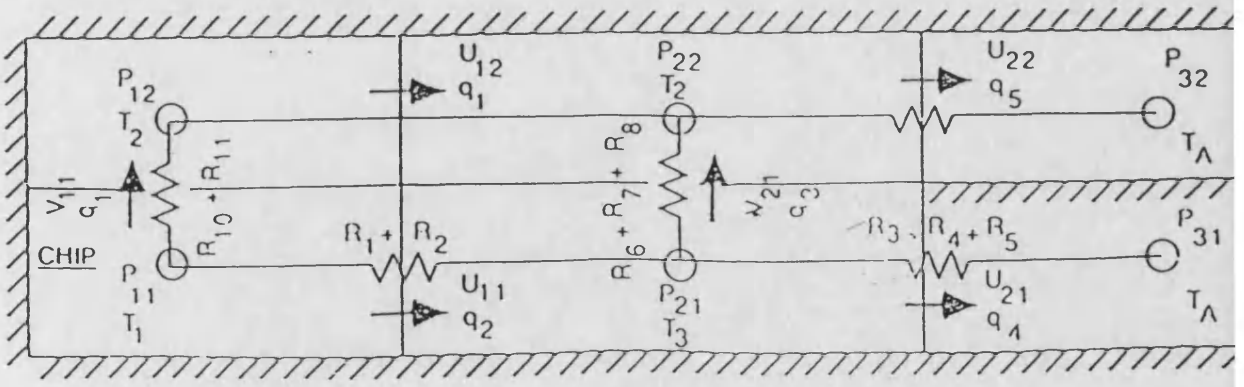

(c)

FIGURE 2.11: NETWORK ANALOGY OF AN AIR–COOLED THERMAL CHIP MODULE; (a) MODULE, (b) NETWORK REPRESENTATION, (c) PHOENICS IMPLEMENTATION

CHAPTER [3]

EQUATIONS OF MOTION AND NUMERICAL PROCEDURE

3.1 INTRODUCTION

In this Chapter the partial differential, conservation equations which govern turbulent flows are summarised, their finite difference forms are derived, and a method of solution of the resulting algebraic equations is outlined. In section 3.2 the time-dependent and time-averaged forms of the equations for the conservation of mass and momentum are presented for two-dimensional(2D) flows. In section 3.3, the corresponding finite difference forms of the differential equations are presented. This section also contains the specification of the computational grid and a description of the special practices needed in the treatment of the boundary layer cells of the grid.
The details of the solution procedure used for the finite difference equations and the related problems of the numerical stability and convergence of the procedure are given in Appendix (1).

3.2 DIFFERENTIAL EQUATIONS

3.2.1 TIME-DEPENDENT CONTINUITY AND MOMENTUM EQUATIONS

For incompressible, constant-property flow, in the absence of external body forces, the time-dependent forms of the mass, momentum and energy conservation equations can be expressed in cartesian tensor notation, Hinze [28], as follows:-

mass conservation: continuity equation

$$\frac{d\hat{U}_i}{dx_i} = 0 \qquad (3.1)$$

momentum conservation (Navier-Stokes equations):

$$\frac{d\hat{U}_i}{dt} + \hat{U}_j \frac{d\hat{U}_i}{dx_j} = -\frac{1}{\rho}\frac{d\hat{p}}{dx_i} + \nu \frac{d^2\hat{U}_i}{dx_j dx_j} \qquad (3.2)$$

energy equation

$$\rho\, Cp\, (\hat{U}_i \frac{dT}{dx_i} + \hat{U}_j \frac{dT}{dx_j}) = k\frac{d^2T}{dx_j^2} + \mu(\frac{d\hat{U}i}{dx_j})^2 \qquad (3.3)$$

Here the summation convention is adopted, i.e. terms containing repeated indices are summed over the three coordinate directions.

Equation (3.1) and (3.2) represent a closed set of equations which, with the provision of boundary conditions

and a suitable finite difference method of solution, are solvable for laminar flows. Although the same approach could in principle be used for turbulent flows, difficulties arise because important changes in the eddy structure occur over a spatial scale which is typically 1000 times smaller than the dimension of the flow domain of interest. Thus to resolve numerically the details of the flow would require a very large number of mesh points in the finite difference grid, far exceeding the capacity of present computers.

However, for practical purposes every detail of the micro-scale of the turbulent motion need not be known. It is sufficient to solve equations for the time-averaged velocity and pressure fields, using a coarser grid and accounting for the effects of turbulence by the "modelling" approach already referred to.

3.2.2 TIME-AVERAGED CONTINUITY AND MOMENTUM EQUATIONS

In a steady flow, the time-averaged (mean) values of velocity U_i and pressure P can be defined as:

$$U_i = \frac{1}{T}\int_0^T \hat{U}_i \, dt \qquad P = \frac{1}{T}\int_0^T \hat{P} \, dt \qquad (3.4)$$

Where

T is a time interval which is short compared with the time scale of the main motion,

closure of the equation set. The full form of closure or modelling adopted in the present work is given in Appendix (1), but it is useful to introduce one aspect at this stage, namely the concept of a "turbulent viscosity"; this allows the equations to be recast into the form in which they will be solved. By analogy with the definition of molecular viscosity in a laminar flow, a turbulent viscosity, μ_t, may be defined such that

$$-\rho \overline{u_i u_j} = \mu_t \left(\frac{dU_i}{dx_j} + \frac{dU_j}{dx_i}\right) \qquad (3.8)$$

where $i \neq j$.

μ_t can be calculated in a number of ways, Launder and Spalding [33]. In the present study it was evaluated from the kinetic energy of turbulence, k, and the dissipation rate of turbulence, ε, which were calculated from their own transport equations. The similarity in the forms of the laminar and turbulent stress relations allows an effective viscosity, μ_{eff}, to be defined as the sum of the molecular and turbulent viscosities:-

$$\mu_{eff} = \mu + \mu_t \qquad (3.9)$$

Combining equation (3.6) to (3.9), the momentum equations (3.7) can then be written in their turbulent-viscosity form as:

where the continuity equation has been used to

$$\frac{d\rho U_j U_i}{dx_j} = -\frac{dP}{dx_i} + \frac{d}{dx_j}\left[\mu_{eff}\left(\frac{dU_i}{dx_j} + \frac{dU_j}{dx_i}\right)\right] \quad (3.10)$$

express the left-hand side in 'conservation' form, this facilitates derivation of the finite-difference equations.

3.2.3 CONSERVATION EQUATION FOR A PROPERTY ϕ

In developing the finite difference versions of the conservation equations, it will be convenient to deal with a single general equation for any dependent variable ϕ. The differential form of this equation is

$$\frac{d\rho U_j \phi}{dx_j} = \frac{d}{dx_j}\left(\Gamma_\phi \frac{d\phi}{dx_j}\right) + S_\phi \quad (3.11)$$

in which the left hand side represents the transport of ϕ by convection. On the right hand side the diffusion of ϕ is taken as proportional to its spatial gradient, the proportionality factor, Γ_ϕ, is called the exchange coefficient.

The "source" term, S_ϕ, contains quantities related to the generation or destruction of ϕ, as well as any other terms which are not accounted for in the convection and diffusion expressions. The similarity between equations (3.10) and (3.11) is evident, and so ϕ may represent any of the mean velocity components, U_i. In addition, it will be demonstrated later that ϕ may represent k, ε or any scalar property of the flow.

For a three-dimensional, steady, uniform property flow, equation (3.11) becomes in **(x,y,z)** cartesian coordinates:

$$\frac{d}{dx}(\rho U\phi) + \frac{d}{dy}(\rho V\phi) + \frac{d}{dz}(\rho W\phi) = \frac{d}{dx}(\Gamma_\phi \frac{d\phi}{dx})$$

$$+ \frac{d}{dy}(\Gamma_\phi \frac{d\phi}{dy}) + \frac{d}{dz}(\Gamma_\phi \frac{d\phi}{dz}) + S_\phi \qquad (3.12)$$

where **U,V,** and **W** are the components of the mean velocity in the **x, y, z** directions. Table 3.1 contains the definitions of Γ_ϕ and S_ϕ for all three momentum equations, the kinetic energy of turbulence and the dissipation.
For a two-dimensional, steady, constant property flow the conservation equation for ϕ is similar to equation (3.12), except that terms containing **W** or derivatives with respect to **z** disappear. The corresponding terms are also omitted from the expressions for S_ϕ in the Table (3.1).

3.2.4 BOUNDARY CONDITIONS

Differential equations of the form of (3.12) are solved within a prescribed solution domain. The boundaries of the solution domain may coincide with an upstream location at which a specified inflow occurs, solid walls, a plane of symmetry, a 'free ' boundary and a downstream location where out-flow takes place. Information must be provided about the values of the dependent variables or their normal

gradients at all these locations. The practices employed in the present study will now be outlined.

(a) INLET PLANE

At an inflow plane, it is necessary to supply distributions of all variables, including **U**, **V**, **W**, **k** and **ε**. Although pressure also appears as a dependent variable in the equations, boundary conditions for **p** are not needed at locations where the normal velocity is prescribed.

(b) WALLS

The application of boundary conditions at walls in turbulent flow requires a more elaborate treatment than at the inflow boundary. Thus, although the velocity components at the wall are set to zero, special formulae are necessary to calculate the resultant wall shear stresses. These, together with the boundary conditions on the turbulence parameters **K** and **ε**, are deduced from "wall functions". Details of these practices will be given in section 3.4.

(c) SYMMETRY PLANE

The boundary conditions at a plane of symmetry can be stated comparatively simply. The normal velocity is zero, and the gradient of other quantities normal to the boundary is zero,i.e.

$$d\phi/dn = 0.$$

(d) FREE BOUNDARY

Although a free boundary condition is not relevant in this study, brief comments are included for sake of completeness.

The conditions at a free boundary are in principle known from the distributions of velocity, turbulence energy, etc. in the external stream. In practice, this information is not always available in complete detail and the extent of the disturbances in the flow introduced by the obstacle is seldom known beforehand. Trial and error is therefore required to locate the computational free boundary sufficiently far from the obstacle that conditions imposed are without significant influence on the region of interest.

If these precautions are taken, constant values of streamwise velocity, k and ε can be specified along a free boundary in 2D flow. The normal velocity is set equal to zero.

(e) OUTLET PLANE

Provided that the downstream boundary is located where the velocity normal to the boundary is directed everywhere outwards, the "parabolic" or boundary layer nature of the flow there ensures that downstream conditions have no influence on the upstream flow. Hence, knowledge of these conditions is not required in the calculations. An exception to this rule is the normal velocity, which is needed in the absence of a specification for the streamwise

pressure gradient.

Fortunately a simple treatment of the following kind usually suffices. The outflow velocities are obtained by extrapolation from the adjacent upstream plane and then adjusted so as to satisfy overall continuity.

3.3 FINITE-DIFFERENCE EQUATIONS

3.3.1 FINITE-DIFFERENCE GRID AND CONTROL VOLUMES

To derive the finite-difference analogue of the differential equations consider a rectangular, three dimensional grid in cartesian coordinates as shown in Figure (3.1). A typical node "**p**" and its neighbours, labelled $\mathbf{X_-}$, $\mathbf{X_+}$, $\mathbf{Y_-}$, $\mathbf{Y_+}$, $\mathbf{Z_-}$, $\mathbf{Z_+}$, represent the locations at which all variables are calculated, except the three velocity components. **U**, **V** and **W** are calculated at points $(\mathbf{x_-}, \mathbf{x_+})$, $(\mathbf{y_-}, \mathbf{y_+})$ and $(\mathbf{z_-}, \mathbf{z_+})$ which respectively lie mid-way between the grid nodes, and are denoted by the arrows in Figure (3.1).

There are two advantages in so displacing the velocity locations.

Firstly, they lie mid-way between the locations of the pressures which drive them, and secondly, the velocities are directly available for calculation of convective fluxes across the faces of the imaginary control volume surrounding the central node as indicated in the Figure. One can obtain algebraic equations relating the value of ϕ at the grid point **p** to the values at the neighbouring grid

points by integrating the differential equation (3.11) over this control volume. It is necessary to make assumptions about the variation of ϕ between nodes.

The derivations of each of the finite-difference equations for continuity, ϕ and momentum, will be considered in turn.

3.3.2 CONTINUITY EQUATION

Integration of the continuity equation (3.5) over the control volume of Figure (3.1) gives:

$$A_x\{\rho_{x_+} U_{X_+} - \rho_{x_-} U_P\} + A_y\{\rho_{y_+} V_{Y_+} - \rho_{y_-} V_P\} + A_z\{\rho_{z_+} W_{Z_+} - \rho_{z_-} W_P\} = 0 \qquad (3.13)$$

where A_x, A_y and A_z are the areas of the **yz**, **xz** and **xy** faces of the cell, respectively. These areas are related to the cell dimensions $\Delta x, \Delta y$, and Δz (Figure (3.1)) as follows:

$$A_x = \Delta y \Delta z \qquad (3.14)$$

$$A_y = \Delta x \Delta z \qquad (3.15)$$

$$A_z = \Delta x \Delta y \qquad (3.16)$$

In equation (3.13), upper case subscripts stands for nodal values and lower case subscripts denote cell-interface values, as used in Figure (3.1). The densities at the faces of the control volume are calculated as the arithmetic means of the nodal values on either side of these faces,

e.g.

$$\rho_{z_+} = \frac{1}{2}\,(\rho_{z_+} + \rho_P) \qquad (3.17)$$

3.3.3 ϕ EQUATION

The finite-difference equation for the general variable ϕ is derived by integration of the differential equation (3.12) over the main control volume. The convection and diffusion terms will be considered separately from the source term, and then their contributions to the finite difference equation will be combined.

(a) CONVECTIVE AND DIFFUSION TERMS

The total transfer of ϕ by convection and diffusion across the faces of the cell is related to the weighted mean of the values at grid nodes on either side of the faces.
The integral expression for the total transfer can be approximated as

$$\int_{X_-}^{X_+}\int_{Y_-}^{Y_+}\int_{Z_-}^{Z_+}\left[\frac{d(\rho U\phi)}{dx} + \frac{d(\rho V\phi)}{dy} + \frac{(\rho W\phi)}{dz}\right.$$

$$\left. -\frac{d}{dx}\left(\Gamma_\phi \frac{d\phi}{dx}\right) - \frac{d}{dy}\left(\Gamma_\phi \frac{d\phi}{dy}\right) - \frac{d}{dz}\left(\Gamma_\phi \frac{d\phi}{dz}\right)\right]\, dx\, dy\, dz$$

$$-A_x\, g_{x_+}\,[(1-F_{x_+})\,\phi_{X_+} + F_{x_+}\,\phi_P] - A_x\, g_{x_-}\,[F_{x_-}\,\phi_{X_-} + (1-F_{x_-})\phi_P]$$

$$+A_y\, g_{y_+}\,[(1-F_{y_+})\,\phi_{Y_+} + F_{y_+}\,\phi_P] - A_y\, g_{y_-}\,[F_{y_-}\,\phi_{Y_-} + (1-F_{y_-})\,\phi_P]$$

$$+A_z\, g_{z_+}\, [(1-F_{z_+})\, \phi_{z_+} + F_{z_+}\, \phi_p] - A_z\, g_{z_-}\, [F_{z_-}\, \phi_{z_-} + (1-F_{z_-})\, \phi_p]$$

(3.18)

Where g_{x+}, g_{x-}, g_{y+}, g_{y-}, g_{z+}, g_{z-} are the mass fluxes of fluid crossing the faces of the cell; for example,

$$g_{z+} = \rho_{z+}\, W_{z+} \qquad \textbf{(3.19)}$$

F_{z+}, F_{z-}, etc. are weighting factors which will now be defined.

A proper weighting of the convective and diffusive terms across the control volume surface is essential to the accuracy and numerical stability of a finite-difference procedure. Three weighting schemes are in common use, namely, the central difference, upwind difference and "hybrid" schemes, the last of which is a combination of the first two. These schemes are outlined briefly here.

In the central difference scheme a linear variation of ϕ is presumed between grid nodes; the weighting factor F_{y+} (for example) is then:-

$$F_{y_+} = \frac{(1 + 2\, Pe_{y_+}^{-1})}{2} \qquad \textbf{(3.20)}$$

Pe_{y+} is the cell Peclet number at y_+ , defined as

$$Pe_{y_+} = \frac{g_{y_+}\, \delta_{y_+}}{\Gamma_{y_+}} \qquad \textbf{(3.21)}$$

The Peclet number is a measure of the ratio of convection flux to diffusive flux. Here, δ_{y+} denotes the distance between nodes (Figure (3.2)) and Γ_{y+} is the arithmetic mean of the values of Γ_ϕ at neighbouring nodes. When the convective flux becomes large relative to the diffusive flux, the central difference schemes fails to give stable and accurate solutions. It can be shown, Runchal [44], that when iterative methods of solution are employed the scheme is stable only for $|Pe|<2$.

The upwind difference scheme originally proposed by Gosman et al [26] and now widely used, is superior to the central difference scheme in that it is stable for all values of **Pe**. In this scheme, a linear variation in ϕ is assumed for the diffusive flux, but for the convective flux, the value of ϕ convected across a cell face is taken to be the value at the node on the upwind side of the face.

The weighting therefore varies according to the flow direction as follows:

$$F_{y_+} = 1+Pe_{y_+}^{-1} \qquad for\ Pe_{y_+} \geq 0 \qquad \textbf{(3.22)}$$

and

$$F_{y_+} = Pe_{y_+}^{-1} \qquad for\ Pe_{y_+} < 0 \qquad \textbf{(3.23)}$$

For the present investigation, the hybrid difference scheme, Spalding [45], was employed. In this scheme, improved accuracy and stability are obtained by employing central difference when $|Pe|<2$ and upwind difference when

|Pe|≥2. For large Peclet numbers, the diffusive flux may be neglected, leading to a simplification of equations (3.22) and (3.23). The weighting factors for the hybrid difference scheme are then

$$F_{y_+} = \frac{(1+2Pe_{y_+}^{-1})}{2} \qquad for\ |Pe_{y_+}| < 2, \tag{3.24}$$

$$F_{y_+} = 1 \qquad for\ Pe_{y_+} \geq 2 \tag{3.25}$$

and

$$F_{y_+} = 0 \qquad for\ Pe_{y_+} \leq -2 \tag{3.26}$$

(b) <u>SOURCE TERM</u>

The integration of the source term over the cell is

$$\int_{X_-}^{X_+} \int_{Y_-}^{Y_+} \int_{Z_-}^{Z_+} S_\phi \, dx \, dy \, dz = S_{\phi_p} \, \Delta x \, \Delta y \, \Delta z \tag{3.27}$$

where $S_{\phi\,p}$ is the average value of the source term over the cell centred at node **p**. For the purposes of later manipulation with $S_{\phi\,p}$ it is convenient to linearise it in the following way:

$$S_{\phi\,p} \, \Delta_x \, \Delta_y \, \Delta_z \equiv S^{\phi}_{U} + S^{\phi}_{p} \, \phi_p \tag{3.28}$$

where S^{ϕ}_{U} and S^{ϕ}_{p} are coefficients whose definition depends on the form of S_ϕ.

(c) FINITE-DIFFERENCE EQUATION FOR ϕ

The full finite difference equation for ϕ is obtained by combining equation (3.18) and (3.28), in a manner given in detail in Appendix (1).

The result is

$$C_p^{\phi}\phi_p = C_{X_+}^{\phi}\,\phi_{X_+} + C_{X_-}^{\phi}\,\phi_{X_-} + C_{Y_+}^{\phi}\,\phi_{Y_+} + C_{Y_-}^{\phi}\,\phi_{Y_-} + C_{Z_+}^{\phi}\,\phi_{Z_+} + C_{Z_-}^{\phi}\,\phi_{Z_-} + S_U^{\phi} \qquad (3.29)$$

where the coefficients have the definitions:

$$C_{X_+}^{\phi} = A_x\, g_{x_+}\,(F_{x_+}-1)$$

$$C_{X_-}^{\phi} = A_x\, g_{x_-}\, F_{x_-}$$

$$C_{Y_+}^{\phi} = A_y\, g_{y_+}\,(F_{y_+}-1)$$

$$C_{Y_-}^{\phi} = A_y\, g_{y_-}\, F_{y_-}$$

$$C_{Z_+}^{\phi} = A_z\, g_{z_+}\,(F_{z_+}-1)$$

$$C_{Z_-}^{\phi} = A_z\, g_{z_-}\, F_{z_-} \qquad (3.30)$$

and

$$C_p^{\phi} = C_{X_+}^{\phi} + C_{X_-}^{\phi} + C_{Y_+}^{\phi} + C_{Y_-}^{\phi} + C_{Z_+}^{\phi} + C_{Z_-}^{\phi} - S_p^{\phi} \qquad (3.31)$$

3.3.4 MOMENTUM EQUATIONS

(a) z-MOMENTUM EQUATION

The derivation of the finite-difference momentum equations is facilitated by their similarity with the conservation equation for ϕ, equation (3.12).

The **z**-momentum equation is integrated over the **W**-control volume shown in Figure (3.2). It should be noted that the **W**-control volume is shifted relative to the ϕ control volume such that the **xy** faces pass through the node **p** and the upstream neighbouring grid node Z_-. The velocity component W_p associated with the node **p** is located at the point z_- in the centre of the volume.

By analogy with equation (3.29), the finite-difference form of the **z**-momentum equation is

$$C_p^W W_p = C_{X_+}^W W_{X_+} + C_{X_-}^W W_{X_-} + C_{Y_+}^W W_{Y_+} + C_{Y_-}^W W_{Y_-} + C_{Z_+}^W W_{Z_+} + C_{Z_-}^W W_{Z_-}$$

$$+ S_U^W + A_Z (p_{Z_-} - p_p) \qquad (3.32)$$

(b) LATERAL MOMENTUM EQUATIONS

Specially displaced computational cells are also employed for the lateral velocities **U** and **V**. The y-momentum cell in Figure (3.3) is shifted such that the **xy** faces pass through **p** and Y_-, and the **x**-momentum cell is similarly shifted in

Figure (3.4).

The finite-difference equations for $\mathbf{U_p}$ and $\mathbf{V_p}$ obtained by integrating the relevant momentum equations over these cells are

$$C_p^V V_p = C_{X_+}^V V_{X_+} + C_{X_-}^V V_{X_-} + C_{Y_+}^V V_{Y_+} + C_{Y_-}^V V_{Y_-} + C_{Z_+}^V V_{Z_+} + C_{Z_-}^V V_{Z_-}$$

$$+ S_U^V + A_y (p_{Y_-} - p_p) \qquad \textbf{(3.33)}$$

and

$$C_p^U U_p = C_{X_+}^U U_{X_+} + C_{X_-}^U U_{X_-} + C_{Y_+}^U U_{Y_+} + C_{Y_-}^U U_{Y_-} + C_{Z_+}^U U_{Z_+} + C_{Z_-}^U U_{Z_-}$$

$$+A_x (p_{X_-} - p_p) \qquad \textbf{(3.34)}$$

Here, the areas $\mathbf{A_x}$ and $\mathbf{A_y}$ are determined from the dimensions of the **U** and **V** cells, as shown in Figures (3.3) and (3.4). There are related to the grid spacings as explained in Appendix (1) section 1.2, parts (b) and (c), where full definitions of the coefficients are given.

3.3.5 TREATMENT OF BOUNDARY CONDITIONS

(a) INLET PLANE

The specified distributions of ϕ are assigned to the appropriate grid nodes in the entry plane of the solution

domain.

(b) WALLS

At solids boundaries the computational grid is modified as shown in Figure (3.5), such that the boundary passes through ϕ nodes, and the locations at which the normal velocity component (in this case, **V**) is calculated are altered from their usual positions so that they also lie on the boundary node, therefore coinciding with the ϕ nodes. Boundary conditions of the specified value type can now be applied by simply assigning the required values of ϕ at the boundary node.

A zero flux boundary condition is achieved by setting to zero the coefficient in the finite-difference equation for the near-boundary cell. For example; if the boundary lies at the 'y_-' face of the cell, the coefficient $C^{\phi}_{y_-}$ in equation (3.29) becomes zero.

Details of the further special practices required for turbulent flows are given in Appendix (1).

(c) SYMMETRY PLANE

At a symmetry plane, the convection and diffusion fluxes are both zero. The condition for convection is imposed by setting the velocity component normal to the boundary to zero. Diffusion can be made zero by way of the flux coefficient Γ_ϕ at the boundary.

(d) FREE BOUNDARY

At a free boundary, specific values are assigned to all variables as described in section 3.2.4.

(e) OUTLET PLANE

The treatment at the outflow boundary, outlined in section 3.2.4(e), requires attention only to the normal velocity component; in the example of Figure (3.6), this is the **W**-component. The practice adopted for this quantity ensures that mass conservation is satisfied for the whole solution domain. The velocity W_{z+} imposed at point Z_+ in the outflow plane is deduced by multiplying the adjacent upstream velocity, W_p, by a factor **f** such that

$$W_{z_+} = f\, W_p \qquad (3.35)$$

The factor **f** is defined as

$$f = m_{in} / m_{out} \qquad (3.36)$$

in which m_{in} and m_{out} are the net mass inflow and outflow of fluid across the upstream and downstream boundaries respectively. As the solution proceeds to convergence, **f** tends to unity, as overall continuity for the solution domain is achieved.

The set of finite difference equations (section 3.3) was solved by an iterative method, called SIMPLE, which is outlined in Patankar and Spalding [40], and Caretto et al. [24]. Appendix (1) contains a complete description of the procedure.

3.4 TURBULENT WALL FUNCTIONS

It has been mentioned that the turbulent model employed in this study is restricted to regions of a flow where the turbulence Reynolds number ($K^{1/2}\ell/\upsilon$) is high; thus it is not applicable to the viscous sublayer of a wall boundary layer. Although the model can be modified to apply to the sublayer regions, Jones and Launder [29], its incorporation into a finite difference calculation scheme for three-dimensional flows would be uneconomical because of the very large number of grid nodes and long computing times required.

An alternative approach avoids the low Reynolds number region by bridging edge to those at the wall. The origins and application of these "wall functions" are described by Patankar and Spalding [39], and Launder and Spalding [33], [34]. Wall function relations are derived from experimental and analytical knowledge of the one-dimensional Couette flow which exists very near the wall.

(a) WALL FUNCTIONS EMPLOYED

The basis of the wall functions used in the present study is as follows.

The variation of the resultant velocity U_w in the region near the wall is assumed to follow a logarithmic law. For a smooth wall, this law can be expressed as:

$$U_w = \frac{U_\tau}{k} \ln(Ey^+) \qquad (3.37)$$

where

$$U_w = \sqrt{U^2+W^2} \qquad (3.38)$$

$$U_\tau = \left(\frac{\tau_s}{\rho}\right)^{1/2} \qquad (3.39)$$

and

$$y^+ = \frac{\rho y_p U_\tau}{\mu} \qquad (3.40)$$

Here, U_τ is the "friction velocity", τ_s is the resultant shear stress and y_p is the normal distance from the wall as shown in Figure (3.5). κ and E are constants whose values are given in Table (3.2).

Information about the turbulence kinetic energy in the near-wall region is obtained from experiment. Tennekes and Lumley [46], found that k is proportional to the shear stress, which in this region is essentially uniform, and equal to the wall value, τ_s. Thus,

$$\frac{\tau_s/\rho}{k} \approx constant = 0.3$$

This relation may be also derived from limiting versions of the k and ε equations, (A1.90) and (A1.92), near the wall (Launder and Spalding 1972).

These give

$$k = \frac{U_\tau^2}{C_\mu^{1/2}} \qquad (3.41)$$

from which the value of the constant C_μ may be deduced.

The variation of the dissipation near a wall is determined from the kinetic energy equation. Within the near-wall region, convection and diffusion of kinetic energy are negligible and equation (A1.88) becomes simply

$$\epsilon = \frac{\tau_s}{\rho}\frac{dU_w}{dy} \qquad (3.42)$$

Combining equations (3.42), (3.39) gives the required value of the dissipation:

$$\epsilon = \frac{U_\tau^3}{ky} \qquad (3.43)$$

(b) INCORPORATION OF WALL FUNCTIONS INTO BOUNDARY CONDITIONS

The wall functions are incorporated into the boundary conditions by modification of the exchange coefficient Γ_ϕ. For the velocity component **U** parallel to the wall, Γ_ϕ depends on the value of y^+ at the near wall node p in Figure (3.5). Using the most recent value of **k**, y^+ is found from the equation

$$y^+ = \frac{\rho k^{1/2} C_\mu^{1/4} y_P}{\mu} \qquad (3.44)$$

which is obtained by combining equations (3.40) and (3.41). The exchange coefficient for the velocity component **U** parallel to the wall may then be modified using the relationship

$$\Gamma_\phi = \frac{\mu k y^+}{\ln(Ey^+)} \qquad (3.45)$$

y^+ should exceed 11.5 to ensure that application of a turbulent wall function is appropriate. Γ_ϕ is then used to modify the source term of the **W**-momentum equation to the form

$$S_\phi = \frac{\Gamma_\phi \Delta x \Delta z}{y_P}$$

where S_ϕ is the normal source term as given in Table (3.1). A similar modification is made to the source term for **U**.

For the velocity, **V**, normal to the wall, the continuity equation applied to a one-dimensional flow gives **dV/dy =0**, and so the normal stress at the wall must be zero. This condition is conveniently incorporated into the computations by setting the exchange coefficient to zero, i.e. $\Gamma_\phi = 0$.

In applying a boundary condition for **k**, the diffusion of kinetic energy near a wall is negligible and so Γ_ϕ is set

to zero. Generation of kinetic energy is, however, important in this region and the source term for **k** must be corrected using the available values of τ_s. For this purpose, τ_s is calculated from equations (3.37) to (3.40) rearranged in the form

$$\tau_s = \frac{y^+ \mu k U_w}{y_p \ln(Ey^+)} \qquad (3.46)$$

wherein U_w is found from the latest value of **U** and **W**, via equation (3.38).

The source term for **k** is finally obtained as the volume-averaged rate of generation across the ϕ cell in Figure (3.5), i.e.

$$\bar{G} = \frac{1}{(vol)} \int_{vol} \tau \frac{dU_w}{dy} \, d(vol) \approx \tau_s \frac{(U_w)_{y_+}}{\Delta y} \qquad (3.47)$$

where $(U_w)_{y+}$ is the resultant velocity at point y_+. **G** is used to modify the source term of kinetic energy for the near-wall cells, in place of the normal expression for generation.

An exchange coefficient for ε at the wall is not calculated; rather, the practice is to replace the finite difference equation at the near-wall node by the log law-based relation given by equation (3.43). For convenience within the computational procedure this equation is replaced by the equivalent expression

$$\epsilon = \frac{C_\mu^{3/4} k^{3/2}}{ky} \qquad (3.48)$$

Table (3.2) lists the values of the various constants in the turbulence models. The values were determined approximately from data for simple turbulent flows and were then optimised by predictions for a wide range of flow situations. Further details of the evaluation of these constants have been given by Launder and Spalding [33].

3.5 CONCLUSIONS

This Chapter has presented the equations of motion and a method for their solution for three-dimensional turbulent flow of a uniform property fluid. The partial differential equations of continuity and conservation of momentum were given in time-dependent and time-averaged forms, and a general conservation equation for any property ϕ was formulated.

Finite difference versions of the equations of continuity and ϕ conservation were derived by integrating the partial differential equations over a micro control volume centred at a representative node of the finite difference grid. The special practices in integrating the momentum conservation equations, needed because of the staggered grid adopted, were also mentioned. Procedures used in the treatment of the boundary conditions were considered.

The method of solution of the finite difference equations was outlined, with particular attention to the momentum equations where a "guess and correct" process is used, based on an estimated pressure field and approximate relations between the velocity and pressure corrections. Methods to enhance numerical stability were summarised, and criteria were stated to check on the convergence and accuracy of the solutions.

Finally, wall functions were presented which describe the low Reynolds number flow in the vicinity of solid boundaries of the solution domain.

TABLE 3.1: EXCHANGE COEFFICIENTS AND SOURCE TERMS

Quantity ϕ	Exchange coefficient Γ_ϕ	Source term S_ϕ
U	μ_{eff}	$\frac{d}{dx}(\mu_{eff}\frac{dU}{dx}) + \frac{d}{dy}(\mu_{eff}\frac{dV}{dx}) + \frac{d}{dz}(\mu_{eff}\frac{dw}{dx}) - \frac{dp}{dx}$
V	μ_{eff}	$\frac{d}{dx}(\mu_{eff}\frac{dU}{dy}) + \frac{d}{dy}(\mu_{eff}\frac{dv}{dy}) + \frac{d}{dz}(\mu_{eff}\frac{dw}{dy}) - \frac{dp}{dy}$
W	μ_{eff}	$\frac{d}{dx}(\mu_{eff}\frac{dU}{dz}) + \frac{d}{dy}(\mu_{eff}\frac{dV}{dz} + \frac{d}{dz}(\mu_{eff}\frac{dW}{dz}) - \frac{dp}{dz}$
k	$\frac{\mu_{eff}}{\sigma_k}$	$G-\rho\varepsilon$
ε	$\frac{\mu_{eff}}{\sigma_\varepsilon}$	$\frac{\varepsilon}{k}(C_1G-C_2\rho\varepsilon)$

TABLE 3.2: TURBULENCE MODEL CONSTANTS

Constant	Value	Method of evaluation
C_μ'	0.09	Near wall measurements of $\tau_s/(\rho k)$
σ_k	0.9	Computer optimisation
σ_ε	1.085	
C_1	1.43	Near wall turbulence measurements
C_2	1.92	Decay of turbulence behind a grid
κ	0.4	Velocity measurements in Couette flows
E	9.0	

FIGURE 3.1: 3D CONTROL VOLUME FOR ϕ's

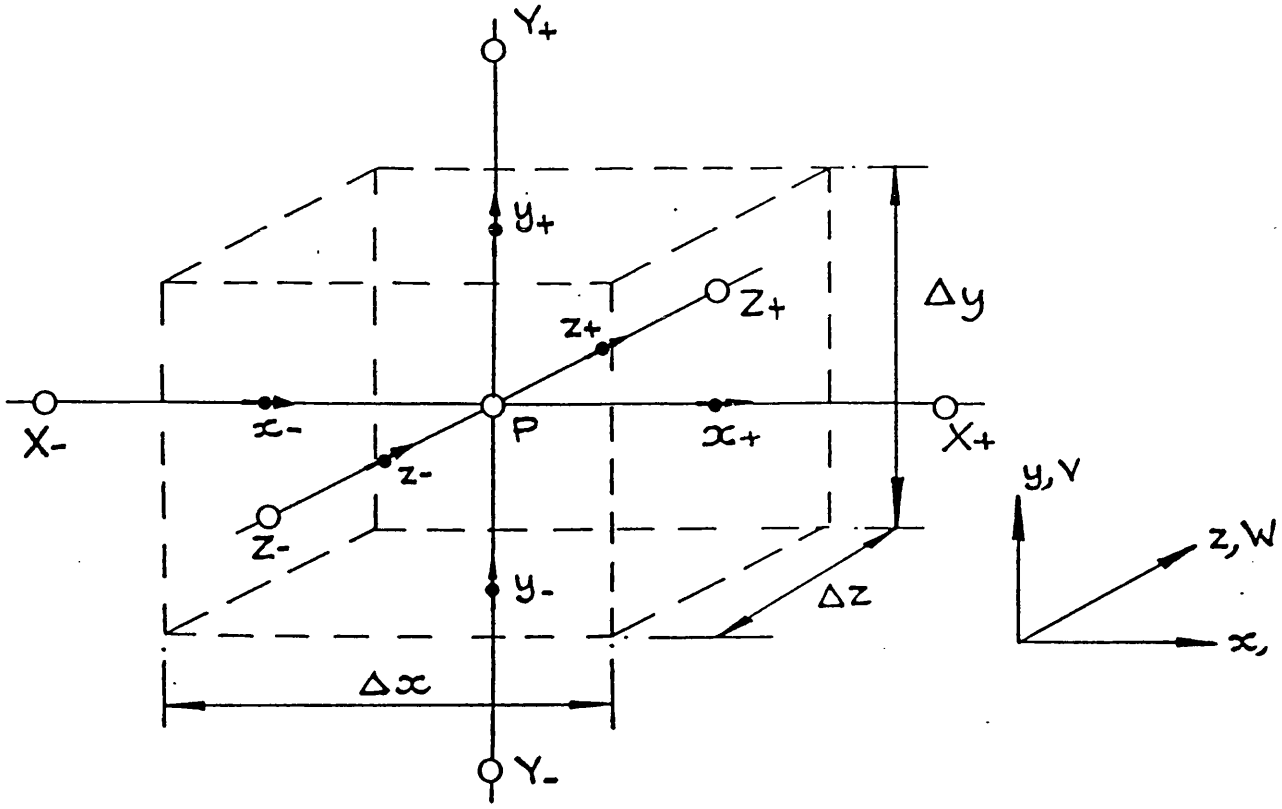

FIGURE 3.2: CONTROL VOLUMES FOR ϕ's AND W

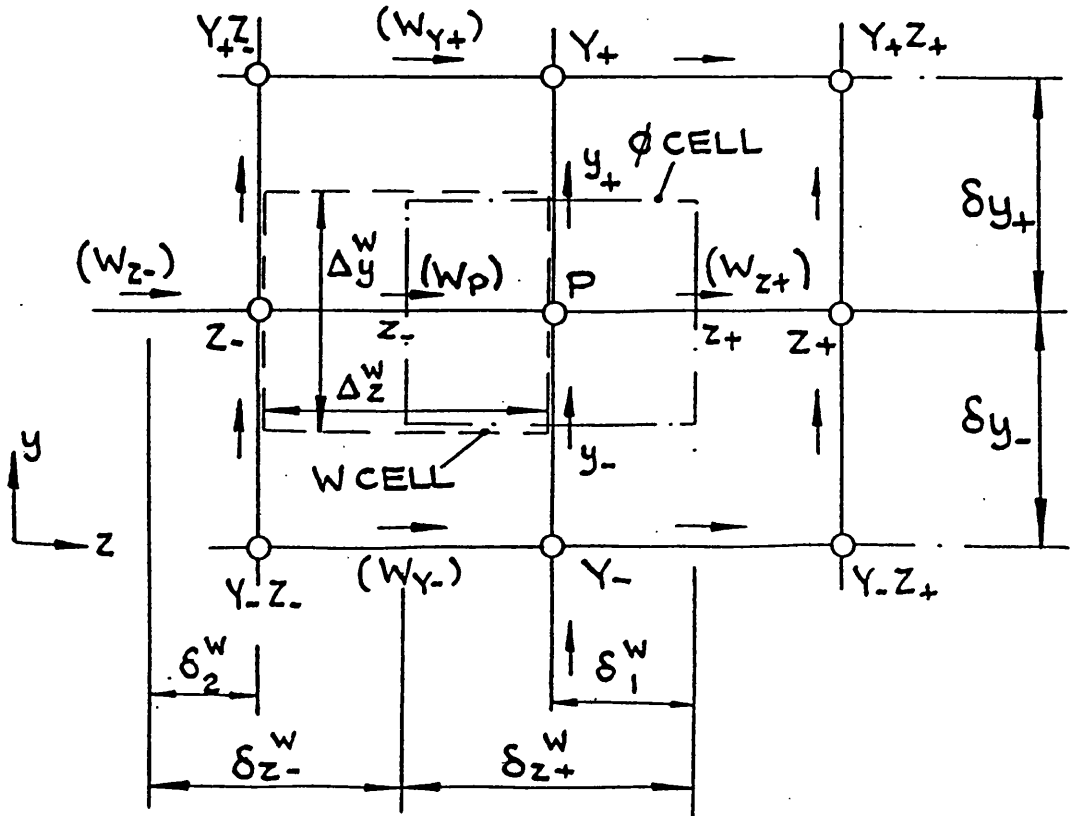

FIGURE 3.3: CONTROL VOLUMES FOR φ's AND V

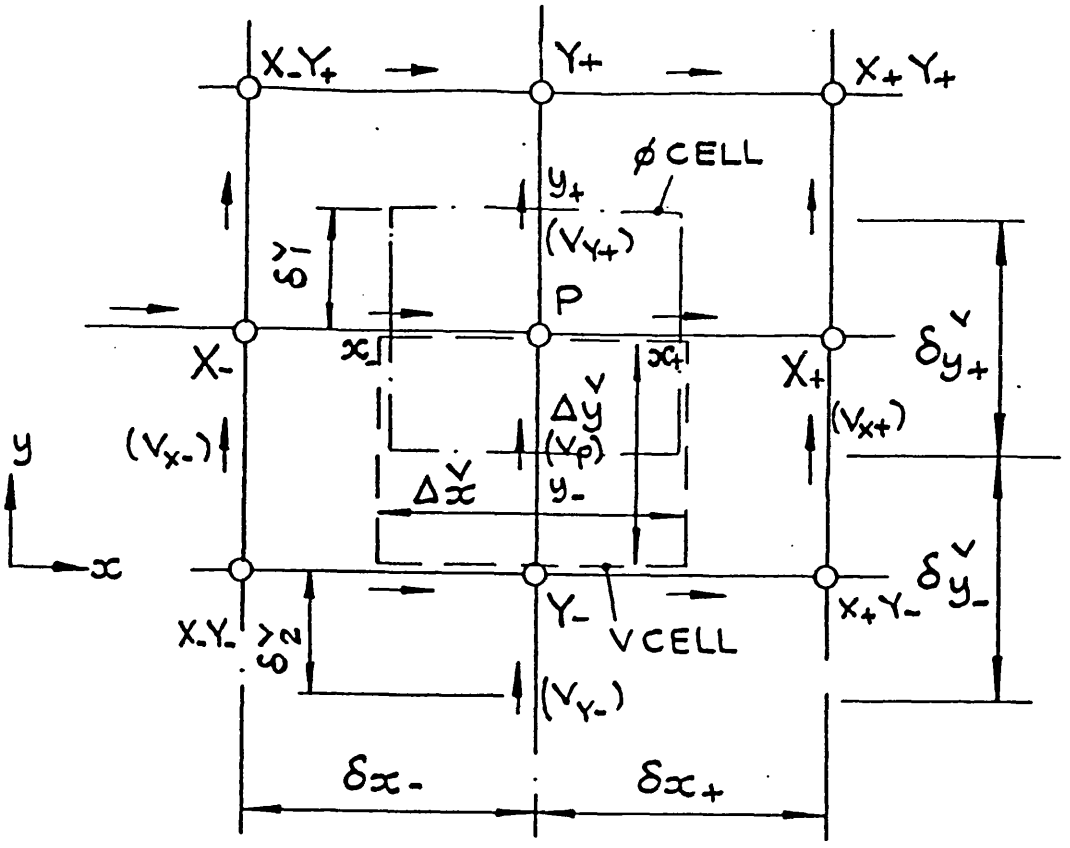

FIGURE 3.4: CONTROL VOLUMES FOR φ's AND U

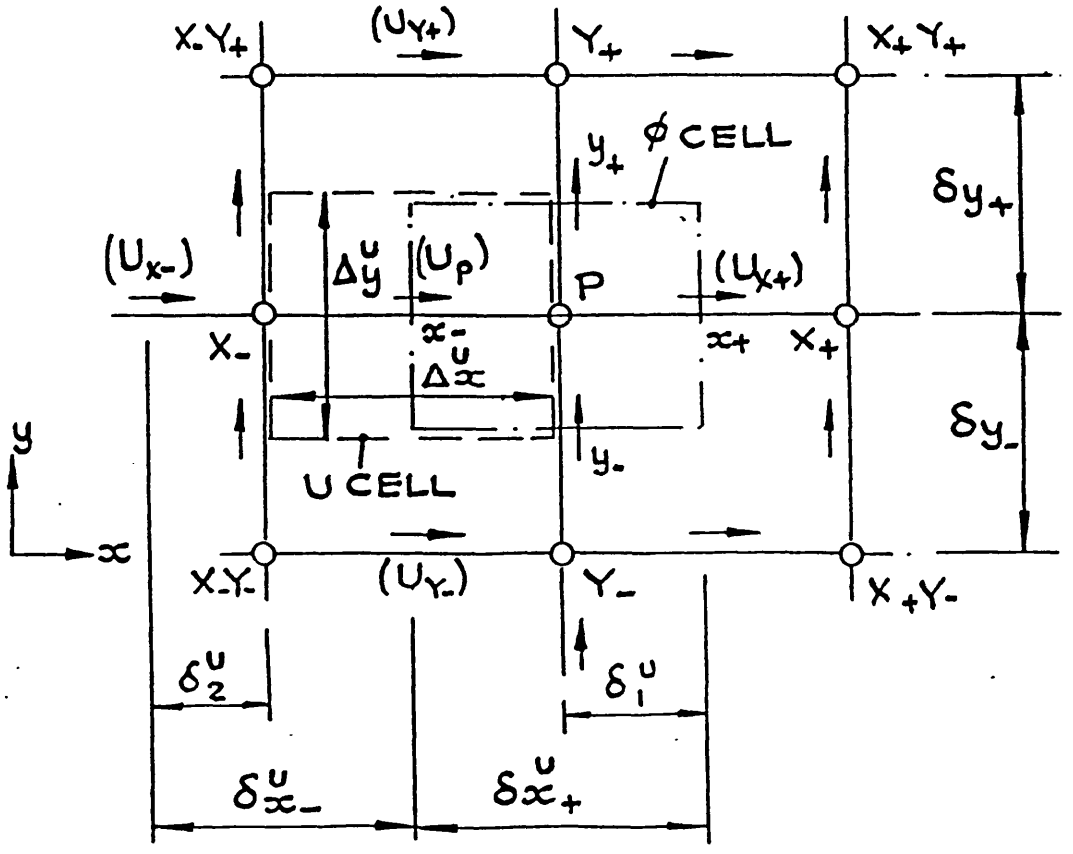

FIGURE 3.5: WALL BOUNDARY CONTROL VOLUMES FOR ϕ's AND V

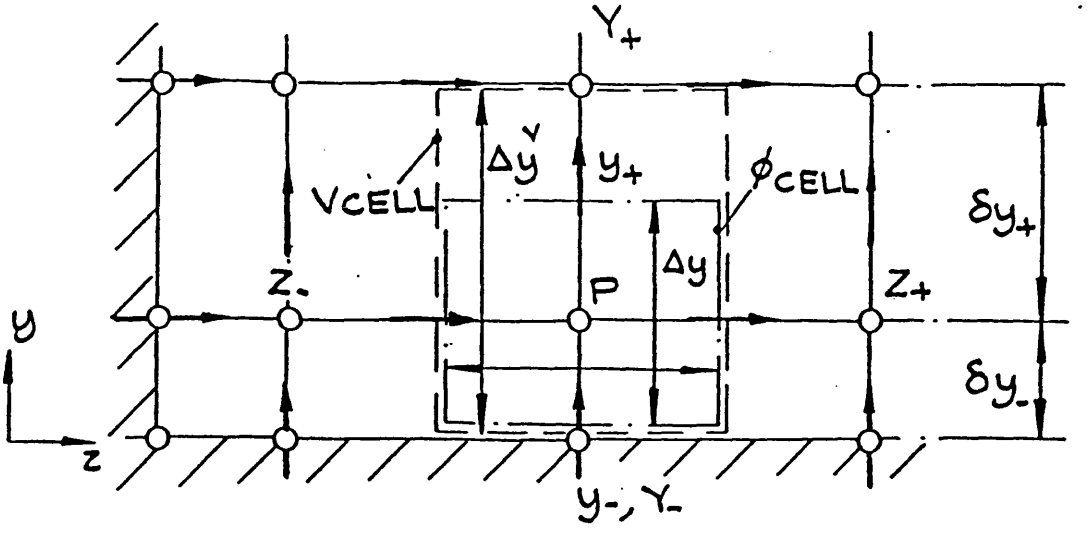

FIGURE 3.6: OUTLET BOUNDARY CONTROL VOLUMES FOR ϕ's AND W

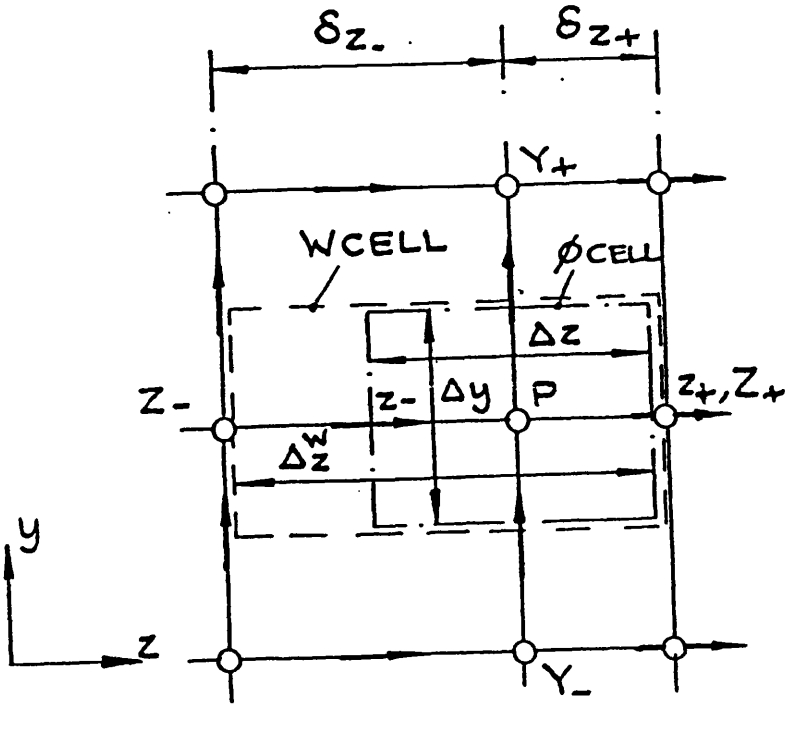

CHAPTER [4]

THE PHOENICS FLUID DYNAMICS PROGRAM

4.1 INTRODUCTION

The CFD package used in this study is PHOENICS version 1.4 developed and marketed by CHAM 1987. The program was run on a SUN4 Spark station. The following sections describe both the package itself, and the additional programming work, carried out by the author, which was necessary for this particular application.

4.2 HOW PHOENICS DESCRIBES PHYSICAL PHENOMENA

(a) DEPENDENT VARIABLES

PHOENICS describes a phenomenon involving the flow of heat or material in terms of distributions in space and time of the dependent variables, p, v, t etc.

(b) INDEPENDENT VARIABLES

In general, a phenomenon simulated by PHOENICS will be four-dimensional; one time and three space dimensions. The latter are called: north-south; east-west; and high-low.

(c) AUXILIARY VARIABLES

Auxiliary variables are distinguished from dependent variables by being derived from algebraic equations rather

than from differential ones. When auxiliary variables are constants, they are represented in PHOENICS as scalars.

(d) DISCRETISATION OF THE CONTINUA

The locations in space and time at which pressure and other scalar dependent variables are computed are finite in number; and they are imagined to lie within a finite set of 'cells' which, added together, make up the whole space-time domain being considered, Figure (4.1). The statement about the dependent-variable locations being within the cells requires modification; PHOENICS computes values of velocities for locations on the walls of the cells. Figure (4.2) illustrates this, a single cell with four of its neighbours being shown in plan view. Temperatures, pressures are evaluated by PHOENICS for the locations such as **P, N, S, E, W** which lie within cells; but west-to-east velocities are evaluated for the locations like **s** and **n**. This convention is called the 'staggered-grid' arrangement.

4.3 THE COMPUTATION OF DEPENDENT VARIABLES

For each dependent variable ϕ, there are as many algebraic equations as there are cells in the integration domain. Thus, there are a set of **NX*NY*NZ** algebraic equations for each dependent variable. In addition to there being a large number of unknowns, the sets of equations are often strongly coupled. PHOENICS therefore solves them in an iterative manner, the object of which is to reduce the

imbalance between the left and right sides of every equation to a magnitude which is acceptably small.

The iterative process involves a multi-stage sequence of adjustments of values, repeated many times. Iteration is needed because although each algebraic equation is linear the fundamental relations are non-linear. The non-linearities are exerted by the functional dependence of the coefficients and sources upon the auxiliary and dependent variables.

Figure (4.3) portrays the 'slab' of cells at constant grid index **IZ**. The strip of cells at constant grid index **IZ** for the two-dimensional **y-z** case is shown in Figure (4.4).

Problems not characterised as parabolic may be elliptic; this means that influences are exerted in both the positive and negative directions for all existent space dimensions. The distinction between elliptic, parabolic and hyperbolic-flows is represented in Figure (4.5) which depicts, for each case, the domain of influence of a small disturbance. In parabolic flows the disturbance has no effect upstream, and in the hyperbolic case region of influence is restricted to the Mach cone. In time however, influences proceed in only one way, from 'early' to 'late'. This is why PHOENICS never needs four-dimensional storage of its dependent variables.

PHOENICS solves discretised versions of the equations; applying them over the sub-domains, or cells, into which the region has been divided. Each cell is topologically cartesian, thus in the general 3D case the cell has six

sides and eight corners.

Within a cell is a typical grid node for which the fluid property values, ϕ's, are regarded as representative of the whole cell. The velocity components are stored on the faces of the cells and thus collectively constitute a staggered grid as shown in Figure (4.6). Thus, the velocity nodes are midway between the pressure nodes.

The pressure difference is seen as a driving potential for the velocity. Integration over each cell leads to a "finite-domain" equation with each grid point ϕ connected with its seven neighbouring grid points, namely the locations at north, south, east, west, high, low and previous time.

4.4 SOLUTION PROCEDURE

The solution of the finite-difference equation employs pressure and velocity as the main flow variables. The "staggered" grid is used to link the pressure and velocity fields. The sequence of the numerical solution may essentially be listed as follows:

(i) The pressure field is estimated

(ii) The corresponding velocity field is computed from the momentum equations

(iii) The resulting errors in the continuity equations are computed

(iv) The errors are then used to correct the pressure field

(v) The sequence is repeated iteratively.

During the solution PHOENICS employs repeated **z**-direction sweeps through the integration domain. The whole set of cells is regarded as consisting of one-cell-thick slabs, extending in the **x** and **y** directions, and piled on top of one another in the **z**-direction. A sweep starts at the bottom (low-**z**) slab using the existing values in the cells. The finite domain equations are solved for all the cells in the slab, the value of ϕ'**s** at the next higher slab being regarded as known. Attention then moves to the next higher slab, the ϕ values adjusted in reference to those slabs above and below. The process is continued until the sweep is completed.

At the end of a sweep the errors are computed. Each dependent variable must satisfy a continuity type equation. After the first sweep the final solution will not have been achieved so the process is repeated until the difference in ϕ between successive sweeps falls within specified limits. In the program the number of sweeps to be performed at each time-step can be set. Thus, once this number has been achieved the solution will automatically move on to the next time-step regardless of whether the continuity errors have fallen to within the desired limits.

Clearly some experimentation is required to set the optimum number of sweeps for any particular problem. A high number of sweeps will result in improved accuracy but there will be a trade-off in the length of the computer run times.

4.5 COMPONENTS OF PHOENICS

PHOENICS consists of two essential computer codes and two auxiliary ones. Data-flow structures for the four programs are in Appendix (2). The essential codes are a pre-processor called SATELLITE and a processor called EARTH. The auxiliary codes are a post-processor called PHOTON and a separate self-instruction program called GUIDE.
The relationships of EARTH to SATELLITE and PHOTON are illustrated in the Figure (4.7).

4.6 METHOD OF ANALYSIS

4.6.1 THE EQUATION SOLVED

The general, single-phase, three-dimensional steady-state conservation equation solved by PHOENICS was shown in Chapter (3) equation (3.11).
The variables which have been solved for this case are:
u1, v1 - velocity components in the two coordinate directions **x** and **y** respectively;
k -turbulent kinetic energy;
ε -rate of dissipation of **k**; and
h -stagnation enthalpy.
The pressure, **p**, does not appear explicitly as the subject of a conservation equation, but is deduced from the continuity equation.

4.6.2 THE SOURCE TERMS

In this section, the source terms are given in the integrated form used in the finite-difference equations; that is they represent the total source of a variable for a finite-difference cell of volume **V**. The source terms are given in the cartesian coordinate system.

(i) The momentum equations

The sources in the momentum equation are:

$$S_{u1} = -dp/dx\ V - \tau_w.A \qquad (4.1a)$$

$$S_{v1} = -dp/dy\ V - \tau_w.A \qquad (4.2b)$$

where τ_w is the wall shear stress; and **A** the wall surface area in a cell parallel to the velocity component in question.

The wall shear stress is calculated from the logarithmic law of the wall, as described later.

(ii) The turbulence equations

The turbulence model used is the high Reynolds number two - equation **k-ε** model of Harlow and Nakamaya [47], as developed by Launder and Spalding [34]. The model is used in its unmodified form, and all the empirical constants take their usual values.

The source terms for the turbulence equations away from the body surface are:

$$S_k = (G_k - \rho\ \varepsilon)V \qquad (4.3)$$

$$S_\varepsilon = (2.4402\ G_k - 1.9202\ \rho\ \varepsilon)\ \varepsilon V/k \qquad (4.4)$$

where

G_k - generation of k by shear;

ρ - density

Adjacent to the body surface, the values of k and ε are fixed to wall values, as given in section 4.6.4.

The generation term, G_k is defined as:

$$G_k = \mu_t\ [2(du^2/dx + dv^2/dy) + (du/dy + dv/dx)^2] \qquad (4.5)$$

where μ_t is the turbulent viscosity defined as:

$$\mu_t = C_\mu\ \rho\ k^2/\varepsilon \qquad (4.6)$$

and C_μ is a constant, 0.09.

(iii) <u>The continuity equation</u>

There are no source terms in the continuity equation, other than boundary sources.

(iv) <u>The enthalpy equation</u>

The source in the enthalpy equation is:

$$S_{h1} = -\ q''_w \qquad (4.7)$$

where q''_w is the heat-transfer rate to the body surface. Its derivation is given in section 4.6.4.

4.6.3 THE EXCHANGE COEFFICIENTS

The exchange coefficients are defined as:

Continuity: $\Gamma_\Phi = 0.0$

Momentum: $\Gamma_\Phi = \mu_{eff}$

Turbulence: $\Gamma_k = \mu_{eff}/\sigma_k$; $\Gamma_\varepsilon = \mu_{eff}/\sigma_\varepsilon$

Enthalpy: $\Gamma_h = \mu_{eff}/\sigma_h$

where:

μ_{eff} = effective viscosity = $\mu_t + \mu_l$;

μ_l = laminar viscosity ;

σ_h = 0.7 ;

σ_k = 1.0 ; and

σ_ε = 1.314.

The above numerical values selected are based on the work of Harlow and Nakamaya [47], as developed by Launder and Spalding [34].

4.6.4 WALL SHEAR STRESS AND HEAT-TRANSFER

At the surface, the wall shear stress and heat-transfer rate are calculated using the logarithmic 'law of the wall'. These conditions are applied to the near-wall grid node which resides in the constant-stress layer. This is known as the wall-function method (Chapter (3) equation (3.37)).

Equation (3.41) in Chapter (3) implies that the local skin-

friction coefficient, C_f, may be obtained from:

$$C_f = 2/(U^+)^2 \qquad (4.8)$$

The wall heat-transfer rate is evaluated from the Chilton - Colburn form of the Reynolds analogy, in which the Stanton Number is related to the friction coefficient by the relation:-

$$St = 1/2\ C_f\ Pr^{-2/3} \qquad (4.9)$$

where P_r = laminar Prandtl Number. The wall heat flux is calculated from the rate equation:-

$$q''_w = St\ \rho\ U\ (h_p - h_w) \qquad (4.10)$$

h_p = enthalpy at near-wall grid node, and h_w = the enthalpy at the specified surface temperature.
The relationships described here are valid in the range $30 < y^+ < 150$; this places a constraint on the location of the near-wall grid points.

4.7 INITIAL FLOW OVER BLOCKS

In the description that follows it is important to stress that using PHOENICS involved a lengthy learning process, the writer having no previous experience of the package. Setting up the model, defining the geometry, boundary conditions, etc, is perhaps the easiest part. The difficulty arises in assessing the validity of the

assumptions made and results obtained. Throughout the work a step- by- step approach was adopted. At each stage some attempt was made to verify results from the model before advancing to the next stage. When possible simple checks were performed, and where this was not possible, every attempt was made to ensure that the results appeared to be reasonable.

Only in this way was it possible to gain confidence in the predicted results as the simulation models became more complex.

4.7.1 CONSTRUCTION OF THE MODEL FOR FLOW OVER BLOCKS

The basis for the construction of the initial model was a PHOENICS library case 4.6. This model detailed is based on a flow over a backward facing step which exhibits both recirculation and turbulence. Following the procedure outlined in the previous sections the necessary information was entered into the satellite.

At first heat transfer was not considered, turbulence was simulated by the use of a two-parameter **(K-ε)** model. The initial geometry of the model is shown in Figure (4.8) and the grid setting is shown in Figures (4.9) and (4.10). At the wall boundary regions shown, the no-slip conditions were applied, and the "wall function" (see section 3.4 in Chapter (3)) was included for the near wall values of the dependent variables.

4.8 ASSESSMENT AND VALIDATION OF RESULTS

Having run the program and ensured that it was working correctly it then was necessary to verify the validity of the output. For the first case with no heating, the two velocity components i.e, **U** and **V** were compared with the experimental velocity components.

To complement this CFD investigation, an extensive program of experimental research was carried out in which a Laser Doppler Anemometer was used to measure air velocity. This experimental work will be fully described in Chapters (7) and (8).

For the inlet velocity of 5m/s, the **U** and **V** components of velocity from experiment were compared with PHOENICS output at different locations. Then the characteristics of the flow over the first block, and its effect on the flow over the second and third, was examined in detail.

Analysis of the monitor printout containing information on convergence continuity errors, etc. obtained from the PHOENICS model indicated that the solution had converged. In solving a finite-difference problem various factors influence the solution, namely:

(a) number and distribution of grid points,

(b) limits set on termination criteria; and,

(c) sweep and iteration numbers.

In optimising the parameters for a particular problem there is no quick and easy method. The only guide-line is to experiment with settings until a point is reached where

further refinement results in no significant changes being noted. However, it is possible, especially as the number of grid nodes is increased, to reach a point where further numerical accuracy is offset by unacceptable computational expense.

The effect of grid spacing on the solution was studied by increasing the number of cells near the walls. Originally the mesh size employed was **125*10**. By sub-dividing the grid further **180*25** it was thought that convergence would be improved, leading to better agreement between the predictions of the velocities. This of course improved the flow definition. It was also considered likely that the wall conditions would require further adjustment. Typical PHOENICS output showing the predicted velocity fields in **x**-plane, is shown in Figure (4.11). Velocity profiles such as these are systematically analyzed in Chapter (5).

4.9 CONJUGATE HEAT TRANSFER

Up to this stage only velocities had been calculated and checked. However since a principal objective was to study conjugate heat transfer, in the next stage it was necessary to calculate temperatures, and to determine the heat transfer coefficients.

A simple case was considered in which the fluid flows through a duct with an internal obstacle, and the duct wall and obstacle have finite thickness and moderate

conductivity. The thermal boundary condition is known at the outer surface of the wall, for instance as a prescribed temperature of that surface. This case represents a conjugate heat transfer problem in that conduction in the solid and convection in the fluid must both be considered, with a proper matching at the fluid-solid interface.
The calculation of separate solutions for the solid and fluid regions would require an involved iterative procedure to match the interface conduction. The harmonic-mean practice for diffusion coefficient offers a much easier alternative that has been described in Patankar [48].

HARMONIC MEAN METHOD

For the finite-difference solution of heat conduction, it is shown that, in the case of non-uniform thermal conductivity the heat flux across the face between two finite-difference cells can be accurately represented by the harmonic mean of the conductivities of the two cells, rather than by the arithmetic mean. The resulting method can handle large discontinuities in thermal conductivity (and other transport properties). A further advantage of the method is that it can be used for fluid-flow calculation in arbitrary geometries by representing the solid regions outside the fluid domain simply as regions of very high viscosity. The method is particularly attractive when a conjugate heat transfer problem involving conduction in the solid and convection in the fluid is to be solved.

In this procedure, the problem is solved by using an overall solution domain within which both fluid and solid regions are included, with the outer surface of the wall coinciding with the boundary of the domain. The boundary conditions for both the velocity and temperature fields are then supplied at the outer overall boundary of the solution domain.

SOLVING FOR VELOCITY AND TEMPERATURE

When the velocity equations are solved, Γ for the grid points that fall in the fluid region is made equal to the viscosity of the fluid, while for the grid points lying in the solid region is set equal to a very large number. This would ensure that the zero velocity specified at the outer surface of the wall would prevail throughout the solid region, and thus the fluid region would experience the correct boundary condition.

To solve the temperature equation, we specify the Γ field by employing the true conductivities of the solid and of the fluid in their respective regions. The problem is solved as a convection-conduction problem throughout the entire calculation domain. However because the velocities in the solid are zero, (the Peclet number in the solid is also zero) a pure-conduction calculation would be performed in the solid region.

The resulting solution should thus give the temperature distribution in the solid and in the fluid, and these would

have been automatically matched at the solid-fluid interface. As far as the calculation is concerned, this interface is simply an interior location, which is treated like any other interface between two control volumes.

Therefore, in order to achieve the above procedure, in the PHOENICS program the main input file (**Q1** file) together with the GROUND subroutine needed some modification so that the correct temperature fields together with correct values of heat transfer coefficient could be calculated. Appendix (2) highlights these settings.

To solve a coupled solid-fluid heat transfer problem a procedure was adopted to solve for temperature directly, using a modified form of the PHOENICS enthalpy **(H1)** equation (4.10).

As it was mentioned above, in conjugate-heat-transfer problems, i.e. problems in which the conductivity has large discontinuities between solid and fluid zones, harmonic averaging should be adopted for the temperature variable, to secure the correct heat flux across solid-fluid interfaces.

Figure (4.12) shows typical PHOENICS output of the predicted temperature fields in **x**-plane.

4.10 SATELLITE PROGRAM

In setting up the model initially, it is necessary to work through the various groups of the SATELLITE program setting variables and including FORTRAN code to define the problem

properly.

In this section the modified input file (**Q1** file) is described for the final model as follows:-

Group 3 180 grid cells are used for the whole field. A non-uniform grid is used to produce a very fine grid near the boundary and a coarse grid in the central region of the flow field.

Group 4 is the same as group 3 but for the vertical direction. In addition, the dimension is different.

Group 7 the variables to be solved are pressure (**P1**), the velocity components in **x**- and **y**-directions (**U1** and **V1**) and the enthalpy (**H1**) as well as the turbulence energy (**KE**) and dissipation rate of turbulence energy (**EP**). The pressure is solved by the whole-field method.

Group 8 the hybrid interpolation scheme is activated.

Group 9 a constant density is assigned for **RHO1**.

Group 11 uniform initial values are employed for the variables solved.

Group 13 boundary conditions are set in this group. The no slip conditions are prevailed on every walls. Heat flux values are set on the base of the each block. The generalised wall function method is used under this group.

Group 15 the sweep number is set to value of 300.

Group 17 the linear model of under-relaxation is only

applied for **P1** with a value of 0.5. The false-time-step model is used for the rest of variables solved. The values are set to 0.1.

Group 19 in this group data is communicated by SATELLITE to GROUND. The variable exchange coefficient is also activated.

Group 22 the spot-value is chosen at 80th grid in **x**-direction and 15th grid in **y**-direction for monitoring the convergence solution.

Complete listing of modified **Q1** file, GROUND and GREX2 subroutines are shown in Appendix 2(a), (b) and (c). The additional coding required "ground" to calculate **h** and **Nu** and is highlighted in Appendix (2b).

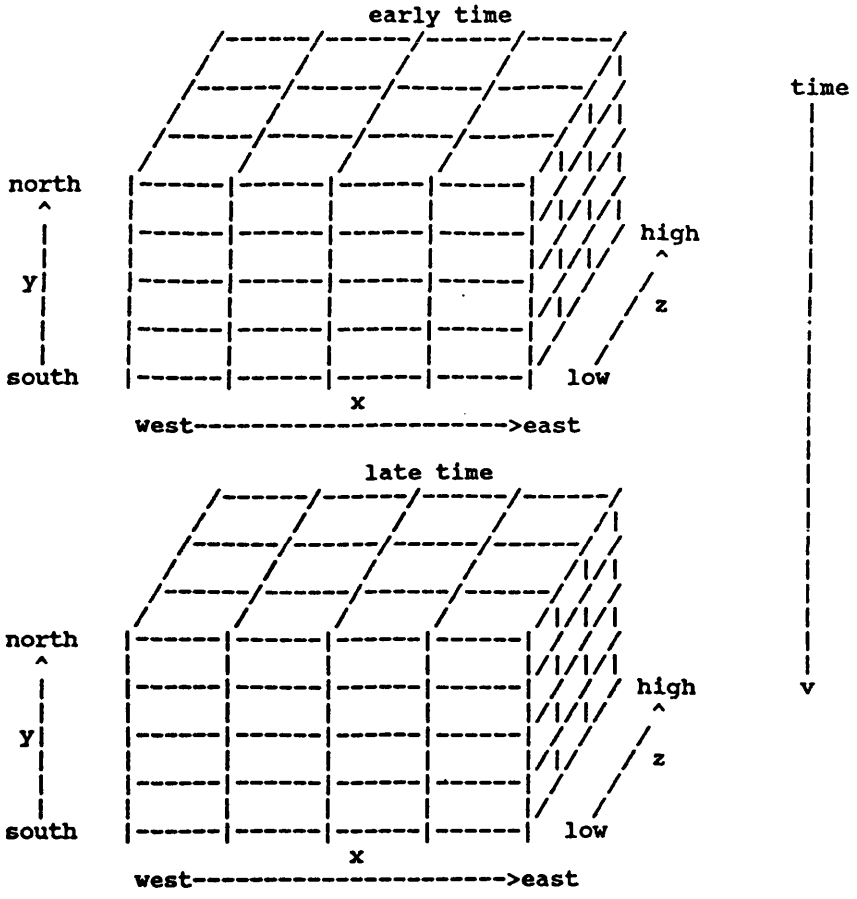

FIGURE 4.1: LOCATION IN SPACE AND TIME

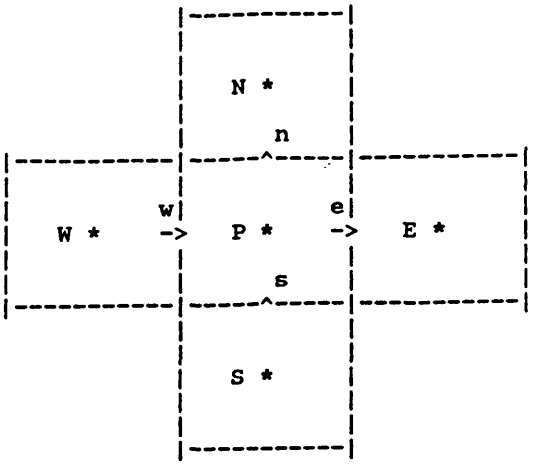

FIGURE 4.2: SINGLE CELL WITH FOUR OF ITS NEIGHBOURS IN PLAN VIEW

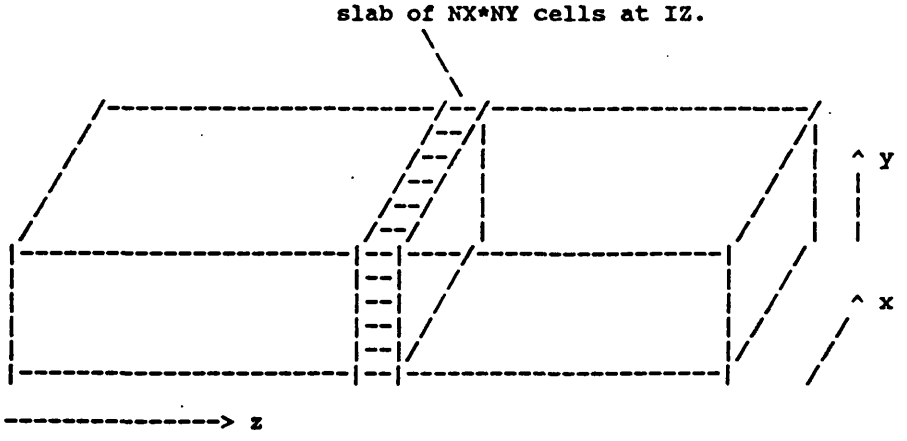

FIGURE 4.3: SLAB OF CELLS AT CONSTANT GRID INDEX IZ

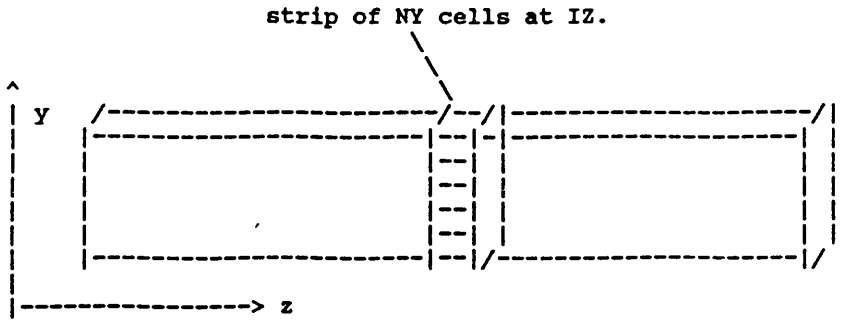

FIGURE 4.4: STRIP OF CELLS AT CONSTANT GRID INDEX IZ FOR THE TWO-DIMENSIONAL y-z CASE

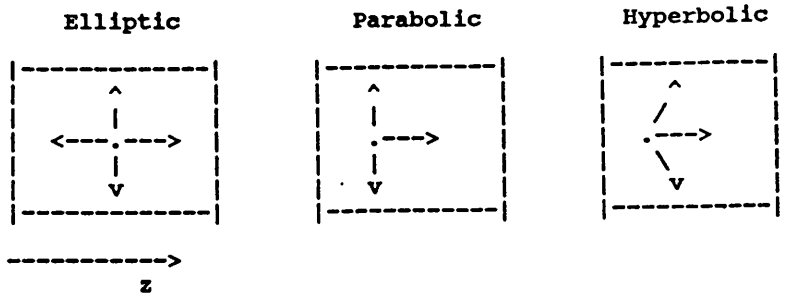

FIGURE 4.5: DISTINCTION BETWEEN ELLIPTIC, PARABOLIC AND HYPERBOLIC FLOWS

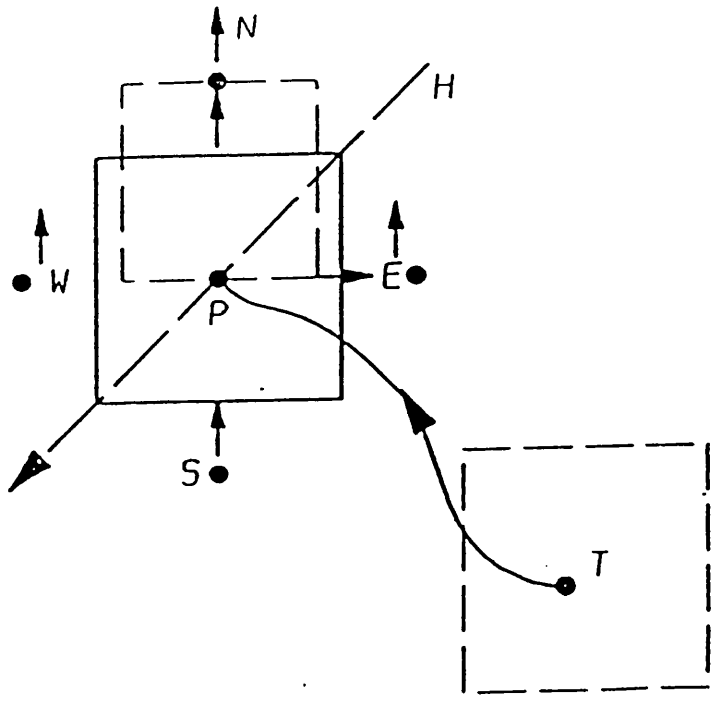

FIGURE 4.6: CELL DEFINITION WITHIN THE PHOENICS PROGRAM

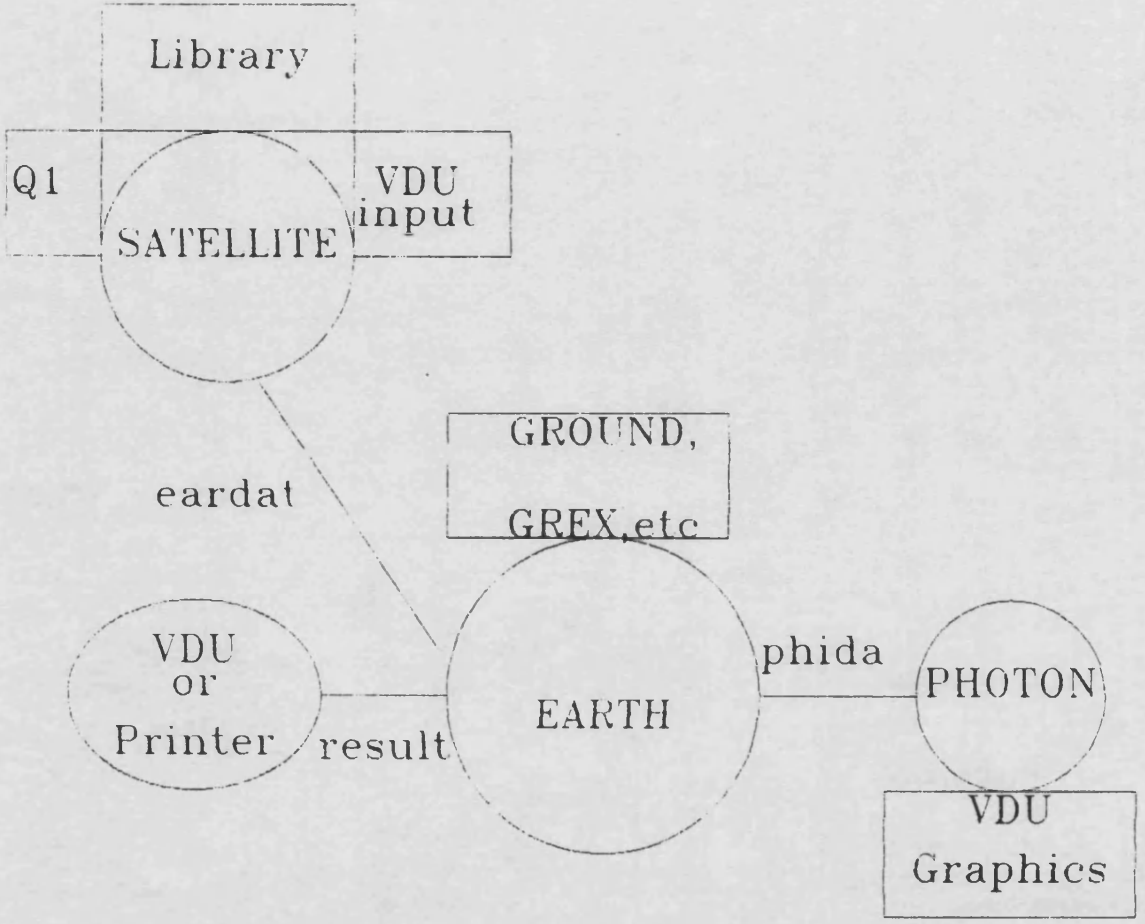

FIGURE 4.7: RELATIONS BETWEEN THE PHOENICS PROGRAMS AND SUBROUTINES

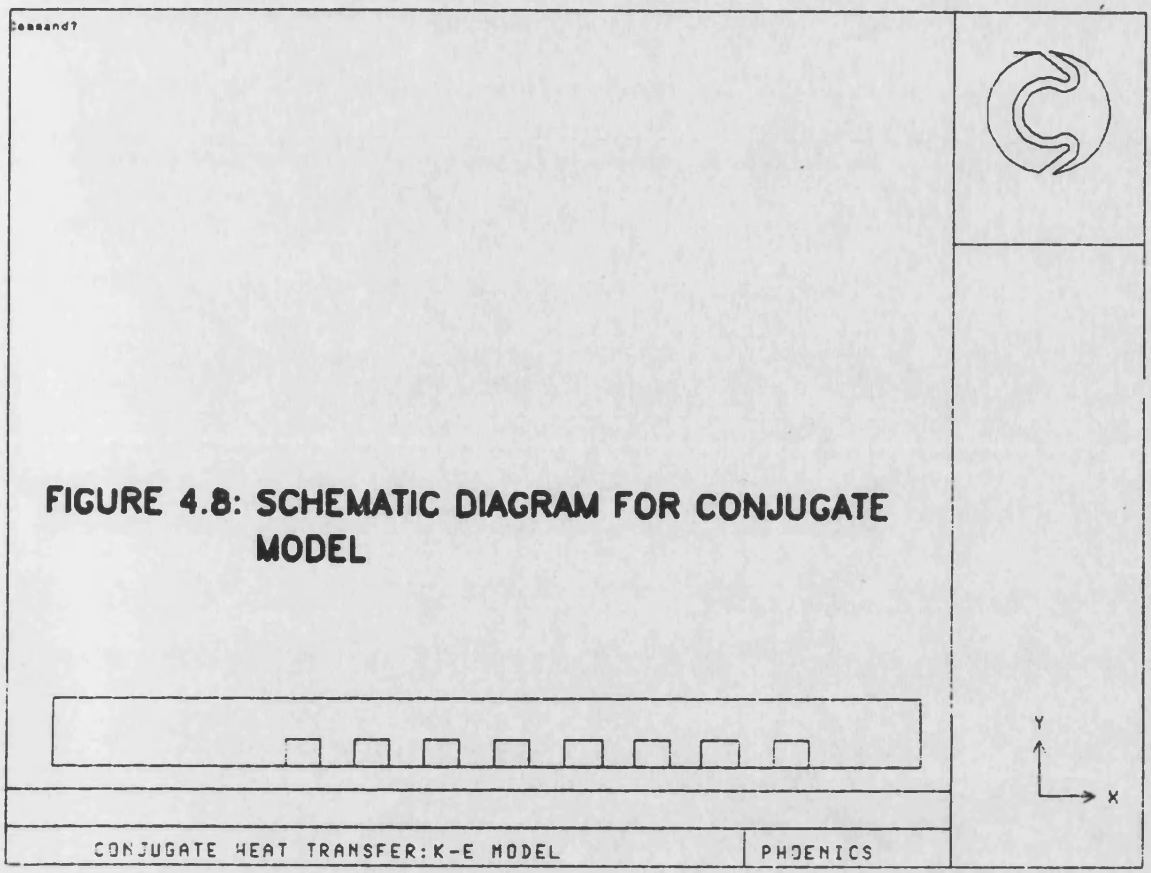

FIGURE 4.8: SCHEMATIC DIAGRAM FOR CONJUGATE MODEL

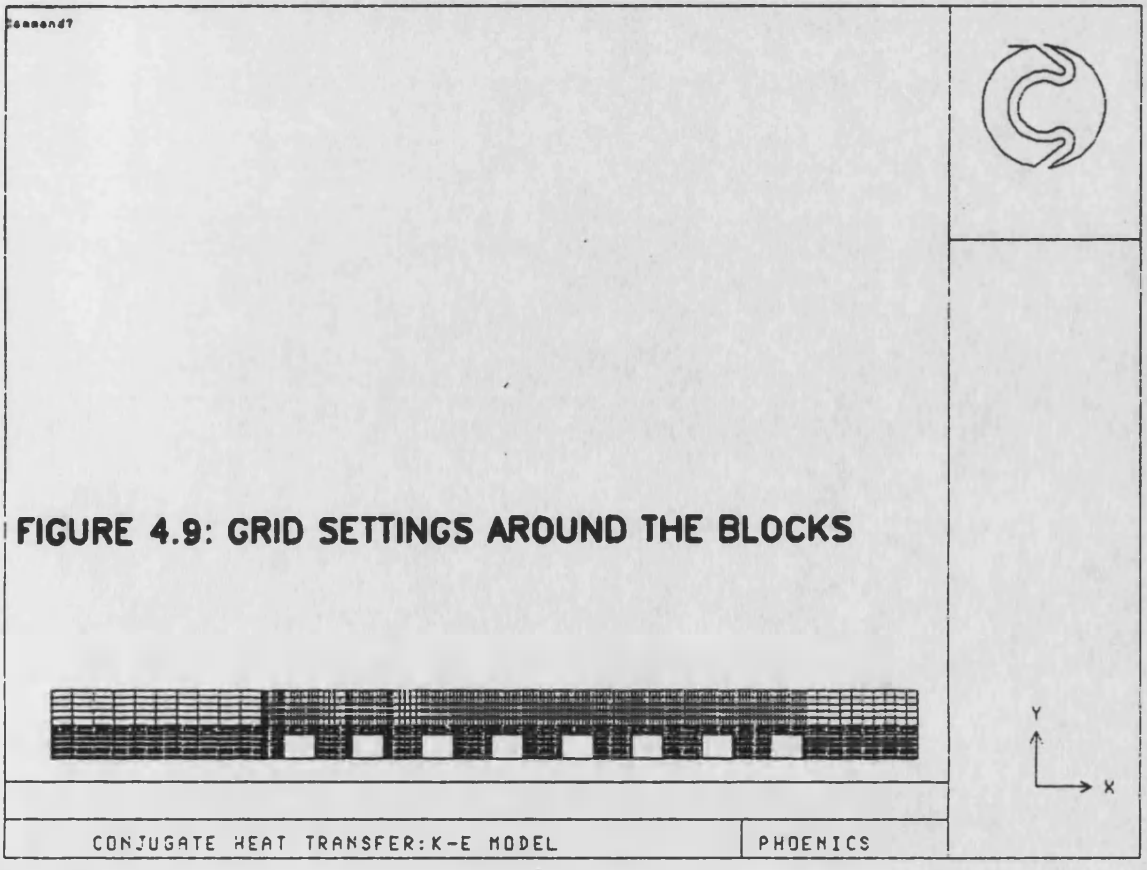

FIGURE 4.9: GRID SETTINGS AROUND THE BLOCKS

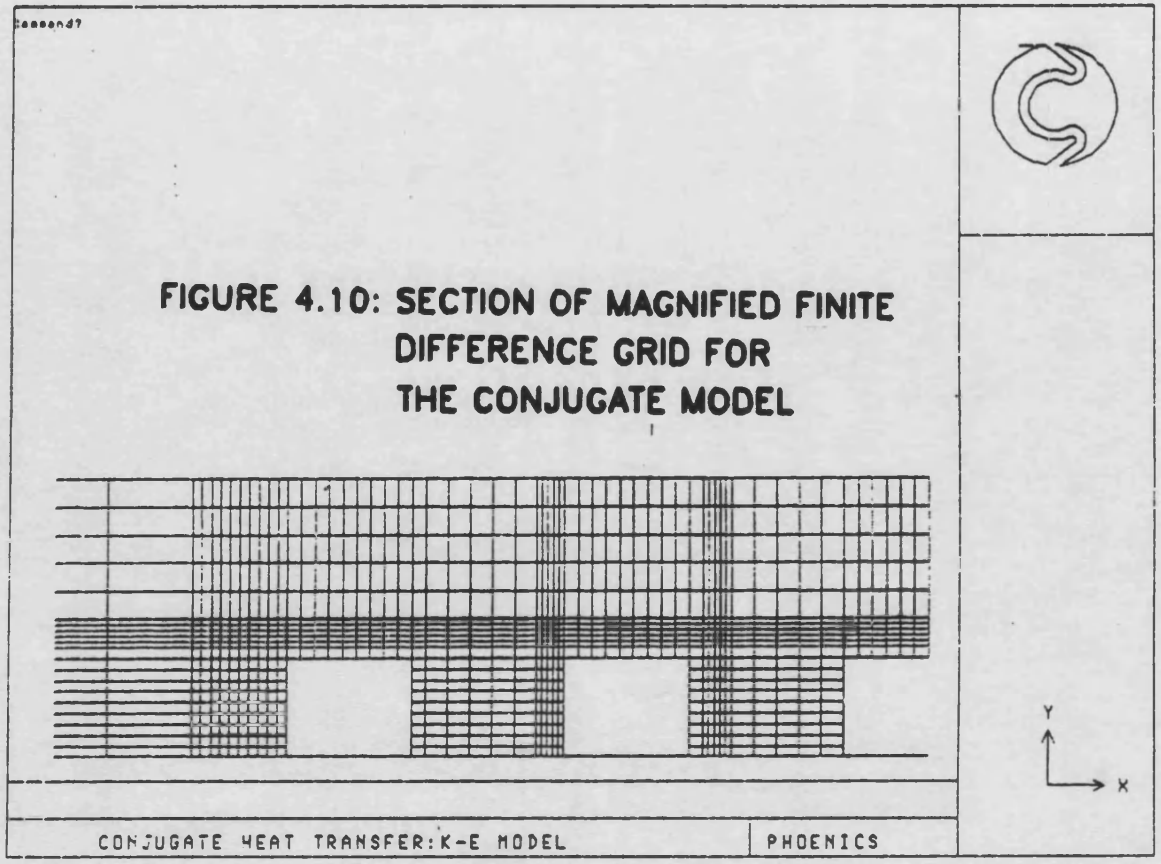
FIGURE 4.10: SECTION OF MAGNIFIED FINITE
DIFFERENCE GRID FOR
THE CONJUGATE MODEL
Y
X
CONJUGATE HEAT TRANSFER:K-E MODEL
PHOENICS

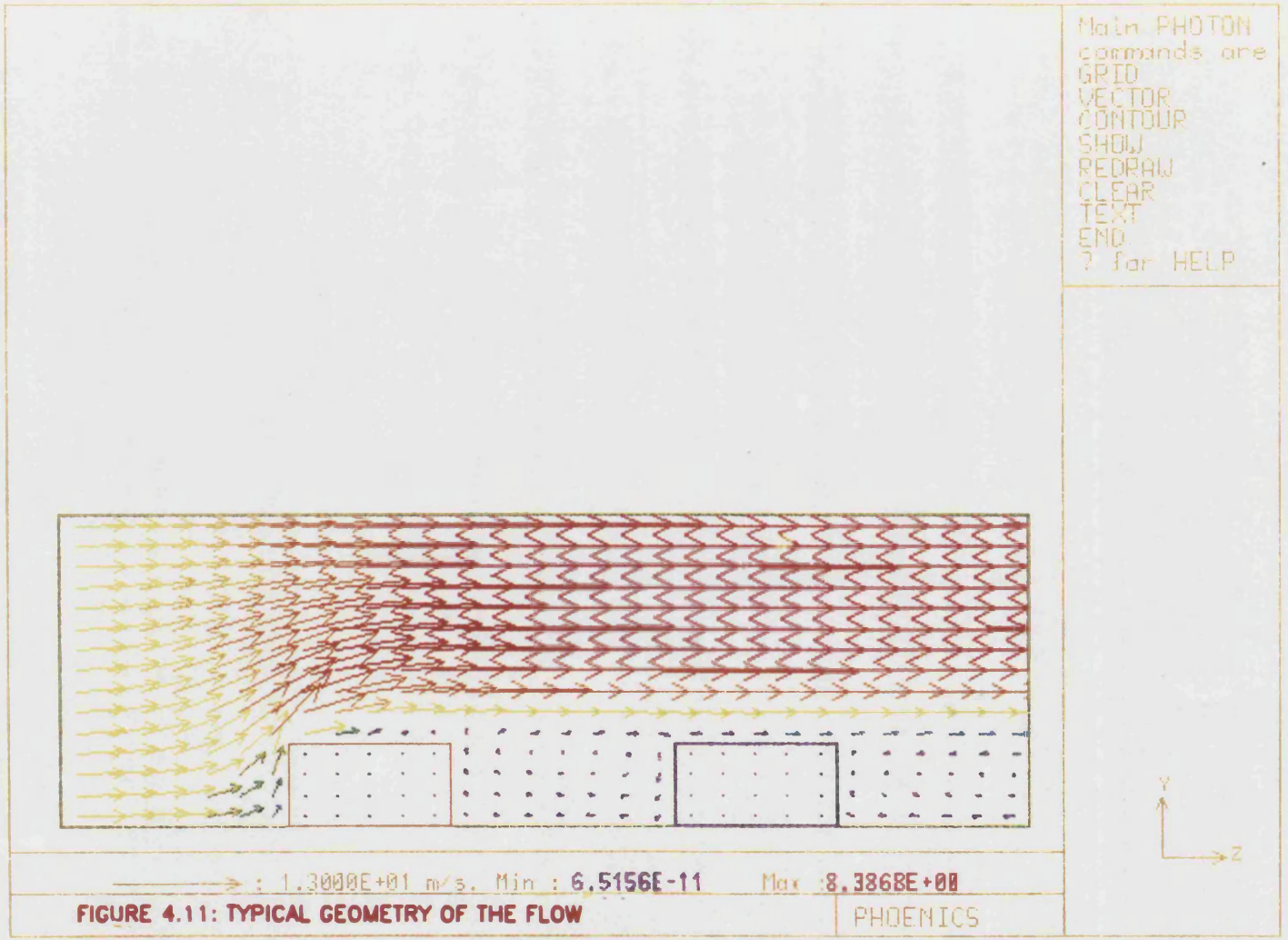

FIGURE 4.11: TYPICAL GEOMETRY OF THE FLOW

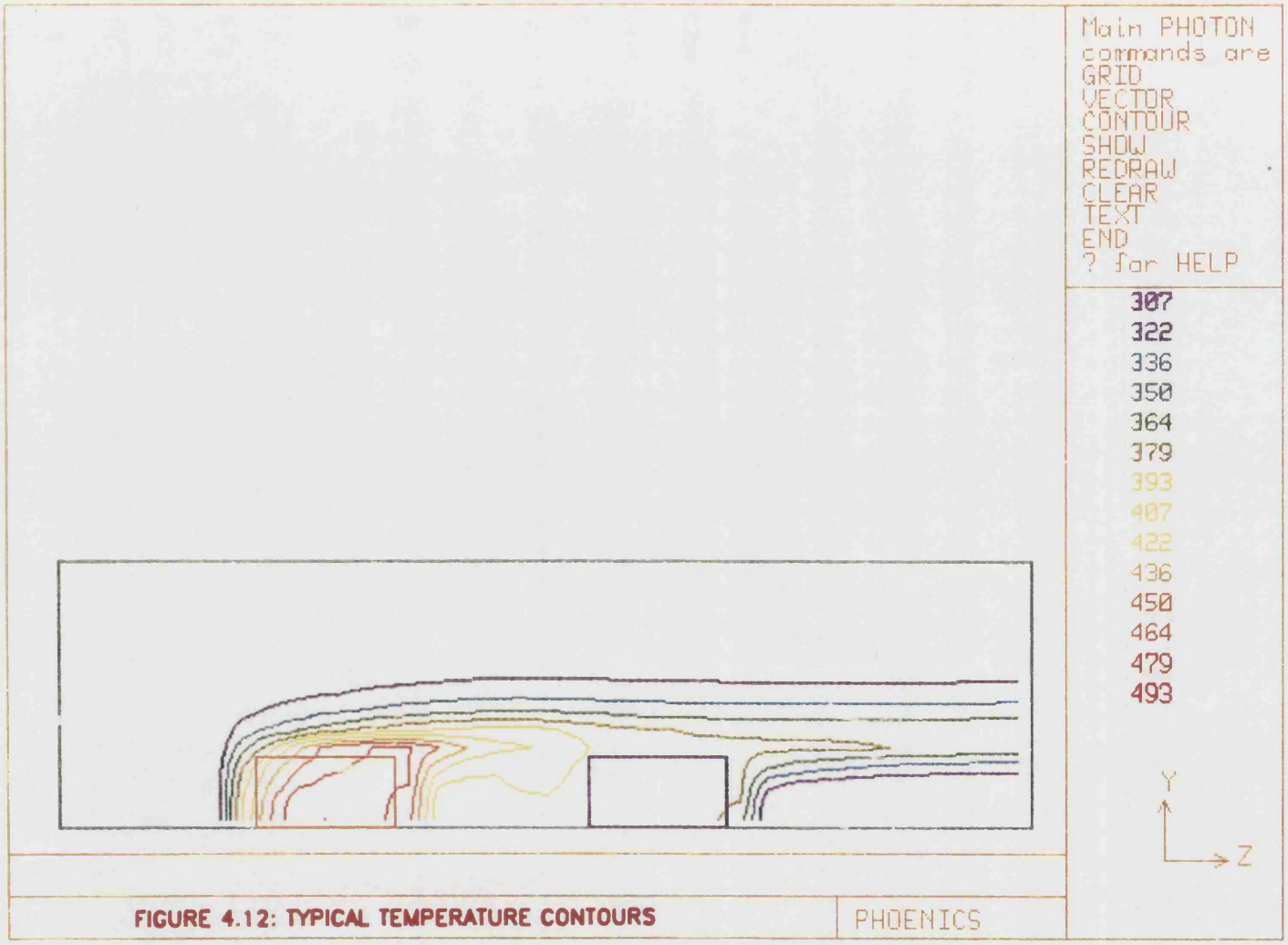

FIGURE 4.12: TYPICAL TEMPERATURE CONTOURS

CHAPTER [5]

COMPUTATIONAL PREDICTION OF TWO-DIMENSIONAL FLOWS OVER BLOCKS

5.1 INTRODUCTION

Details of the geometry and boundary conditions relevant to the above case are outlined in section 5.2. The description of an overall model is presented in section 5.3. In section 5.4 grid dependence tests are described. Predicted velocity distributions are presented in section 5.5, which also contains a comparison of these predictions with experimental data. In sections 5.6 and 5.7 the effect on the velocity distribution of making a series of parametric changes to the geometric boundary conditions is presented. Section 5.8 is an introduction to vector plots.
Finally section 5.9 concludes the Chapter.

5.2 GEOMETRY AND BOUNDARY CONDITIONS

For prediction purposes the flow is assumed to be two-dimensional constant property flow over a series of square-section aluminium blocks Figure (5.1).
To effect the solution of the foregoing system of equations presented in Chapter (3), the region of interest is overlaid with a rectilinear grid system with unequal spacing in the **y**- direction. In this grid layout, nodes are

more closely spaced in the vicinity of solid boundaries and in the shear layer where steeper gradients of the dependent variables are expected. The calculation domain in the **y**-direction is extended to a distance sufficient to make sure that for the smallest value of the Reynolds number the top plane lies well outside of the boundary layer region over the top of the blocks.

The numerical procedure used is based on the iterative scheme outlined in Chapters (3) and (4). This procedure used the hybrid central/upwind difference scheme for the convection terms with central differences for the diffusion terms.The procedure incorporates the SIMPLE solution technique initiated by Patankar and Spalding [40]. This technique is based on the solution of difference equations obtained by integrating the differential equations for momentum and energy over the control volumes enclosing the nodal points. The solution of the set of difference equations over the entire region of interest is obtained by evaluating new values for any desired variables by taking into account the latest known estimated value of the variable on neighbouring nodes. One iteration of the solution is completed when, in a line-by-line technique, all the lines in a chosen direction have been accounted for.

In the present study calculations were performed for three inlet velocities, 3, 5 and 10m/s. By first assuming a pressure distribution within the calculation domain, the set of difference equations for the **x**- and **y**-momentum and

energy equations is solved by line iteration. After a sweep of the solution domain has been completed, adjustments are then made to the pressure field so that the continuity equation is satisfied. The procedure is repeated until the continuity, momentum, and energy equations are simultaneously satisfied. The convergence criterion used is that the percentage change of a variable at any node should be less than 0.1 percent. The majority of the computation is performed using a **180*25** of non-uniform grid system. Convergence is typically achieved after about 300 iterations with a central processor time of 20 minutes on the SUN4 Spark station computer.

BOUNDARY CONDITIONS

The quantities calculated were the two mean velocity components (streamwise **u**, and normal **v**) the pressure, **p**, the turbulence kinetic energy, **k**, the dissipation rate of kinetic energy, ε and the enthalpy, **H1**.

The specifications of the variables at the boundaries of the calculation domain are listed in Table (5.1).

Inlet:-

Mean velocity values at the inlet boundary were prescribed from experimental conditions. The inlet kinetic energy level was assumed as appropriate for a low turbulence level in the oncoming flow. The inlet dissipation level was fixed by an assumed length scale distribution. The

inlet conditions were also used as initial values throughout the solution domain.

Outlet:-

As was discussed in Chapter (3) section 3.3.5, conditions at this boundary were unnecessary except for the velocity component, **u**, normal to the boundary, **u** at the outlet plane was related to its values at the adjacent upstream plane in such a way as to satisfy mass conservation over the solution domain.

Top and bottom Walls:-

Boundary conditions for **u**, **k** and ε at nodes adjacent to the wall were applied through the wall function treatment described in Chapter (3) and (4). The velocity, **v**, normal to the wall was set to zero. The calculations of **u**, **v**, **k**, ε, **p** and **H1** were under-relaxed to produce numerical stability. Suitable values for the under-relaxation factor, α_ϕ, defined in Appendix (1), equation (A1.78) were determined by trial and error. The values of these variables which were used in the 2-D computer model are summarised in Table (5.2).

5.3 DESCRIPTION OF AN OVERALL MODEL

When developing a theoretical model of a complex flow regime it is most desirable first to formulate the essential physical characteristics of the flow field. Based

on this preliminary physical model the expected form can be visualised. Actual results from the computer model can then be compared with these expectations. Thus results can be checked, errors detected and theoretical modelling techniques modified. The analysis proceeds by successive improvements, until both experimental model and theoretical predictions coincide.

5.4 GRID DEPENDENCE TESTS

The complex nature of the turbulent flow over a series of blocks has already been considered and discussed in Chapter (2).

The non-uniform distribution of the grid in the **x**- and **y**-directions was first achieved by calculating the co-ordinates from a geometrical progression, thus:

$$x_i = x_{i-1} + \epsilon_x (x_{i-1} - x_{i-2}) \qquad (5.1)$$

$$y_j = y_{j-1} + \epsilon_y (y_{j-1} - y_{j-2}) \qquad (5.2)$$

where x_i is the **x**-coordinate of the i^{th} node and y_j is the **y**-coordinate of the j^{th} node. Here ϵ_x and ϵ_y are expansion/contraction factors in the **x**- and **y**- directions respectively. Since then a total computational domain was discretized by a non-uniform **180*25** grid. The values indicate, respectively; the number of horizontal and vertical grid lines. Of the 25 vertical grid lines, 15 were deployed on the fluid side. These lines were closely spaced

near the solid/fluid interface and in the shear layer, Figure (5.2). In the vertical (**y**) direction, 3 different grid spaces were employed. A medium spacing to cover the region of the blocks themselves, a fine spacing over the boundary layer over the blocks, and a coarse spacing in the free stream region at some distance away from the block, see Figure (5.2).

An investigation of the dependence of the finite-difference solution on the number and distribution of the grid nodes was carried out as follows:-

a) THE EFFECT OF GRID SIZE ON VELOCITY PROFILES

Two different grid sizes were investigated, **125*10** and **180*25**. The axial locations for which the profiles are plotted were over the leading blocks, where the predictions were particularly sensitive to grid changes. Figure (5.3) shows the non-dimensional velocity profile taken at the centre (mid-span) of the first, second and third block respectively. Considering the first block for the grid setting of **125*10**, the **U**-component has entirely positive values; whilst for the case of **180*25**, the **U**-component becomes negative near to the wall. This is also clearly evident for the case of second and third block. Hence the course grid of **125*10** fails to show the region of recirculation above the surface of the first block which is a very important region.

The maximum difference in streamwise velocity for the case

of the second block at region **y/B=0.2** was only 20%, while for the third block this difference was 15%. The interesting point to mention is that, away from the wall the difference in streamwise velocity becomes negligible for the two grid settings mentioned above over the three blocks. This clearly shows the advantage of setting a high number of grids around the wall and in the region of interest i.e. shear layer region, of course this means paying the penalty of longer computing times and reduced economy.

Figure (5.4) shows the non-dimensional **U**-velocity component in the wake of the blocks, i.e., the recirculating region behind the blocks. Again the difference in **U**-velocity component for the two sets of grid setting is evident. In the wake of the first block the maximum difference in streamwise velocity is about 40%, whilst in the wake of the second and third blocks is 25% and 10% respectively. This difference in streamwise velocity becomes once again negligible as it approaches the wake region behind the top of a block.

Finally Figure (5.5) shows the non-dimensional **U**-velocity profile taken at 33cm from the leading edge of the channel, and again the negative values are shown for the case of the finer grid setting. The difference in the streamwise velocity at **y/B=0.2** is about 25%.

b) THE EFFECT OF GRID SPACING ON TEMPERATURE PROFILES

The grid dependence tests were repeated to check the effect of different grid spacings on the calculated values of air temperature, comparative tests at the two grid spacings used above (**125*10** and **180*25**) were repeated. For these tests velocity was taken as 10m/s, and temperature profiles were calculated over the first three blocks. In the case of the **180*25** grid spacing, Figure (5.6a), the air temperature at the first grid point next to the wall has a value of 40°C, while in the case of the **125*10** spacing, it has a value of 23°C. This is a large discrepancy in air temperature 17°C which would lead to an unacceptable error in the calculations based upon it. It is very important to set a sufficiently fine grid spacing, but of course there is a practical limit on the number of grid points which can be used. Results for the second and third blocks, Figures (5.6b) and (5.6c) show a similar discrepancy.

Figure (5.7) shows the grid dependence tests for the temperature profiles in the middle of each of the cavities between the first four blocks. In the first cavity the temperature values for the grid settings of **180*25** are 3% greater than the grid setting of **125*10**. In the second cavity (between the second and third block) the temperature is 3% greater. In the third cavity the values of temperature become greater by 5% for a grid setting of **125*10** which is different from the two cases mentioned above.

Eventually after careful study of all the Figures mentioned above, it was finally decided to adopt the (**180*25**) grid distribution for future tests because of its greater accuracy near the wall. In complex flow models fine grid spacing is vital to show up regions of separation and of recirculation. Also, to ensure accurate heat transfer calculations the regions of rapidly changing temperature near a wall require particular attention.

5.5 PREDICTION OF FLOW AROUND THE BLOCKS

The geometry for the flow passing the blocks is shown in Figure (5.8). The expected behaviour of the flow is as follows:-

(a) FLOW PATTERN UPSTREAM OF BLOCKS

As the oncoming, initially uniform, flow approaches the obstacles, a thin boundary layer develops on the board. Just in front of the first block, this forms a small recirculating eddy as a consequence of deceleration of the flow caused by the increase in static pressure.

(b) FLOW PATTERN ABOVE FIRST BLOCK

The flow will separate at the top edge of the front face where it is unable to undergo the very large acceleration necessary to follow the abrupt change of orientation of the

solid boundary. Separation results in reverse flow along the top surface. This separated flow merges with a recirculation zone in the wake of the first block, beyond which the flow reattaches to top face of the second block. These disturbances from the first block produce downstream effects on the second and third block. After the third block the disturbances tend to die down, and the flow then gradually recovers and approaches that of a normal wall boundary layer.

The static pressure, **p**, just downstream of separation is approximately equal to that in the main flow immediately prior to separation. Because the flow accelerates in passing over the front face, the static pressure falls, and the pressure coefficient becomes negative in the separated region.

This type of flow behaviour was later confirmed by a comprehensive experimental study carried out by LDA technique in the laboratory. Flow visualisation also clearly shows separation at the leading edge of the top surface when the incident flow was uniform and also the regions of recirculation between the blocks.

(c) FLOW PATTERN DOWNSTREAM REGION OF LAST BLOCK

Behind the last block (block no 8), the fluid forms a large recirculation zone with characteristics of low velocity and pressure similar to those already observed in the separated zone.

In the downstream regions the profiles are also similar. The obstruction caused by the front face of the block apparently provides the strongest influence in the flow, which indicate the strong influence of the shear layers generated from the sharp edge of the block on the downstream flow.

5.6 THE EFFECT OF VARYING THE HEIGHT PARAMETER H/B

Three different values of the channel height/block height ratio were investigated (**H/B**=2.5, 2.0, 1.5).

Figure (5.9) shows the non-dimensional velocity profile over each of the first three blocks for an inlet velocity of 3m/s. For the case of **H/B**=2.5, Figure (5.9a), the profile over the first block shows a negative velocity near the wall which becomes positive away from the wall into the main stream. This indicates a region of separation where small recirculation eddies exist. Unlike the first block, there is no sign of recirculation on the second and third blocks, i.e, the profile is positive near the wall.

As the height of the channel is reduced (**H/B**=1.5), Figure (5.9c), the velocity profile over the first block becomes entirely positive, indicating no recirculation on the top of this block. This clearly means that by increasing the channel height, the separation region over the first block increases, creating a larger recirculation region. As the channel height is reduced to **H/B**=1.5, there will be no

separation over the first block as the flow accelerates over that region. The velocity profiles over the second and third blocks for this case becomes almost identical.
This is also true for the inlet velocities of 5 and 10m/s. Similarly, for **H/B**=2.5 and 2.0, the velocity profiles over the first block are negative near the wall indicating the regions of recirculating eddies. However for the case of **H/B**=1.5, the velocity profiles are entirely positive Figures (5.10) to (5.11).

5.7 THE EFFECT OF VARYING THE BLOCK SPACING PARAMETER S/B

Figure (5.12) shows the velocity profiles over first three blocks for **Uin**=3m/s and **H/B**=2.5, 2.0 and 1.5, but in this case for a different block spacing of **S/B**=1.25.
It can be seen that these profiles are similar to previous results at **S/B**=2.0 (Figure (5.9)), and that the effect of making these changes of pitch has been small. This effect is also true for the case of **Uin**=5m/s and 10m/s. These results are shown in Figures (5.13) to (5.14). Therefore for the pitch spacings studied in the present research it was found that there was little interaction of the channel flow with the cavity flow, which would enhance the heat transfer in the cavity.
The experimental data show that the thermal conditions of the flow outside the cavity are little affected by the presence of the cavity. This may signify the insensitivity

of the flow inside the cavity to the detail of the flow outside though, obviously, the magnitude of the velocity is an influencing parameter.

FLOW OVER THE LAST FIVE BLOCKS

Figure (5.15) shows the velocity profiles over the last five blocks. The similarity of the profiles over each of these blocks indicates that the flow appears to be fully developed before reaching these regions.

VELOCITY PROFILES IN THE WAKE OF THE BLOCKS

Figures (5.16a), (b) and (c) show the velocity profiles in the wake of the each blocks, for **Uin**=3m/s, **H/B**=2.5, 2.0 and 1.5. In the case of **H/B**=1.5 and 2.0 the profiles are similar, but in the case of **H/B**=2.5, the velocity profiles in the wake of the first block are greater in magnitude, and therefore a stronger recirculation exists. The similarity of the profiles is also shown in the case of **S/B**=2.0, Figure (5.9).
The same profile is repeated for the **Uin**=5m/s and 10m/s in Figures (5.18a) and (b).

5.8 VECTOR PLOTS

Although the data has been presented in the form of individual velocity profiles, individual graphs do not

allow the main characteristics of the flow to be observed. The data has been therefore re-presented as vector plots, so that the hypotheses made regarding flow structure (eg., bypass flow, region of separation, cavity flows etc) can be checked.

In this section the field values of dependent variables are shown in forms of PHOTON graphical output. In all cases the magnitude of the velocity, normalised by U_∞ is proportional to the length of the arrows. A velocity scale is marked on each Figure as a fraction of U_∞, the uniform inlet velocity (5m/s).

a) THE EFFECT OF INCREASED CHANNEL HEIGHT

A non uniform grid, with a fine mesh close to the blocks, is used to show the true flow structure in the region of separation, cavity flow etc. Figures (5.19a), (b) and (c) show the velocity vectors for an inlet velocity of 5m/s, a block spacing of S/B=1.25, but for different channel heights. Comparing the above three figures, it can clearly be seen that the effect of increasing the channel height is merely to allow increased quantities of fluid to pass through the channel without interacting with the blocks.

In the region upstream of the blocks, the results shows the expected deceleration of the flow for small (**y**), and the flow deflection over the top of the first block. From the velocity vectors it is clear that there is a recirculation

region at the top of the first block and between blocks and also downstream of the last block; in these regions the velocities are much lower than that in the main flow. The above Figures show that the most interesting features of the flow are to be found in the vicinity of the blocks.

UNIFORM GRID SPACING

It should be noted, that although the overall structure of the flow is adequately predicted with a uniform grid, detailed vector magnitudes in regions of flow separation etc are approximate only.

Figures (5.20a), (b) and (c) show the velocity vectors over the first three blocks for the case of uniform grid spacing. For the inlet velocity of 5m/s and the two channel heights, no recirculation eddies are formed on the first block, neither on the top, nor in front of it. There is a region of strong recirculation in the rather large spaces between the blocks. A separated flow region occurs between the first two blocks and becomes a recirculating closed vortex. Acceleration by the first block starts and contributes to the acceleration within the next two or three blocks. After that, small eddies are generated on the heated surface, and contribute to the increase of local turbulence intensity.

The results shown in Figures (5.21a) and (b) are essentially similar to those described above, but for the smallest practical block spacing of 5cm. The only changes

to be noted are that the recirculation between the blocks is not as strong as in the case of maximum block spacing, and that such changes in recirculation which did occur had virtually no effect on the main flow.
The above procedure was repeated for the other two inlet velocities of 3 and 10m/s, and it was found that they produced similar results. Due to the large volume of results obtained from the above condition it was decided not to present them in this thesis.

5.9 CONCLUSIONS

The methods of CFD have been successfully used to predict the complex case of turbulent flow over a row of square-section blocks mounted in a rectangular duct.
A grid dependence test was carried out for two different grid sizes, **125*10** and **180*25**. After careful examination it was decided that a grid size of **180*25** would both improve the convergence, and yield the required accuracy of prediction.
An extensive investigation into the effect on the flow of making systematic changes of the main geometric parameters was carried out. The results obtained by varying the channel height showed that this has little effect on the velocity profiles over second and third block, which are in the vicinity of the disturbance caused by the first block. The variation of channel height only affected the velocity profile over the first block, where there is a large area

of separation taking place over the block caused by its presence.

The effect of streamwise spacing of the blocks was investigated. At smaller streamwise spacings, confined flow exists in the cavities between blocks, in which heated fluid recirculates. For the larger spacings between blocks, the flow that separates from the leading edge of block reattaches in the cavity just downstream. For the ranges of spacings examined in this work, there was little interaction of main flow with the cavity flow.

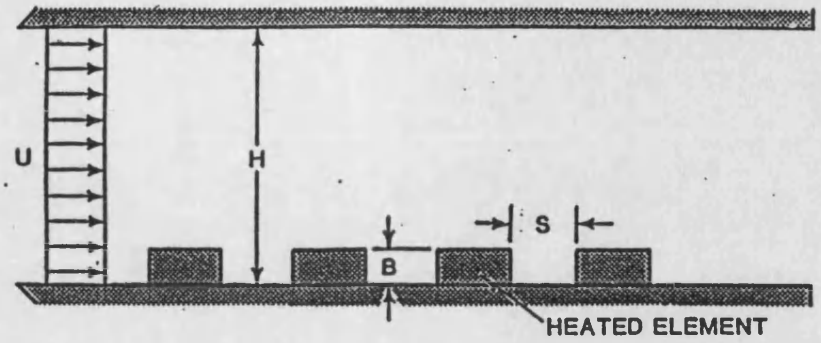

FIGURE 5.1: SCHEMATIC DIAGRAM FOR 2-DIMENSIONAL FLOW

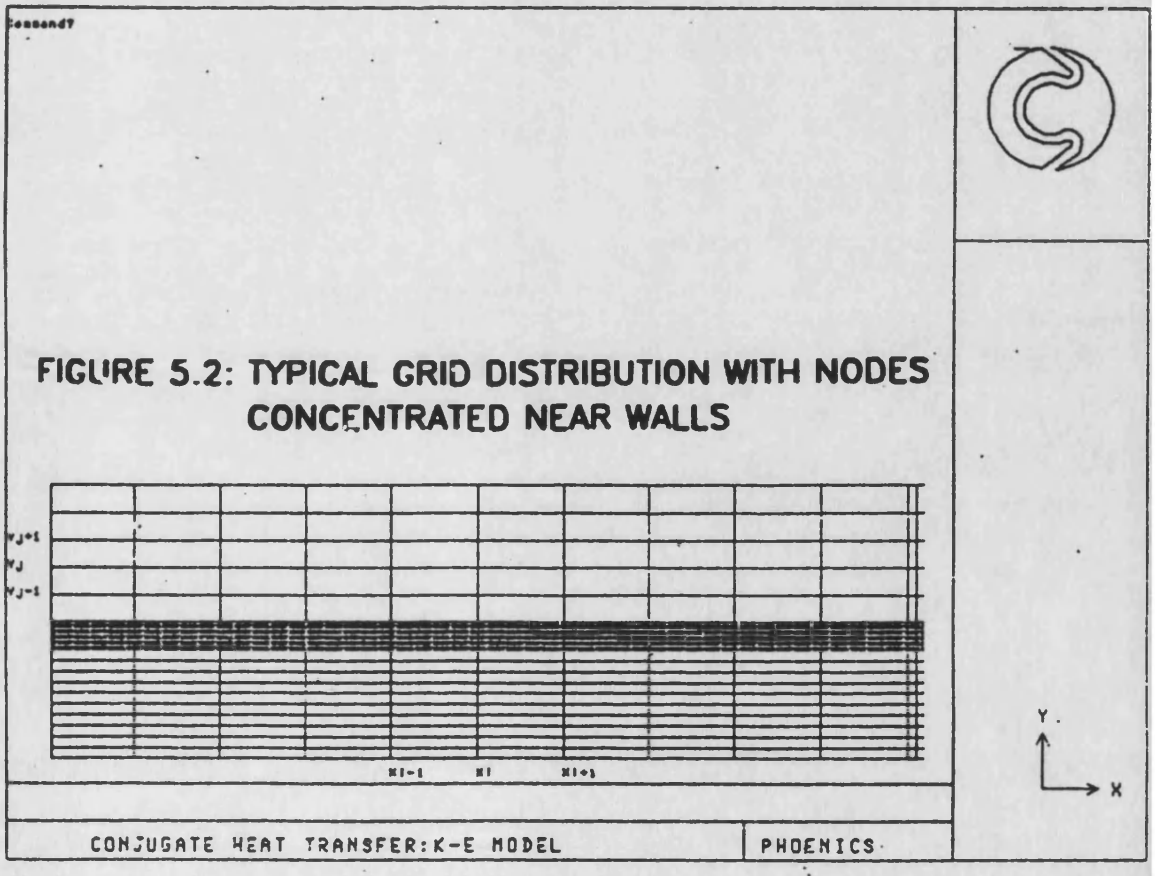

FIGURE 5.3: GRID–DEPENDENCE: U–VELOCITY PROFILES MEASURED AT MID–POINT OVER BLOCKS

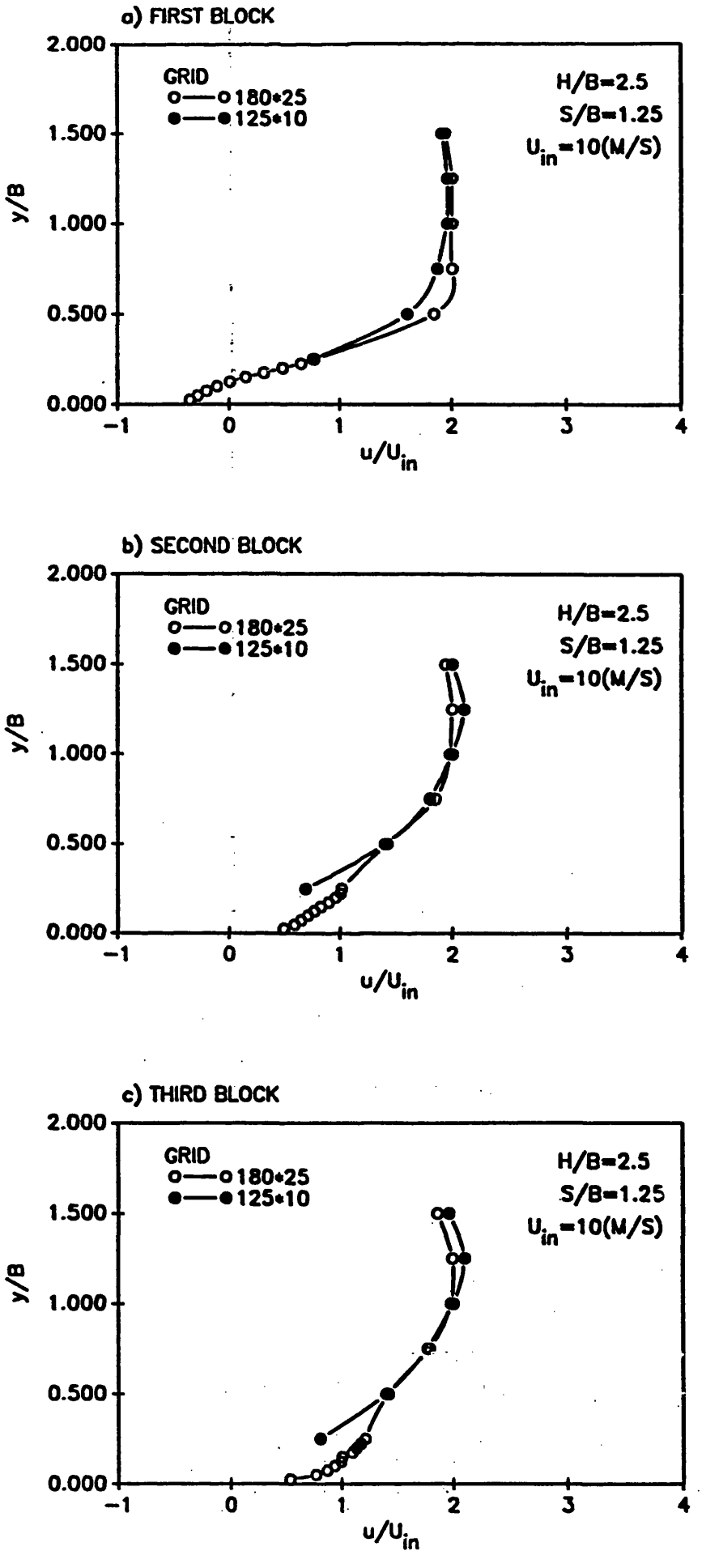

FIGURE 5.4: GRID–DEPENDENCE: U–VELOCITY PROFILES MEASURED AT MID–POINT BETWEEN BLOCKS

a) BETWEEN FIRST AND SECOND BLOCKS

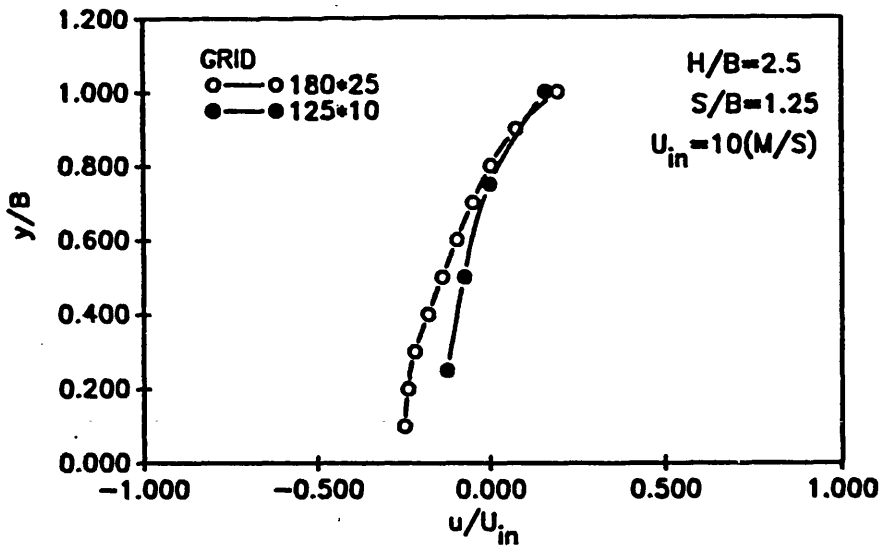

b) BETWEEN SECOND AND THIRD BLOCKS

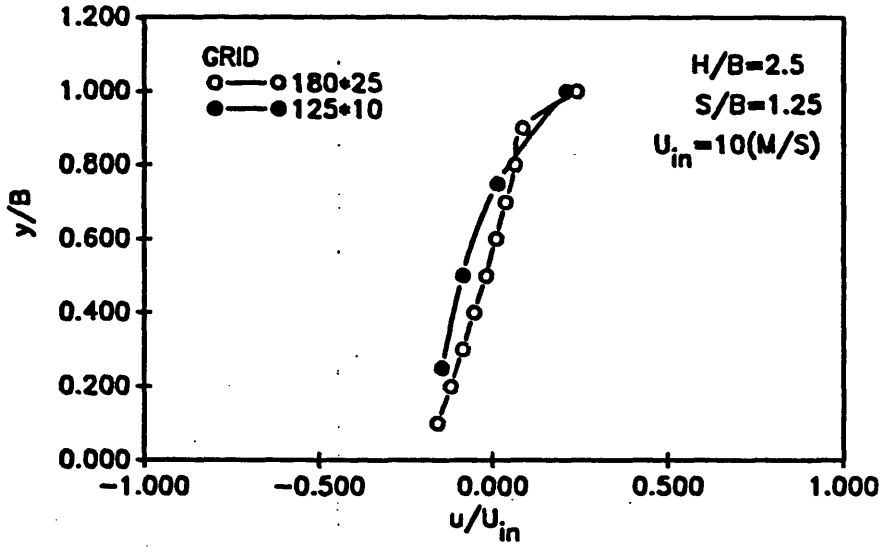

c) BETWEEN THIRD AND FOURTH BLOCKS

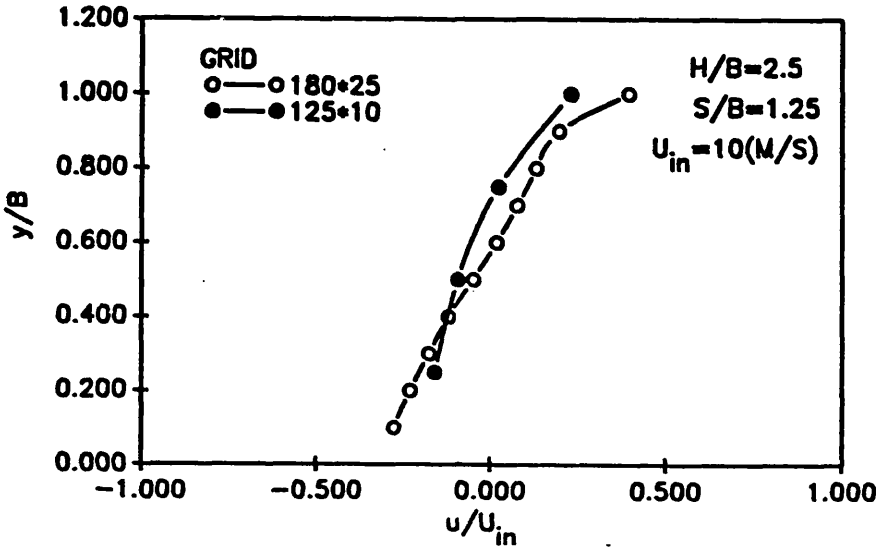

FIGURE 5.5: GRID-DEPENDENCE: U-VELOCITY PROFILES MEASURED AT 33 (CM) FROM THE INLET OF DUCT

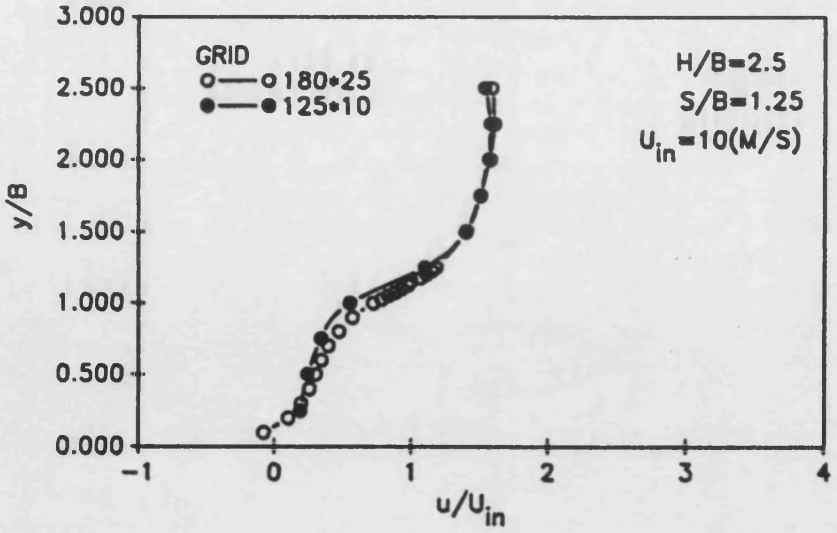

FIGURE 5.6: GRID–DEPENDENCE: TEMPERATURE PROFILES MEASURED AT MID–POINT OVER BLOCKS

a) FIRST BLOCK

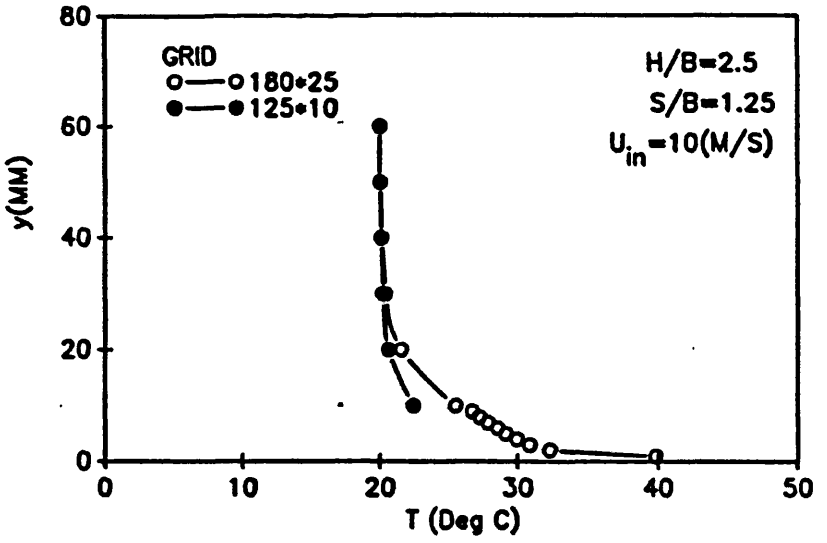

b) SECOND BLOCK.

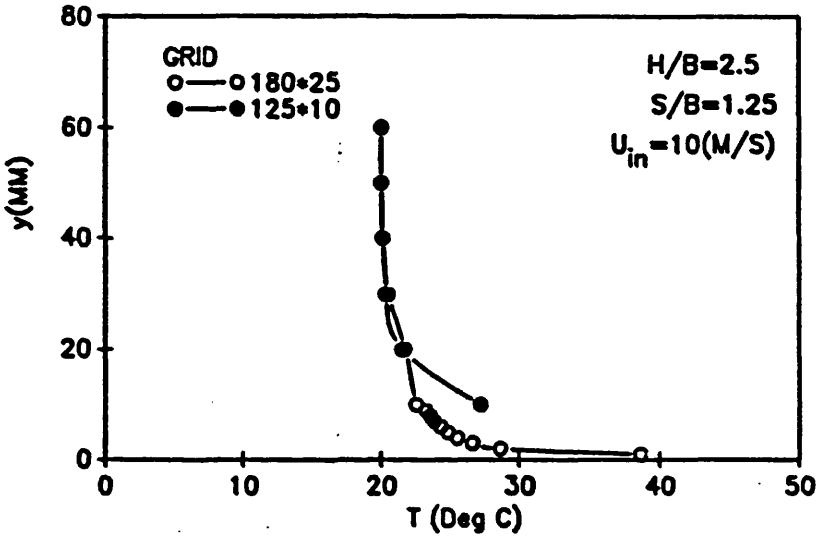

c) THIRD BLOCK

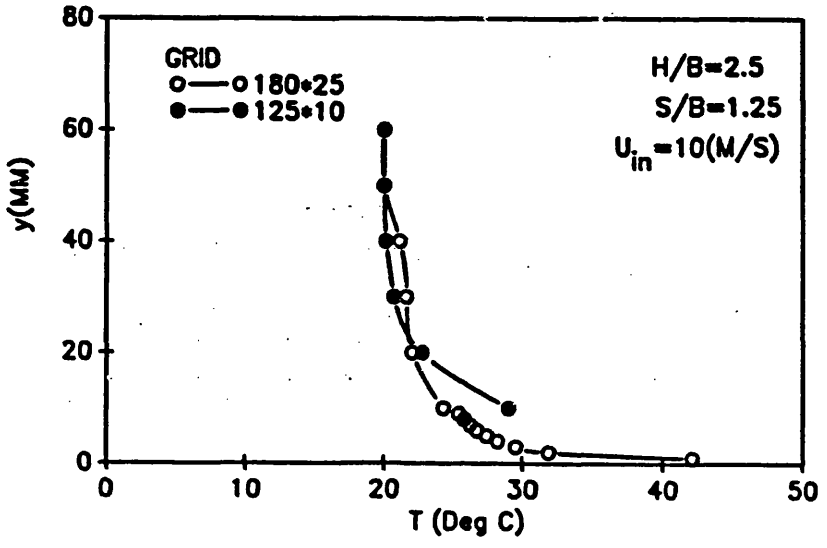

FIGURE 5.7: GRID–DEPENDENCE: TEMPERATURE PROFILES MEASURED AT MID–POINT BETWEEN BLOCKS

a) BETWEEN FIRST AND SECOND BLOCKS

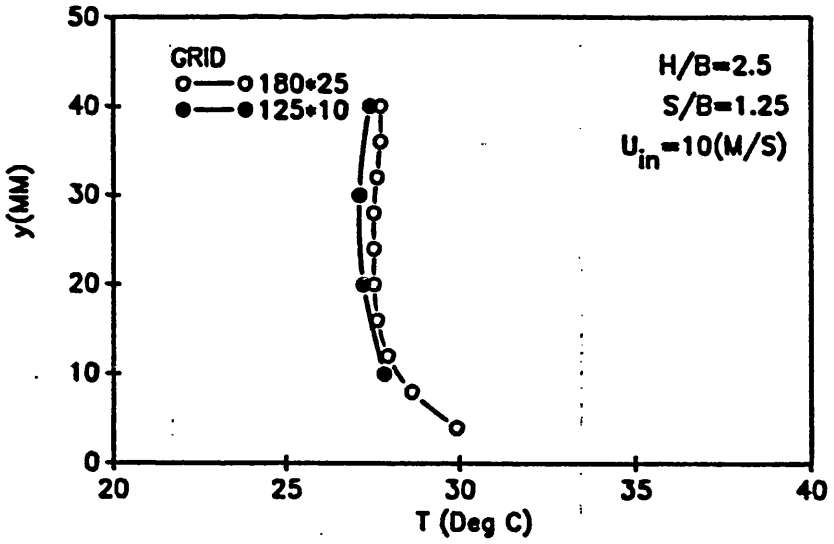

b) BETWEEN SECOND AND THIRD BLOCKS

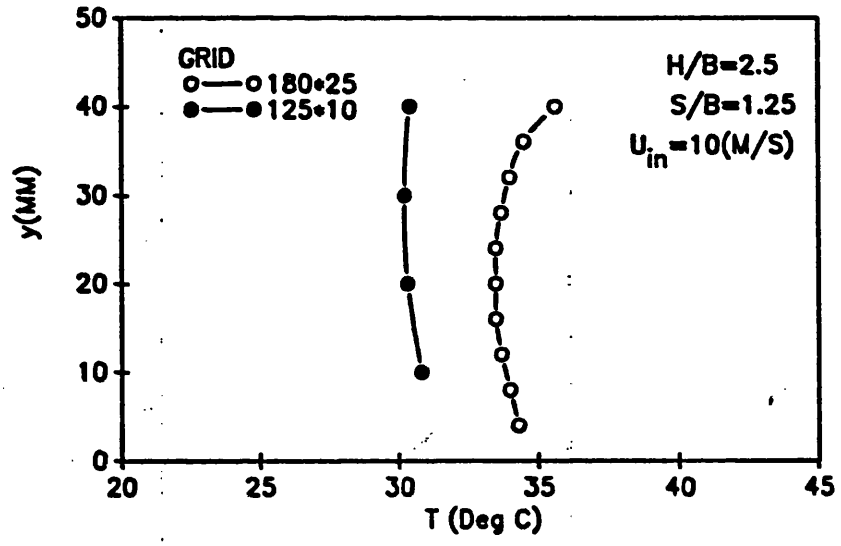

c) BETWEEN THIRD AND FOURTH BLOCKS

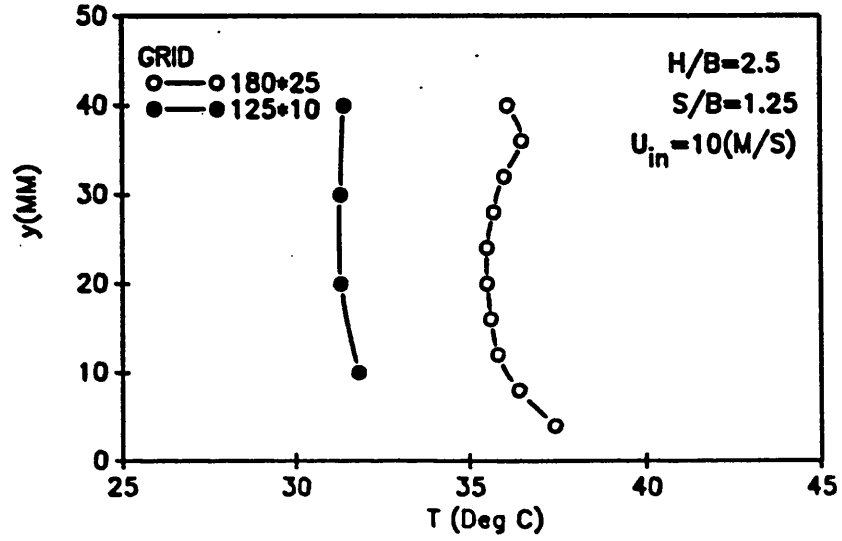

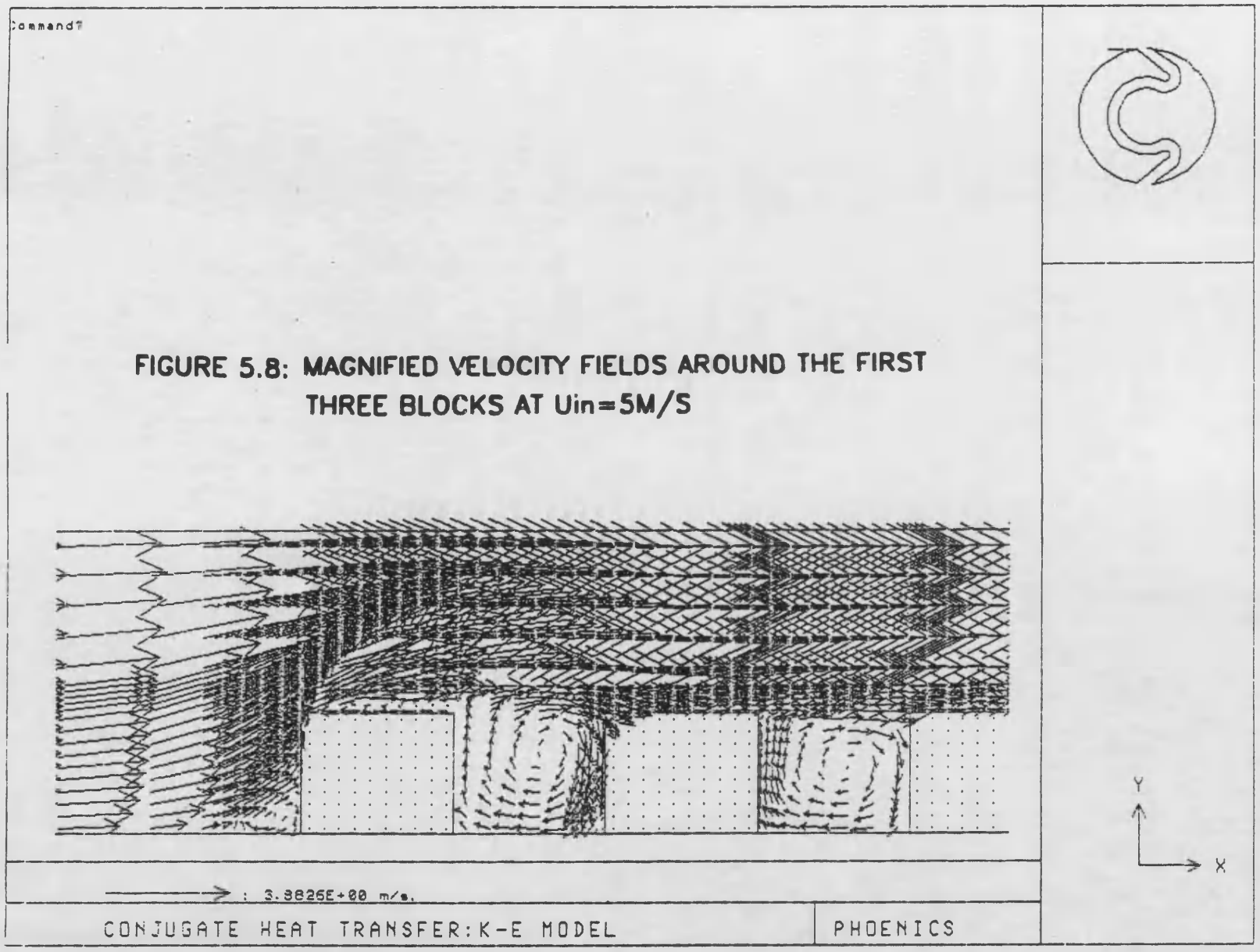

FIGURE 5.8: MAGNIFIED VELOCITY FIELDS AROUND THE FIRST THREE BLOCKS AT Uin=5M/S

FIGURE 5.9: VELOCITY PROFILES OVER FIRST THREE BLOCKS MEASURED AT MID-POINT OVER BLOCKS, U_{in}=3(M/S)

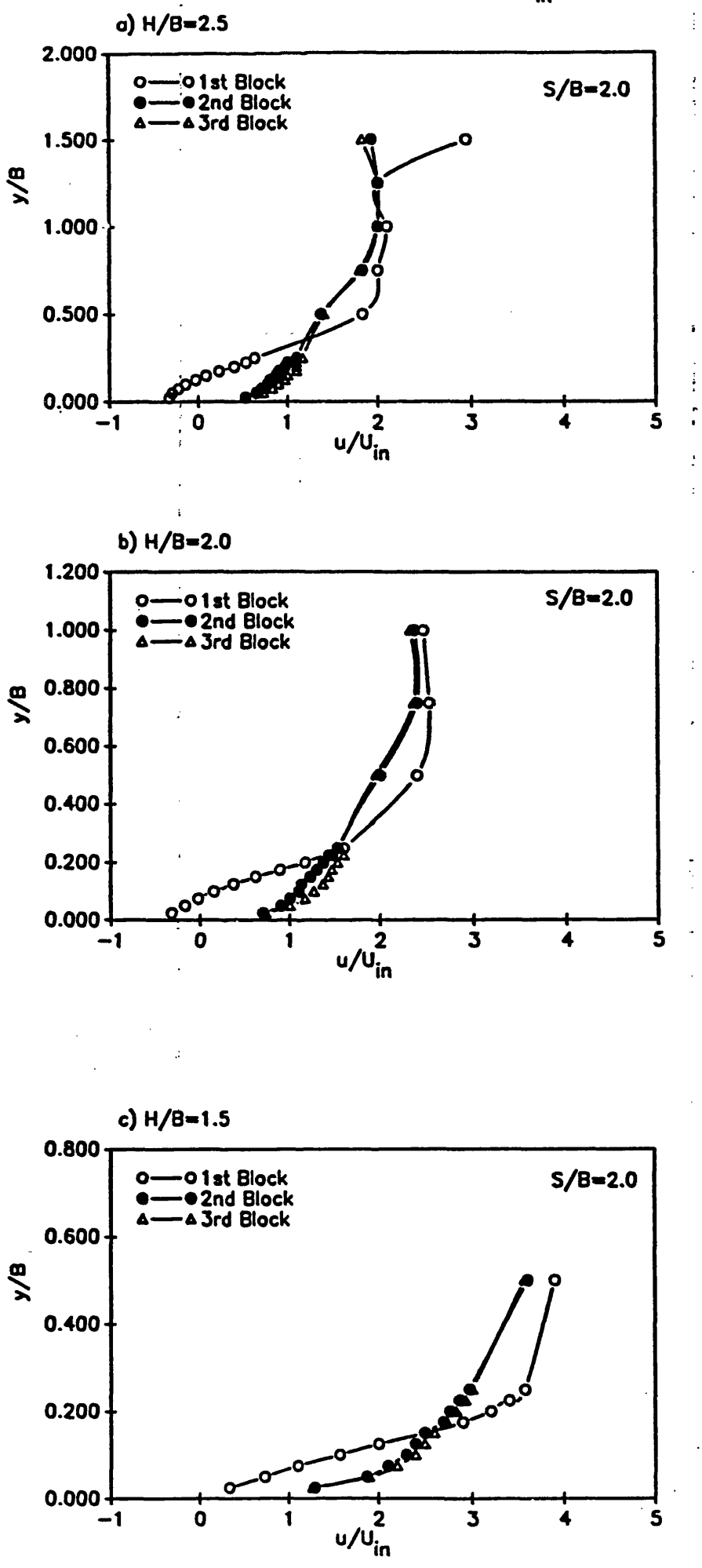

FIGURE 5.10: VELOCITY PROFILES OVER FIRST THREE BLOCKS MEASURED AT MID-POINT OVER BLOCKS, U_{in}=5(M/S)

a) H/B=2.5

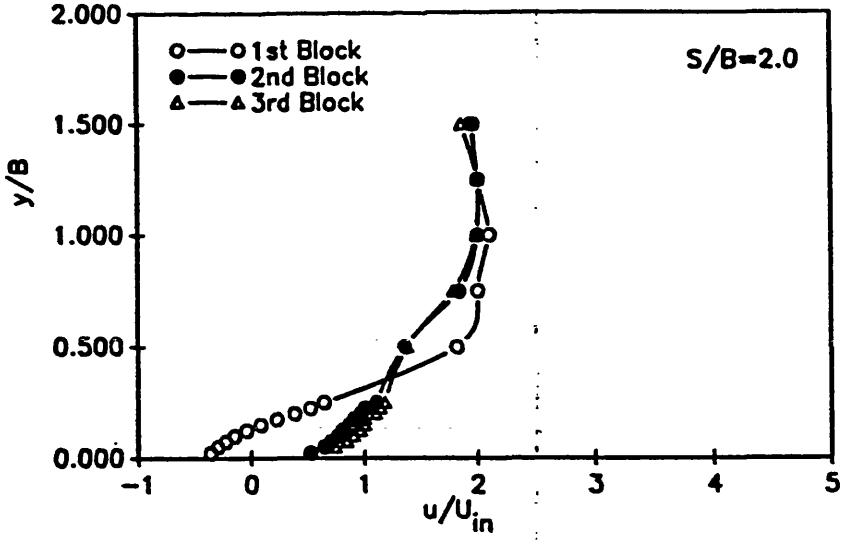

b)H/B=2.0

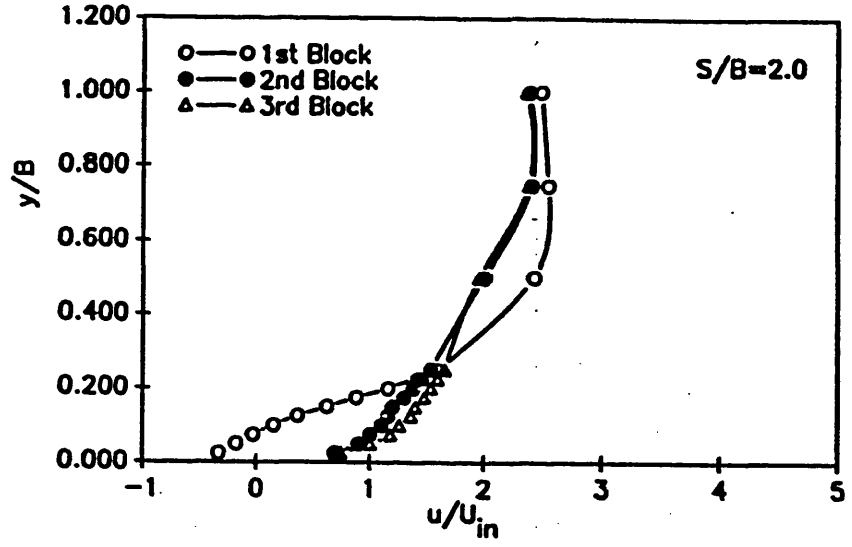

c)H/B=1.5

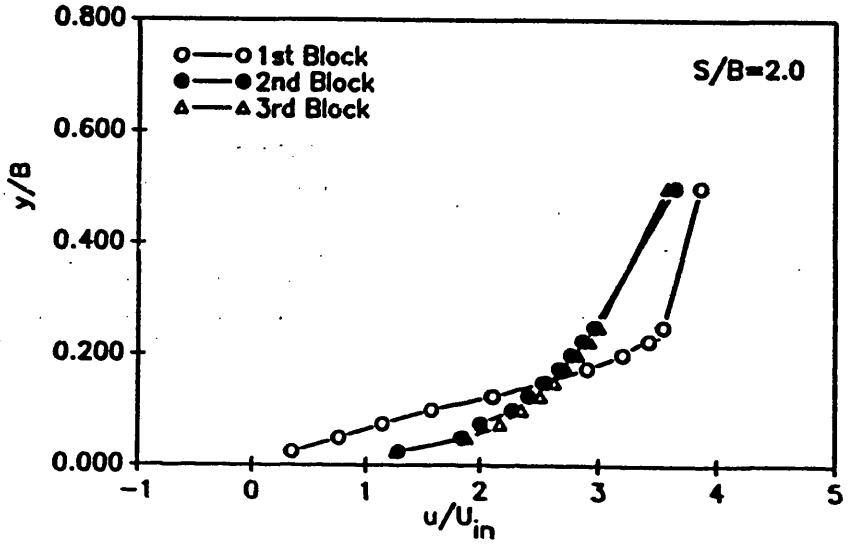

FIGURE 5.11: VELOCITY PROFILES OVER FIRST THREE BLOCKS MEASURED AT MID-POINT OVER BLOCKS, U_{in}=10(M/S)

a) H/B=2.5

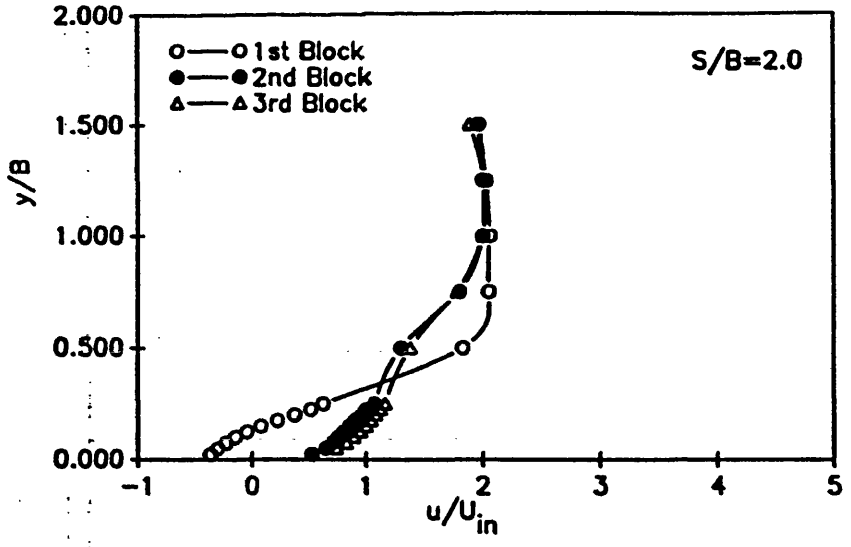

b)H/B=2.0

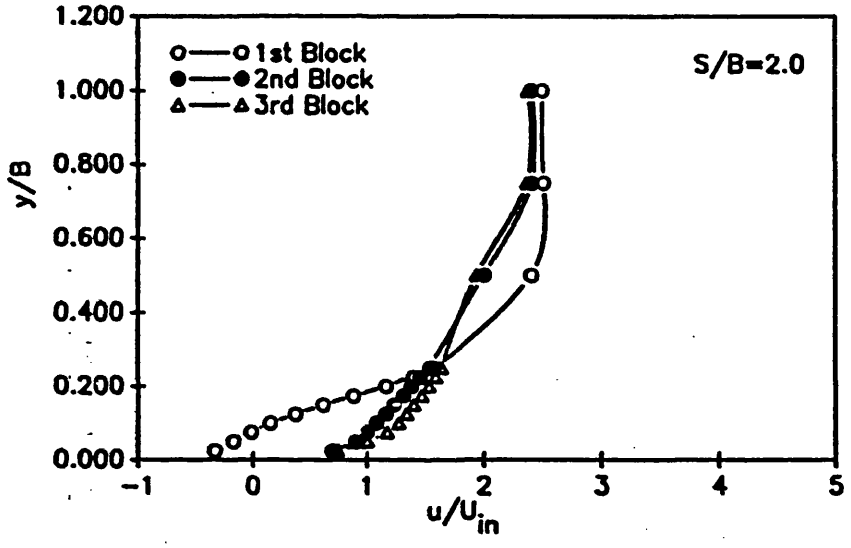

c)H/B=1.5

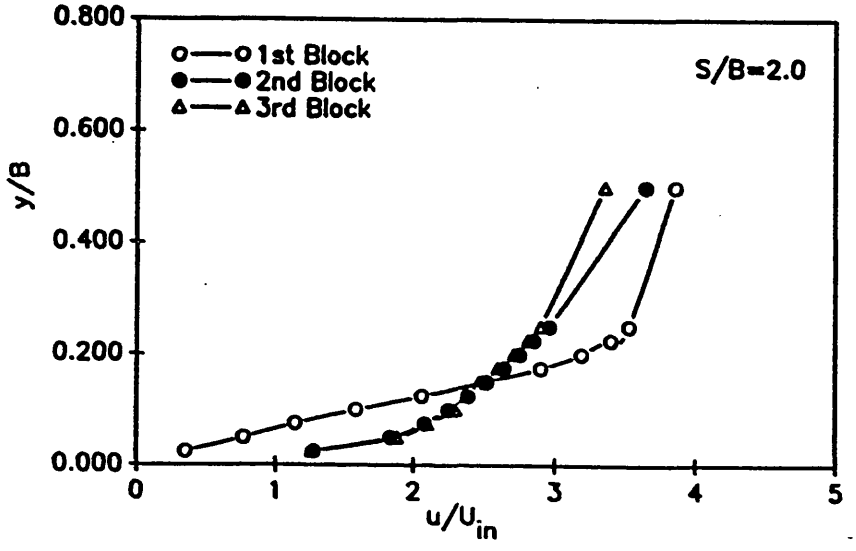

FIGURE 5.12: VELOCITY PROFILES OVER FIRST THREE BLOCKS MEASURED AT MID-POINT OVER BLOCKS, U_{in}=3(M/S)

a) H/B=2.5

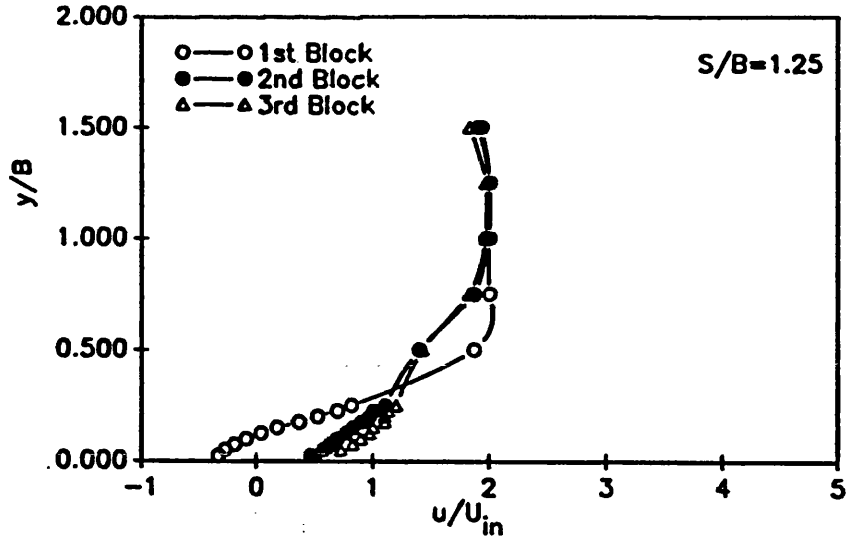

b)H/B=2.0

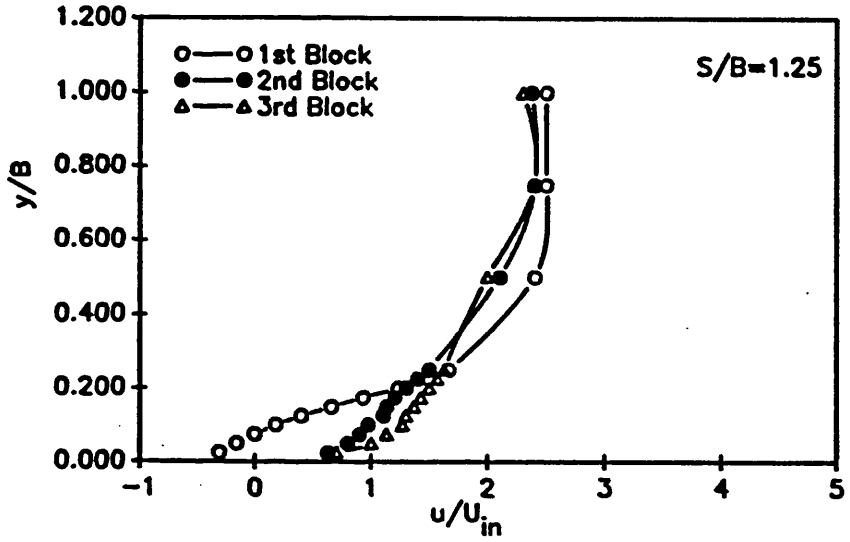

c)H/B=1.5

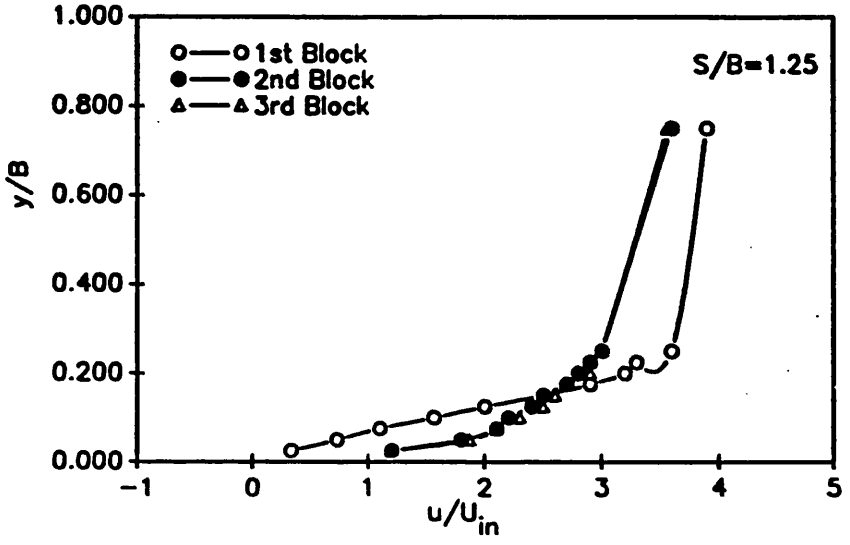

FIGURE 5.13: VELOCITY PROFILES OVER FIRST THREE BLOCKS MEASURED AT MID-POINT OVER BLOCKS, U_{in}=5(M/S)

a) H/B=2.5

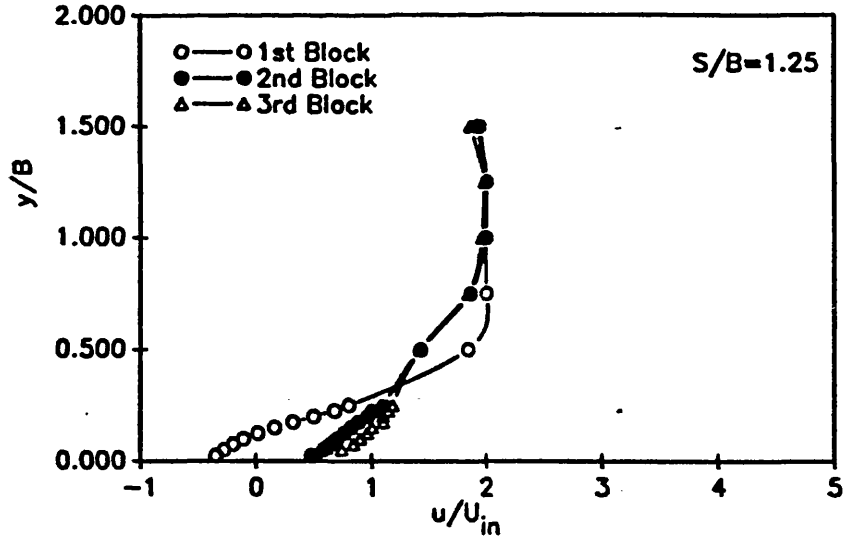

b)H/B=2.0

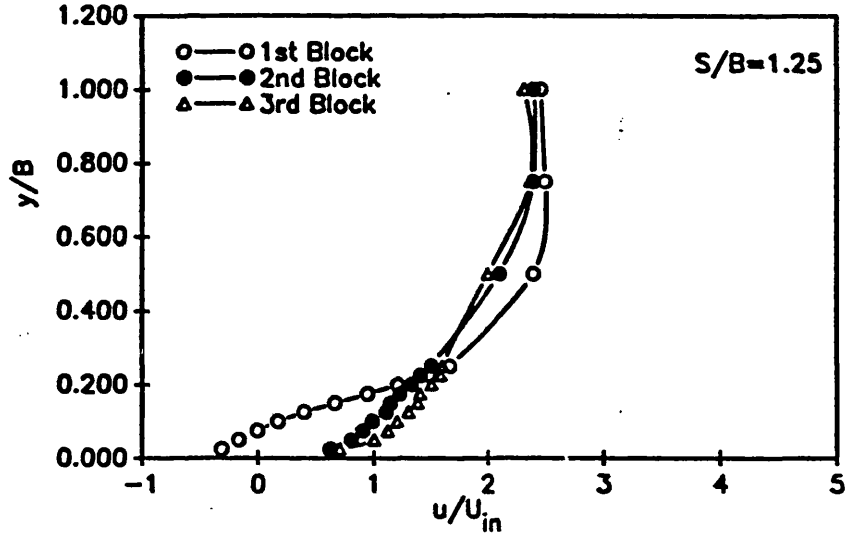

c)H/B=1.5

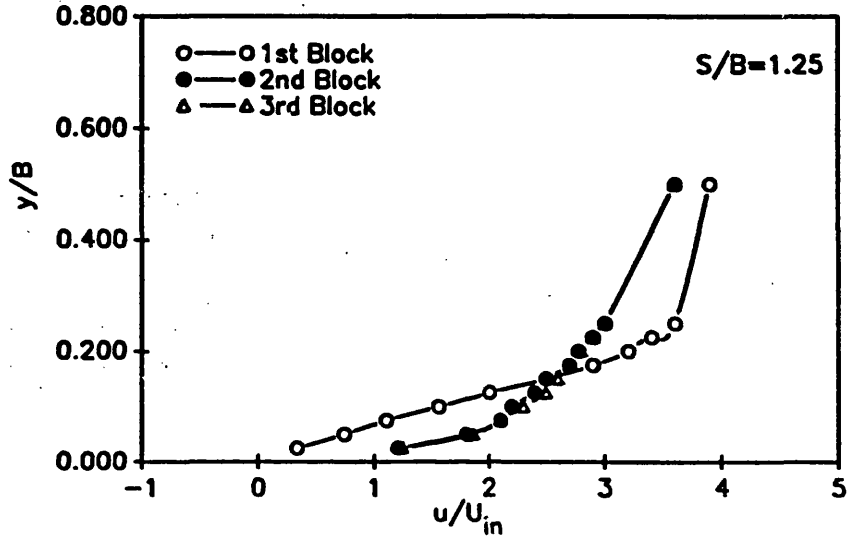

FIGURE 5.14: VELOCITY PROFILES OVER FIRST THREE BLOCKS MEASURED AT MID-POINT OVER BLOCKS, U_{in}=10(M/S)

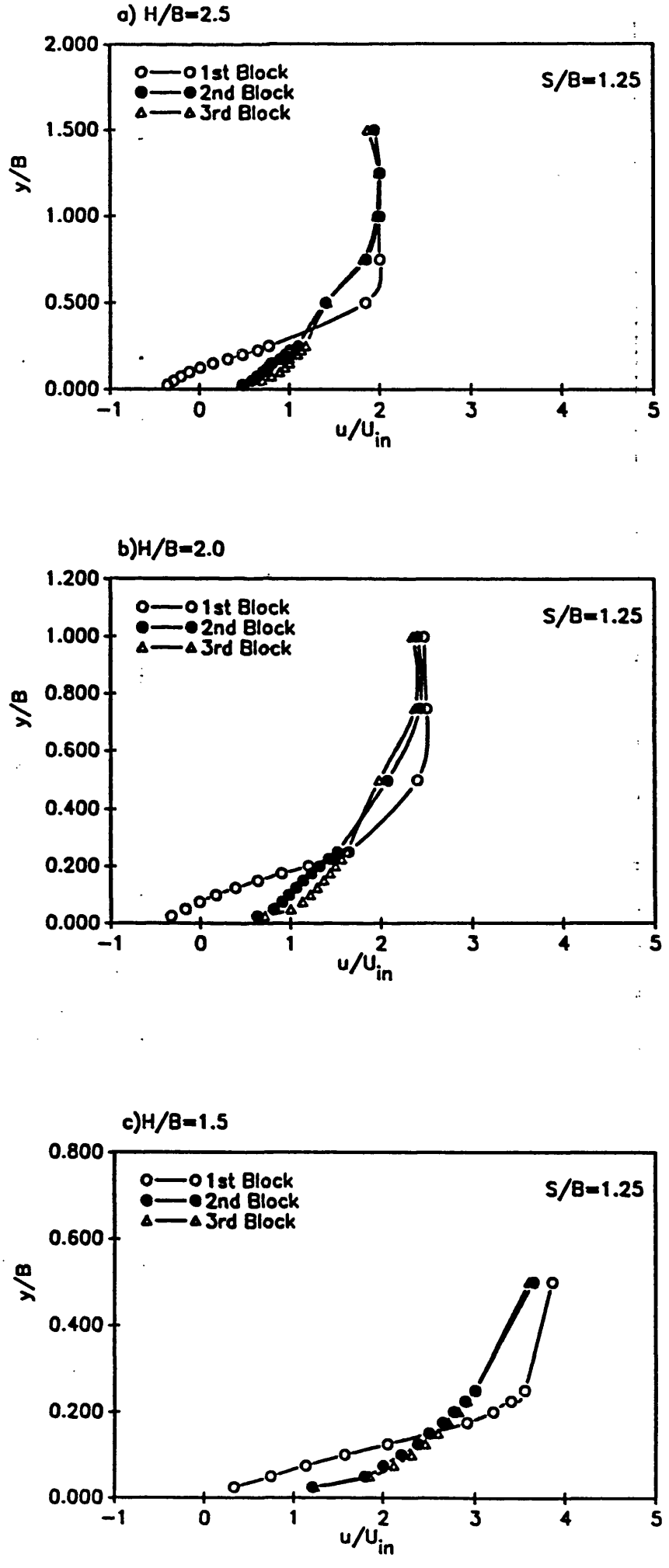

FIGURE 5.15: VELOCITY PROFILES OVER LAST FIVE BLOCKS MEASURED AT MID-POINT OVER BLOCKS, U_{in}=10(M/S)

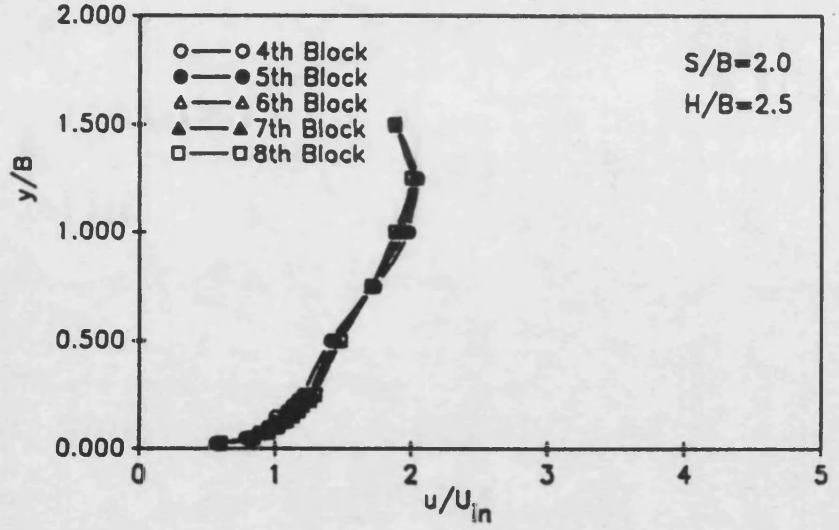

FIGURE 5.16: VELOCITY PROFILES IN THE WAKE OF EACH BLOCK MEASURED AT MID-POINT BETWEEN EACH BLOCK

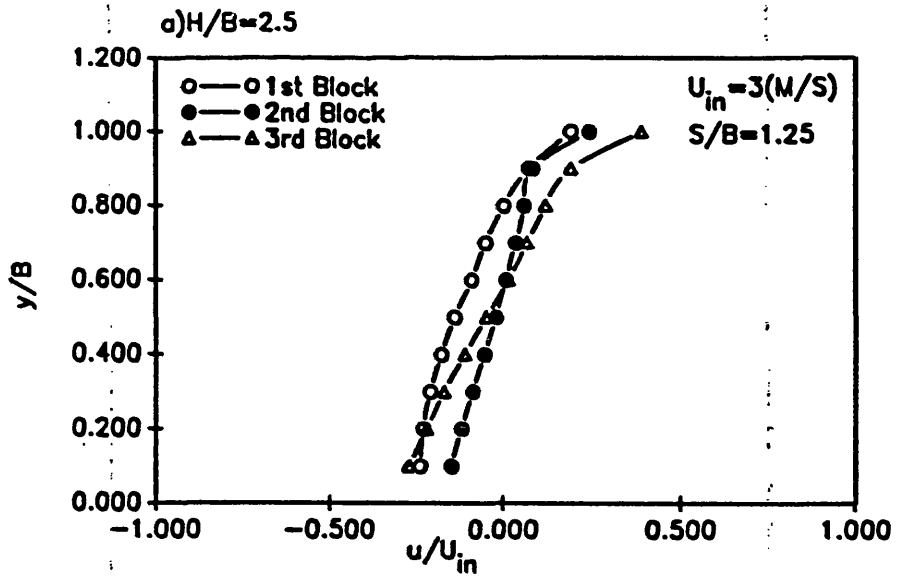

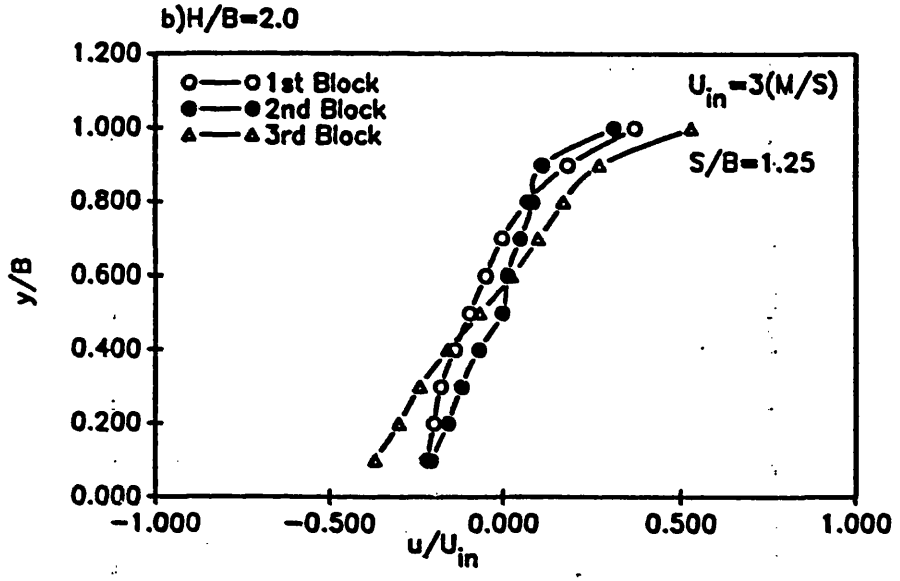

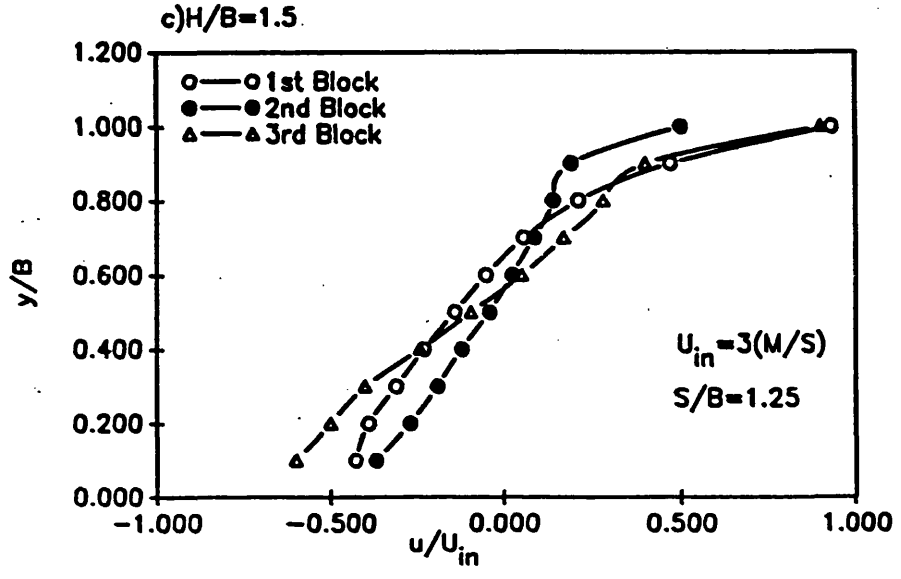

FIGURE 5.17: VELOCITY PROFILES IN THE WAKE OF EACH BLOCK MEASURED AT MID-POINT BETWEEN EACH BLOCK

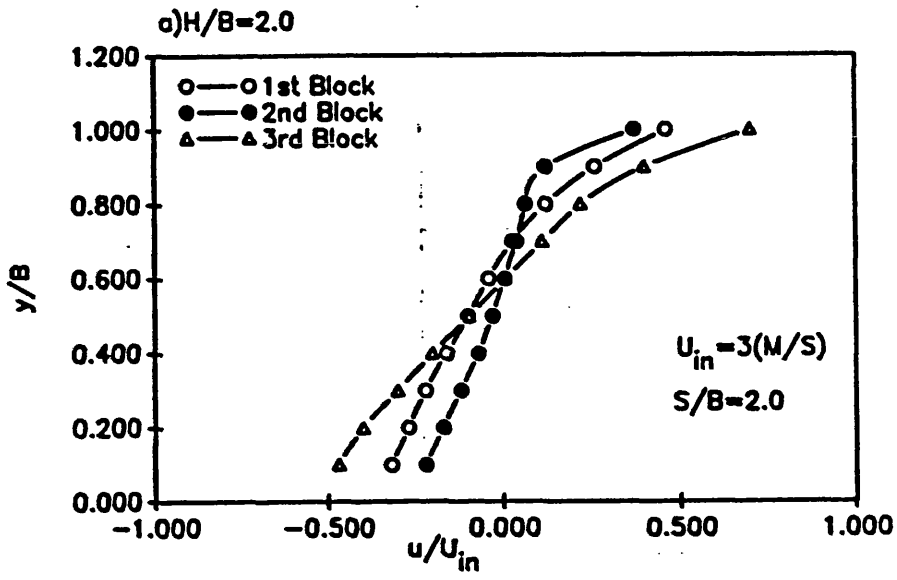

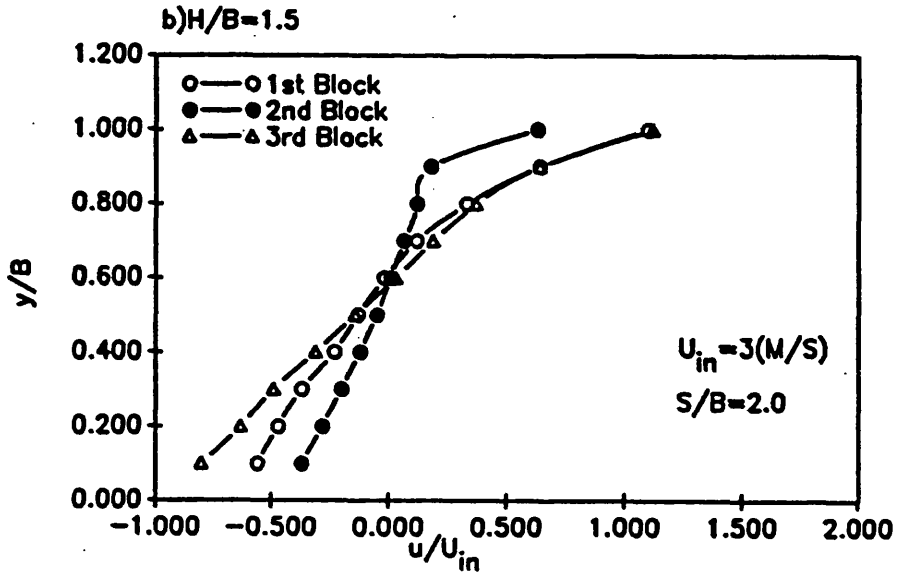

FIGURE 5.18: VELOCITY PROFILES IN THE WAKE OF EACH BLOCK MEASURED AT MID-POINT BETWEEN EACH BLOCK

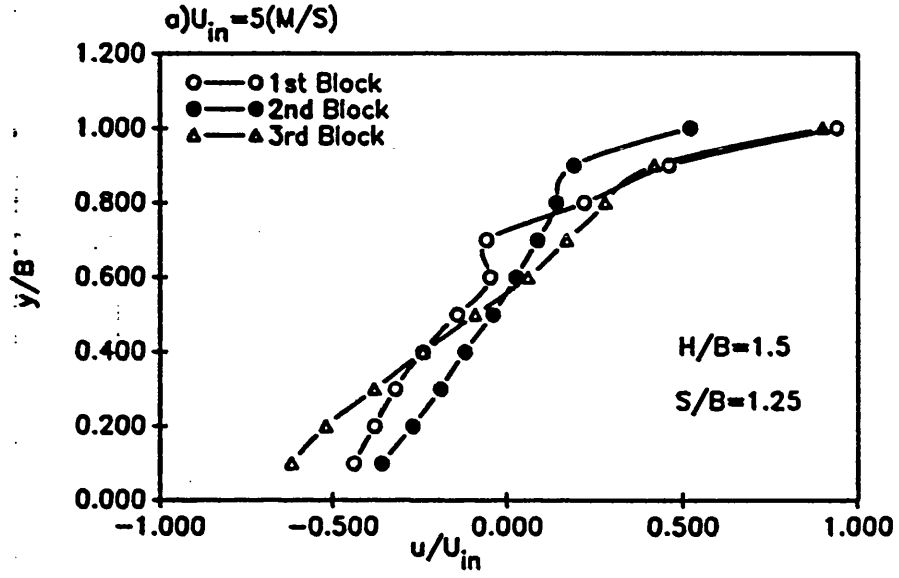

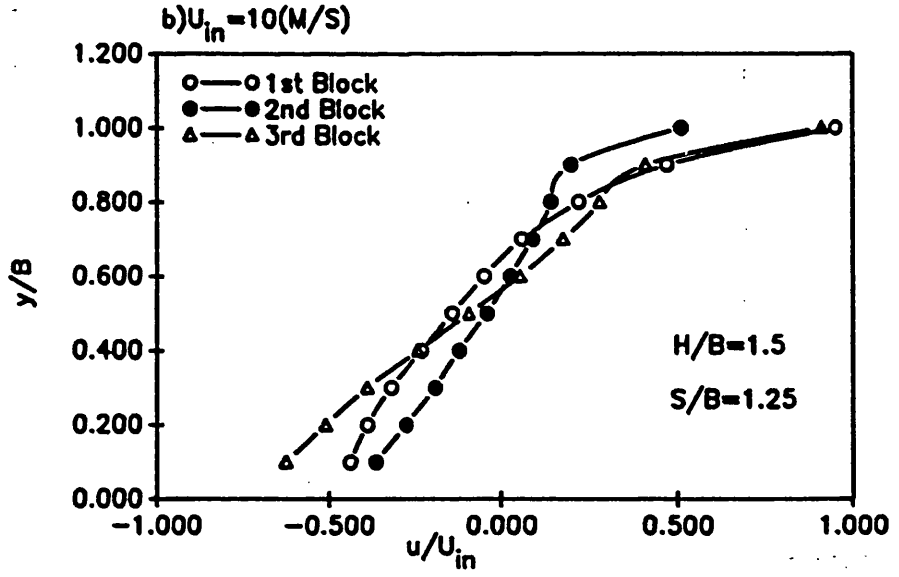

FIGURE 5.19: VELOCITY VECTORS OVER FIRST FOUR BLOCKS, Uin=5, q=6750, S=5 NON-UNIFORM GRID

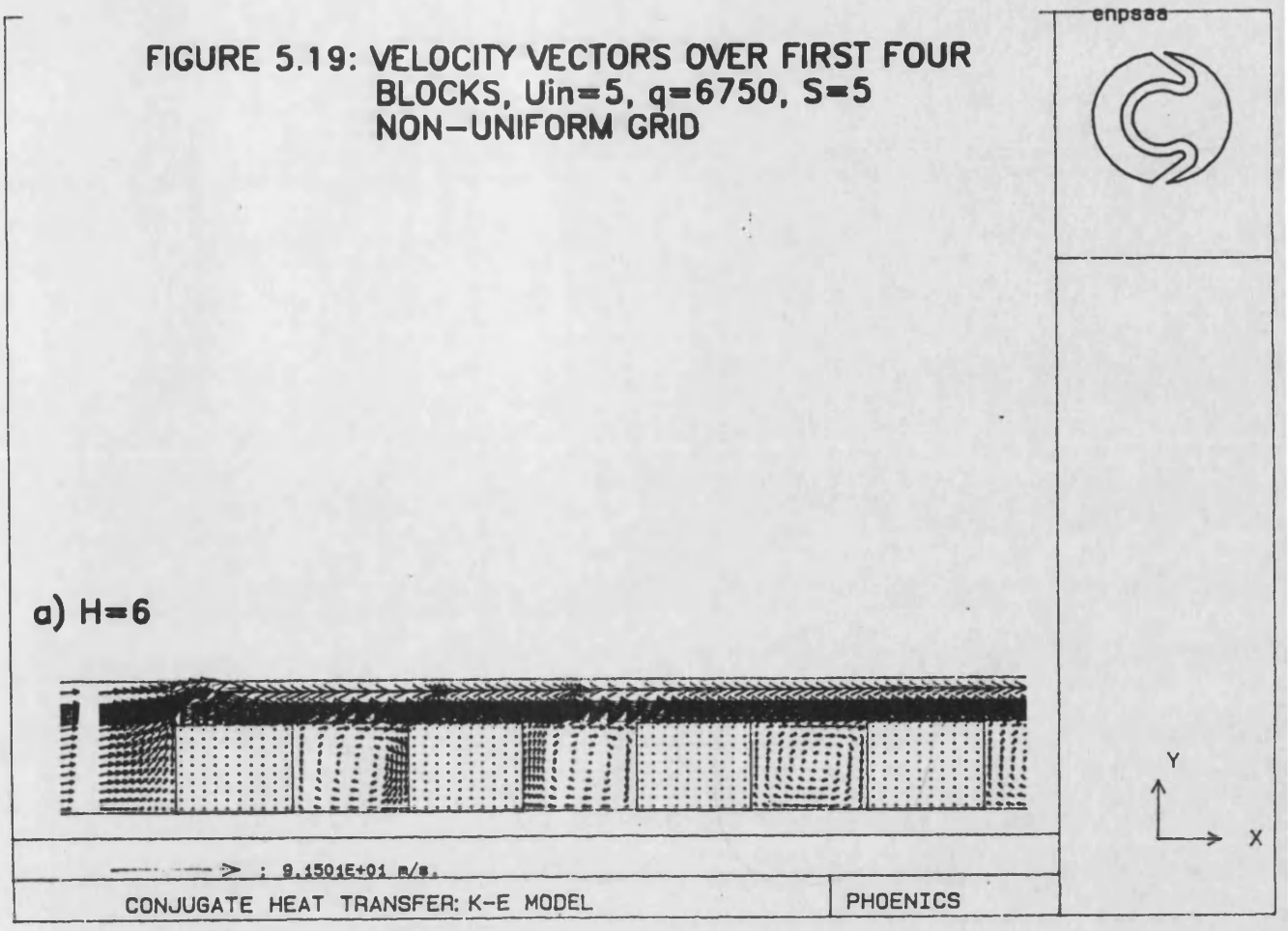

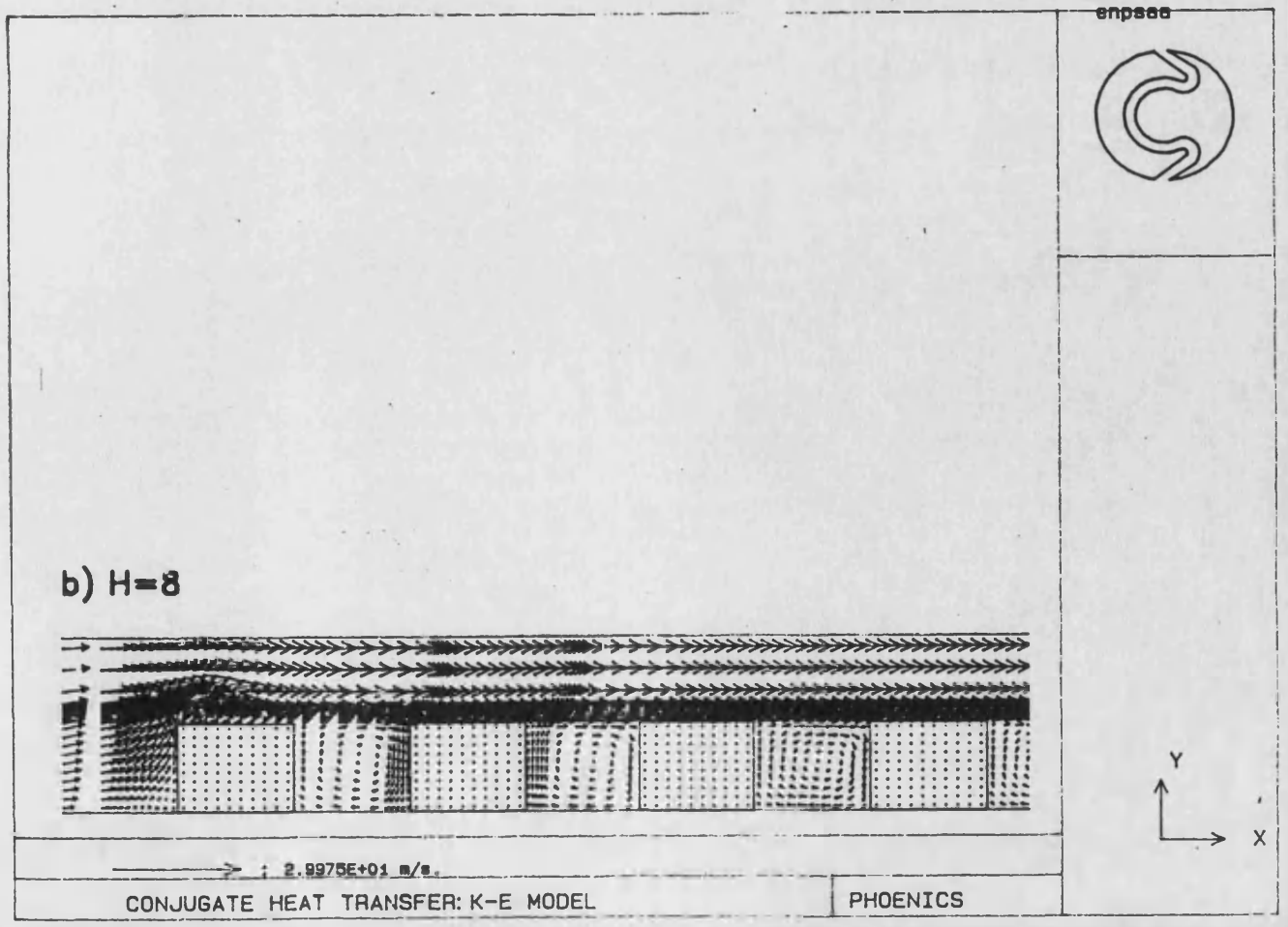

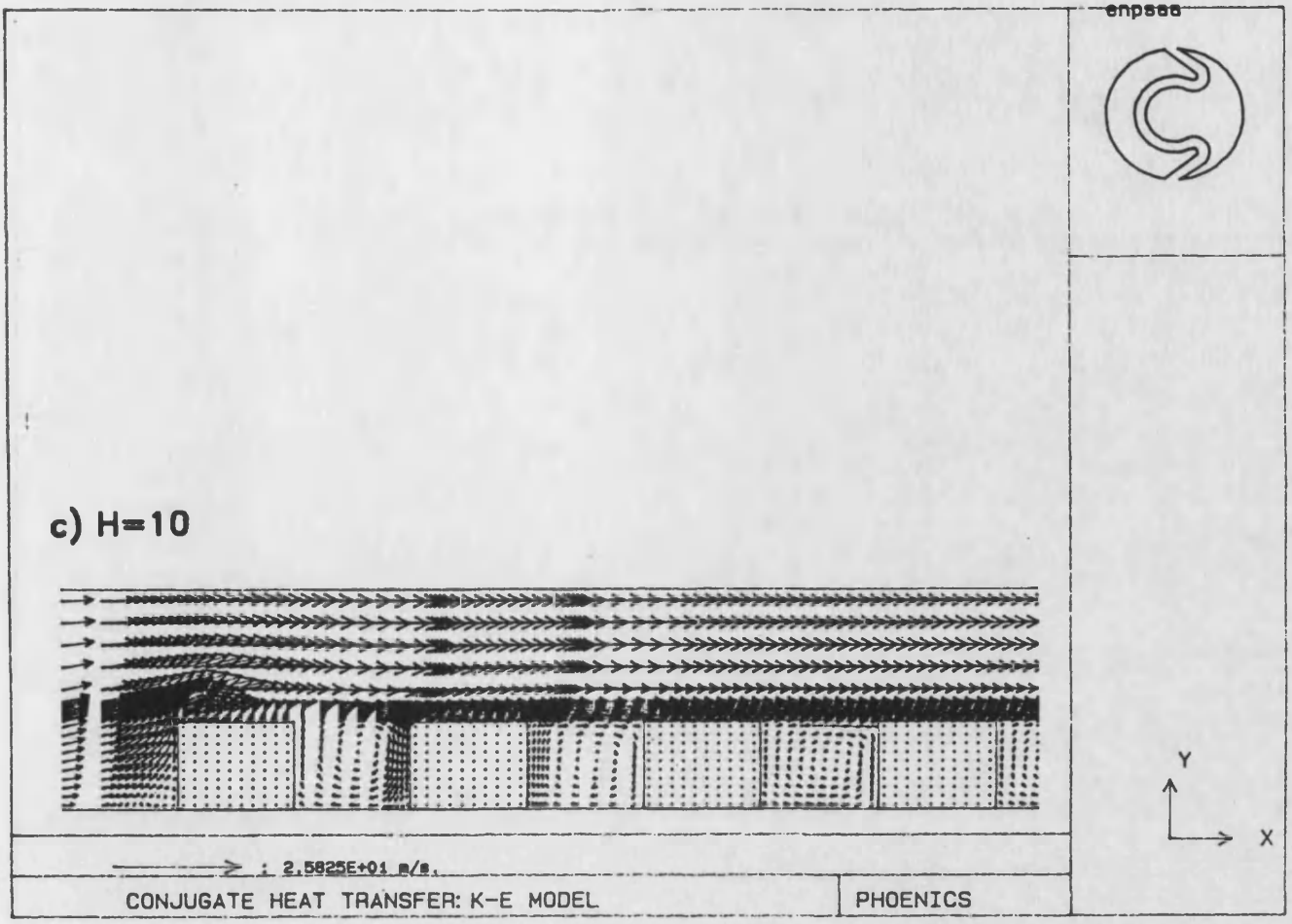

FIGURE 5.20: VELOCITY VECTORS OVER FIRST THREE BLOCKS Uin=5, q=6750, S=10 UNIFORM GRID

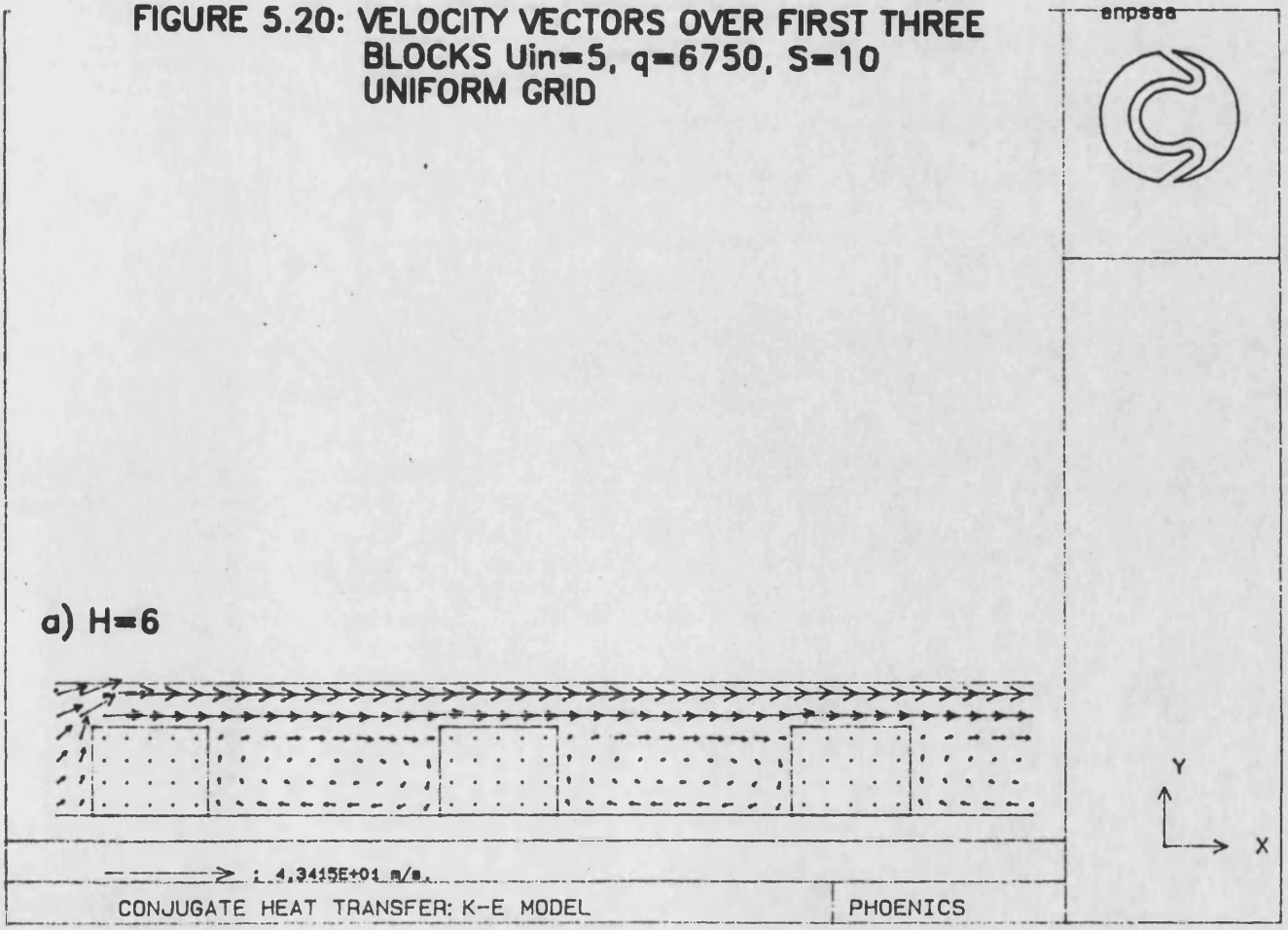

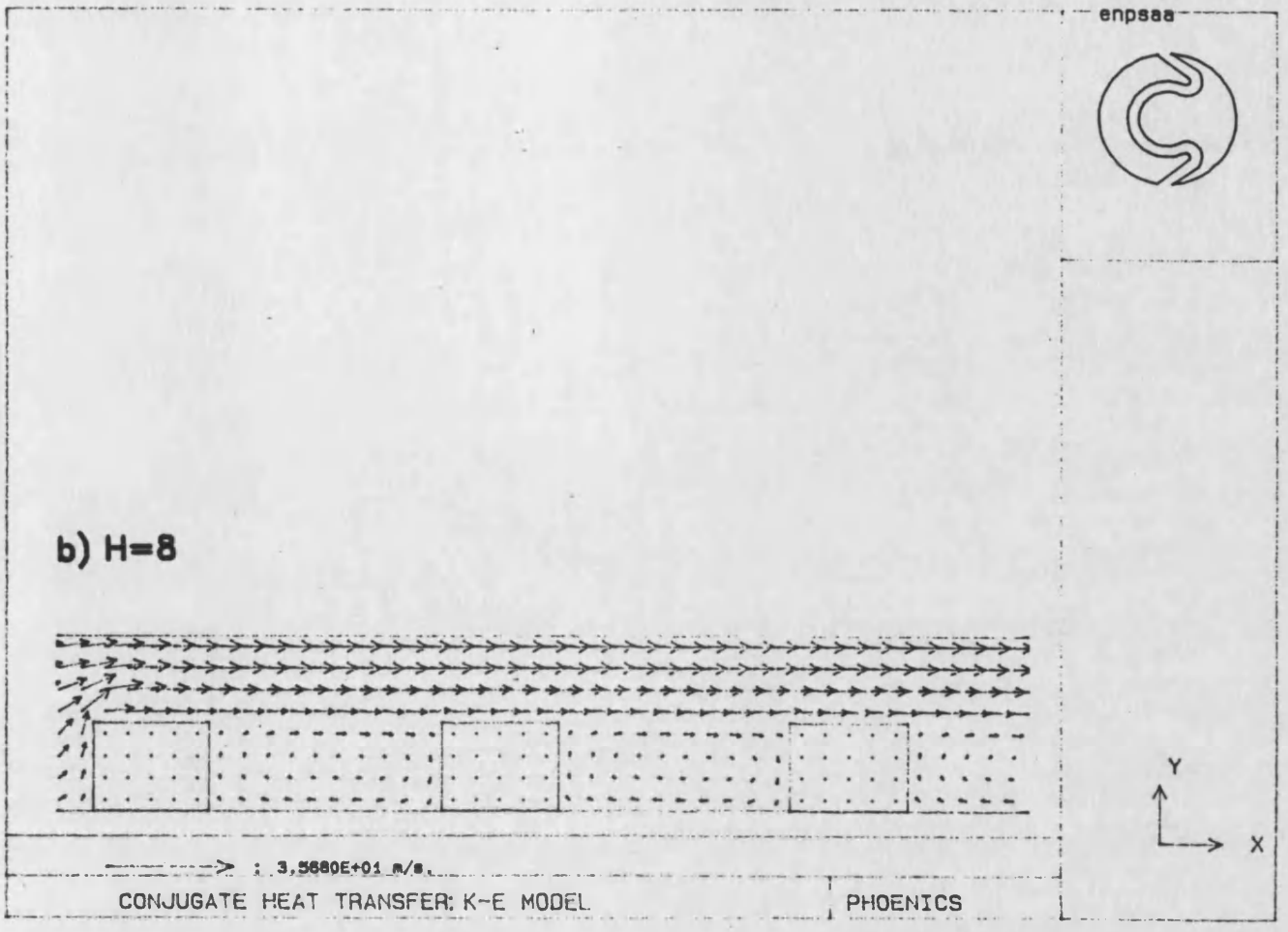
enpsaa
b) H=8
Y
X
: 3,5680E+01 m/s.
CONJUGATE HEAT TRANSFER: K-E MODEL
PHOENICS

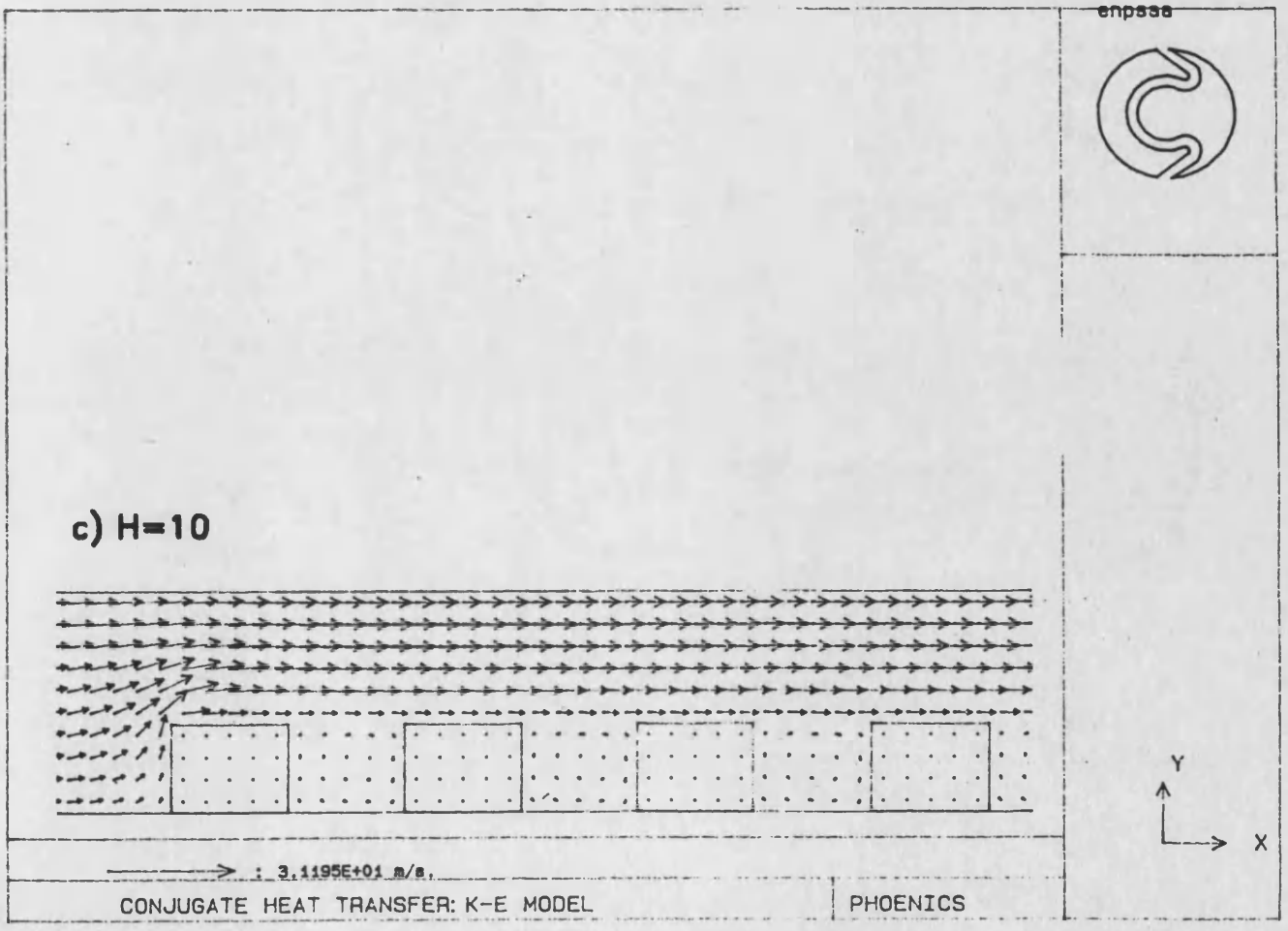
enpsaa
c) H=10
Y
X
: 3,1195E+01 m/s.
CONJUGATE HEAT TRANSFER: K-E MODEL
PHOENICS

FIGURE 5.21: VELOCITY VECTORS OVER FIRST FOUR BLOCKS Uin=5, q=6750, S=5 UNIFORM GRID

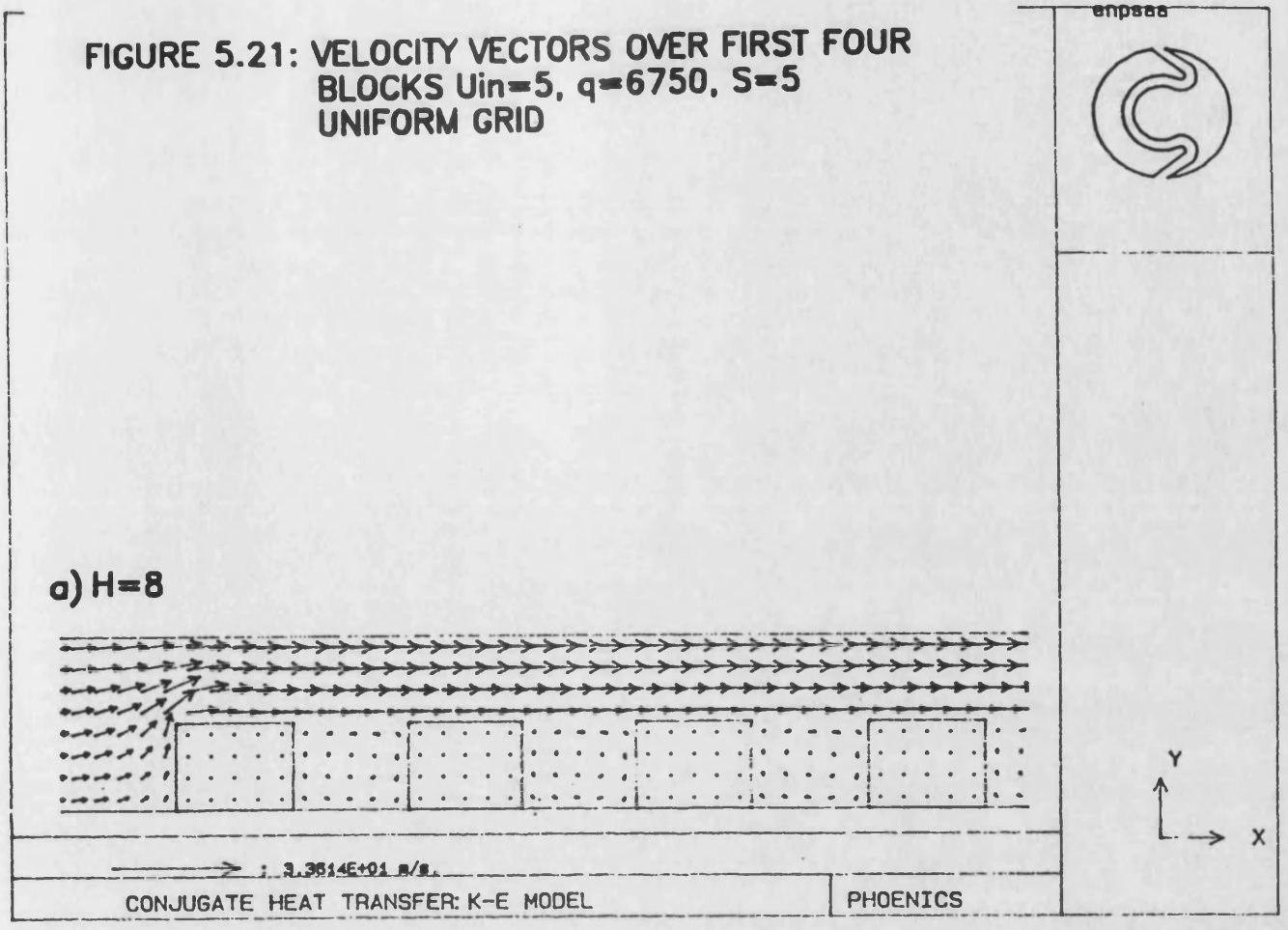

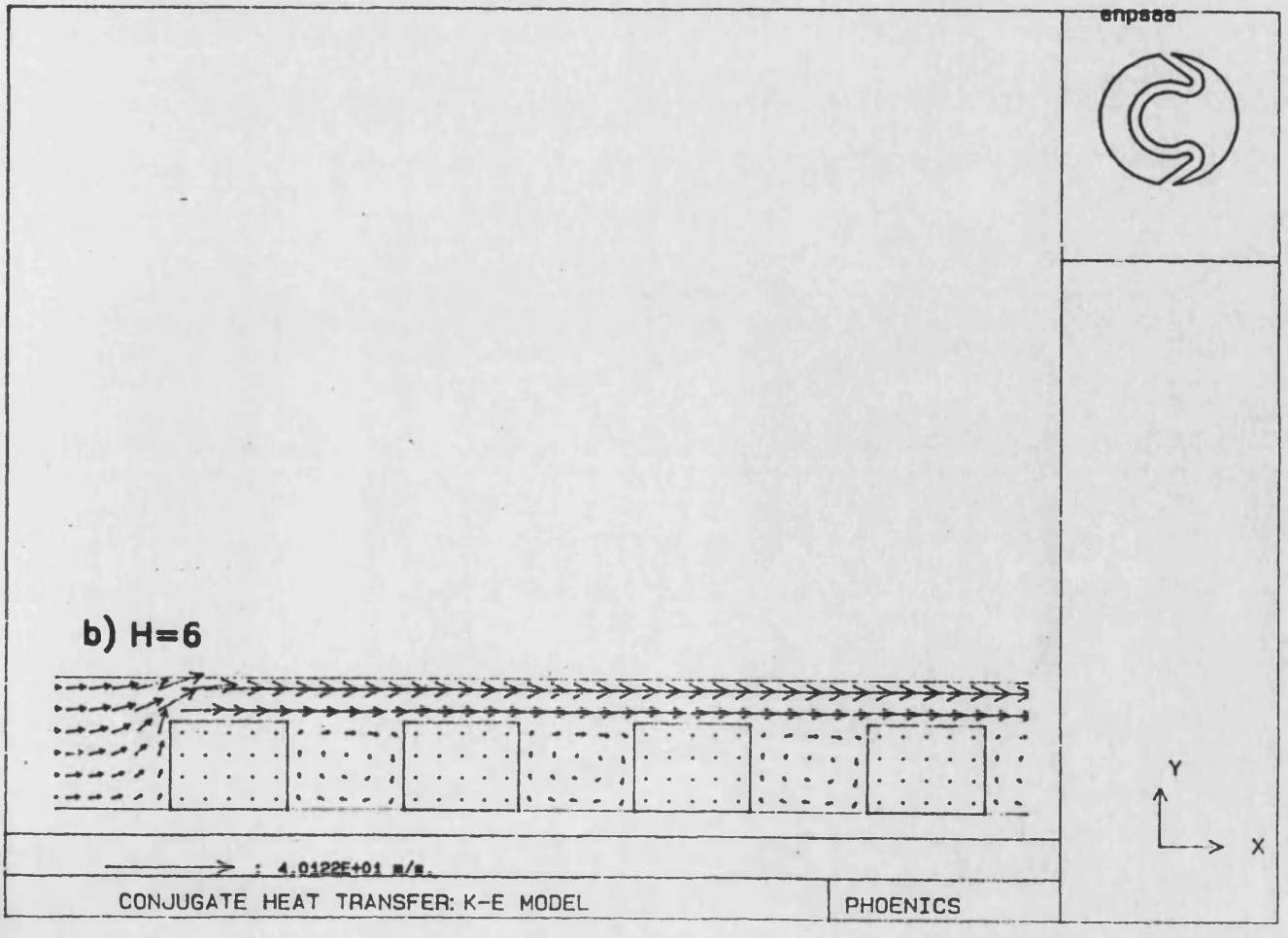

CHAPTER [6]

THEORETICAL AND EXPERIMENTAL INVESTIGATION OF HEAT-TRANSFER

6.1 INTRODUCTION

To simulate the dissipation of heat in electronic components, energy source terms were introduced into the energy equations of particular blocks. The problem is one of conjugate heat transfer from heated blocks to a cooling fluid. Temperature profiles in the solution domain have been predicted, and these have been used to derive values of the heat transfer coefficient **h** at the fluid/block interface. The effect of flow velocity and model geometry on h has been investigated.

The heat transfer predictions of this Chapter are based on the flow model, and velocity profiles, described previously in Chapter (5).

The problem of calculating the temperature distribution in a regular array of arbitrarily heated blocks on an adiabatic wall in a channel is readily seen to be quite involved. It is first necessary to isolate the geometric parameters of interest so that they may be expressed as non-dimensional ratios. The effect of varying these geometric ratios on both the velocity and temperature profiles was systematically investigated. The block height **B** was chosen as an appropriate length scale with which to

normalise the other geometric variables. Later the effect of these parameters on the heat transfer correlation was also investigated.

The four variables which are to be investigated in this Chapter: (1) **H/B**, channel-to-block height ratio (2) **S/B**, the array sparseness described by the spacing, **S** (3) the position within the array (i.e., one would not expect the heat-transfer characteristics of a first element to be the same as an element in the middle of the array; and finally (4) the flow rate in the channel.

6.2 ELEMENTS SURFACE TEMPERATURE DISTRIBUTION

The computational model under study contained eight rectangular elements, 4cm high and 5cm wide. Although elements could be heated arbitrarily, the special case when all elements were heated uniformly was considered to be an important datum state. The heat transfer coefficient and the surface temperature of individual elements were determined as functions of flow rate and channel spacing. Three channel spacing were used (**H/B**=1.5, 2.0, and 2.5), and two array densities (**S/B**=1.25 and 2.0). The approach velocity (velocity in the channel ahead of the first element) ranged from 3.0 to 10.0m/s.

Figure (6.1) shows typical temperature distributions corresponding to a range of air velocities at a power dissipation of 22.5W. As the approach velocity was increased to 10m/s for the same channel spacing, the

surface temperature of each element decreased. This is because of the increased local velocity over the top surface of each element. The higher heat transfer rate from those surfaces (at a fixed rate of power dissipation) leads to a reduction in surface temperature of the elements. For a given approach velocity, the surface temperatures of the elements increase in the direction of flow so that the highest temperature occurs on the last element (number 8). Figure (6.2) shows the element surface temperature rise for three power inputs and an approach velocity of 5m/s. This Figure shows that the rise in temperature of the surface of an element, measured above the inlet temperature, is directly proportional to the level of power dissipation. This result is to be expected because when the coolant velocity is held constant then the distribution of surface heat transfer coefficient will also remain constant.

6.3 GENERAL DEFINITION OF THE HEAT-TRANSFER COEFFICIENT

The rate **Q** at which heat is transferred by convection from a solid body of surface area $\mathbf{A_s}$, and at a surface temperature $\mathbf{T_s}$, to an adjacent fluid at an ambient temperature $\mathbf{T_f}$, is expressed in terms of the rate equation:-

$$Q = h A_s (T_s - T_f) \qquad \textbf{(6.1)}$$

In experimental heat transfer research Equation (6.1) is used as a definition of the heat transfer coefficient, **h**. Substituting the experimental data yields an empirical value of **h**

$$h = \frac{Q}{A_s(T_s - T_f)} \qquad (6.2)$$

or

$$h = \frac{q}{(T_s - T_f)} \qquad (6.3)$$

Although **h** cannot be regarded as a transport property of the solid/fluid interface, its value does depend only on the dynamic state of the fluid local to the surface, and the thermodynamic properties of the fluid. Provided that these properties are essentially independent of temperature then the great utility of the **h** concept is that its value is independent of the magnitude of either the temperature difference ($T_s - T_f$) or the heat flux **q**.

6.4 SELECTING AN APPROPRIATE FLUID AMBIENT REFERENCE TEMPERATURE

It would appear from Equation (6.3) that the empirical evaluation of h is straightforward. In electronic cooling systems the power dissipation rate can be readily measured to give **Q**. The surface area of the component is known, and its surface temperature is measured by an appropriate

sensor. The only unknown required to complete the data set is the ambient fluid temperature T_f.

Unfortunately for the case of air flowing over an array of arbitrarily powered electronic modules in a duct, the air temperature rise along the duct is difficult to specify without ambiguity. The practice for flow in ducts is to use the energy balance equation to define the bulk mean temperature of the fluid at any point along the duct

$$\Sigma Q = m\, Cp\, (\overline{T_b} - T_{inlet}) \qquad (6.4)$$

where ΣQ is the total power added between the inlet and the location in question.

The mixed mean temperature or bulk mean temperature T_b is convenient because it can be calculated from equation (6.4) at any location in a duct, if the flow rate and the heat added up to the point in question are known:-

$$\overline{T_b} = T_{inlet} + \frac{\Sigma Q}{m\, Cp} \qquad (6.5)$$

The above equation is really a definition of T_b, and is based on an assumption of perfect transverse mixing of the fluid at each point along the duct. Thus the bulk mean temperature is a statistical convenience not a value which can be measured.

It should be noted that in electronic cooling the mass flow rate is relatively large and the power dissipation levels

used are relatively small in practice. Therefore the total rise in bulk temperature through the duct is quite small (1 or 2°C) in comparison with the temperature difference $(T_s - T_f)$.

It was explained in Chapter (5) that in fact the transverse mixing in the channel is poor. Heating effects of upstream modules are confined to a rather thin layer of fluid adjacent to the modules which is convected downstream as a thermal wake. This heated wake forms the local ambient temperature for the downstream modules. Thus the temperature of a module cannot be predicted from the local fluid dynamic state alone, the temperature of the thermal wake shed by any powered module upstream must also be known.

Unfortunately the cumulative contributions to this wake of the arbitrarily powered upstream modules are difficult to determine.

Thus, in the evaluation of h from experimental data, there are a number of possibilities for the choice of T_f. In the experimental research of Hardisty et al [52] the bulk mean air temperature calculated from Equation (6.4) was used. This leads to the following definition of **h**

$$h_b = \frac{q}{(T_s - \overline{T_b})} \qquad \textbf{(6.6)}$$

Alternatively the air temperature at duct inlet could be used

$$h_{inlet} = \frac{q}{(T_s - T_{inlet})} \qquad (6.7)$$

In electronic cooling because the rise in bulk temperature is small for the application considered, h_b and h_{inlet} do not differ greatly. Thus, because of its convenience Equation (6.7) is favoured by some investigators.

In the theory of heat transfer across external boundary layers the free stream temperature outside the boundary layer (T_∞) is used as the constant reference temperature

$$h_\infty = \frac{q}{(T_s - T_\infty)} \qquad (6.8)$$

This choice was considered for the experimental work at Bath, and some preliminary temperature traverses across the duct were made.

However, the difficulties of measuring T_∞ consistently, together with the fact that in practice it might not differ materially from T_b, led to the abandonment of this approach.

6.5 DEFINITION OF "LOCAL" h

It will be apparent that for a module in the first row of an arbitrarily heated array, all the above definitions yield the same value of h, because T_{inlet}, T_b and T_∞ are equal. Furthermore, for the case of a single heated module at any position in the array the same equivalence holds,

and again all definitions of **h** yield the same value. Finally consider the case of fully developed flow, when the fluid dynamic conditions are identical over all modules. For this case, for a single heated module, **h** will have a constant value, which will be independent both of the position of the module in the array and of the equation which is used for its calculation. Experiments to demonstrate this proposition were carried out by Hardisty et al [52].

The above characteristics demonstrate that the heat transfer coefficient can be considered to have "local" value h_i which depends only on the characteristic state of the flow (velocity, turbulence etc) local to the surface. It is this value of h_i which can be predicted by means of computational fluid mechanics and in particular by the PHOENICS program.

It will be appreciated that considerable care must be exercised when making use of **h** values reported in the literature for design purposes, to ensure that the calculation is based on a consistent definition of **h**.

For example consider the important datum case of fully developed flow with all modules in the array dissipating the same power which was investigated by Hardisty et al [52]. For fully developed flow h_i will be the same for all rows in the array, and the value of h_i can be calculated from the temperature difference $(T_s - T_{inlet})$ for the first row. However, the temperature of the thermal wake progressively rises as it is heated in its passage

downstream. Thus the surface temperature of the downstream modules also progressively rises. When the bulk mean temperature was taken as the fluid reference temperature, and h_b was calculated from Equation (6.6), it was found that because $(T_s - T_b)$ increased in the downstream direction, there was a corresponding decrease in h_b. It is worth reiterating that this decrease in h_b with downstream distance is not in conflict with a constant value of h_i for all rows.

In an array of modules with an arbitrary distribution of power dissipation it is difficult to measure h_i directly because of the largely unknown effects of the thermal wake. Moffat [50] has proposed a method of overcoming this difficulty by defining an "adiabatic temperature of the heated element", T_{ad} which is the temperature the component achieves when its own power is shut off. The rise in surface temperature when power to the component is switched on is used to define an "adiabatic" heat transfer coefficient h_{ad}

$$h_{ad} = \frac{q}{(T_s - T_{ad})} \qquad (6.9)$$

h_i and h_{ad} are alternative ways of expressing the same concept. Moffat [50] has suggested that the temperature rise above the channel inlet temperature can be broken up into two terms

$$T_s - T_{inlet} = (T_s - T_{ad}) + (T_{ad} - T_{inlet}) \qquad (6.10)$$

$(T_s - T_{ad})$ = the "self-heating" temperature rise of the module due to the internal power dissipation

$(T_{ad} - T_{inlet})$ = the "adiabatic temperature rise" due to the thermal wake effect of upstream heated elements.

Thus to determine the temperature of a particular module in an arbitrarily powered array the two temperature rises of Equation (6.10) may be computed separately. The first temperature rise, that of the module above the local ambient (T_{ad}) due to its own power dissipation, may be computed from Equation (6.9) provided that the adiabatic heat transfer coefficient is known. In the present investigation h_{ad} (h_i) is obtained from predictions using the PHOENICS code.

The second temperature rise, the thermal wake effect, consists of a summation of separate heating effects from upstream modules, powered in a more or less arbitrary manner. A method of carrying out this summation process based on the principle of superposition is described below.

6.6 SUPERPOSITION METHOD

If it may be assumed that the properties of the fluid are essentially independent of temperature (a reasonable assumption for air in these low temperature applications), then the thermal energy equation of the boundary layer is linear and homogenous, Shah and London [55]. In this case a sum of solutions of the temperature field is again a solution of the thermal energy equation. In the theoretical analysis of the boundary layer for flow in a duct this principle has been used by first breaking up the specified distribution of wall temperature (or heat flux) into a number of step changes in boundary conditions. Then the solution to the separate step changes are summed (superimposed) to obtain the solution of the specified distribution of boundary conditions.

The principle of superposition may also be used to predict the temperature of the thermal wake shed by an array of arbitrary heated modules. For the datum condition of a single heated module dissipating unit power, temperature measurements can be used to construct a wake function for that module. This will show how the wake temperature decays as it passes over succeeding downstream rows of modules. A complementary view of this wake function is that it shows the effect on the temperature of a downstream module of heating an upstream module. It will be apparent that this effect is greatest on the module which is immediately downstream of the powered module and falls off after this.

For the case of fully developed flow this effect will become a universal function which will be independent of which particular row is heated, but will depend only on the relative distance, measured in the downstream direction, from the powered module.

It also follows immediately from the linearity of the thermal energy equation that increasing the power dissipation merely serves to increase the absolute values of temperature differences. Provided that temperature distributions, or wake functions, are expressed in a suitable non-dimensional form these will be unaffected by changes in power.

It is perhaps worthy of note that in practice heat is transferred between adjacent modules not only by convection in the wake, but by conduction through the PCB. This conduction effect, which is the subject of a separate investigation, will be negligible in the present model.

6.7 HEAT-TRANSFER COEFFICIENTS FROM PHOENICS

The manner in which the finite difference form of the momentum equation is solved in the PHOENICS program to yield the velocity field, has been described in Chapter (3) and (4). Earlier in this section it was explained that the local value of the heat transfer coefficient, $\mathbf{h}_i$, depended only on the state of this velocity field. The manner in which the value of **h** is calculated in PHOENICS was presented in Chapter (4).

This value of **h** is derived directly from the velocity distribution that it is equivalent to the local value of h_i (or h_{ad}) defined earlier. Numerical values of this heat transfer coefficient, together with a suitable empirical expression for the wake function, allow the temperature of a module to be predicted.

6.7.1 THE EFFECT OF CHANNEL SPACING

Figures (6.3a) and (b) show the velocity and temperature profiles over the third block for different approach velocities and channel heights. The objective of this test was to maintain the same local velocity for the three conditions shown, so that the fluid temperature near to the block surface could be compared for the same fluid dynamic conditions. From the above Figures it was clear that with small values of both approach velocity of (3m/s) and channel spacing (**H/B**=1.5) the fluid temperature near the wall has a higher value than the case when both have high values ie approach velocity of 10m/s and channel spacing of **H/B**=2.5. This is because by reducing the channel spacing, although the approach velocity is small, the area of the gap above the blocks has reduced, which will increase the local velocity of air above the blocks for the same volume flow rate. The increase in the local heat transfer coefficients over the blocks leads to more effective cooling of the blocks.

Again, and referring to the last Chapter, reducing the height ratio causes the contribution of the flow velocity to cooling the blocks to increase. Conversely, increasing **H/B** reduces the local velocity around an element, even at constant approach velocity. In this case, **H/B** can be regarded as a factor which, combined with the approach velocity, controls the effective velocity.

The above tests were repeated for the block in row 6 and similar effects were noticed, Figures (6.4a) and (b). The similarity of the profiles over these two blocks indicates that the flow is "fully developed".

a) LOCAL HEAT TRANSFER COEFFICIENT

Figure (6.5) shows data for the local heat transfer coefficient over the last six elements (Nos 3-8) for **H/B**=1.5 and three approach velocities. Because the flow conditions over the first two elements in the channel are affected by flow separation, results for rows 1 and 2 have not been shown.

Figure (6.5) shows that the local heat transfer coefficient increases with approach velocity. For the given approach velocity the heat transfer coefficient is the same for all blocks, independent of row number, indicating that the flow is fully developed. This is confirmed by a plot of the velocity profiles for the six elements, these lying virtually on top of each other (refer to Figures (6.3) and (6.4)).

Referring back to Figure (6.1), showed that the element surface temperature was increasing with row number for a given approach velocity. However, as elements with the same velocity profile would be expected to have the same heat transfer coefficient, the only explanation for the rise in surface temperature of elements with row number appears to be that it is the effect of thermal wake of upstream elements on downstream rows.

This thermal wake effect will be discussed in full detail in the later section.

From an examination of the data in Figure (6.5) and all other data from this study, it was deduced that the heat transfer coefficient can be considered to have reached a row-number-independent, fully developed value by the third row for all test runs.

b) FULLY DEVELOPED REGIONS

Heat transfer in the fully developed region of the array is also strongly affected by channel spacing **H/B**, even in tests conducted at constant approach velocity, as shown by the data in Figure (6.6). Here **h** (measured in row 6) drops significantly as the channel height increases for all values of approach velocity. At 10m/s, for example, h drops from 91.8 to 52W/m^2 $^\circ$C as **H/B** increases from 1.5 to 2.5.

As **H/B** is increased to larger values, the effect on **h** becomes greater. The flow seems to take the path of least resistance, and more of the flow bypasses the elements.

This causes a lower local velocity and results in the lower heat transfer coefficients.

As channel height increases, the heat transfer coefficient becomes less dependent on channel height and seems to approach an asymptotic value. This might indicate that beyond a certain **H/B**, there is only an insignificant change in the velocity seen by the elements with further increase in the channel height, leading to an almost-invariant value for the heat transfer coefficient.

The decrease in the dependency of heat transfer coefficient on channel height is seen from Figure (6.6) to be less pronounced at the lower Reynolds numbers. The resistance offered by the elements can be characterised by the pressure drop across the channel. Since the pressure drop varies as the square of velocity, the resistance to flow decreases more rapidly than the Reynolds number. This implies that at lower values of $\mathbf{Re_H}$, the elements offers a smaller resistance to flow, less of the flow bypasses the elements, and the channel height has a smaller influence on the heat transfer coefficient.

6.7.2 THE EFFECT OF ARRAY DENSITY

In this section the effect of array density on the local value of **h** over the element in row (6) is reported.

Figure (6.7a) show the effect of varying **H/B** at a constant array density, **S/B**=1.25.

At an approach velocity of 10m/s the heat transfer

coefficient drops more than 39 percent when **H/B** changes from 1.5 to 2.5. At smaller streamwise spacings, confined flow exists in the cavities between elements. Heated fluid is trapped in these cavities and continuously recirculates. In contrast, with the larger spacings between elements, it appears that the flow that separates from the leading edge of an element reattaches in the cavity just downstream. Heated fluid between elements is carried away by the main flow, resulting in higher heat transfer coefficients. Flow visualization support this theory. However, it is apparent that the more dense spacing is more sensitive to variations in channel height.

Similar remarks can be made when the array density is larger ie **S/B**=2.0, Figure (6.7b).

For the relatively small ranges of block spacing tested the effect of this parameter on heat transfer coefficient was found to be small.

Figures (6.3) through (6.7) serves to illustrate the complex nature of the effects on **h** for the different geometries tested.

6.7.3 LOCAL NUSSELT NUMBER

The effects of **S/B** and **H/B** on the heat transfer coefficient are demonstrated in Figure (6.8). For this Figure the data from Figures (6.7a) and (6.7b) have been brought together and plotted as local Nusselt number, (**hB/k**) against local

Reynolds number, (uB/υ). It can be seen that the data for two array densities have been successfully correlated.

The correlation can be expressed in the form

$\mathbf{Nu = 0.011\ Re^{0.62}}$, Figure (6.9).

Other studies have suggested values for the proportionality constant, **C**, and exponent, **n**, for different flow geometries.

For the turbulent flow through parallel planes, value of 0.8 was observed for exponent **n**. It is not surprising that, as the regular array of rectangular elements becomes very dense, the Reynolds number exponent increases to approach the behaviour observed in turbulent flow between smooth parallel planes, i.e., $\mathbf{Nu \propto Re^{0.8}}$.

The conclusion which must be drawn from the data presented so far is that the heat transfer behaviour is specified at least by five parameters, these are: channel height, approach velocity, element spacing, element size and position within the array.

By assuming that heat transfer to an element depends mainly on the velocity around it and that the flow bypasses the array whenever a clearance gap existed over the tops of the elements, ($\mathbf{H/B}>1$), the dimensionality of the problem can be reduced by eliminating **H/B** as a parameter.

6.7.4 THERMAL WAKE PROFILE

Consider a regular array of passive elements, with the exception of a single element which is heated. The energy

released from the heated element will be convected downstream in the form of a heated wake, and the passive elements downstream will be heated by the wake and rise in temperature. In the steady-state condition, these elevated temperatures are the adiabatic temperatures of those passive elements.

Consider next a condition where a neighbouring element adjacent to the first heated element is also heated to some different power level. Again, its energy release is convected downstream. A passive element which is located in a position common to the wakes of both heated elements would then receive a contribution to its adiabatic temperature (in steady-state) from both heated elements.

It is to be expected that the contribution from a heated element a number of rows upstream of some passive element would be smaller than the contribution of an element with same heat release just one row upstream. If, as previously discussed in section 6.6, it is postulated that the governing equations are linear, then the calculation of the adiabatic temperature of this passive element can be made by simply adding the contributions of each of the two heated elements. If this procedure is generalised when many heated elements are upstream of a passive element, the adiabatic temperature of this element may be determined by superposing the separate contributions of the upstream heated elements. Thus if the thermal wake profile for a single heated element can be determined then this can be used, together with the principle of superposition, to

construct a general solution for any multiply heated arrangement.

Furthermore, the thermal wake profile will be a function of those parameters which describe the system as **H/B, S/B,** position in array, and mass flow rate.

For a known energy input, the adiabatic temperature of an element may be determined, and by using the known value of the adiabatic heat-transfer coefficient, its temperature rise above the adiabatic temperature may be calculated.

6.8 DETERMINATION OF THE ADIABATIC TEMPERATURE RISE

6.8.1 INTRODUCTION

It was proposed in section 6.5, Equation (6.10), that the total temperature rise of an element could be split into two terms, the self-heating temperature rise ($T_s - T_{ad}$), and the temperature rise due to the thermal wake ($T_{ad} - T_{in}$).

Methods of using an appropriate value of the heat transfer coefficient to calculate ($T_s - T_{ad}$) were discussed in previous sections, it now remains to discuss methods of estimating ($T_{ad} - T_{in}$).

Any general theoretical method capable of predicting the heating effect of a thermal wake produced by an array of arbitrarily shaped modules, arbitrarily powered, would appear to beyond the capability of current CFD techniques. Thus attempts to analyse thermal wake effects have been

largely empirical. There appear to be two principal approaches:-

i) Experiments are carried out on an array of simple cubical elements on a non-conducting substrate. One of these elements is heated and the adiabatic temperatures of the elements in the downstream rows are measured. Attempts are made to correlate the data curves with empirical equations of lesser or greater complexity [40].

ii) Provided that fully developed flow is assumed, then h_{ad} should be the same for all elements in whatever row. If element temperatures are measured for the case of all elements powered equally, then it should be possible to separate out the heating effect of the wake from the self heating effects. Such a method was proposed by Wills [10], but little data was given as validation of the proposed method.

In a later section an attempt will be made to compare a wake correlation function of the type proposed by Moffat [50] with the results of the present investigation. It should be pointed out that any general analysis of the thermal wake will be difficult to achieve because of the changes in shape both of the industrial packages (it is almost impossible to quantify "shape"), and of the cooling duct, which occur continuously in practice. Also for most experimental research investigations the heated modules are mounted on an adiabatic substrate, which eliminates conduction between adjacent modules. Experiments by Hardisty and Abboud [51] on real PCBs have indicated that

preferential conduction through the copper conduction layers in the PCB may play a significant role in the heat transfer process.

6.8.2 ADIABATIC TEMPERATURE RISE - ELEMENT NO 1 HEATED

Figures (6.10a), (b) and (c) shows the adiabatic temperature rise of the elements downstream of the first heated element for three power inputs and three upstream velocities. As the approach velocity is increased for the same power input Figure (6.10a) the adiabatic temperature rise of each element decreases. This is because the greater mass flow through the duct which is associated with the higher approach velocity reduces the magnitude of the temperature rise in the thermal wake. The element immediately downstream of the heated element will be hotter than the mean fluid temperature, because the thermal energy will not have been diffused across the stream, most of it will remain concentrated near the heated surface. This behaviour is intuitively acceptable. Immediately downstream of the heated element not much mixing has occurred, the adiabatic temperature is high. Further downstream the thermal wake from the first element has been broken up in its passage over many elements. The adiabatic temperature has been reduced, approaching the mean temperature.

For clarity, the data at a constant approach velocity of 3m/s has been extracted from the above Figure and

replotted as Figure (6.11). It can be seen from this Figure that the adiabatic temperature rise of each element is directly proportional to the power input. Thus once a relationship between adiabatic temperature rise and row number has been determined for a particular power, the relationship at other powers can be deduced prorata.

6.8.3 ADIABATIC TEMPERATURE RISE - ELEMENTS 2 AND 3 HEATED

Figures (6.12a), (b) and (c) shows the adiabatic temperature rise of the downstream elements when power was supplied to both elements 2 and 3. In a similar manner to the data presented in Figure (6.10), tests were run at three values of upstream velocity and at three power inputs. As expected, the curves of Figure (6.12) have similar characteristic shapes to those already discussed in Figure (6.10).

Because the heating effect represents the contribution from 2 heated elements it is now possible to carry out a simple check on the superposition principle. For any passive element n, the total adiabatic temperature rise ΔT must be the sums of the contributions from elements 2 and 3.

$$_{2,3}\Delta T_n = {}_2\Delta T_n + {}_3\Delta T_n \qquad (6.11)$$

Consider the first passive element, n=4

The data from Figure (6.12c) shows that

$$_{2,3}\Delta T_4 = 7.9 \qquad _2\Delta T_4 = 3.0 \qquad _3\Delta T_4 = 4.9$$

which numerically verifies Equation (6.11).

This summation process has been expressed graphically in Figure (6.13), which shows that adiabatic temperature rise when both elements 2 and 3 are powered, can be obtained from the addition of the curves for elements 2 and 3 powered singly.

6.8.4 THE G-FUNCTION

The approach described here is based on earlier work by Sellars et al. [53], who presented a solution for the adiabatic wall temperature in a tube whose wall heat flux varied arbitrarily, although remaining peripherally uniform. Their method was based on the superposition principle, taking advantage of the linearity of the differential equation governing the temperature distribution in the fluid. Their solution is:

$$Tad(X^+) - Tin = \frac{r_0}{K} \int_0^{x+} g(X^+ - \xi)\, q_0(\xi)\, d\xi \qquad (6.12)$$

$$g(X^+) = 4 + \Sigma_m \frac{\exp\{-\gamma_m X^+\}}{\gamma_m^2 A_m} \qquad (6.13)$$

Discretizing this solution for a one dimensional problem in which the heat flux varies only on a row by row basis we

can write the following equation for the adiabatic temperature rise on the nth row:

$$(Tad\text{-}Tin)_n = \sum_{i=1}^{n-1} \frac{q_i}{mCp} G(n-i) \qquad (6.14)$$

Where **i**=1 is the first row of elements and **i**=1 through **i**=**n**-1 is the summation over all upstream elements. The adiabatic rise of an element is the sum of contributions from all the upstream elements. **G** is the one dimensional superposition Kernel function. From the above equation it is obvious that **G** is the ratio of the adiabatic temperature rise of the air to the mean temperature rise at the nth row of elements, due to heating the **i**th row of elements.

$$G(n-i) = \frac{T_{ad,n-i} - Tin}{T_{m,n-i} - Tin} \qquad (6.15)$$

Figure (6.14) is a plot of the predicted one-dimensional superposition Kernel function, **G**, versus row number for several typical configurations. In this case the first element was heated (i.e., **i**=1) and temperature measurements were made on all of the downstream elements.

The Figure shows the function **G** for two channel spacings, **H/B**=2.5 and 2.0, and for two velocities, **V**=5.0 and 10.0m/s. The value of **G** is highest in the first row downstream of the heated element and decreases exponentially in the downstream direction. **G** asymptotically approaches zero as the downstream distance increases, this is because the adiabatic temperature approaches the bulk mean temperature.

Moffat and Anderson [50] carried out research on the above effect, in which they called the **G**-function the Unit Pattern Factor. The pattern factor displays the one-dimensional effect of a single uniformly heated row on its downstream neighbours. They showed that the **UPF** is strongly affected by passage height, but only slightly affected by the approach velocity. This latter effect is confirmed by the present research.

Figure (6.14) shows that for the two approach velocities considered, the velocity had only a small effect on **G**.

6.9 EXPERIMENTAL VALUES OF HEAT TRANSFER COEFFICIENT

6.9.1 THERMAL WAKE

As discussed in the previous section, the present method of calculating the distribution of temperature in the array uses superposition of the wake functions of individual heated blocks.

A typical thermal wake behind a single heated block in the array may be presented in the form of a dimensionless temperature ratio, θ, defined as

$$\theta \triangleq \frac{T_{measured} - T_{amb}}{T_{heated\ block} - T_{amb}} \qquad (6.16)$$

θ is the dimensionless temperature of a passive element scaled on the temperature rise of the heated element. Note, by definition, the heated block has a θ value of 1.

6.9.2 EFFECT OF VELOCITY ON THE DIMENSIONLESS TEMPERATURE RATIO

a) PHOENICS RESULTS

Figures (6.15a), (b) and (c) shows the dimensionless temperature ratio behind a single heated block for three different approach velocities. It can be seen that the approach velocity has no significant effect on the thermal wake profile when this is expressed in dimensionless form. These Figures also show that the position of the heated block in the array does not affect θ significantly.

b) EXPERIMENTAL RESULTS

Similar temperature ratio data was also measured experimentally Figure (6.16). A comparison of the curves in Figures (6.15) and (6.16) shows that there is good agreement between the shapes of the curves.
Figures (6.16a), (b), (c) and (d) show the experimental data produced for four different approach velocities. The discrepancy between some of the profiles is considered to be mainly due to the experimental errors, due to small temperature differences. Once again it is shown that neither the approach velocity nor the position of the

heated block have a significant effect on the thermal wake profile.

c) THEORETICAL AND EXPERIMENTAL COMPARISON FOR θ

The first block downstream of the heated block was selected as the reference block. A plot of θ for this block vs. Reynolds number based on channel height and approach velocity is shown in Figure (6.17). The data shows that position in the array does not affect θ significantly.
The experimental data diverge from the theoretical values. The cause of this divergence is thought to be the uncertainties which arises in the estimates of the small temperature difference in the experiment which arises at high values of Reynolds number. Also conduction losses occur in the experiments which are not present in the theoretical model.
The next step was to establish some empirical relation between the temperatures of the blocks downstream of the heated block to the value of θ. This relationship with blocks 2 and 3 heated is shown in Figures (6.18a) and (b). The data are plotted as measured dimensionless temperature, θ, normalized on $\theta_{(row\ 1)}$ vs the row number downstream of the heated blocks. A simple **1/N** type dependence is observed, although, initially, it was not clear weather **N** should be the number of rows or some measure of distance. This was later clarified from other results when a similar **1/N** dependence was found, see Figures (6.19a) and (b). This

later Figure exhibits some data scatter due to the experimental uncertainties.

This type of behaviour appears to be analogous to the characteristics of the dispersion of pollution behind a single source. A recent literature survey by Hosker [54] summarizes work on flow and diffusion near obstacles. In his report, several experiments are cited of dispersion measurements for varying geometric conditions. The propagation mechanism seems to be the mode of energy transfer in the present array of elements.

6.9.3 THE ADIABATIC TEMPERATURE RISE

Figure (6.20) shows experimental data for both the adiabatic temperature rise and the mean temperature rise against the approach velocity over the third block. This Figure shows that when the approach velocity is small the adiabatic temperature rise is nearly twice that of the mean temperature rise. However, as the approach velocity increases (large mass flow rate), the discrepancy between the two temperature rises become negligible.
This indicates highly effective mixing over the third block.

6.9.4 EFFECT OF VELOCITY ON h FOR BLOCK 3

Figure (6.21) shows the three different definitions of **h**: $\mathbf{h_{ad}}$, $\mathbf{h_m}$, and $\mathbf{h_{in}}$ calculated experimentally over the third

block for different approach velocities. For large channel spacing, **H/B**=2.5, the three values of **h** are nearly the same. This clearly demonstrates that complete thermal mixing is achieved by the third block.

The report by Arvizu and Moffat [40], using three definition of **h**, has also shown that for large channel spacing (**H/B**=4.6), the three values of **h** are almost the same, but they also showed that for low channel spacing, however, there is a significant difference, with $\mathbf{h}_{ad}$ is more than twice $\mathbf{h}_{in}$, and 33% larger than $\mathbf{h}_{m}$.

6.9.5 h VALUES OBTAINED BY FLUXMETER

Figure (6.22) shows the heat transfer coefficient vs. approach velocity for the second and third block when powered separately. The upper data show the heat transfer coefficients measured by attaching fluxmeters to the top faces of the second and third blocks. Heat flow sensors were cemented onto the surfaces so that they became integral with the surface. (The construction and principle operation of the fluxmeter is fully described in Chapter (7)).

The lower data show the heat transfer coefficients calculated directly from the experimental data, based on the measured power dissipation and a surface area equal to three exposed faces of the heated block. Both methods of estimating the heat transfer coefficient showed similar general characteristics, increasing with increase of

approach velocity, and decreasing slightly from second element to third element. However comparing the absolute values of **h** from the two experimental methods showed a significant discrepancy, especially at the higher approach velocities. There could be two reasons for this:-

a) The experimental values are average values for all three faces of the heated block, while the fluxmeter gives a point value at one location on the top face. This point value would be expected to be significantly greater than the space average.

b) Experimental uncertainties

In the all cases mentioned above the radiation losses were neglected because of the low level of the absolute temperature. In addition, it was found that large losses were taking place by conduction through the end and bottom faces of the elements which were not exposed to the flow. The theoretical model was two dimensional with no conduction or radiation losses, and therefore the theoretical predictions of heat transfer coefficients were lower than the experimental values. Hence it was difficult to make comparisons of experiment and theory.

6.9.6 THE EFFECT OF UPSTREAM HEATING ON h

Figure (6.23) shows the effect of upstream heating on the heat transfer coefficient over the third block. This Figure shows that with the second element heated, the heat

transfer coefficient from the third block is reduced for the given approach velocity. This is clearly the effect of the thermal wake shed by the second element which will increase the temperature of the third element, and hence reduce the calculated value of the heat transfer coefficient.

Figure (6.24) shows both the Nusselt and Reynolds numbers based on channel height, **(H)**, the adiabatic heat transfer coefficient, $\mathbf{h_{ad}}$, and the approach velocity, **U**. The experimental Nusselt number values are higher than those obtained from the theoretical model. It was considered that the cause of this difference were the large conduction losses from the three faces of the heated element as mentioned above (since the theoretical model is a two-dimensional model, hence those faces were assumed to be adiabatic).

6.10 TEMPERATURE CONTOURS

A selection of the temperature contour plots produced using the PHOENICS Photon Subroutine are shown. Figures (6.25a), (b) and (c) shows the temperature contours over the unheated elements with the fourth element heated, for three approach velocities. It can be seen that the effect of increasing the approach velocity on the thermal wake over element 6 is very small. This effect was also illustrated in Figure (6.14).

a) EFFECT OF CHANNEL SPACING

Figures (6.26a), (b) and (c) shows the temperature contours over the first four elements all heated, for the same approach velocity of 10m/s and different channel spacing. The thermal boundary layer over the first heated block is thinnest for the case of the smallest channel spacing (**H/B**=1.5). This is because the air must be accelerated to a higher velocity through the smaller gap conversely increasing the channel spacing (**H/B**=2.5), causes the thermal boundary layer over the blocks to thicken.
Therefore for the given approach velocity, the decrease in channel spacing, decreases the thermal wake.
Figures (6.27a), and (b) shows the temperature contours over the whole domain with all the elements heated at uniform power. Inspection of these Figures shows that a well defined thermal boundary layer is formed over the surfaces of heated blocks which increases in thickness in its passage downstream. This constitutes a thermal wake which is contributed by each heated block to those lying downstream.

6.11 COMPARISON WITH THE ANSYS MODEL

ANSYS is a Finite Element Package used extensively by previous and present researchers on cooling of micro electronic components in the School of Mechanical Engineering, Abboud [98].

The FE package was used to construct two simple models of a single heated solid block. A two-dimensional model was used to check the two-dimensional PHOENICS model. A three-dimensional FE model was used to check data from the experimental rig. Values of heat transfer coefficient produced by a particular PHOENICS run were used as the boundary conditions for the two-dimensional ANSYS model. The surface temperatures produced from the ANSYS model matched well with those produced by the PHOENICS model.
The surface temperature of solid model in PHOENICS run was at 102.9°C and that of ANSYS model at 102.87°C.
The next stage was to compare the three-dimensional experimental model with the three-dimensional FE model Figure (6.28). Experimental data was used as the boundary conditions for the FE model. Initially the surface temperature produced by ANSYS did not match the measured experimental values of surface temperature. However because the experimental model was three-dimensional, there were heat losses by convection from the ends of the block which had not been allowed for in the ANSYS model. The ends of the block in the ANSYS model had been assumed to be adiabatic. Once the boundary conditions of the ANSYS model had been changed, there was good agreement between the predicted surface temperatures and those measured on the experimental rig.
Figure (6.29) shows the temperature distributions over the surface of the model for the three-dimensional model, Figure (6.30) shows the temperature distributions for the

two-dimensional ANSYS model.

6.12 CONCLUSIONS

Data are presented here for heat transfer from arrays of rectangular elements on an adiabatic wall for two array densities (**S/B**=1.25 and 2.0), three channel heights (**H/B**=1.5, 2.0, and 2.5) and three approach velocities (3.0, 5.0, and 10.0m/s).

The research has shown that the thermal wake behind a single heated element in an array is influenced by the **H/B** ratio, **S/B** ratio, position in the array, and the mass flow rate. The dimensionless channel height, **H/B**, can be regarded as a factor in determining the local flow as a fraction of total flow.

The study of channel spacing showed that it has a strong effect on the local temperature field and hence on local heat transfer coefficient. Decreasing the channel spacing, increases the local air temperature (increases the heat transfer coefficient).

For the range of block spacing (pitch) considered, the parameter **S/B** had no real effect on the temperature field and hence no effect on the overall heat transfer coefficient.

For a single heated element in the channel it was revealed that the thermal wake produced from this heated element would only affected those elements in its near vicinity.

The thermal layer produced by a single heated element will diffuse into the main stream after a distance equivalent to three block spacings.

The above study also showed that the first block has a strong effect on the flow field over the second and third element. The flow is almost fully developed by the fourth element.
The heat transfer coefficient was constant over the last five blocks, and the temperature rise of those blocks was due only to the effect of thermal wake received from the upstream elements.
From the temperature contours for different channel spacing and approach velocity, it was revealed that a very thin thermal boundary layer exists just above the blocks which will increase in thickness with distance downstream of the channel. This effect will increase the component temperatures, and cause failure of the components (or reduce the life of components).
By increasing the thermal mixing in the channel, the adiabatic temperature rise of the components can be reduced.

Heat transfer coefficient over the range of channel spacings, array sparseness values, position in the array, and mass flow rate tested in this study can be correlated using the local Reynolds number based on the height of the surface cell and the local velocity. The dependence takes

the form $\mathbf{Nu = 0.011\ Re^{0.62}}$.

It was shown that the adiabatic temperature rise of a passive element is due to the thermal wake it receives from the heated element upstream. The effect of a number of upstream heated elements (not necessarily at the uniform power) on the passive element will be the sum of contribution of those heated elements upstream.
In the fully developed region it was shown that the effect of heating one element on the adjacent element is the same as heating some element far downstream on its adjacent element.

The experimental data showed a satisfactory degree of agreement with the theoretical data obtained by PHOENICS. Both theory and experiment demonstrated that the temperature rise of an element is the sum of the self-heating due to its internal heating and the wake it receives from the upstream heating.
It was demonstrated that the approach velocity had a relatively small affect on the thermal wake compared with the effect of channel spacing which was relatively large.
The thermal wake behind a single heated element was defined in terms of the dimensionless temperature, θ. The data showed that the position in the array did not affect θ.
The first element downstream of the heated element was selected as the reference element and temperatures of the elements downstream of the heated element were related to

this value in which a simple **1/N** (1/row number) type dependence was observed. The above dependence was also observed experimentally.

The experimental heat transfer coefficient from the heated element was calculated, h_{ad}, based on T_{ad} (the adiabatic temperature). h_{ad} was then compared with h_m based on T_m (the mean temperature calculated from the energy balance) and h_{in} based on T_{in} (the inlet temperature). For different approach velocities and for large channel spacing, **H/B**=2.5, the three values of h are nearly the same over the third block. This shows that thermal mixing is taking place over the third block caused by the first block upstream.

FIGURE 6.1: COMPONENT TEMPERATURE DISTRIBUTION
POWER INPUT=22.5W

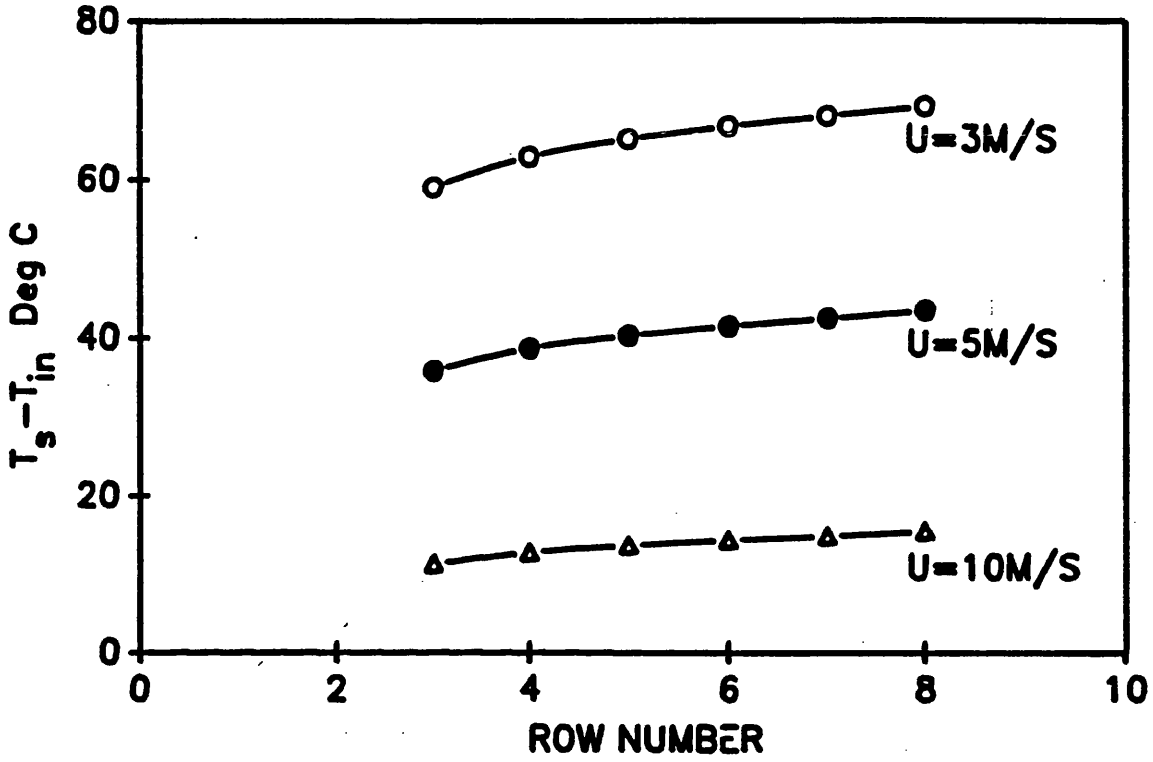

FIGURE 6.2: ELEMENTS SURFACE TEMPERATURE RISE

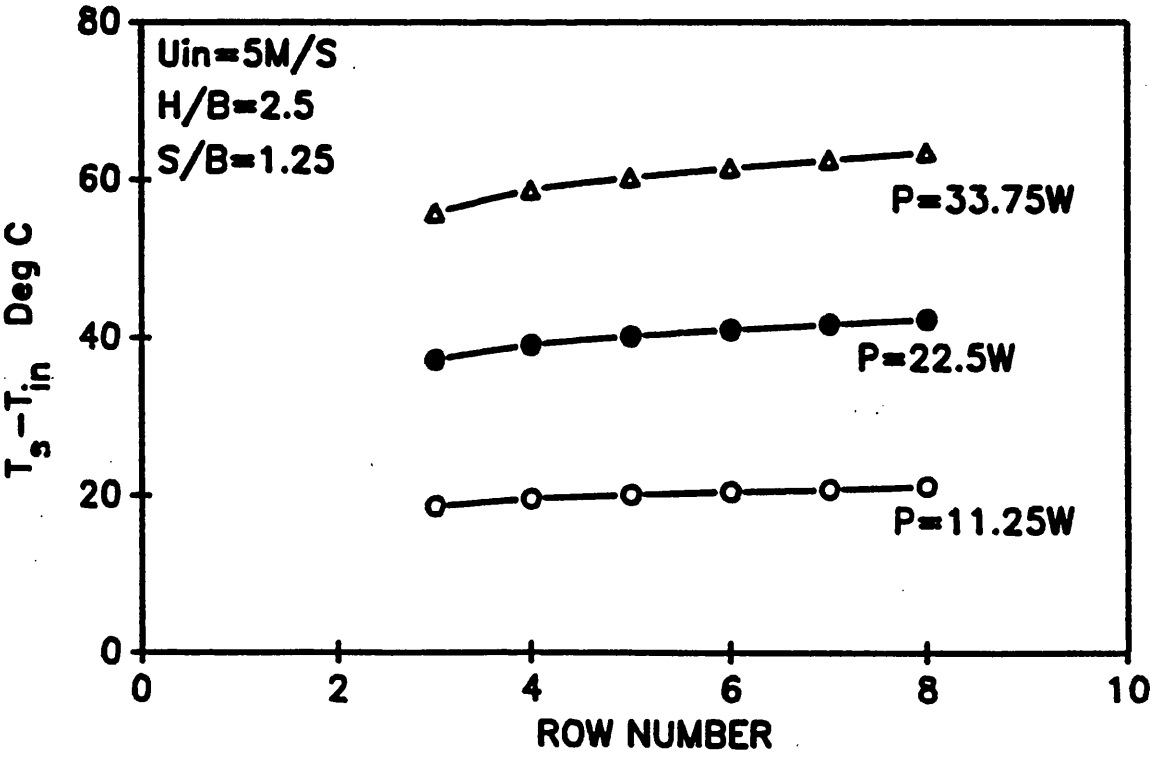

FIGURE 6.3: EFFECT OF CHANNEL SPACING ON: a)VELOCITY PROFILES, b)TEMPERATURE PROFILES

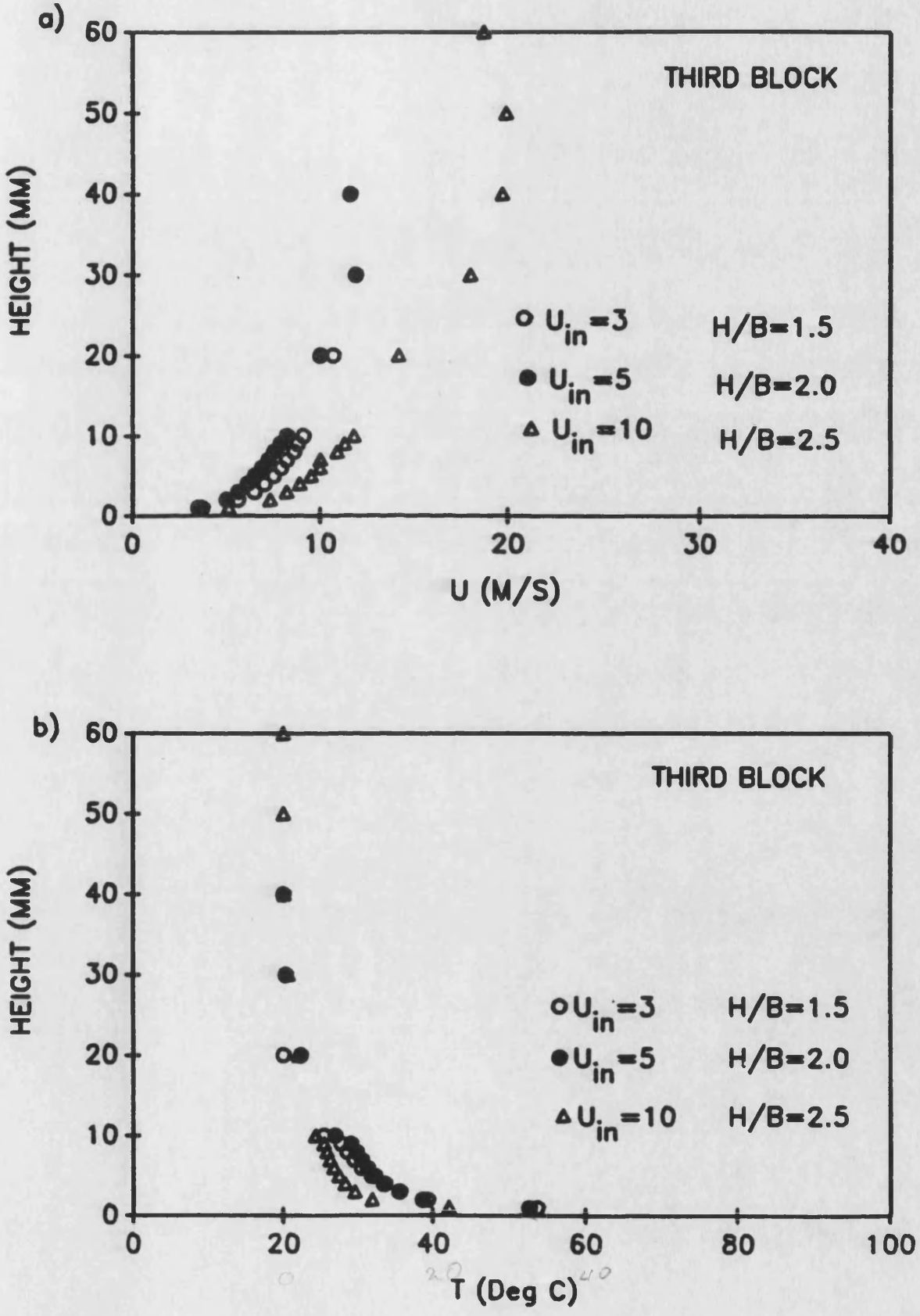

FIGURE 6.4: EFFECT OF CHANNEL SPACING ON: a)VELOCITY PROFILES, b)TEMPERATURE PROFILES

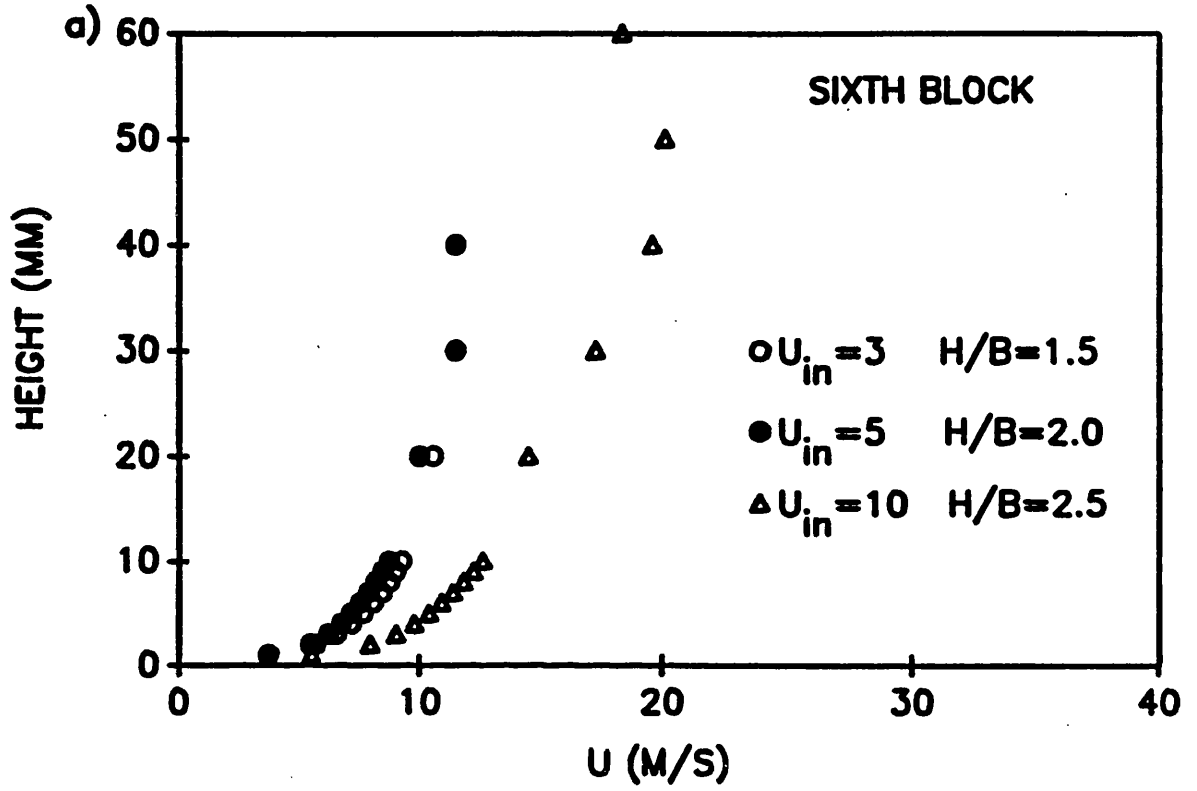

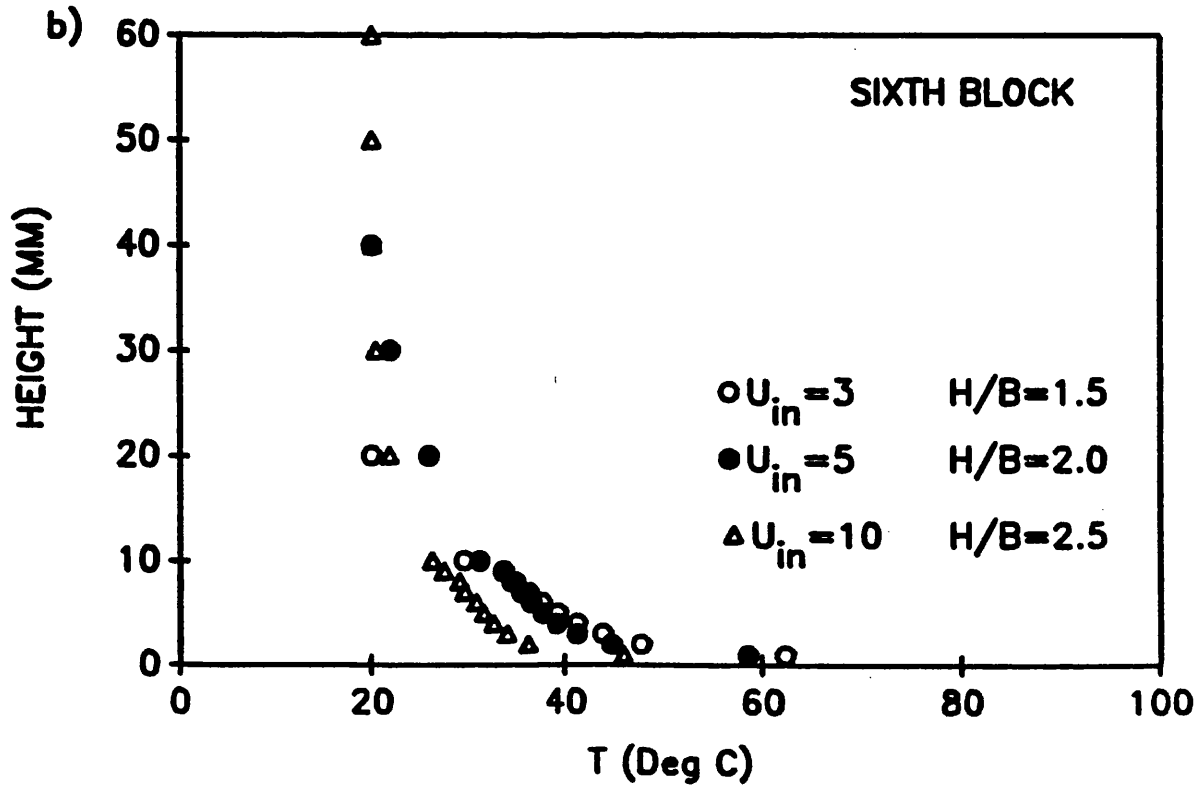

FIGURE 6.5: LOCAL HEAT TRANSFER COEFFICIENT
PARAMETRIC IN VELOCITY

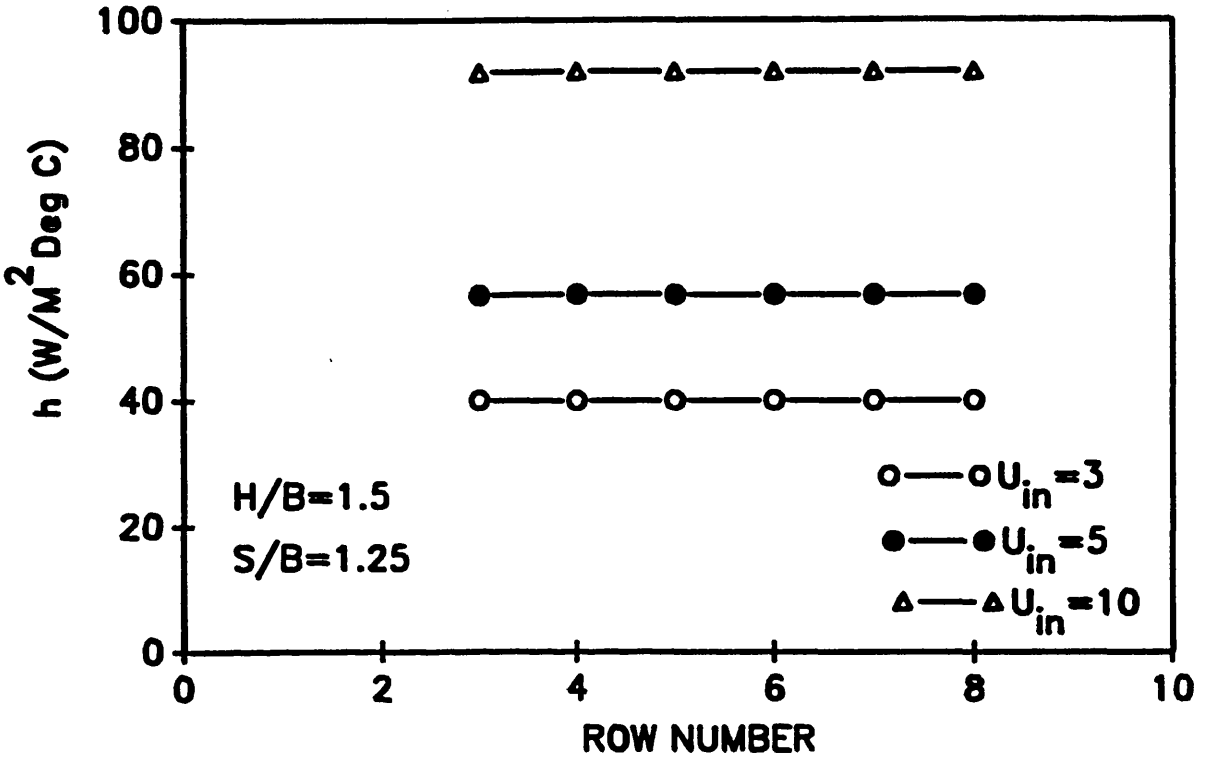

FIGURE 6.6: FULLY DEVELOPED HEAT TRANSFER COEFFICIENT
(ROW 6) VS. CHANNEL HEIGHT

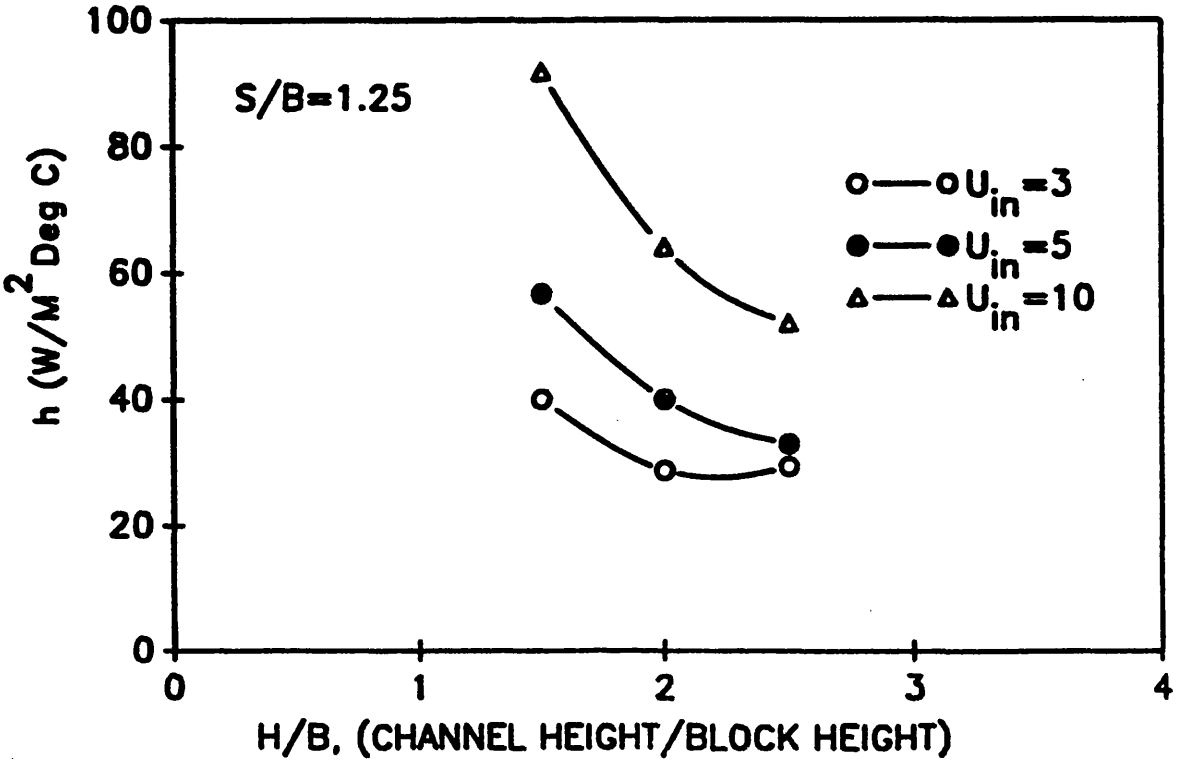

FIGURE 6.7: FULLY DEVELOPED HEAT TRANSFER COEFFICIENT (ROW 6) VS. APPROACH VELOCITY: a)S/B=1.25 b)S/B=2.0, PARAMETRIC IN H/B

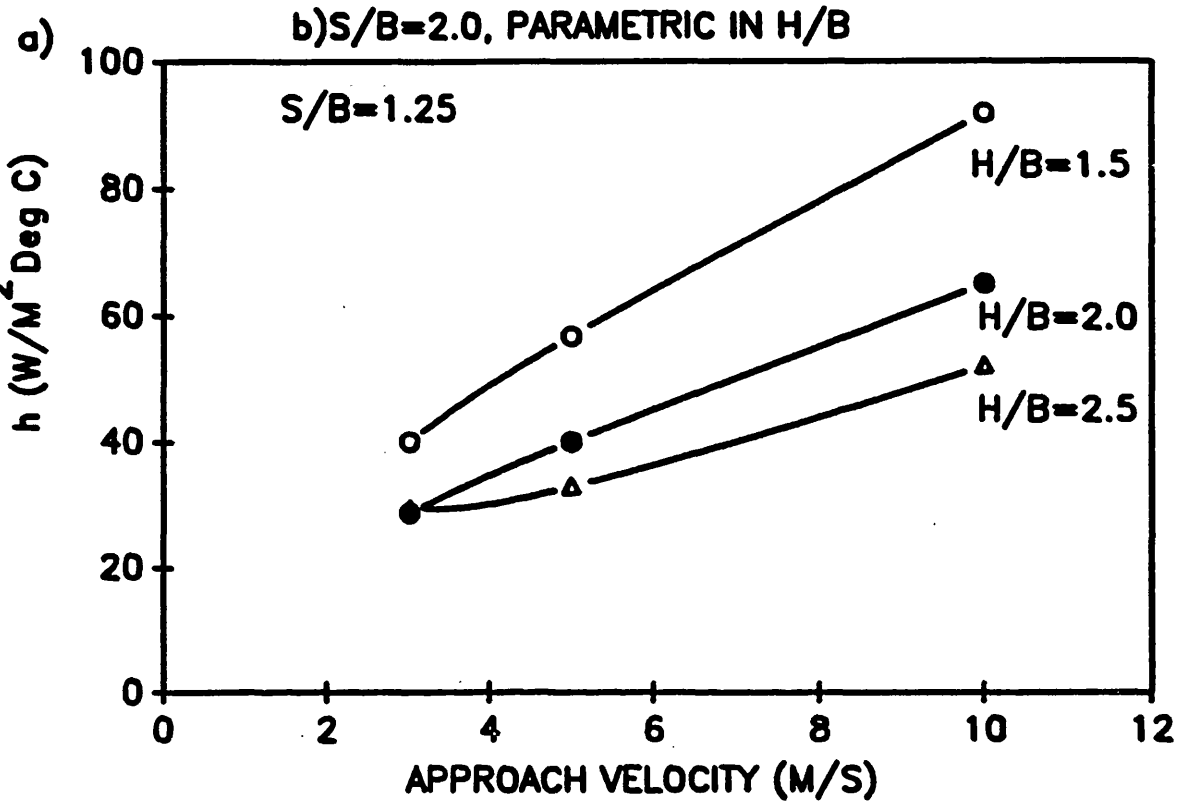

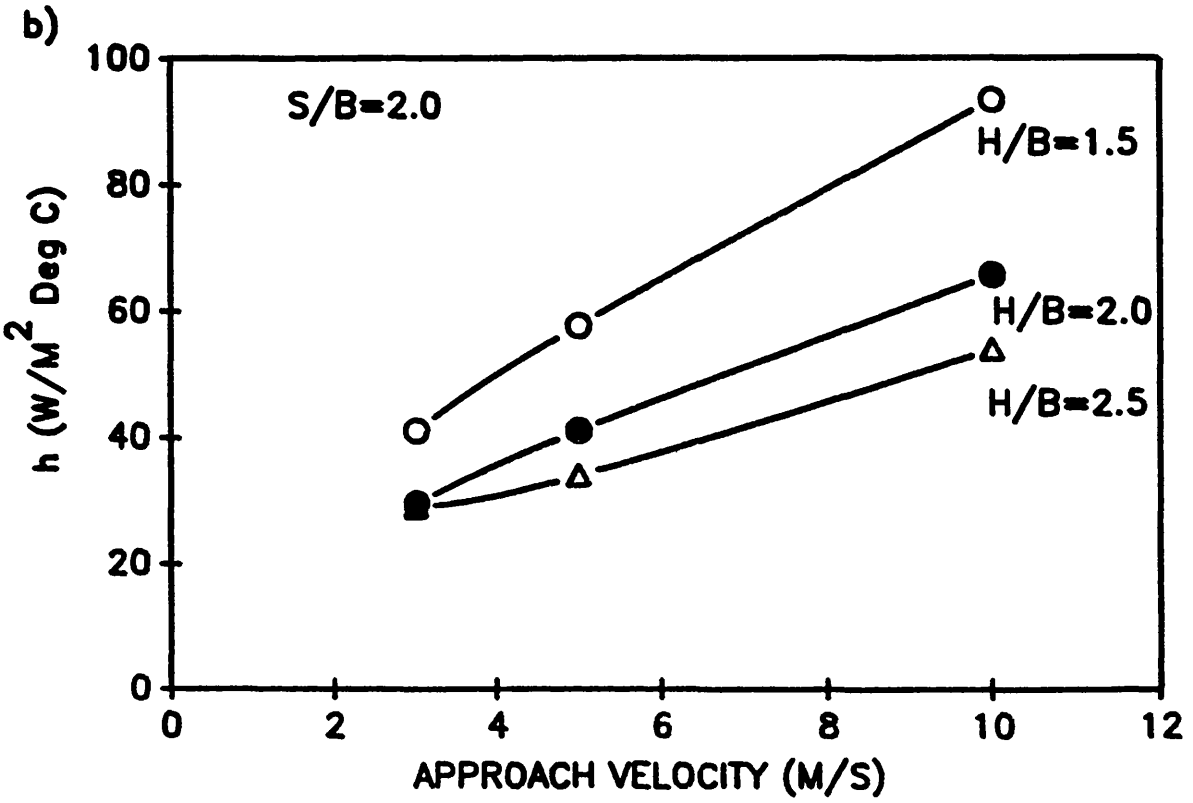

FIGURE 6.8: LOCAL NUSSELT NUMBER BASED ON BLOCK HEIGHT VS. LOCAL REYNOLDS NUMBER BASED ON BLOCK HEIGHT AND LOCAL VELOCITY (ROW 6)

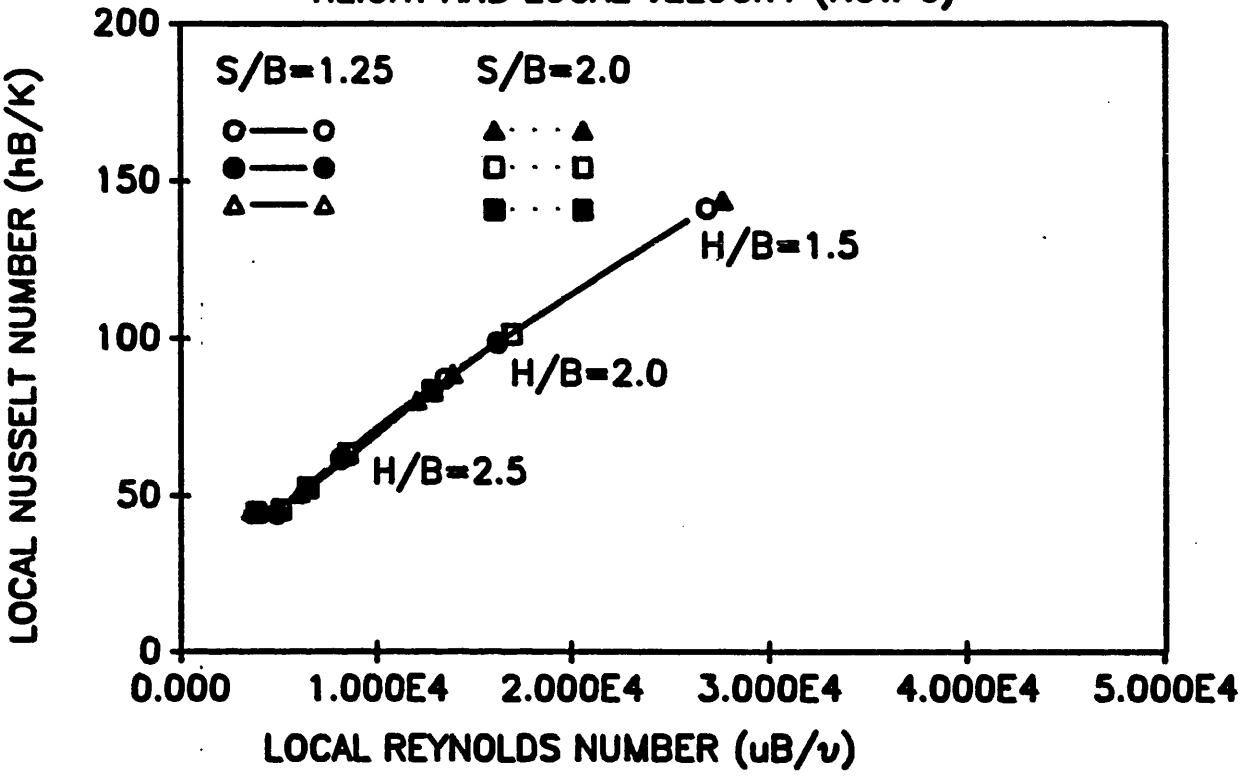

FIGURE 6.9: LOCAL NUSSELT NUMBER VS. LOCAL REYNOLDS NUMBER (ROW 6)

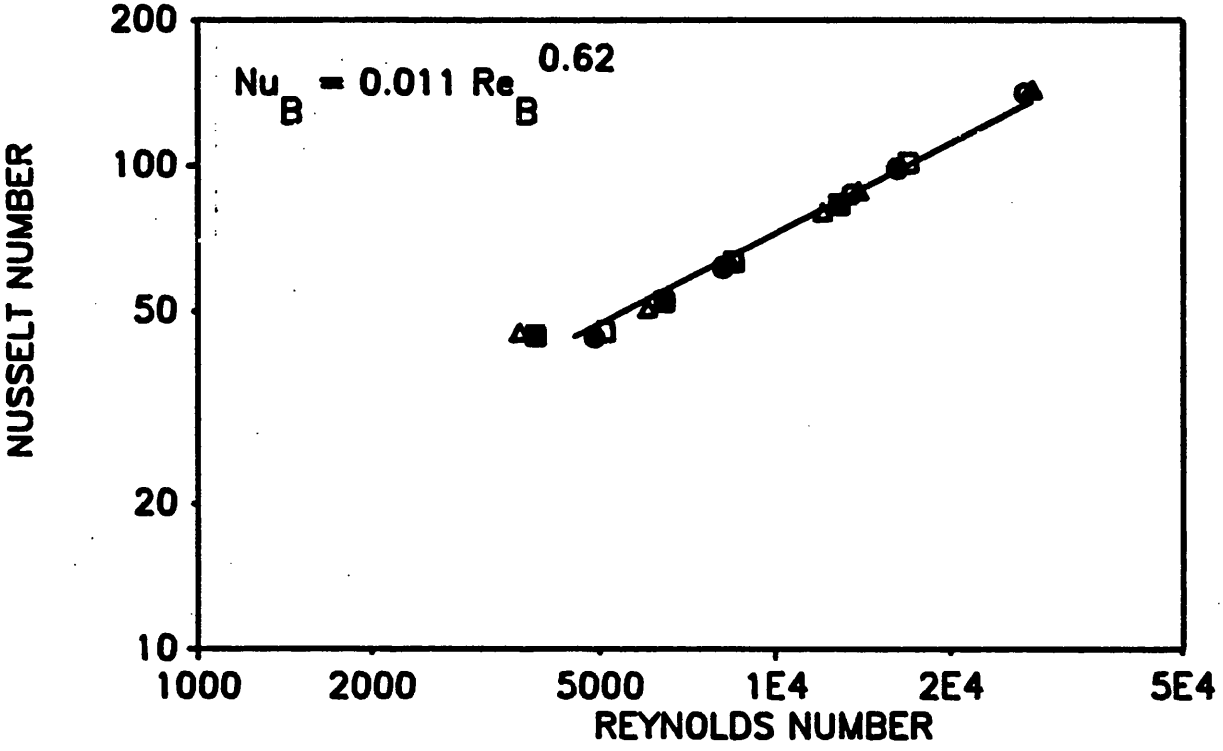

FIGURE 6.10: ADIABATIC TEMPERATURE RISE:
a)POWER INPUT=11.25W, b)22.5W, c)33.75W

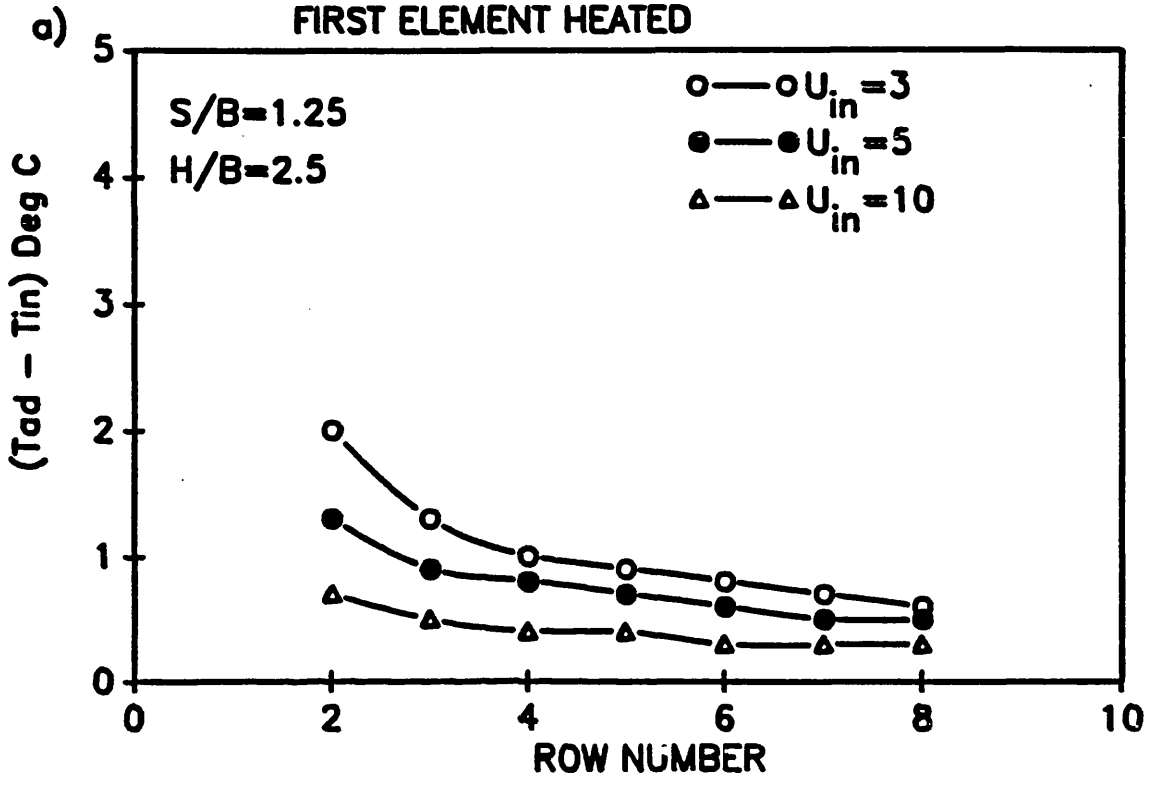

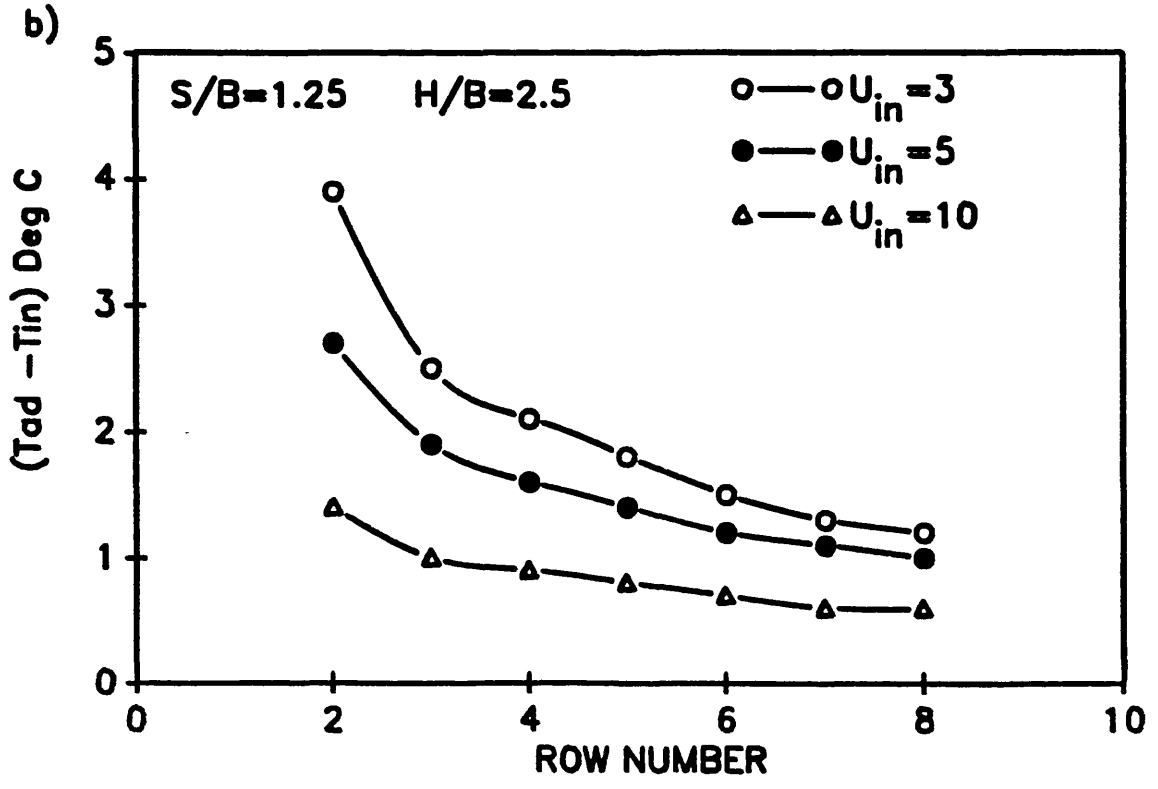

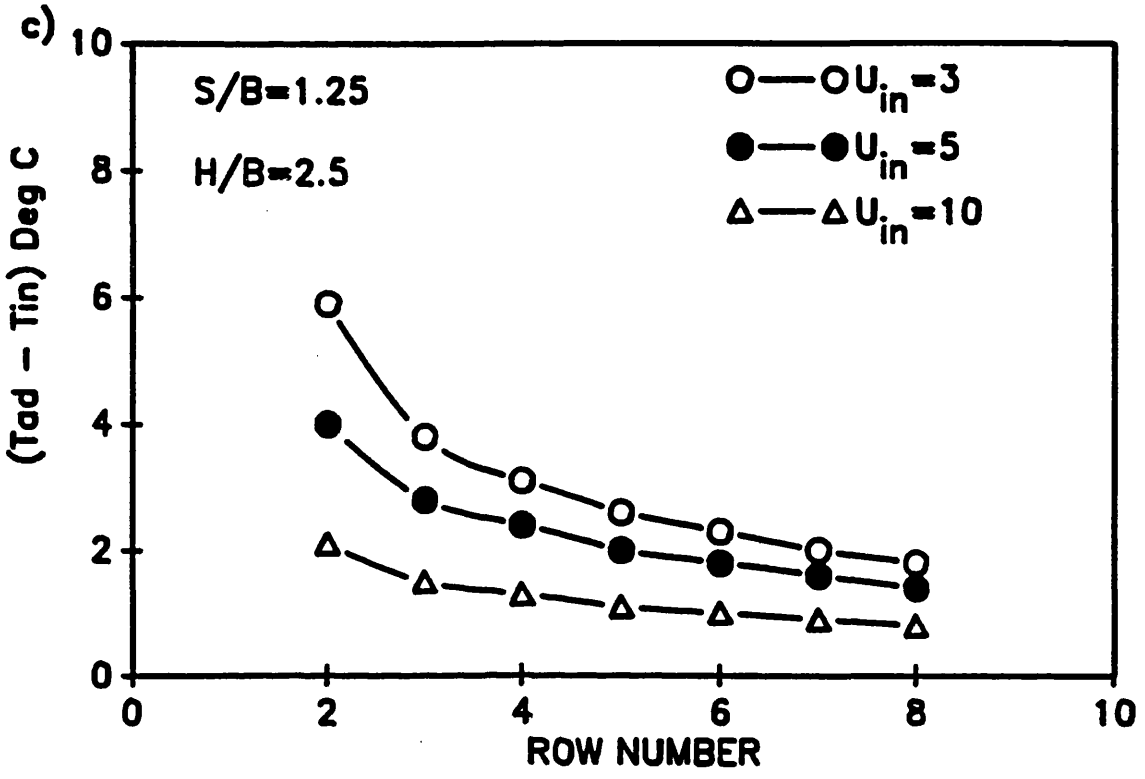

FIGURE 6.11: ADIABATIC TEMPERATURE RISE:
EFFECT OF POWER INPUT
FIRST ELEMENT HEATED, U_{in}=3M/S

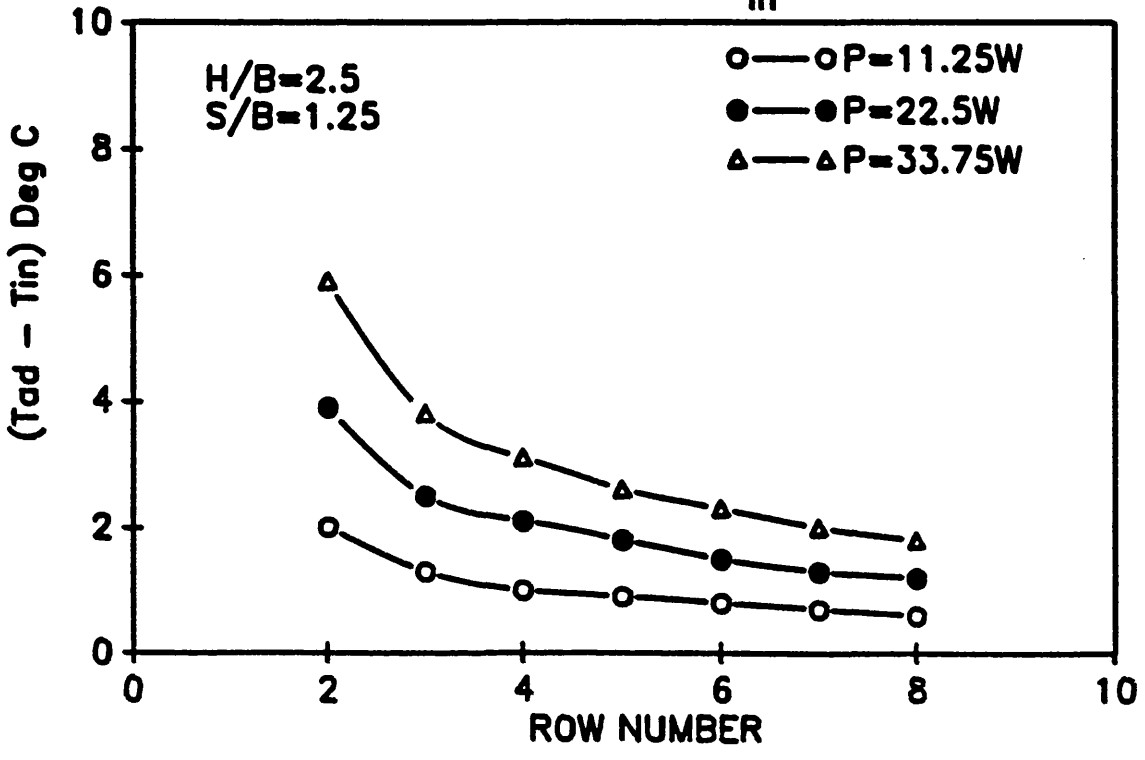

FIGURE 6.12: ADIABATIC TEMPERATURE RISE:
a)POWER INPUT=11.25W, b)22.5W, c)33.75W
SECOND AND THIRD ELEMENTS HEATED

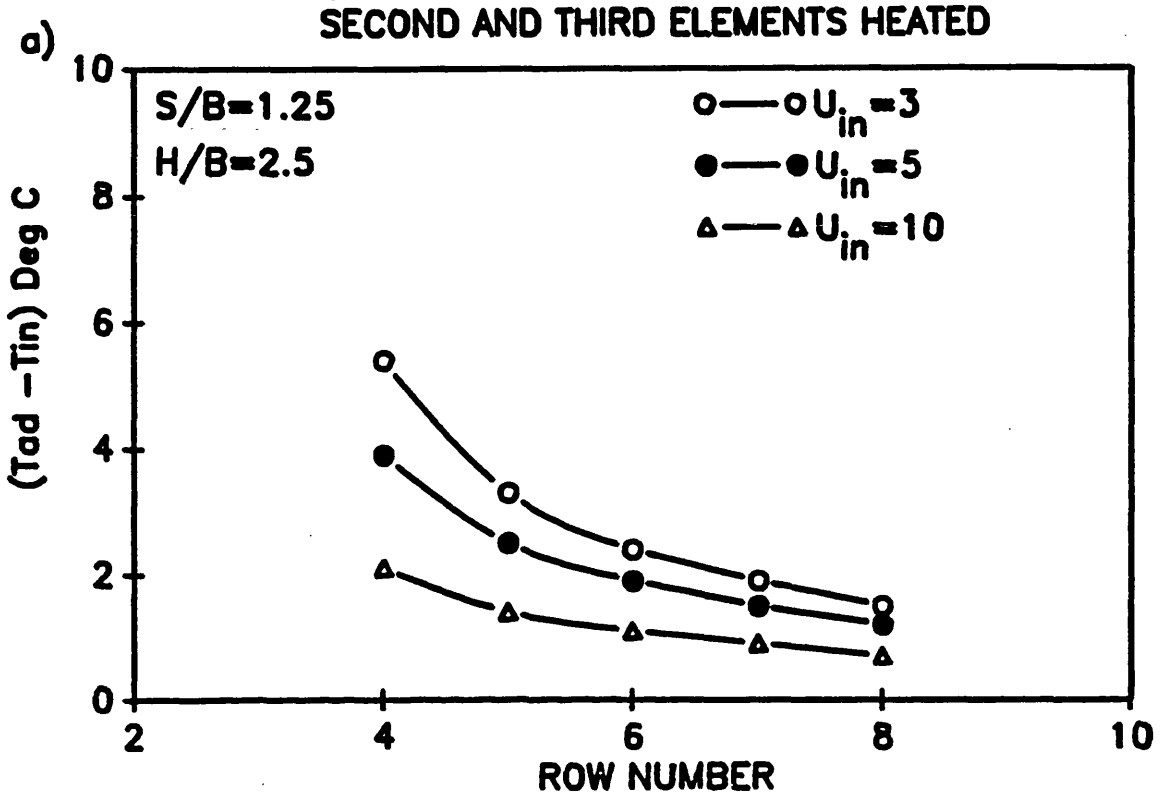

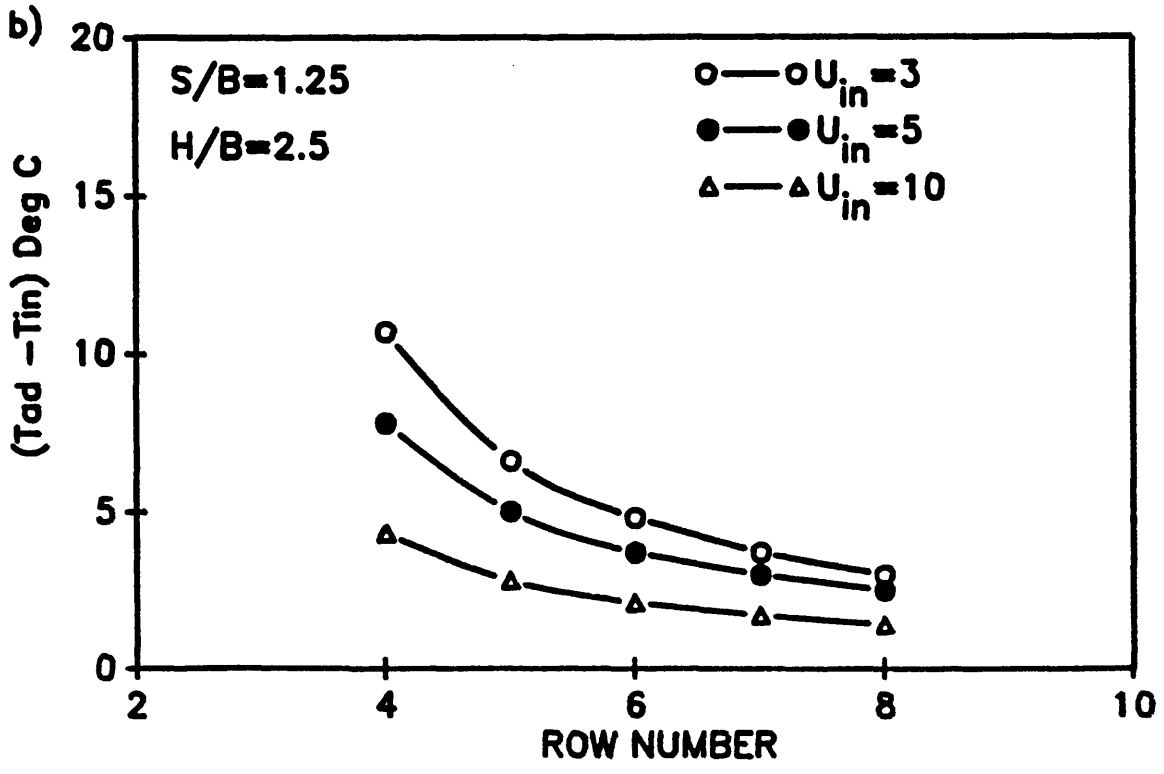

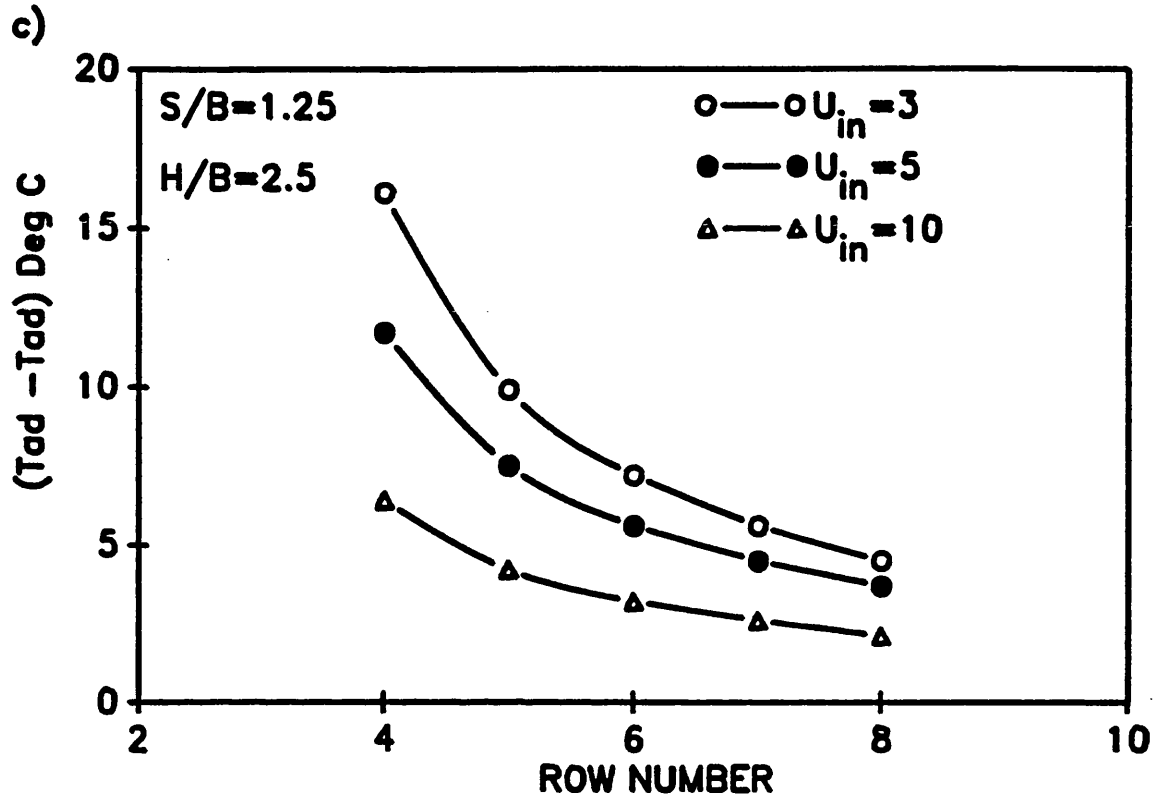

FIGURE 6.13: ADIABATIC TEMPERATURE RISE:
EFFECT OF HEATING SECOND AND THIRD ELEMENTS
ON DOWNSTREAM ELEMENTS, U_{in}=5M/S
POWER INPUT=22.5W

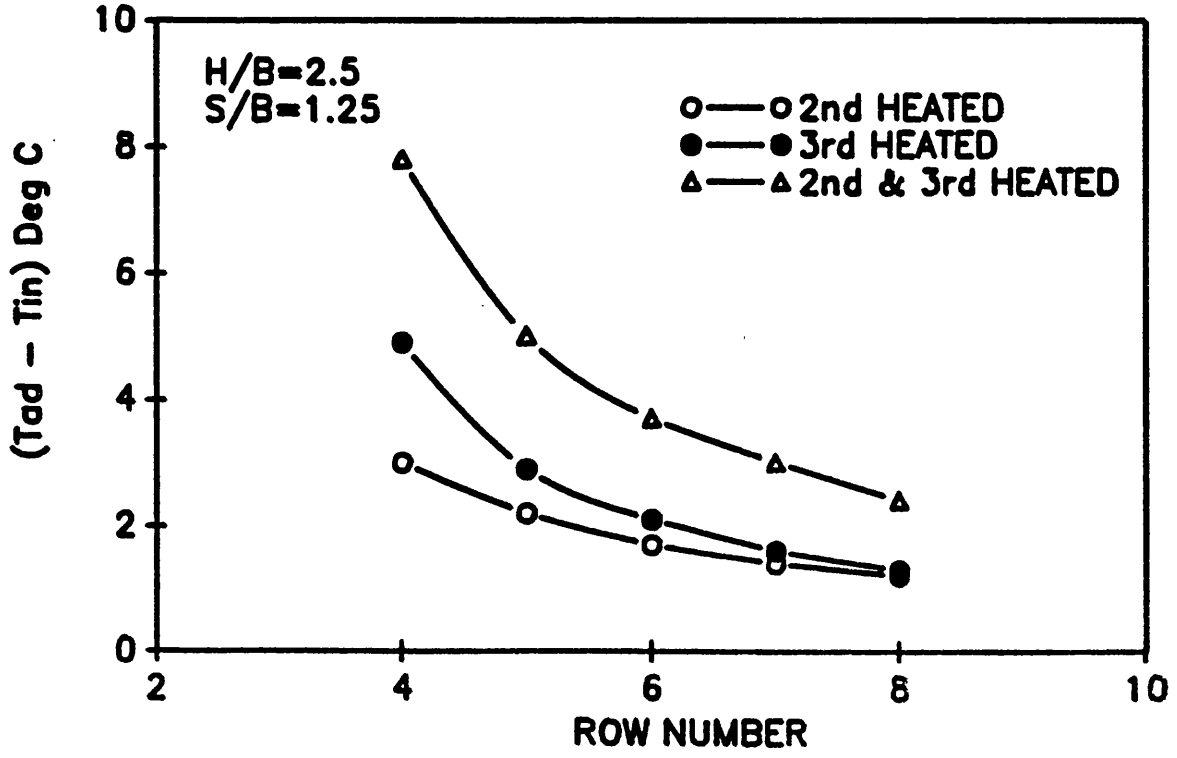

FIGURE 6.14: SUPERPOSITION KERNEL FUNCTION

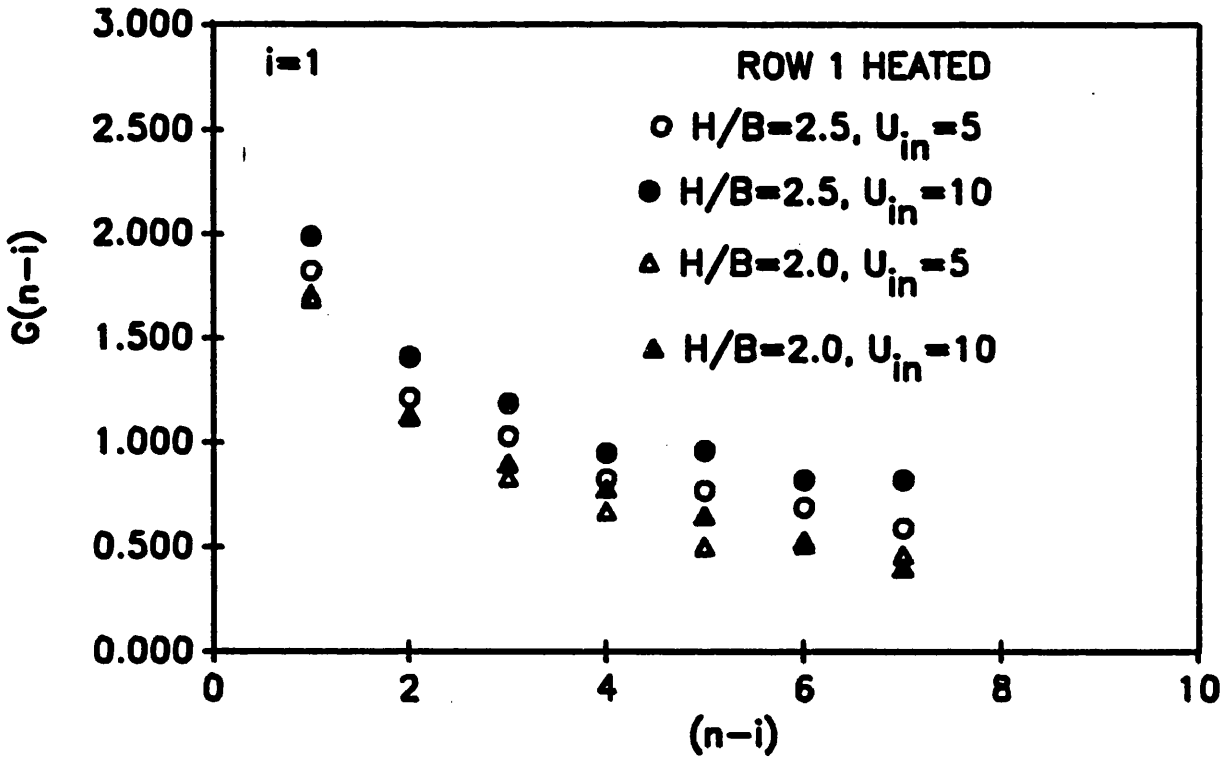

FIGURE 6.15: DIMENSIONLESS TEMPERATURE PROFILE BEHIND A SINGLE HEATED ELEMENT, POWER INPUT=22.5W

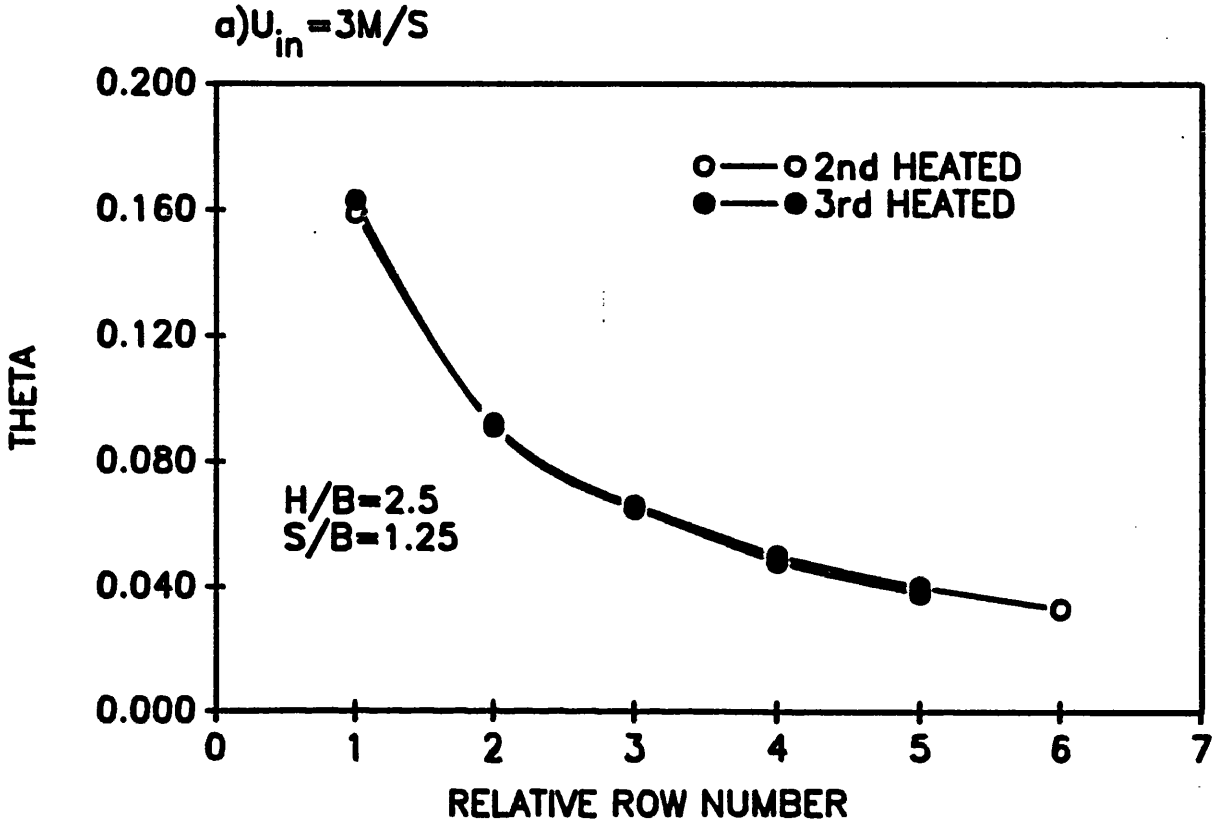

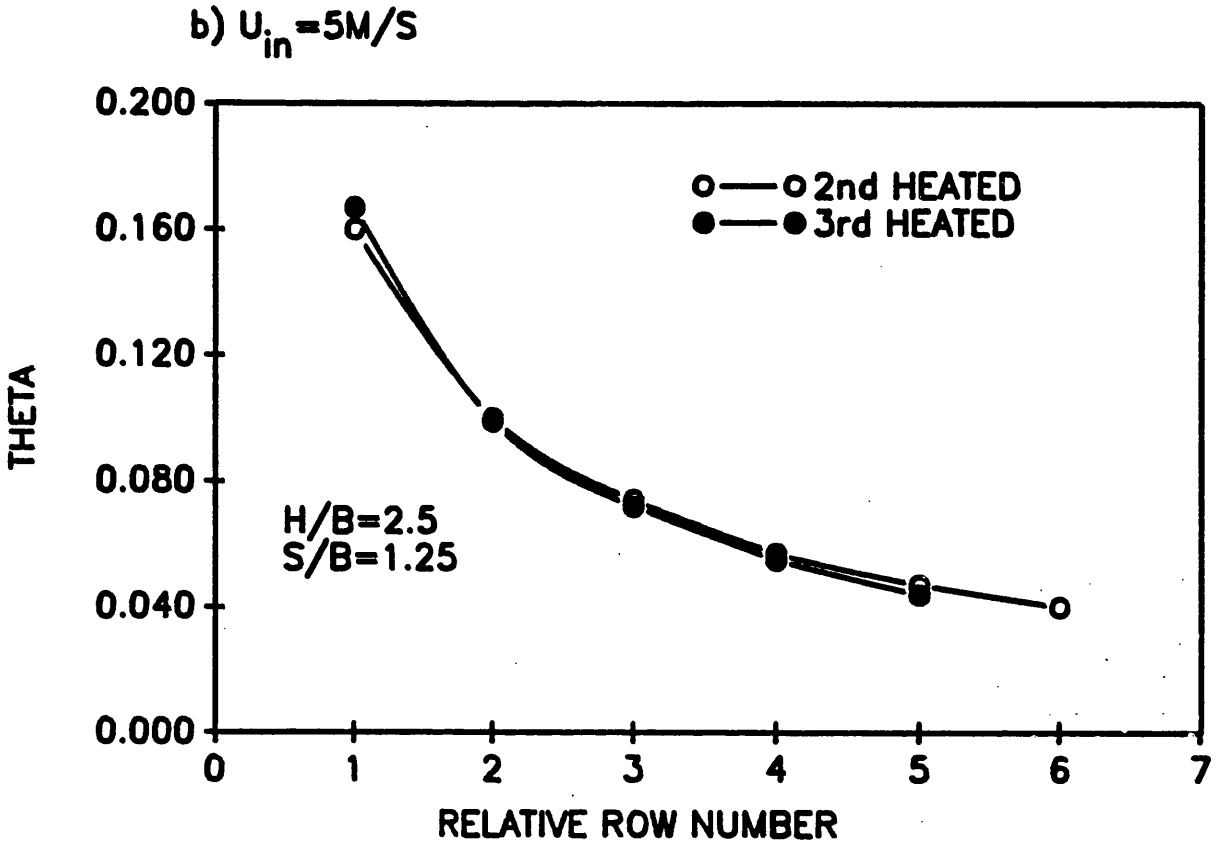

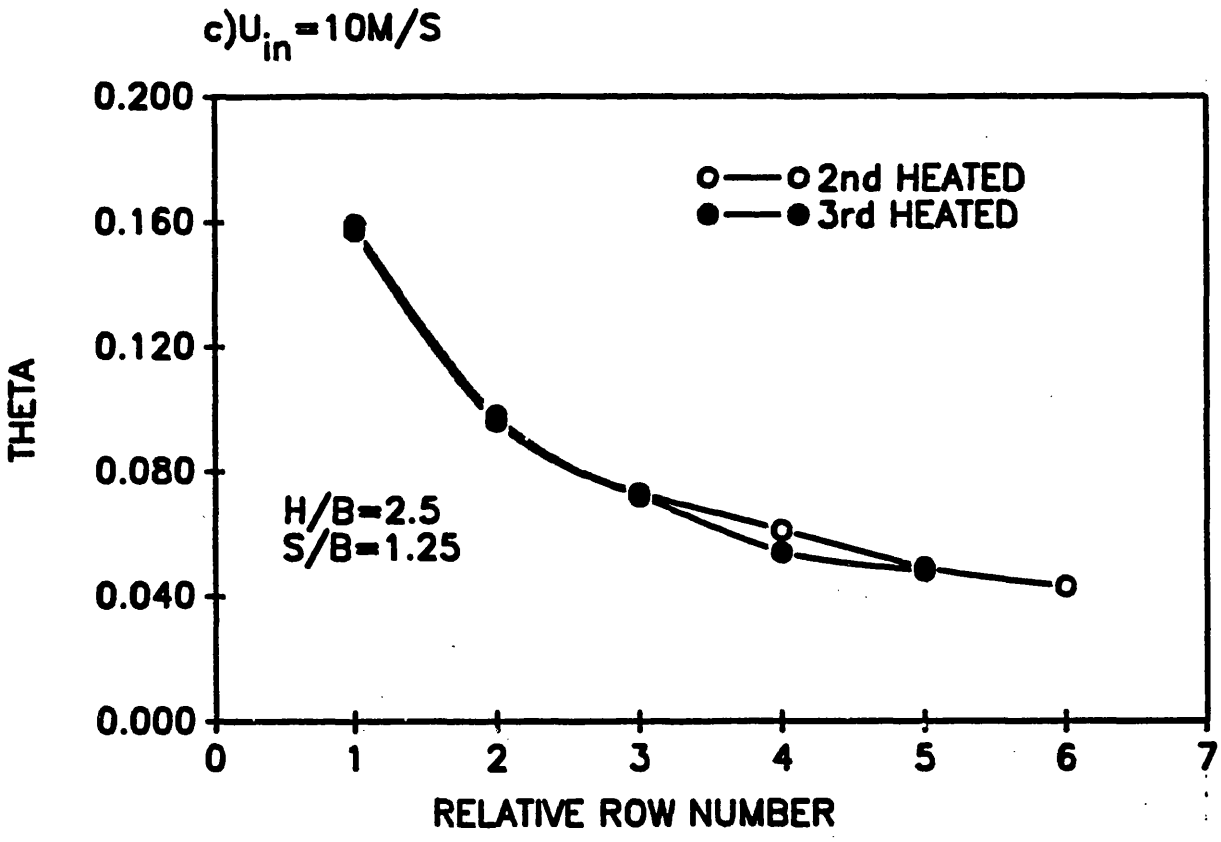
c)U_in=10M/S
0.200
0.160
0.120
0.080
0.040
0.000
THETA
o—o 2nd HEATED
●—● 3rd HEATED
H/B=2.5
S/B=1.25
0
1
2
3
4
5
6
7
RELATIVE ROW NUMBER

FIGURE 6.16: DIMENSIONLESS TEMPERATURE PROFILE BEHIND A SINGLE HEATED ELEMENT, POWER INPUT=22.5W

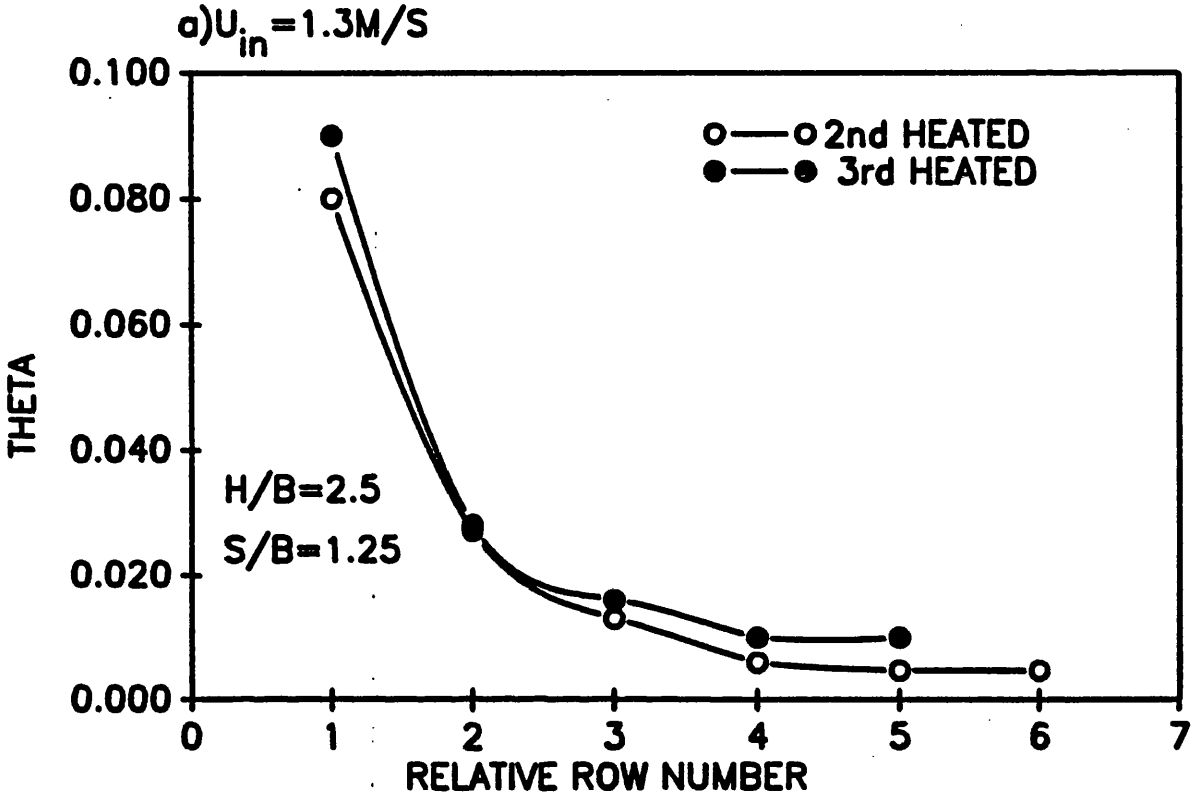

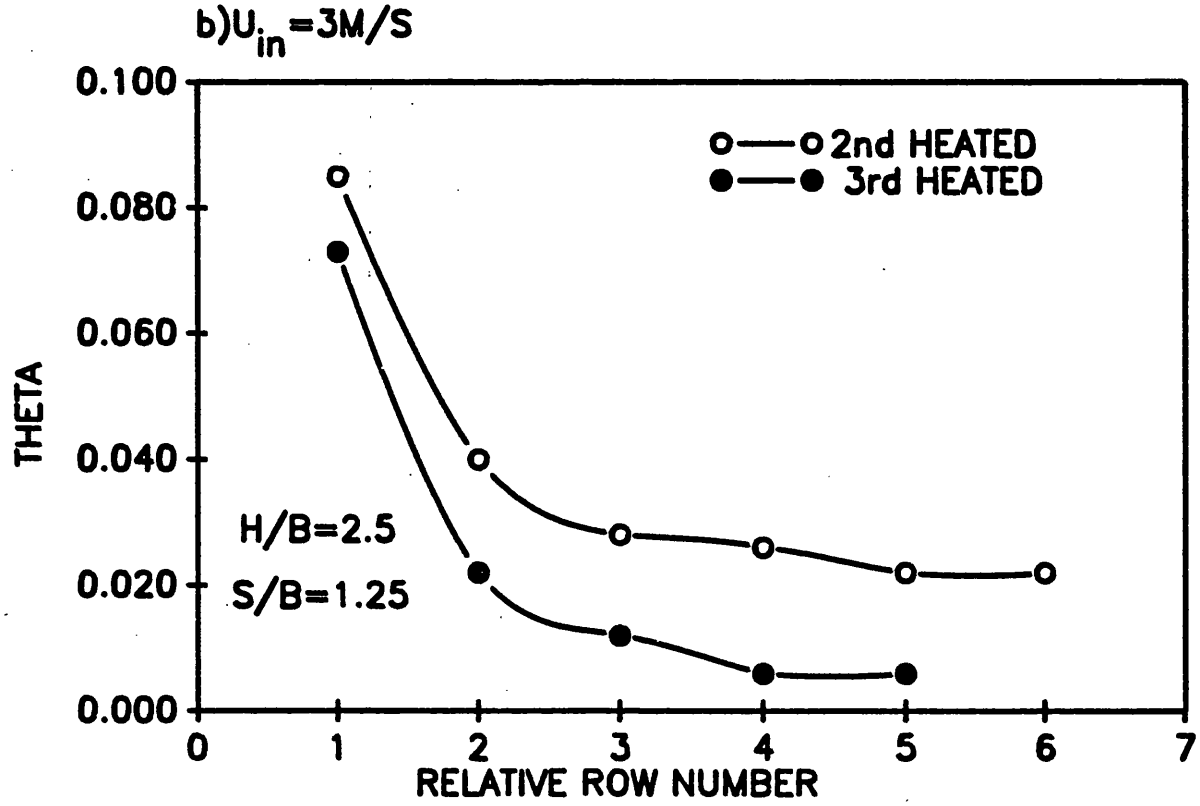

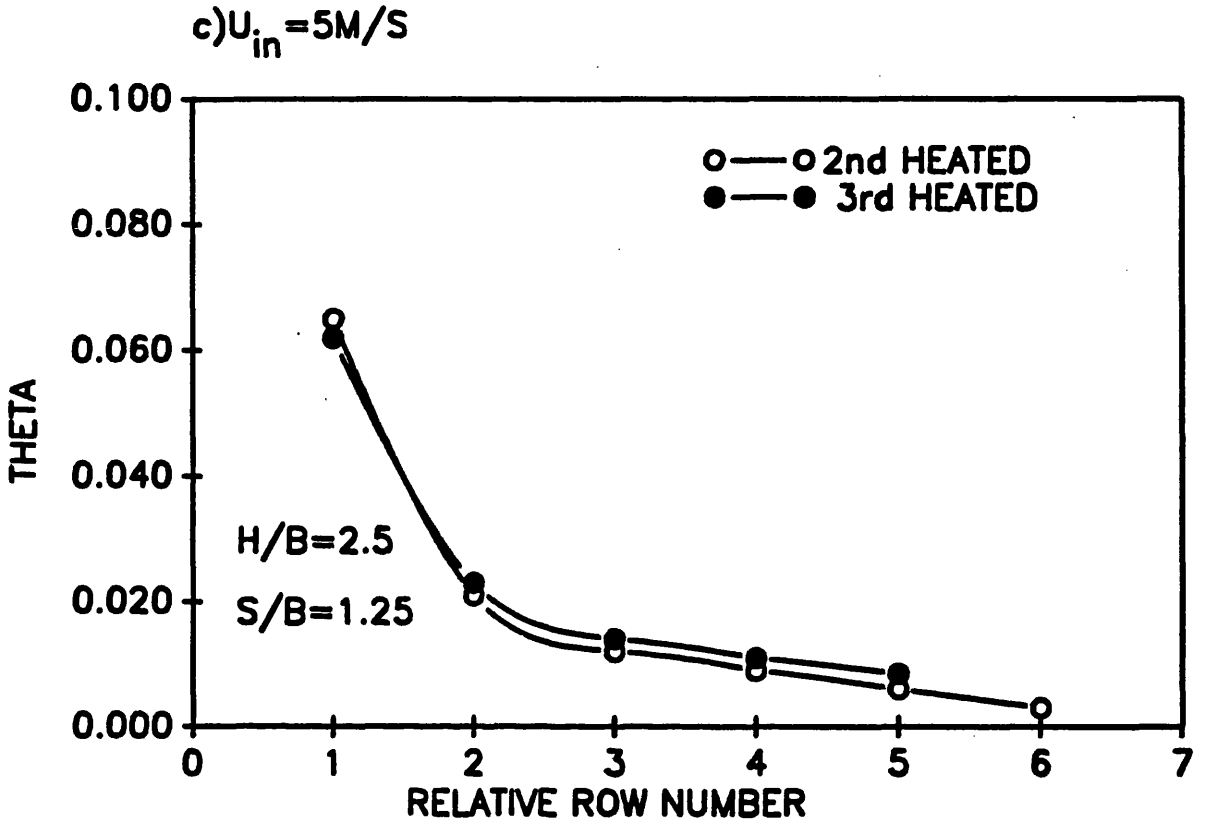
c)U_{in}=5M/S
0.100
0.080
0.060
0.040
0.020
0.000
THETA
o—o 2nd HEATED
●—● 3rd HEATED
H/B=2.5
S/B=1.25
0
1
2
3
4
5
6
7
RELATIVE ROW NUMBER

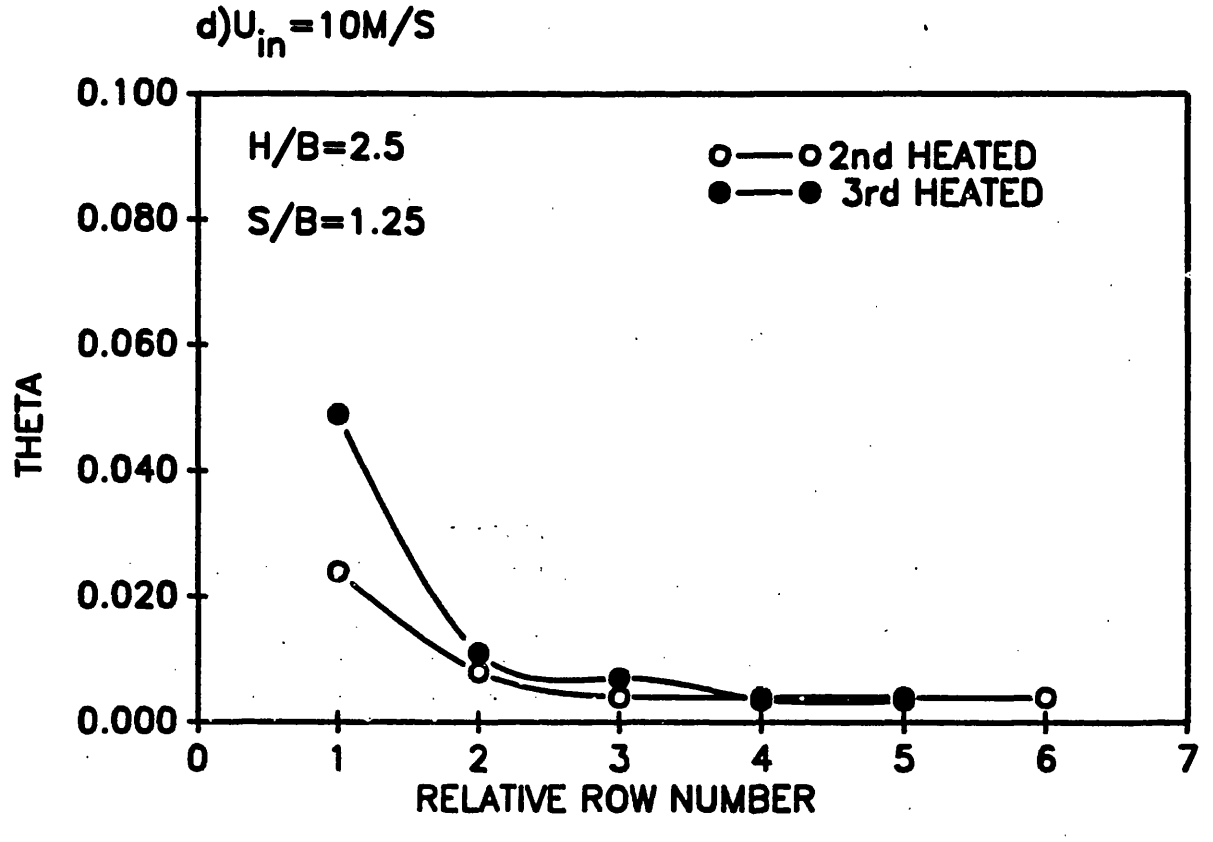
d)U_{in}=10M/S
0.100
0.080
0.060
0.040
0.020
0.000
THETA
H/B=2.5
S/B=1.25
o—o 2nd HEATED
●—● 3rd HEATED
0
1
2
3
4
5
6
7
RELATIVE ROW NUMBER

FIGURE 6.17: DIMENSIONLESS TEMPERATURE OF AN ELEMENT DIRECTLY BEHIND A SINGLE HEATED ELEMENT VS. DUCT REYNOLDS NUMBER

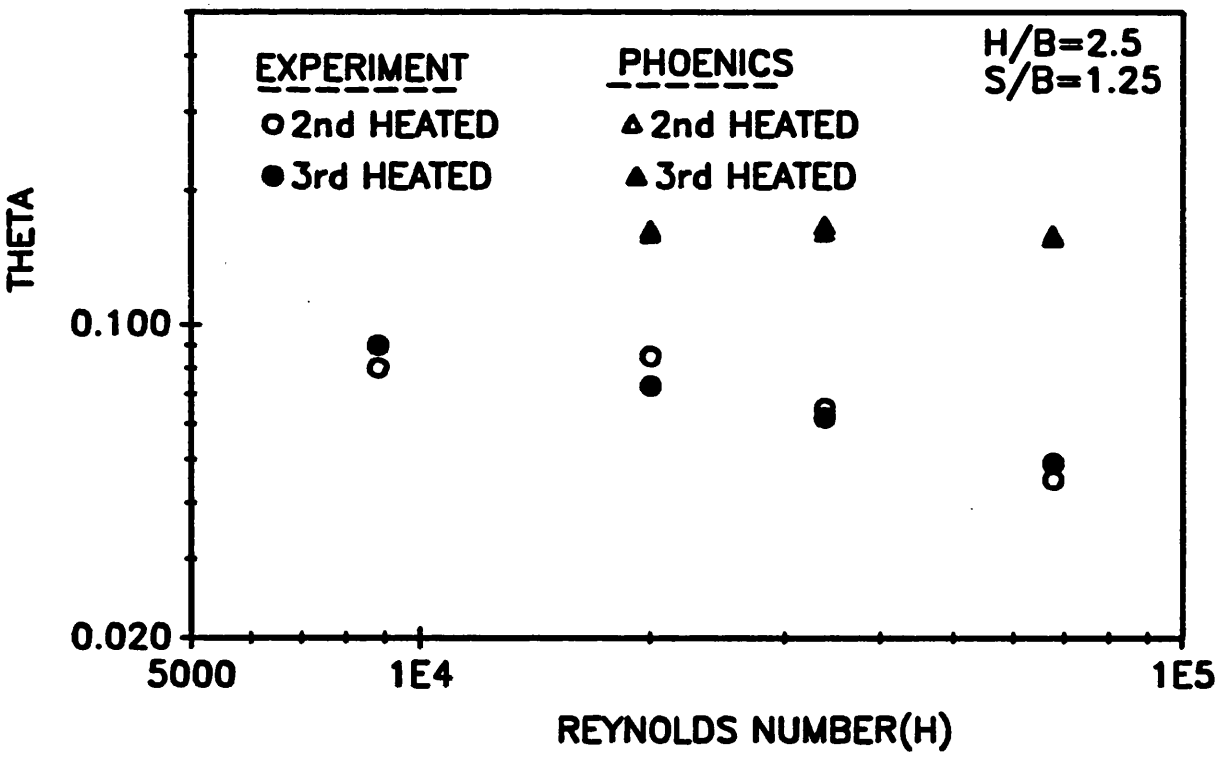

FIGURE 6.18: NORMALISED DIMENSIONLESS TEMPERATURE OF THE ELEMENTS VS. ROW POSITION PHOENICS

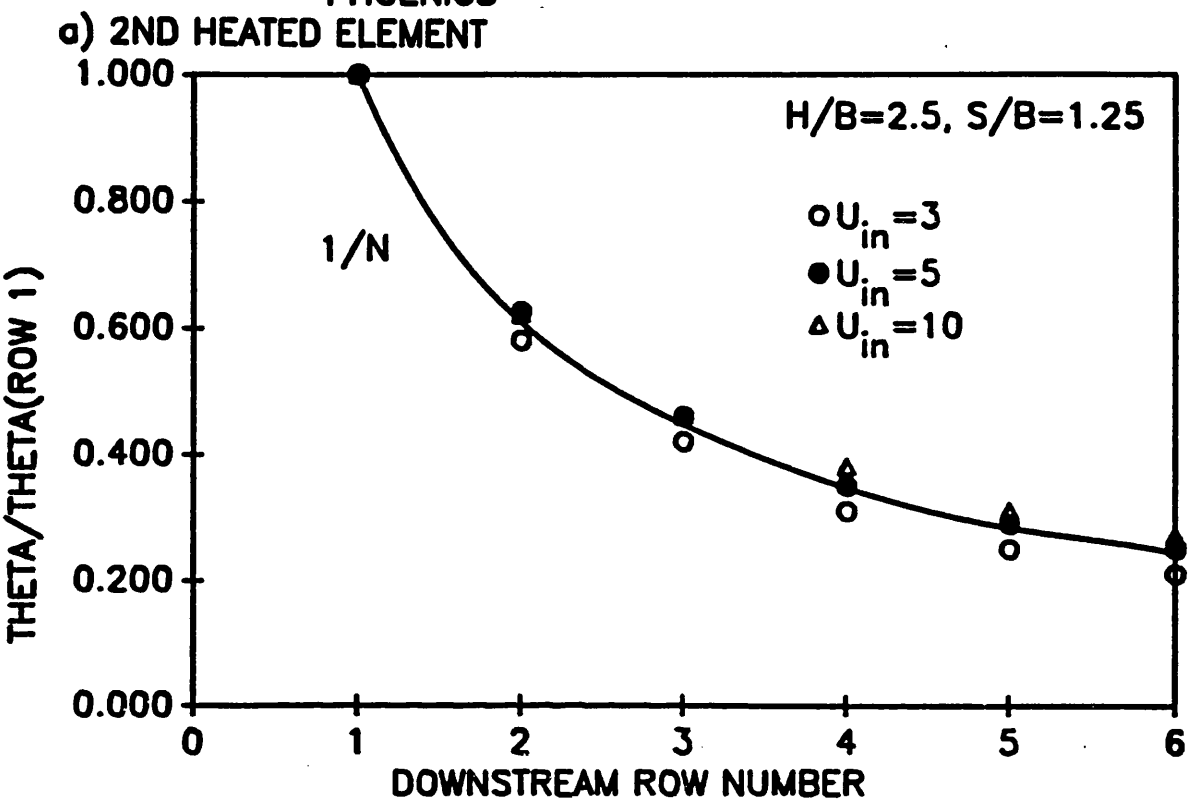

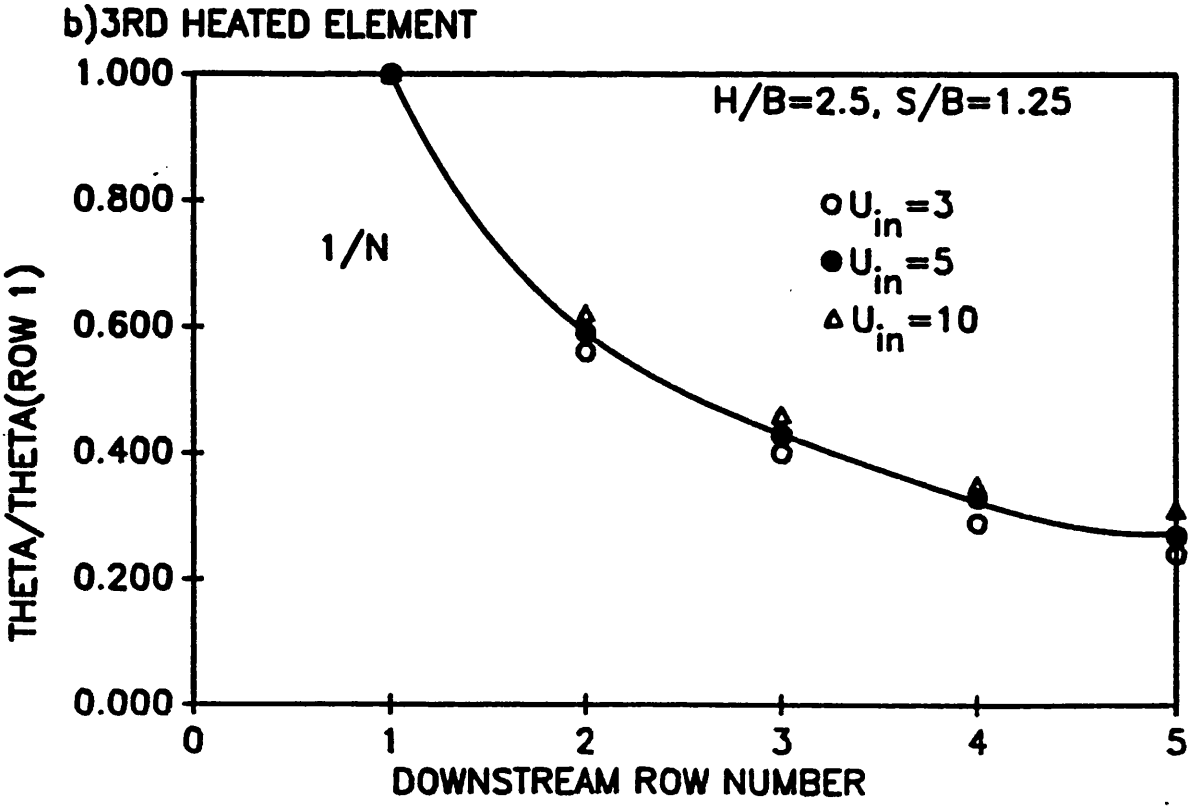

FIGURE 6.19: NORMALISED DIMENSIONLESS TEMPERATURE OF THE ELEMENTS VS. ROW POSITION EXPERIMENT

a)2ND HEATED ELEMENT

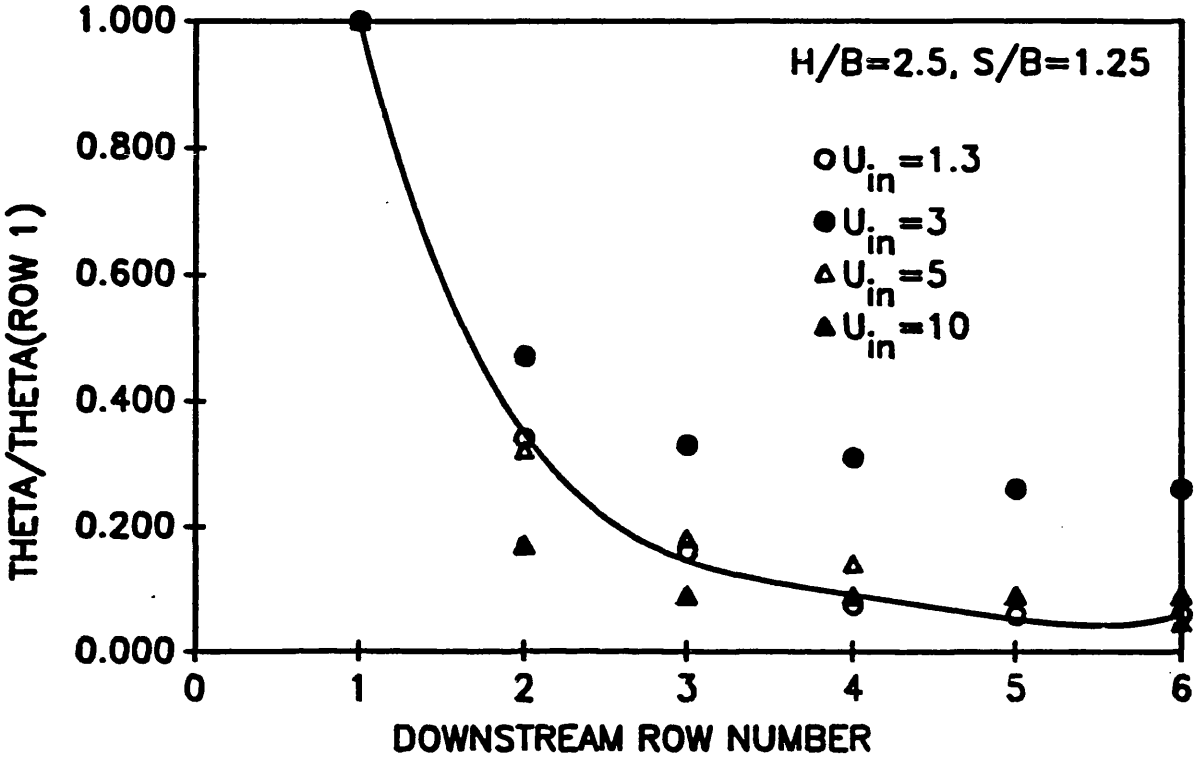

b)3RD HEATED ELEMENT

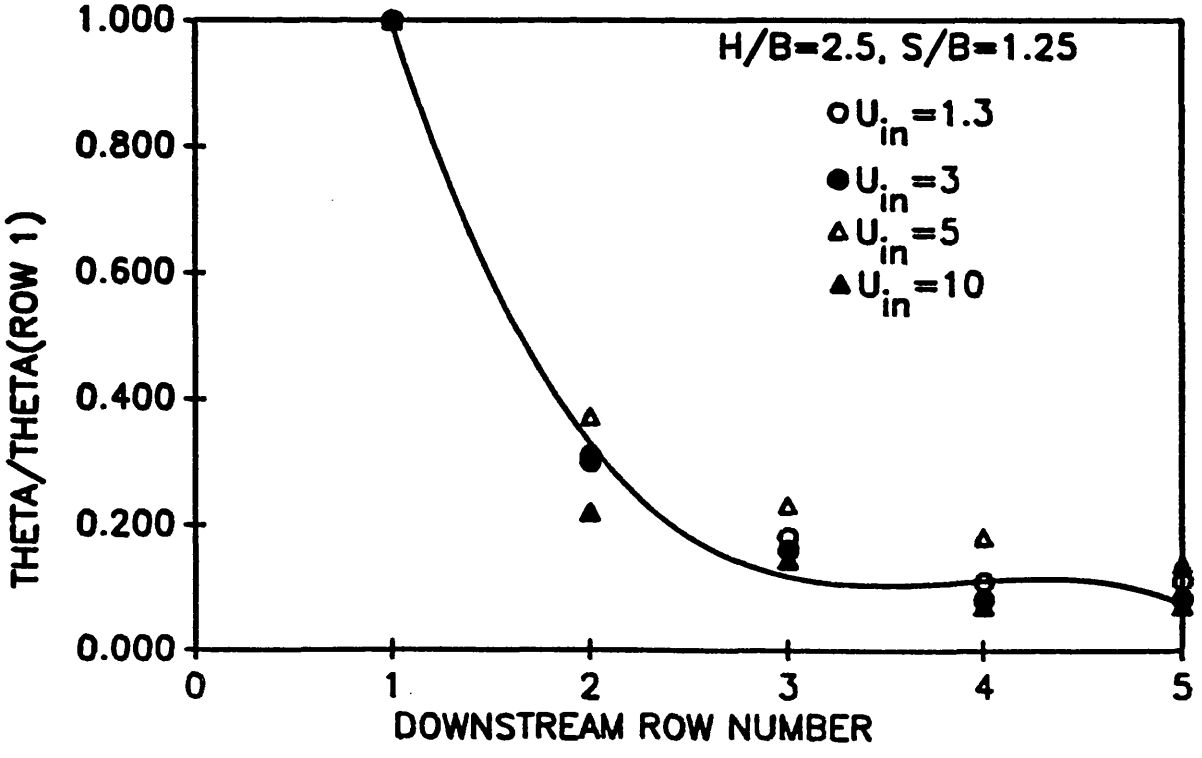

FIGURE 6.20: ADIABATIC TEMPERATURE RISE COMPARED TO THE MEAN TEMPERATURE RISE OVER THIRD ELEMENT

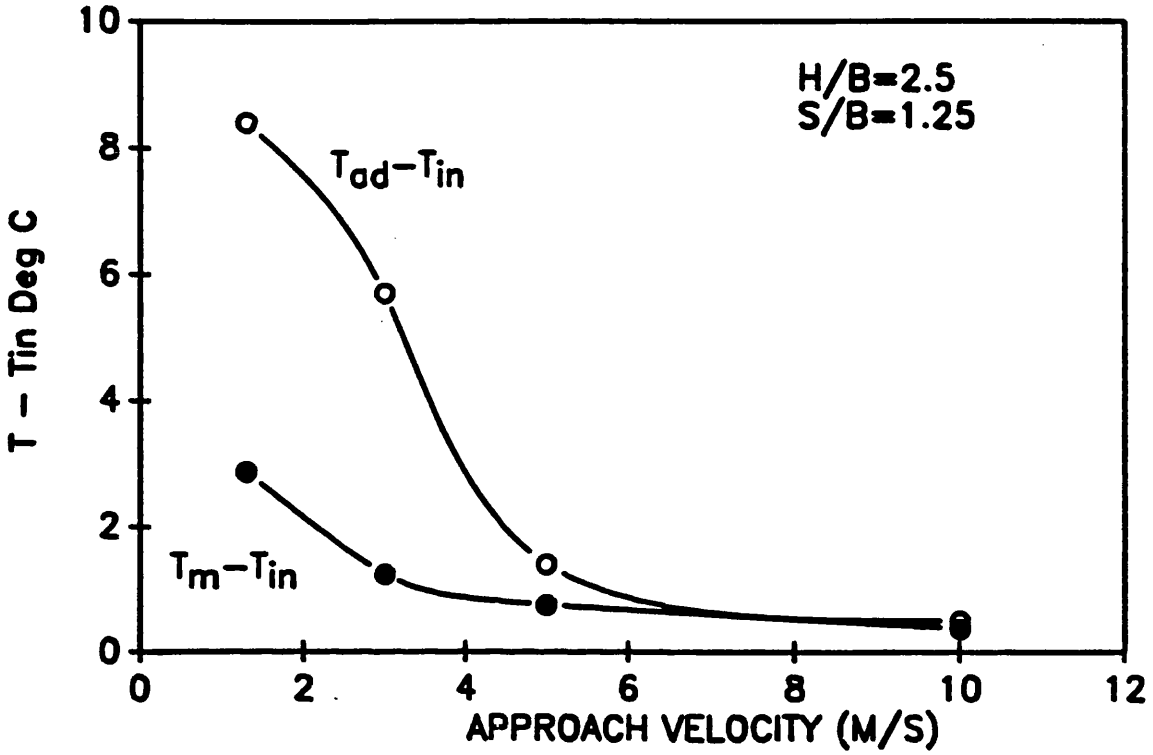

FIGURE 6.21: HEAT TRANSFER COEFFICIENT VS. APPROACH VELOCITY OVER THIRD ELEMENT

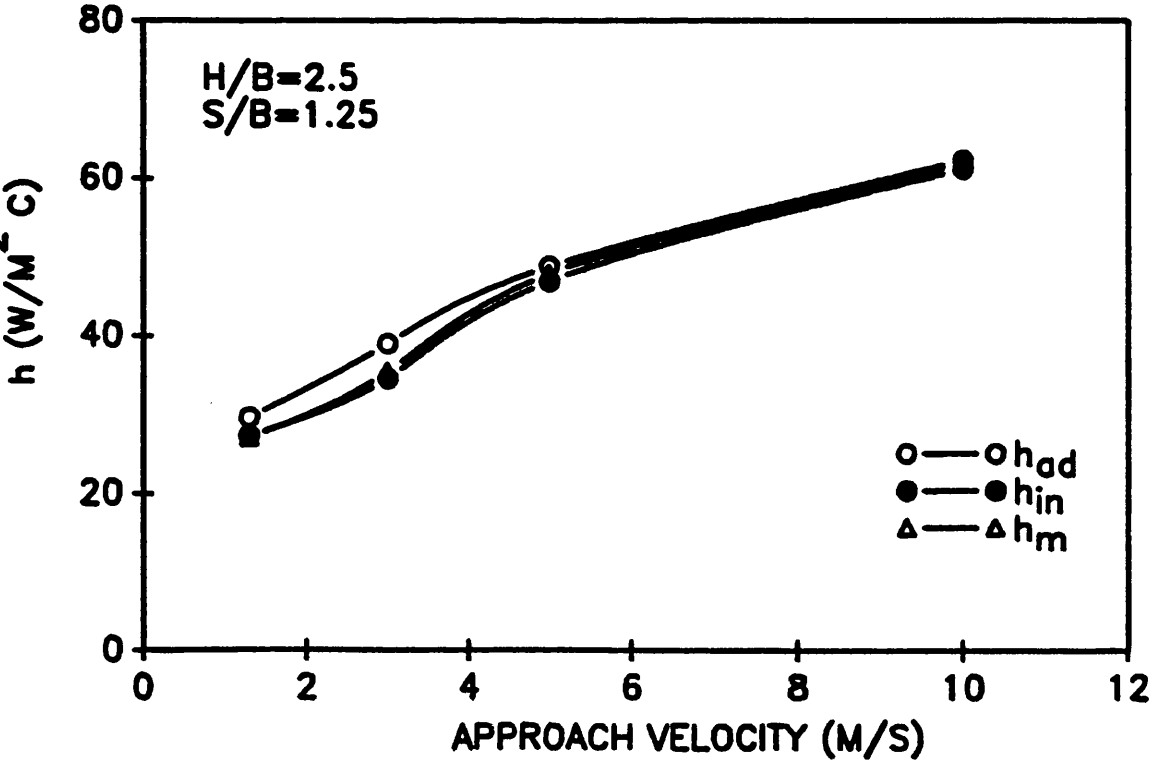

FIGURE 6.22: COMPARISON OF HEAT TRANSFER COEFFICIENT OBTAINED BY a)FLUXMETER, b)EXPERIMENT OVER SECOND AND THIRD ELEMENTS

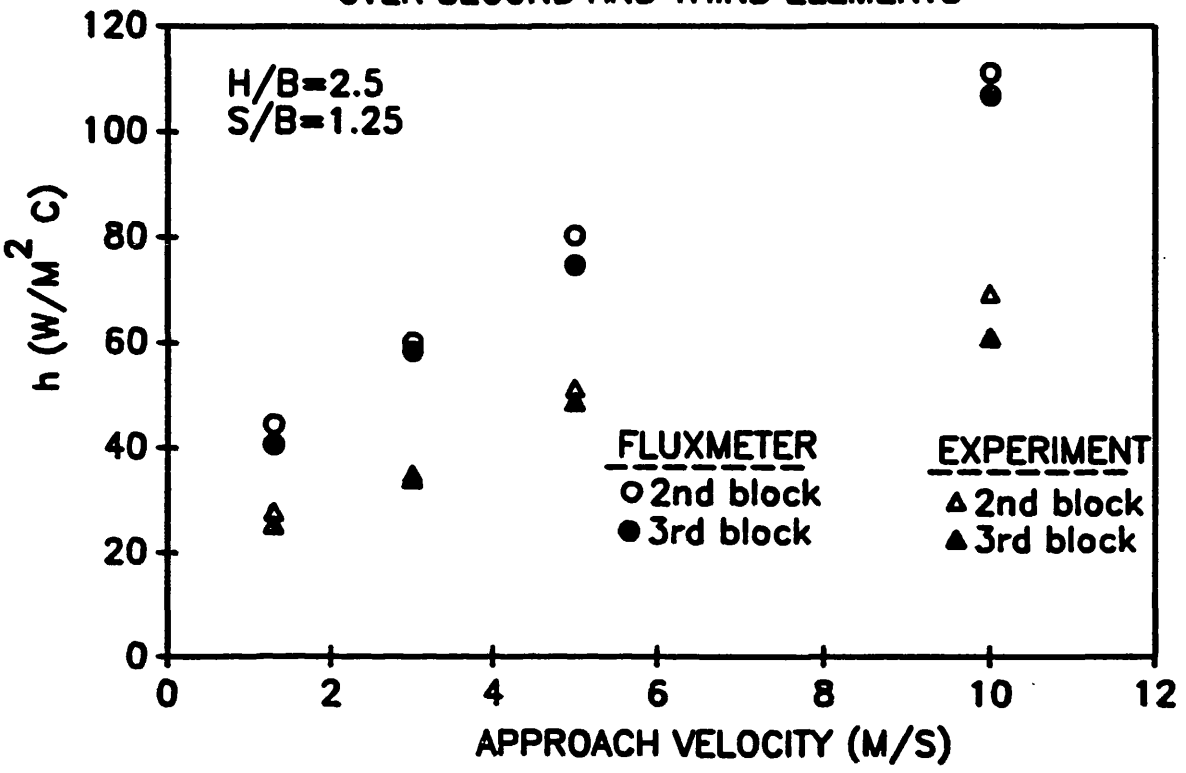

FIGURE 6.23: EFFECT OF UPSTREAM HEATING ON HEAT TRANSFER COEFFICIENT OVER THIRD ELEMENT

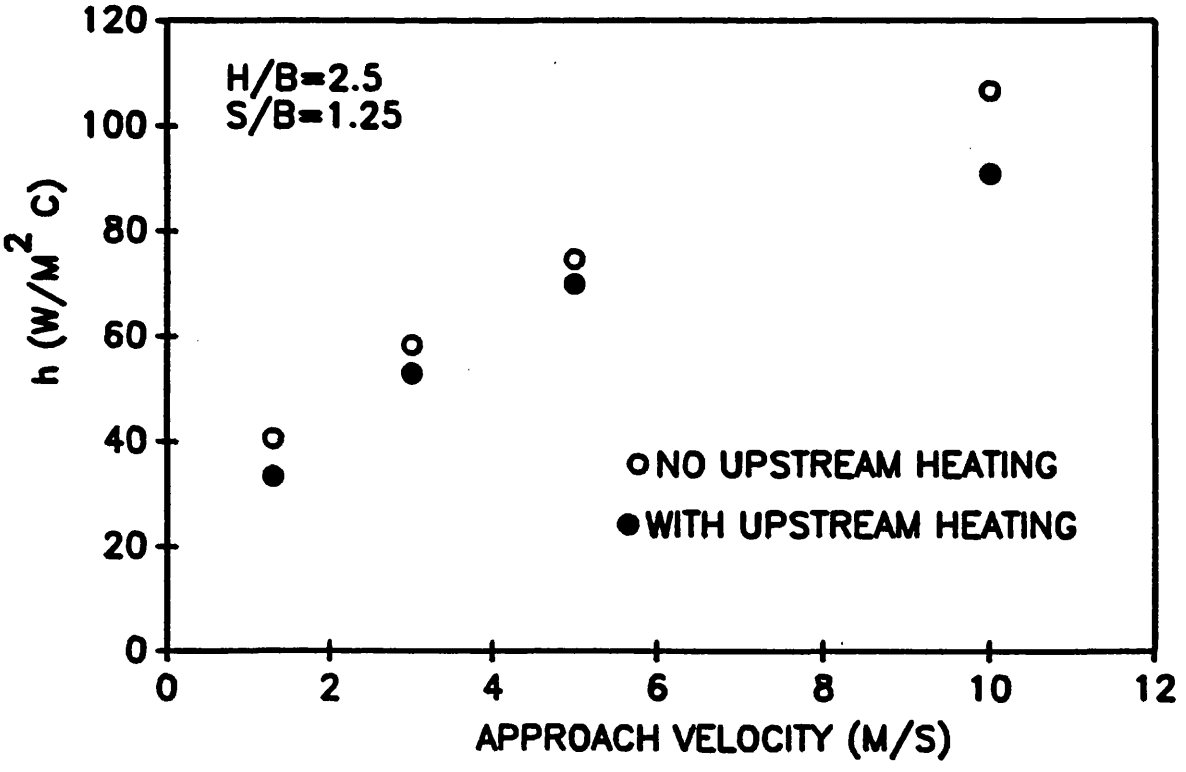

FIGURE 6.24: EXPERIMENTAL AND THEORETICAL COMPARISONS OF NUSSELT NUMBER, OVER THIRD ELEMENT

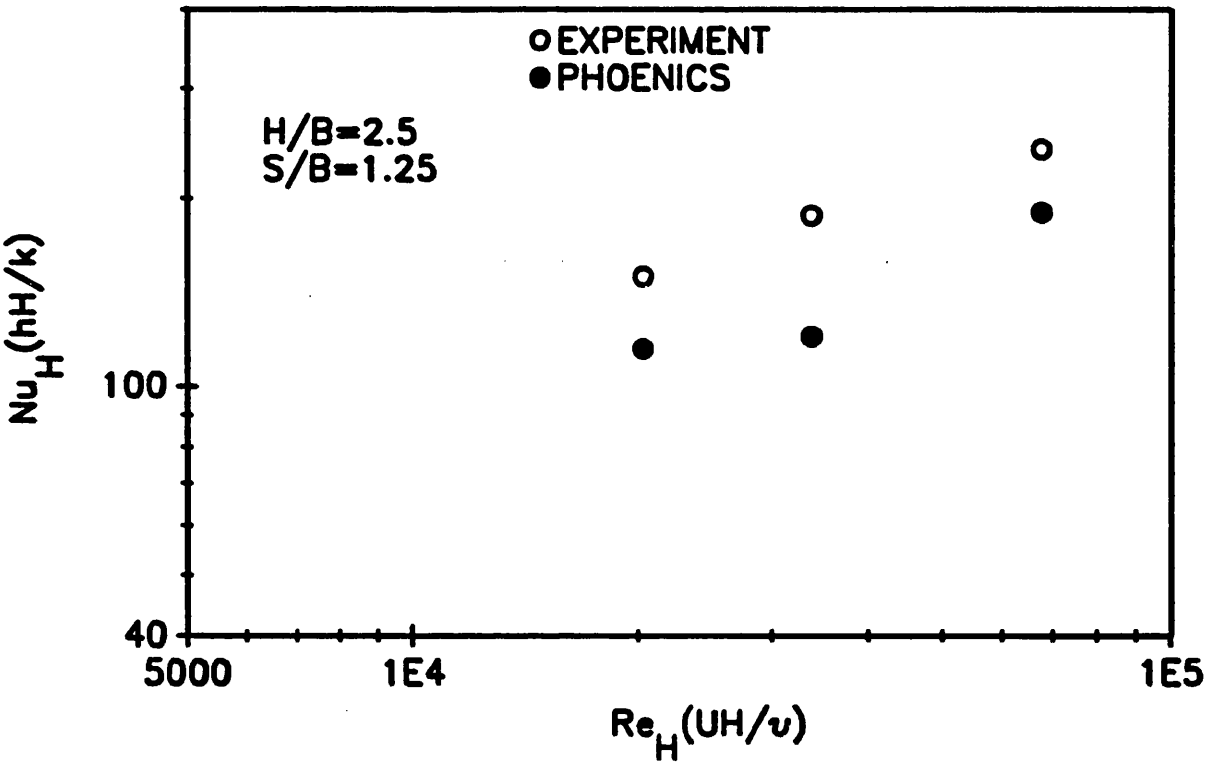

FIGURE 6.25: EFFECT OF APPROACH VELOCITY ON TEMPERATURE PROFILES,

FOURTH ELEMENT HEATED, S/B=1.25, H/B=2.5
POWER INPUT=33.75W

a)U_{in}=3M/S

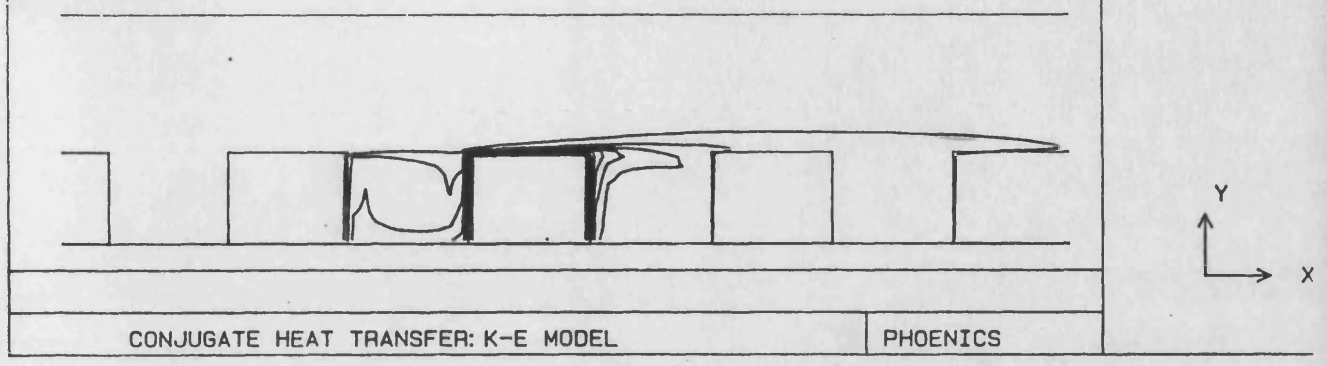

b)5

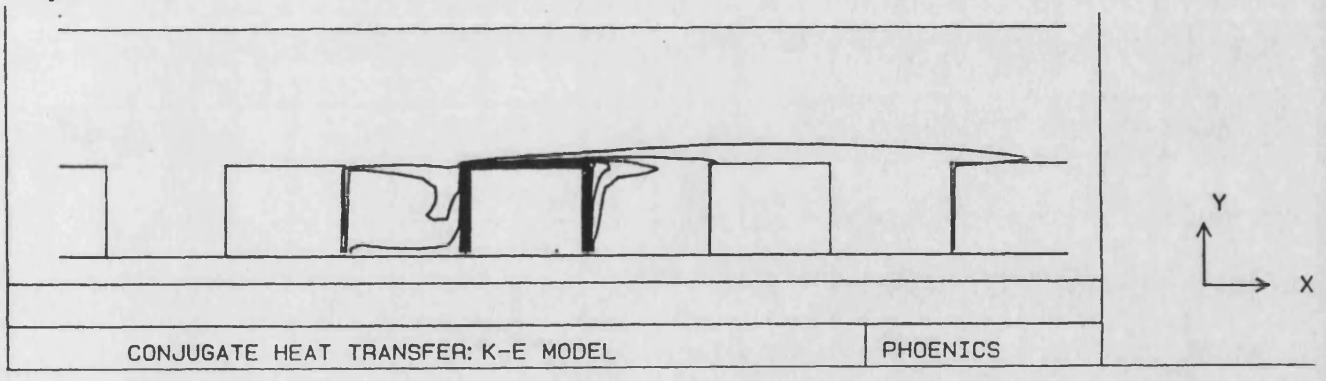

c)10M/S

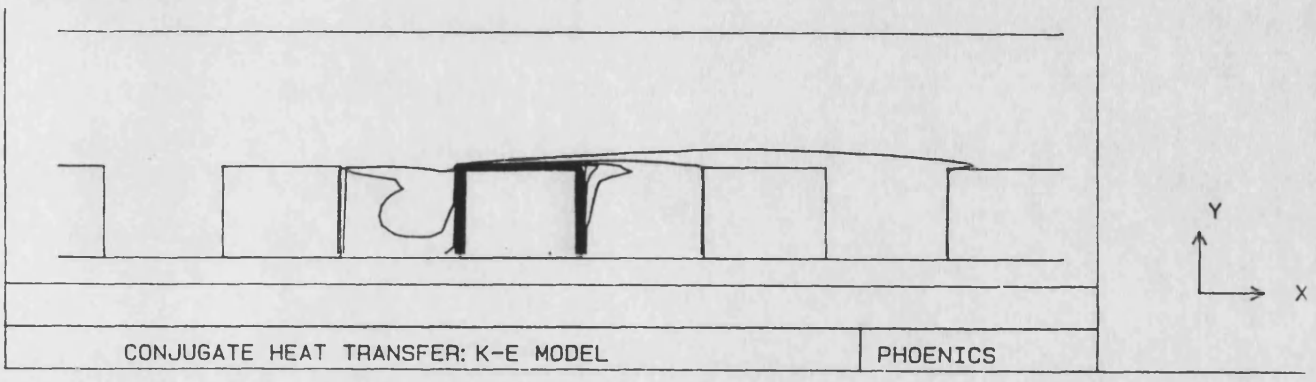

FIGURE 6.26: EFFECT OF CHANNEL SPACING ON TEMPERATURE PROFILES

OVER FIRST FOUR ELEMENTS, U_{in}=10M/S, S/B=1.25
POWER INPUT=33.75W

a)H/B=2.5

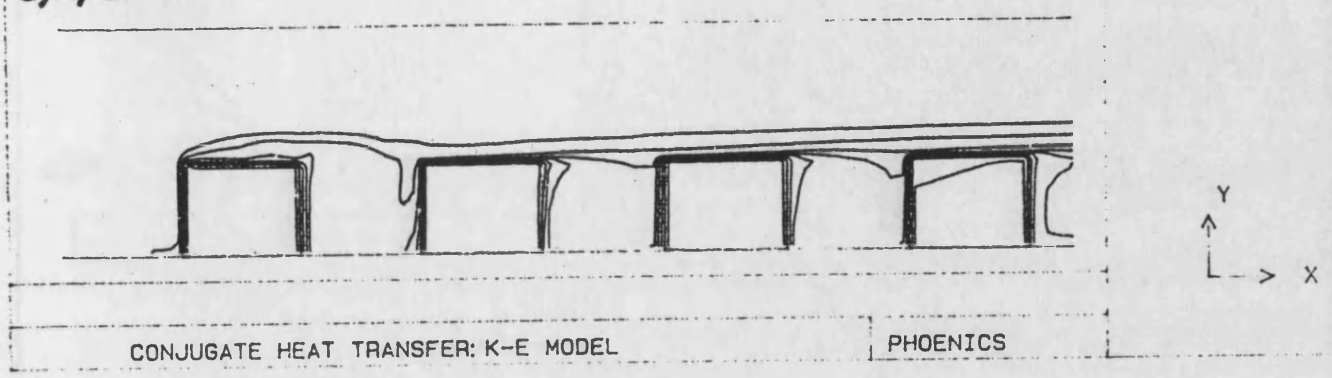

b)H/B=2.0

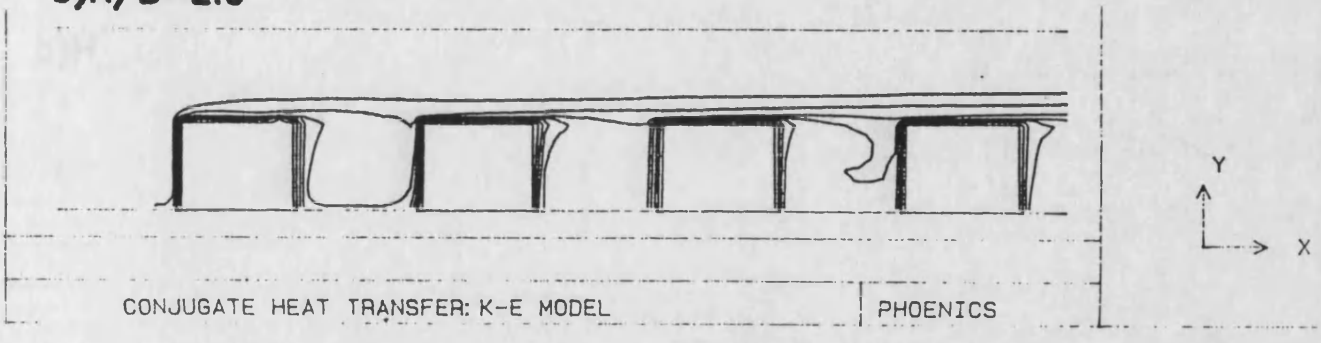

c)H/B=1.5

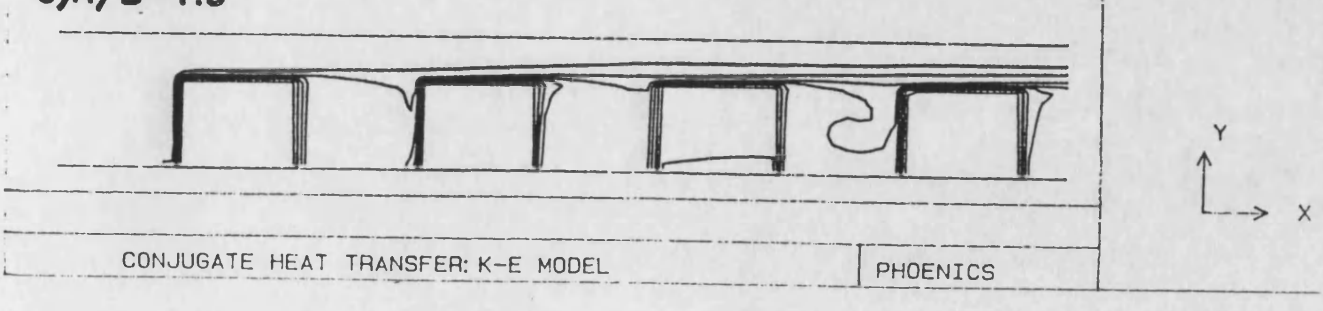

FIGURE 6.27: EFFECT OF CHANNEL SPACING ON TEMPERATURE PROFILES

, ALL ELEMENTS HEATED

U_{in}=5M/S, S/B=2.0, POWER INPUT=33.75W

a)H/B=1.5

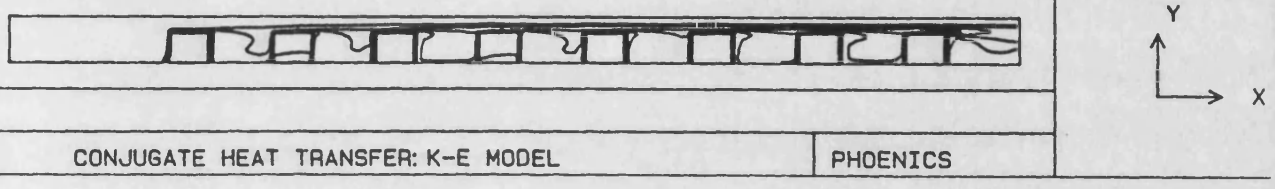

b)H/B=2.5

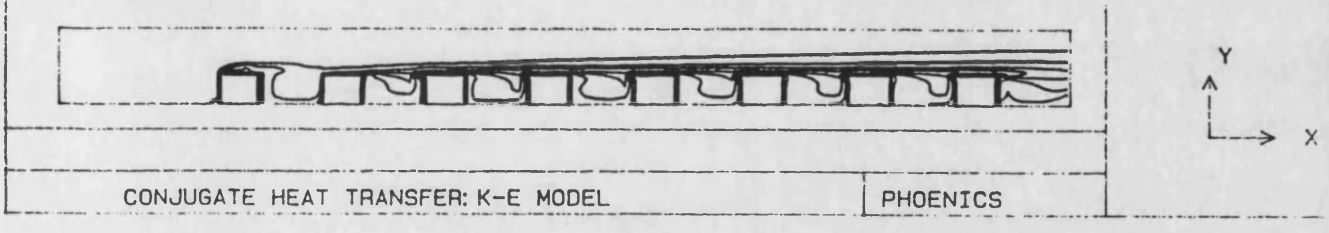

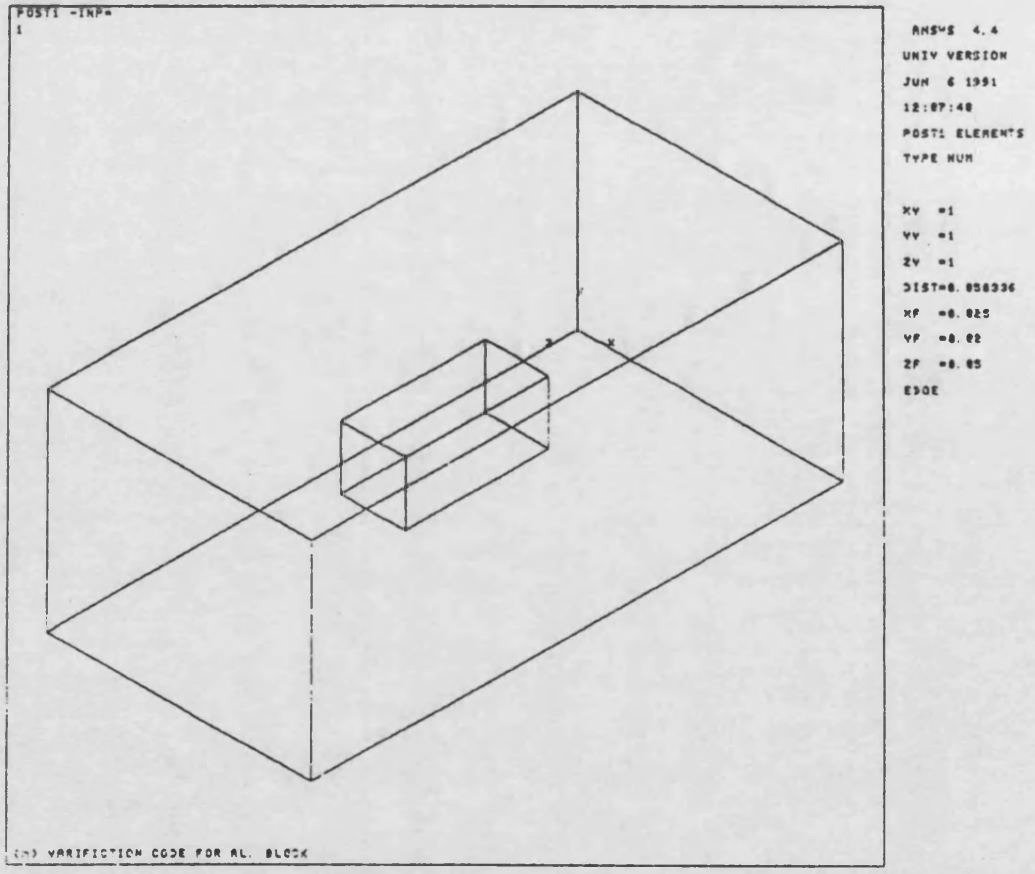

FIGURE 6.28: THREE–DIMENSIONAL ANSYS MODEL OF THE ELEMENT

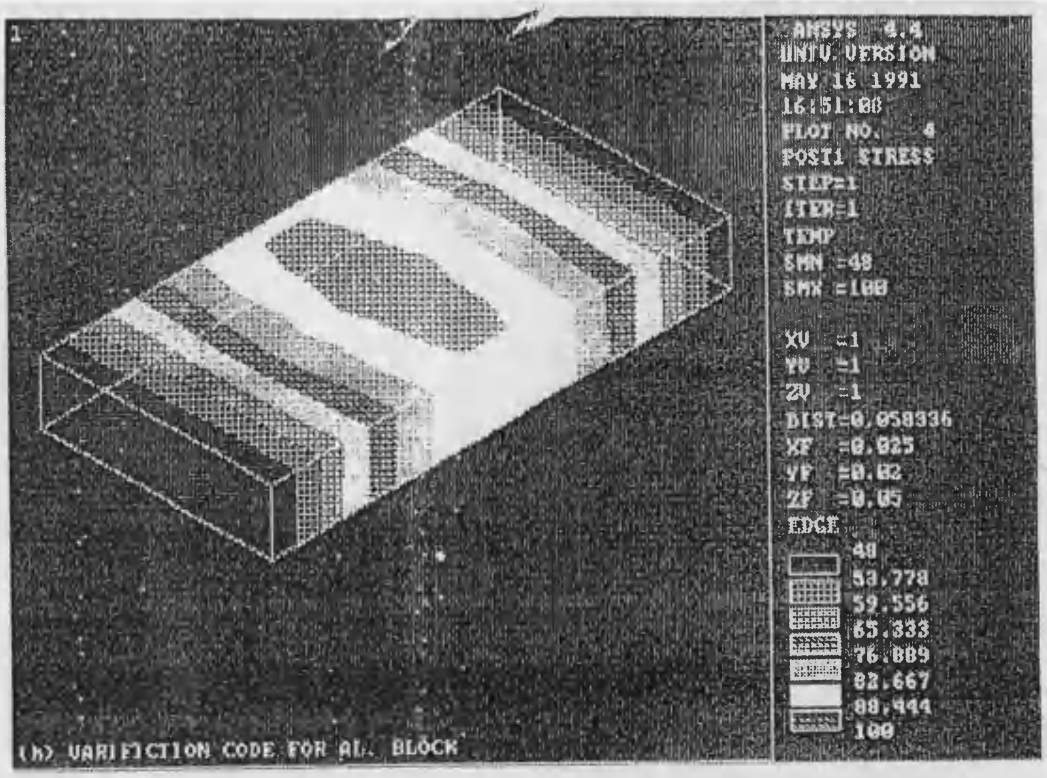

FIGURE 6.29: TEMPERATURE DISTRIBUTION OVER THE TOP SURFACE OF THE THREE-DIMENSIONAL ELEMENT

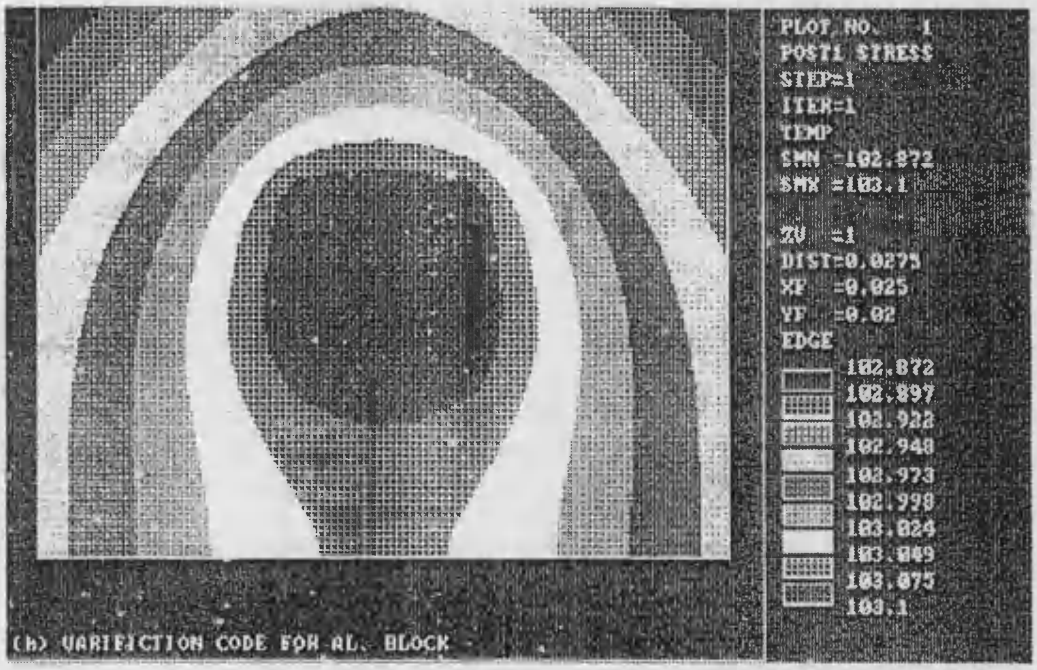

FIGURE 6.30: TEMPERATURE DISTRIBUTION OF THE TWO-DIMENSIONAL MODEL

CHAPTER [7]

EXPERIMENTAL STUDY

7.1 INTRODUCTION

In this Chapter the experimental techniques used to measure the velocity and temperature of the airflow are described. The background to the experiments are discussed in section 7.2. There follows in section 7.3 a review of measuring techniques suitable for the investigation of flow velocities and temperatures around the heated blocks.
The principle operation of LDA is described in section 7.4. The choice of velocity measurements is the subject of section 7.5.
Details of the experimental apparatus and techniques used in this study are given in section 7.6 to 7.12 including the design of the test section, and the instrumentation used. Section 7.12 describes the Schlieren method.
The conclusions of this study are summarised in section 7.13.

7.2 NEED FOR MEASUREMENTS

The fluid flow problems for which analytical solutions are available, tend in the main, to be limited to laminar flows, or those cases in which the geometry of the system is quite simple. Many of the solutions have been extended

to give answers to those engineering problems which can be adapted to fit the simplifying assumptions.

However practical problems which involve complex (turbulent) flows generally do not have simple analytical solutions. The complexity of practical fluid dynamic problems, and the difficulty of analytical solutions, has led to the development of computational fluid dynamics, in which the governing equations are solved using finite difference methods, or other similar techniques.

There is a need to make measurements in these complex flows, both to understand the basic properties of the flow, and also to develop better mathematical models.

The purpose of the experimental study was to provide data that could be used to obtain a more precise check on the computer predictions than was possible solely by a comparison with previously published data. The available information on flow over heated blocks was limited with respect to the quantities measured, and the regions of the flow where they were obtained.

For the proper assessment of the numerical predictions an extensive field of data was required. Thus the present experiments were made with the objective of obtaining more extensive information of the flow field.

7.3 REVIEW OF VELOCITY MEASURING TECHNIQUES

Before undertaking the velocity measurements, careful consideration was given to the choice of the appropriate

experimental technique. In this section a brief examination is made of the various techniques available for measurement of velocity around the heated blocks from which the method best suited for the present investigation was selected.

TECHNIQUES AVAILABLE

There are many techniques available to study flow problems both qualitative and quantitative, Table (7.1) summarises some of these techniques. For many practical purposes simple mean flow measurements are adequate and a pitot static tube offers a simple solution to many problems.
In order to get more detailed information it is necessary to study the turbulent processes occurring within the flow. An ideal instrument for measuring the two-dimensional velocity field in the vicinity of the heated blocks would provide the two components of mean velocity and the corresponding Reynolds stress components. It should be usable in regions of high turbulence intensity and reverse flow. Instruments which satisfy some of these requirements include the pitot probe, the heated body anemometer and the laser Doppler anemometer.

A 5-hole pitot probe is necessary in two-dimensional flows to indicate the direction and magnitude of the total velocity. Details of various types of 5-hole probes are given by Bryer and Pankhurst [56]. This instrument has the advantage of requiring only simple pressure measuring

instruments, but suffers from several disadvantages.

Hot wire (thermal) and laser anemometry are presently the most commonly used techniques. Both methods measure the instantaneous velocity and thus it is possible to extract information on both the mean and fluctuating components. Used in conjunction with flow visualisation this represents a powerful tool in the understanding of many fluid flow problems. In addition to mean quantities other parameters of interest such as normal stresses and Reynolds stresses can be measured.

These terms represent energy dissipation within the flow. With the increasing complexity of turbulence models the measurement of higher order correlations is becoming increasingly important, it is possible to measure these quantities using thermal and laser anemometry. Table (7.2) outlines the relative merits of the two techniques.

Three different types of the heated body anemometer have been used for velocity measurements around heated blocks; these include the heated sphere employed by Wise et al. [57], the hot wire anemometer used by Castro [58] and Castro and Robins [59] and the pulsed wire anemometer also employed in the latter two studies.

The heated sphere operates on the same principle as the much more common hot wire anemometer which is well described by Bradshaw [60].

Compared with 5-hole pitot probe, the hot wire anemometer has better spatial resolution and much faster response, allowing it to resolve turbulent fluctuations. However, it

responds more strongly to velocity components normal to the wire than to the parallel component and hence is not well suited to determining flow direction or to measuring in regions of high turbulence intensity.

The pulsed wire anemometer, Bradbury and Castro, [61] employs three closely spaced wires. A current pulse fed to the central wire heats the adjacent air which is then convected by the flow towards one of the two outer wires. The velocity is determined in magnitude and direction by the time required for the hot gas to reach either one wire or the other.

By virtue of its directional response, the pulsed wire anemometer is more suitable than the hot wire anemometer for measuring in a recirculation region. It has a fast time response to velocity fluctuations, but requires calibration.

The laser Doppler anemometer, described for example, by Durst, Melling and Whitelaw [62], is an optical method for fluid velocity measurement which does not require the insertion of a probe into the flow. The technique measures the Doppler frequency shift in light scattered by particles following the flow; this frequency is proportional to velocity and no calibration is required. Unlike the hot wire anemometer, the LDA responds to only one component of velocity which is uniquely defined by the orientation of the laser beams; the two velocity components can thus be determined independently, by suitable aligning of the optical system.

Frequency shifting allows the instantaneous flow direction to be determined, permitting measurements in regions of high turbulence intensity and reverse flow. Spatial resolution and response time of a typical laser Doppler anemometer are both sufficient for measuring velocity fluctuations. Its many experimental advantages are to some extent offset by its high cost; the need to seed the flow with small particles may be a disadvantage.

7.4 THE PRINCIPLE OPERATION OF LDA

All LDAs measure either the rate of change of phase (ie frequency) of the light scattered from particles in the flow (Laser Doppler Anemometer) or time of flight between two points in the flow (Laser Transit Anemometer). Figure (7.1) is a diagram of a Laser Doppler Anemometry system.

DOPPLER EFFECT

Consider a source of waves moving towards a stationary observer. Due to the motion of the source, the frequency that the observer experiences is higher than would be the case if the source were stationary. This applies to a moving light source, and to the light scattered from a moving object. The frequency of the light scattered from a moving objects is different from that scattered by a stationary object. This is the principle on which the Doppler anemometer operates. Figure (7.2) illustrates the

characteristics of the signal scattered from a particle. Figure (7.3) shows the details of Doppler difference geometry and Figure (7.4) shows the reference beam laser Doppler anemometer.

FRINGE MODEL

Two incident laser beams may be considered to form interference fringes at the intersection of the beams as shown in Figures (7.5) and (7.6). A particle crossing this point in the flow would appear to cross a series of light and dark regions. The scattered light would then vary depending on whether the particle was in a light or dark region. The fringe spacing is given by:

$$\delta_f = \frac{\lambda}{2 \sin \frac{\theta}{2}} \qquad (7.1)$$

The Doppler frequency of the light scattered by a particle is given by:

$$f_D = \frac{2U}{\lambda} \sin\frac{\theta}{2} \qquad (7.2)$$

where **U** is the velocity of the particle and θ is the angle of intersection of the beams.

LASER DOPPLER SYSTEMS

It is not easy to measure the Doppler shift from a particle scattering light from a single laser beam. It is far easier to look at the light from two laser sources and combine them to obtain interference patterns which have much lower frequencies than the original Doppler signals. There are a number of practical methods for achieving this.

SEEDING

The laser anemometer requires the presence of some particles in the flow to scatter light from the laser beams. The selection of seeding particles is an important consideration when making velocity measurements.

PROCESSOR

There are a number of different methods of processing signals from laser Doppler anemometers. The signals from the light scattered from the particles in the flow is oscillatory. It is possible to analyse these signals by using spectrum analysers and transient recorders but these methods tend to be inefficient. It is more common to use trackers, counters or correlators.

SIGNALS

Having found a suitable material with which to seed the flow which is of interest, the scattered light from the particles generates a current at the photo detector. This current contains the frequency information relating to the velocity.

FREQUENCY SHIFTING

One of the main advantages of the laser anemometer is that it is able to detect the direction of the flow, and can measure negative velocities. There are many situations where it is necessary to measure the direction and magnitude of the flow, examples of this would be swirling flows, flow around a bluff body and flow over a step, the main characteristic of all these flows is that they are all capable of supporting reversed flow.

Consider the fringe model described earlier and shown in Figure (7.5). A particle passing through the fringes at velocity **U** ms^{-1} would have exactly the same Doppler frequency as a particle travelling at velocity **-U** ms^{-1}. However if it were possible to arrange for the fringes to move the Doppler frequency would be different in each case. If the fringes move in the opposite direction to the flow the positive velocity would appear to be higher by an amount equivalent to the velocity of the fringes, while the negative velocity would appear lower. To obtain the actual

velocity it is then a simple matter of subtracting the velocity of the fringes from the measured velocity. The frequency shift applied should be equivalent to a velocity greater than the maximum expected negative velocity. The most common method of achieving the frequency shift are:

i) Bragg cell

ii) Rotating diffraction grating

The bragg cell is an acousto-optical unit and consists of either a block of solid transparent material or a cell filled with a liquid. The rotating diffraction grating consists of an optical quality glass disc onto which is etched a series of radial lines.

7.5 CHOICE OF VELOCITY MEASUREMENT TECHNIQUE

The choice of the most appropriate experimental method for the present study was dictated by the limited time available to obtain the desired measurements of mean velocity and turbulence intensity at a number of points in the flow field. This constraint favoured the selection of the laser Doppler system. The 5-hole pitot probe was not chosen because of its deficiency in the wake of the blocks.

The hot wire anemometer suffered from the same disadvantage and, like the pulsed wire anemometer, would be considerably more difficult to use. The laser Doppler anemometer offered the best prospects for measuring in the recirculation zone, but the time required to gain familiarity with the

instrument and to set up the equipment for the present experiment detracted from the time necessary to complete the measurement programme.

7.6 DESCRIPTION OF EXPERIMENTAL RIG

7.6.1 CHANNEL CONTAINING TRANSVERSE SOLID BLOCKS

The main experiments were carried out in an open circuit experimental duct whose test section, shown in Figures (7.7), (7.8) and (7.9) has the dimensions 1.25m long, 0.1m wide and 0.1m high. Air was drawn through the duct by a centrifugal fan. The elements used for the experiments were rectangular section aluminium blocks of 0.04m height, 0.1m width and 0.05m length shown in Figure (7.10). Eight blocks were fixed (with epoxy) to the base of the test section with a space of 0.05m between each block.

The test section was originally fabricated from perspex sheets (7mm thick) but this was later changed to glass of thickness 0.005m, to reduce scratching and improve cleaning. The upstream and downstream lengths of the plates were chosen to produce uniform flow. This ensures that the outflow boundary condition of a fully developed velocity profile had no effect on the flow solution around the blocks.

In order to reduce the losses at the duct entry, a curved rectangular nozzle was fitted. A honeycomb flow

straightener was used at inlet to direct the flow through the duct, and to maintain a uniform free stream core velocity.

The test section was housed in a horizontal, flat rectangular duct whose overall length included the test section, and a component-free exit length. A transition section connected the rectangular duct to a length of pipe (2" dia) which equipped with an orifice plate (BS 1042) for flow measurements. The blockage ratio, defined as the ratio of the frontal area of the block to the tunnel cross-section, was 40%. A wooden model of the same dimensions, painted matt black, was used for flow visualisation tests.

7.7 MEASUREMENTS TECHNIQUES

a) FLOW VISUALISATION

i) SMOKE VISUALISATION

Smoke tunnels, which are wind tunnels designed exclusively for visualization tests using smoke, can give unrivalled presentations of the entire flow field around a model. These wind tunnels operate at very low speeds and elaborate precautions are taken to achieve a non-turbulent flow so that the smoke streams which are introduced in front of the model remain clearly defined. Because the Reynolds number available is necessarily very low, smoke tunnels are of limited value for investigating flow separation phenomena. Observation of the flow inside the test duct was performed

by painting the blocks surfaces black. Smoke introduced into the stream of air was used. Smoke in this study was produced by a model 3020 smoke generator, which generated a visible mist by evaporating a light mineral (kerosene) which subsequently condenses in the cool air stream. The kerosene smoke is non-corrosive and non-toxic.

The smoke was injected into the tunnel through a tube 8mm diameter at the inlet position in the tunnel mid-plane about 0.34m upstream from the first block. In some tests the smoke was injected close to the model using a smaller tube of 3mm diameter, so as to reduce disturbance of the flow. In this way some details of the flow were revealed such as separation and reverse flow at the top, recirculation between blocks, and the reattachment zone.

The smoke patterns were illuminated by flood lights and photographed using ASA400 film with an exposure of 1/60 to 1/4 second at **f**/8.

b) VELOCITY MEASUREMENTS

The measurements of velocity were obtained by a laser Doppler anemometer Figure (7.11).

A Pitot static tube was inserted at inlet of the duct section to measure the inlet velocity upstream of the test region. This was connected across a meriam inclined-tube water manometer.

Originally the type of laser used was an Spectra Physics 30mW Helium Neon (wavelength 632nm) for measuring velocity

components and turbulent intensity in the test section. The laser Doppler system was comprised of:

Optics : Malvern Instruments RF 340M General Purpose Optics Unit.

Frequency shift: Malvern Instruments K9023 Phase Modulator 20KHz- 1MHz.

Processor: (i) Malvern Instruments K7026 20ns Photon Correlator

(ii) Cambridge Consultants Frequency Tracker.

A large number of readings were taken with this type of laser at a very low flow rate (ie, inlet velocity of 1 to $2ms^{-1}$).

The operation of a Laser Doppler Anemometer depends on the introduction of particles into the test section to scatter incident light on to a photodetector. The particles must have a certain size to produce good Doppler signals and yet be small enough to follow the turbulence of the medium.

The DISA type 55L 18 seeding Generator used mineral oil to produce such seeding particles. Later problems were encountered with this seeding system. These started when the air flow rate was increased. It was found that the generator could not produce sufficient particles for the laser to pick up. Half way through the experimental program, troubles were also encountered with the laser processor. Eventually it was found that the processor was worn out.

These problems lead to abandoning the LDA described above

and to continuing the investigation with the new type of LDA which had then become available for a short time. Also a new seeding generator produced a greater volume of vapour particles became available.
The specification of the new laser system was as follows:-

Laser : COHERENT INNOVA 70, 3W Argon Ion operating at 488 and 514nm.

Optics : Aerometrics Fibre Drive including a 40MHz Bragg cell, 500mm Fibre optic Transmitter and 500mm Receiver unit with 100μm spatial filter.

Processor: Aerometrics DSA (Doppler Signal Analyser) processor, with Aerometrics DSA software control.

The seeding generator used was Vital boneco US. 7.5 Liter Ultrasonic Humidifier.
Figure (7.12) shows the data acquisition system for the LDA.

7.8 TEMPERATURE MEASUREMENTS

Temperature measurements were made with thermocouples in the solid and a hot wire in the fluid region.
The elements were instrumented by drilling a number of sensor holes round the surfaces of the heated elements, and thermocouple were inserted into these holes.
Eight blocks were used in this experiment with 2 as active

elements (second and third blocks) and the rest as a passive elements. On the passive elements only one thermocouple was attached to measure the adiabatic temperature of the elements. The thermocouple used were of PTFE insulated (type K) with composition of 95% Ni and 5% Alu.

Calibration of the thermocouples was accomplished by a selective process. Several thermocouple were tested at the steam and ice point and only those with the desired accuracy were used. The thermocouple were monitored manually with a selector switch and a digital handheld Fluke 52 K/J Thermometer Multimeter Temperature Indicator. The active elements were used for measuring h, and the passive elements were used for measuring the thermal wake function.

7.9 HOT WIRE ANEMOMETRY

HOT-WIRE MEASUREMENTS

The hot wire technique relies on the convective heat loss from a heated sensor to the surrounding fluid. The sensor is electrically heated. The heat loss is dependent on the temperature difference between the probes and the fluid, the convective heat transfer coefficient, and the properties of the fluid. The heat transfer coefficient is proportional to the fluid velocity.

In this study the anemometer was used in its constant current mode. The Hot-Wire probe were designed and

calibrated by author. The Hot-Wire was calibrated each time before measurements were taken using procedures consistent with those outlined in DISA operating manuals. The wire was manufactured by Dantec Denmark, SPCE.WIRE PT 10% RH, Diameter ϕ=10μ and ohms per foot 756Ω. Figure (7.13) shows the purposed built manipulator for hot-wire welding.
A manual traversing gear was designed to carry the hot wire probe in three directions inside the test section. Figure (7.14) shows the hot wire probe carried by the traversing gear. Temperature profiles were measured with an anemometry system consisting of a DISA type 56C16 CTA Bridge and the DISA type 56C01 CTA Unit.

7.10 POWER MEASUREMENTS

The elements that were to be heated were each equipped with a 25W resistor (potentiometer mounted on a 2.4°C/W heat sink). The length of each resistor is 28mm and width 28mm, with a maximum power of 25W derated to 12W in free air and a maximum working voltage of 550 V.a.c. and maximum surface temp of 200°C. To adapt them for this purpose the potentiometers were machined into a cylindrical shape (1.2cm diameter and 2.7cm length) and then fitted into the centre of the blocks which were drilled for this purpose. The resistors were covered with silicon gel, which is a good conductor and has a low thermal resistance (see Figure (7.10)). A thermocouple also was placed in the same hole attached to the body of resistor, in order to give the

source temperature readings. This hole was then plugged with aluminium and filed so that the faces of the element were flush except for the lead wires on the either ends of element which were connected to the power supply. The power supply used was Kingshill stabilised power supply model 36V5C. The power input was then calculated from the current and voltage values set for the test.

7.11 FLUXMETER MEASUREMENTS

A Micro-Foil heat flow sensor was used to measure the heat flow from the surface of one of the heated elements. The Micro-Foil heat flow sensor is a differential thermocouple type sensor which utilizes a thin foil type thermopile bonded to both sides of a known thermal barrier as shown in Figure (7.15). Heat convected from the surface of the sensor must pass by conduction through the thermal barrier. This creates a temperature difference proportional to the heat flux which is measured by the thermopile. Each heat flow sensor is calibrated individually at a base temperature at 70°F (21°C).

One thin and flexible sensor was attached to the top surface of the second block in the test section by using a double adhesive backed Mylar tape. The leads from the sensor were connected to a millivoltmeter device and a calibration curve giving the surface heating rate in $Btu\text{-}ft^{-2}\text{-}h^{-1}$ was provided.

7.12 THE SCHLIEREN SYSTEM

The thermal boundary layer can be conveniently made visible with the aid of a Schlieren system together with the interferometric photographs produced from it. A parallel beam of light is passed through the boundary layer in a direction parallel to the plate and produces shadows on screen placed at a large distance from the body. The density gradient in the air at right angles to the surface causes the rays of the light to be deflected outwards as shown in Figure (7.16a).

The deflection is largest at the points where the density gradient is steepest, i.e., near the surface of the heated body. The rays of light which are deflected out of the temperature field create an illuminated zone around the dark shadow. The outer edge of this zone of light is formed by the rays which just skirt the surface; consequently their deflection is proportional to the density gradient at the surface, i.e., to the local coefficient of heat transfer.

A small finite line source is produced, shown as **ab** in Figure (7.16b). This source is combined into the system shown diagrammatically in Figure (7.16c). When a knife edge is interposed halfway across the gas the image formed at **cd** will be uniform grey.

Figure (7.17) shows a hand sketch of the thermal boundary layer produced by the Schlieren apparatus, superimposed on the velocity vectors produced by laser anemometry. From the

above Figure it is clear that a large separation is taking place over the first block. However the thermal effects produced by the heated blocks are relatively small and soon diffuse into the broader region of the main stream; and become difficult to make visible. This is also shown in Figures (7.18) and (7.19) Schlieren photographs taken over the second heated block. From these Figures it was evident that by placing a block (passive) upstream of second and third block (active), there exists a very thin thermal layer over the second and third block close to the wall. Unfortunately it was not possible to follow this thin thermal layer further downstream of the test section since only the second and third blocks could be powered, and away from these blocks the density gradient was not high enough to show any trace of thermal path.

7.13 CONCLUSIONS

This Chapter has described the experimental apparatus and the instruments used. The flow visualization techniques used have been explained. Various velocity measurement techniques were studied and the most suited technique was chosen.

The experimental techniques of LDA and hot wire anemometry have been described. These techniques represent valuable tools in the understanding of fluid flow problems. Both techniques are under constant development, especially laser anemometry. The laser techniques described here are the

most commonly used. The use of fibre optics has enabled laser anemometry to be applied to situations which were previously inaccessible.

TABLE 7.1: TECHNIQUES AVAILABLE

Flow Visualisation	Shadowgraph Schlieren Interferometry Tracer Methods
Anemometry	Pitot Static Thermal Anemometry Laser Anemometry

TABLE 7.2: LASER AND THERMAL ANEMOMETRY

Advantages	LASER No calibration Non-intrusive Direction Sensitive	THERMAL Cost No Particles
Disadvantages	Seeding Particles Optical Access Transparent Medium	Calibration Flow Interference Low Turbulence Levels

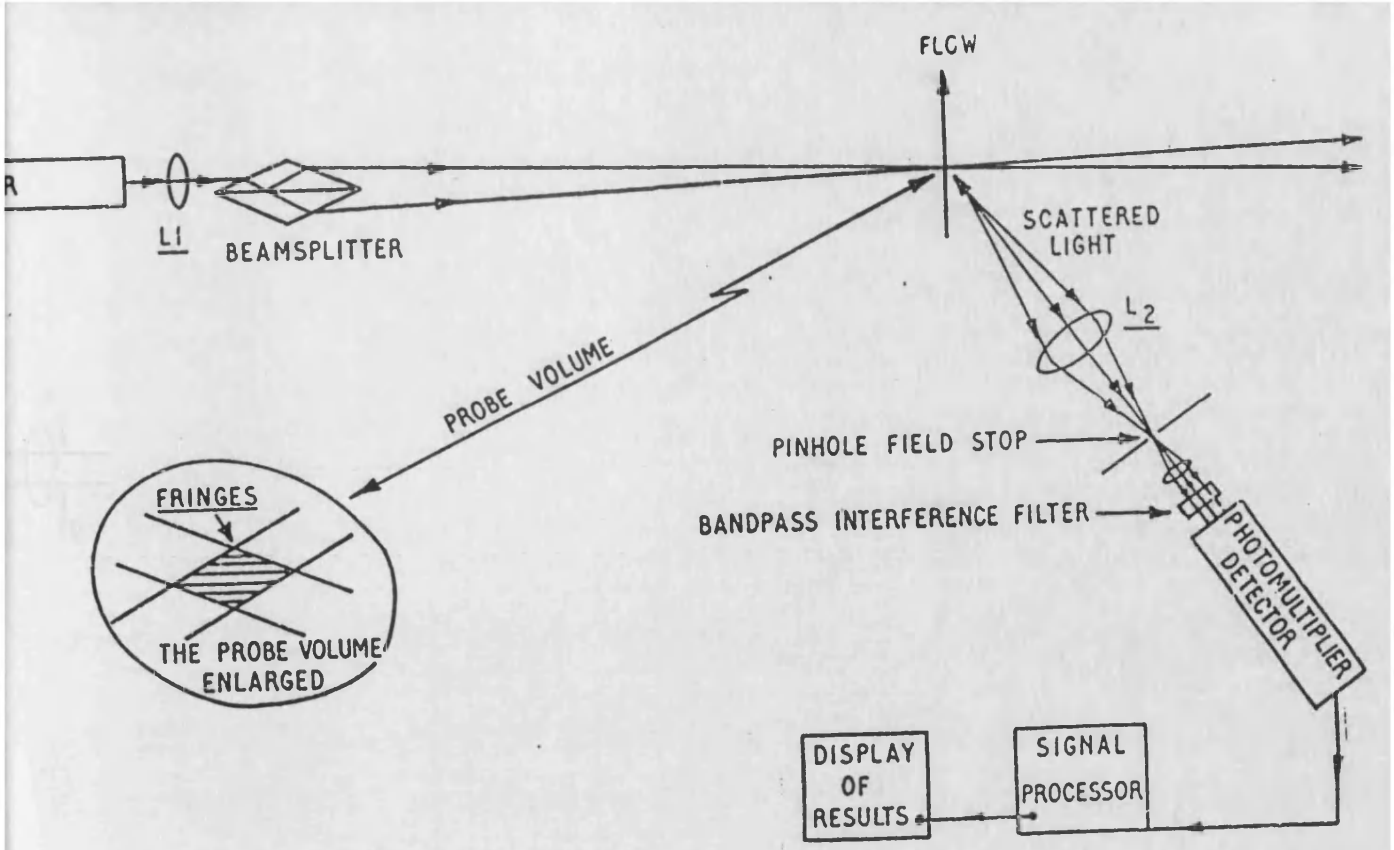

FIGURE 7.1: LASER DOPPLER – DIFFERENCE OR REAL FRINGE ANEMOMETER

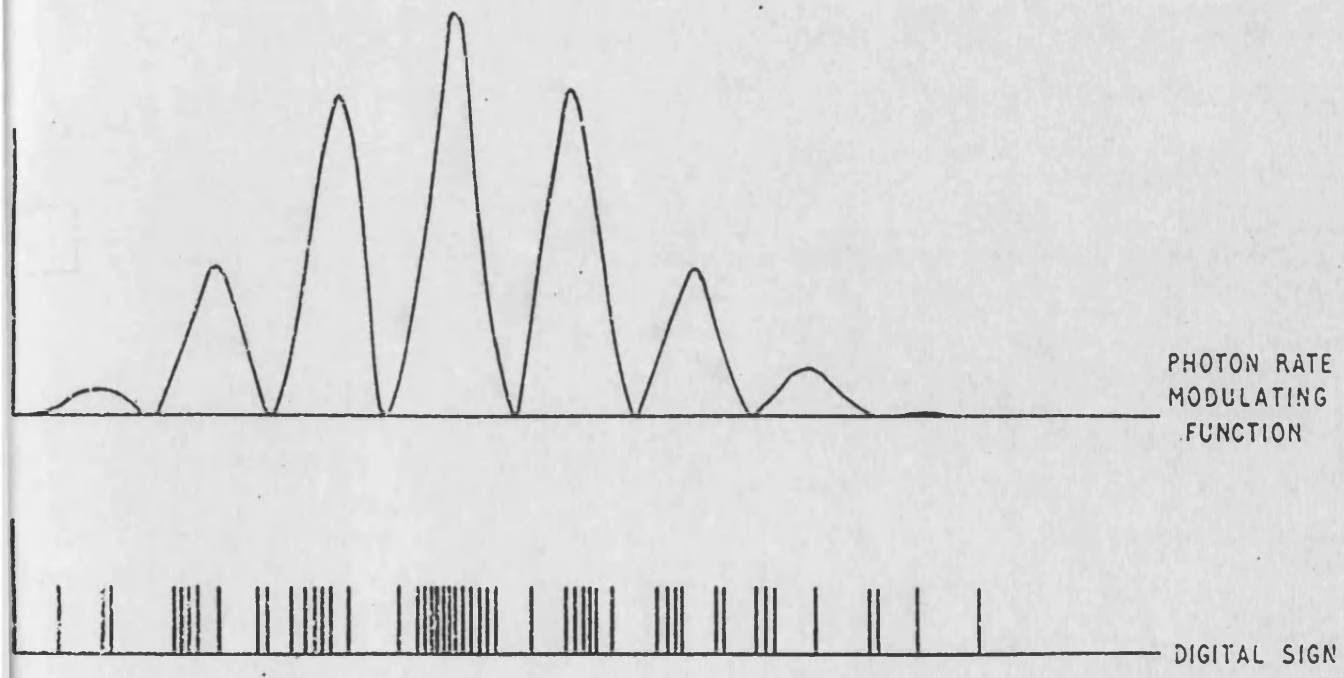

FIGURE 7.2: SIGNAL DUE TO A SCATTERING PARTICLE

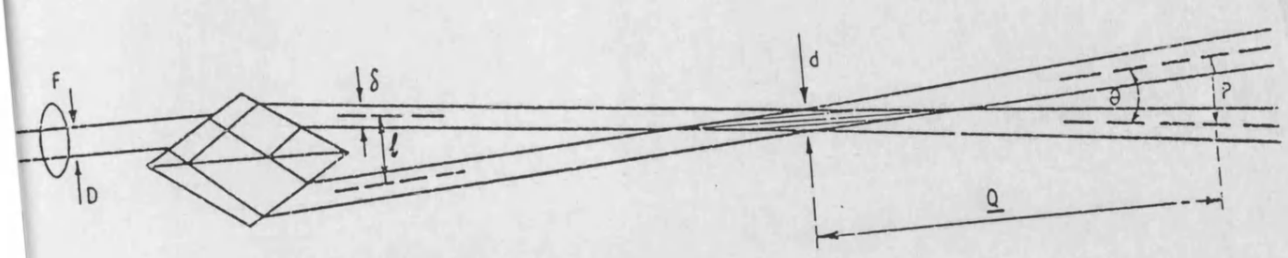

FIGURE 7.3: DETAILS OF DOPPLER DIFFERENCE GEOMETRY

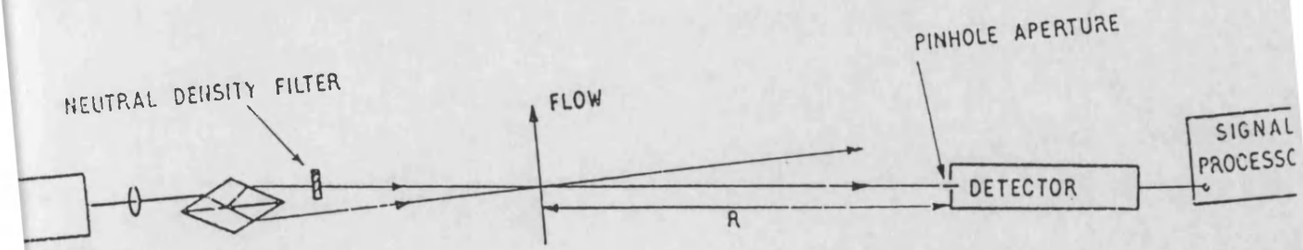

FIGURE 7.4: A REFERENCE BEAM LASER DOPPLER ANEMOMETER

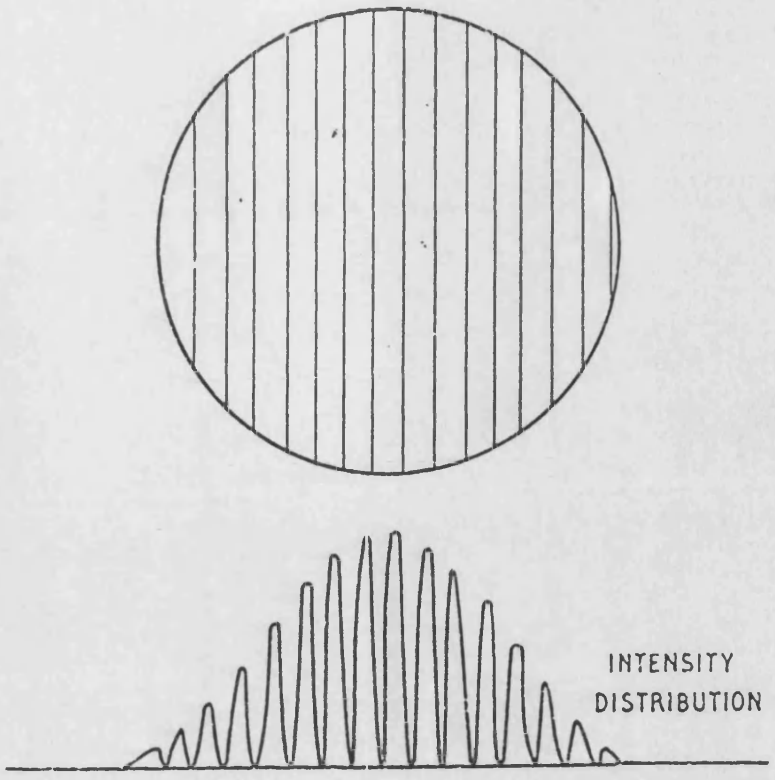

FIGURE 7.5: THE PROBE VOLUME CROSS SECTION FIELD WITH FRINGES

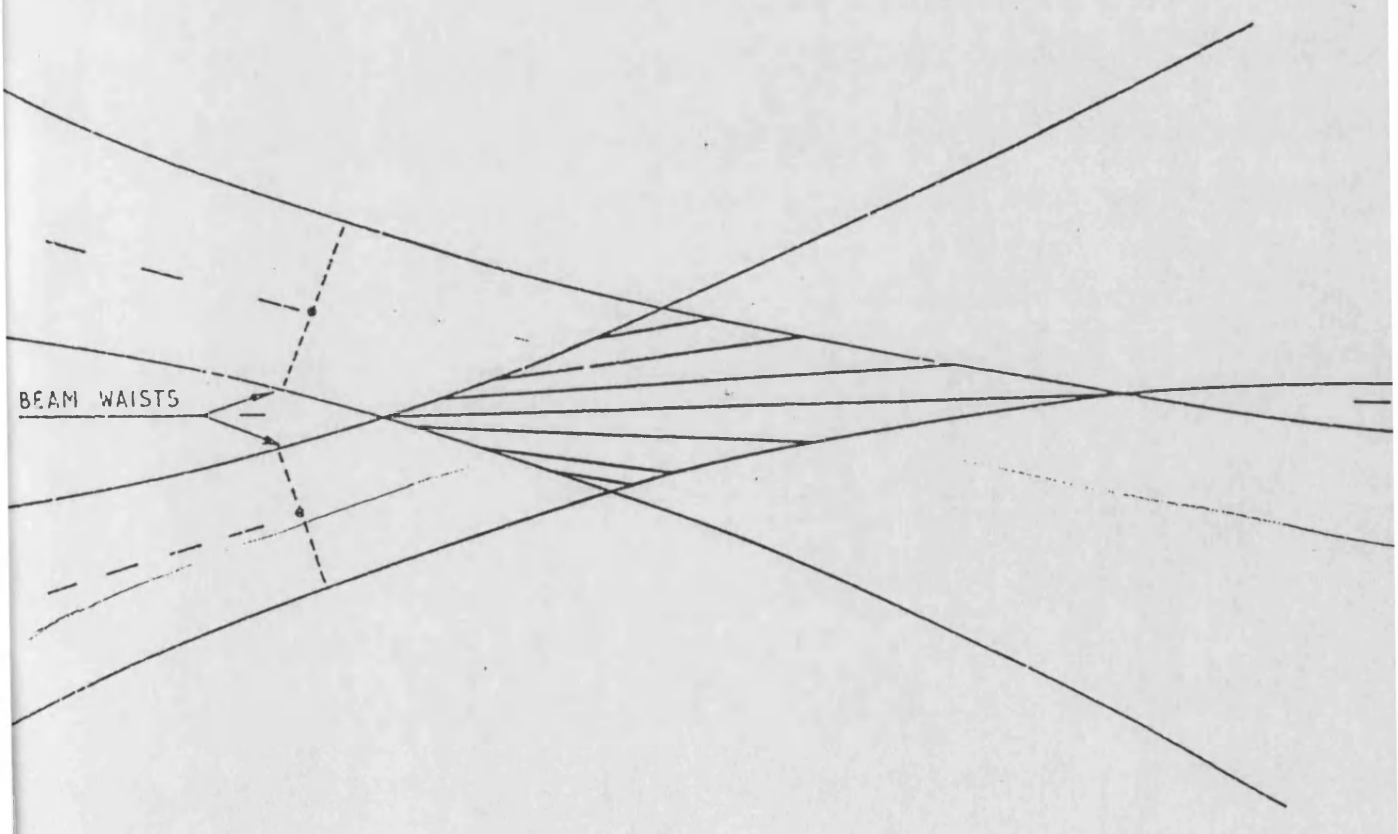

FIGURE 7.6: INTERSECTION ERROR OF TWO LASER BEAM WAISTS

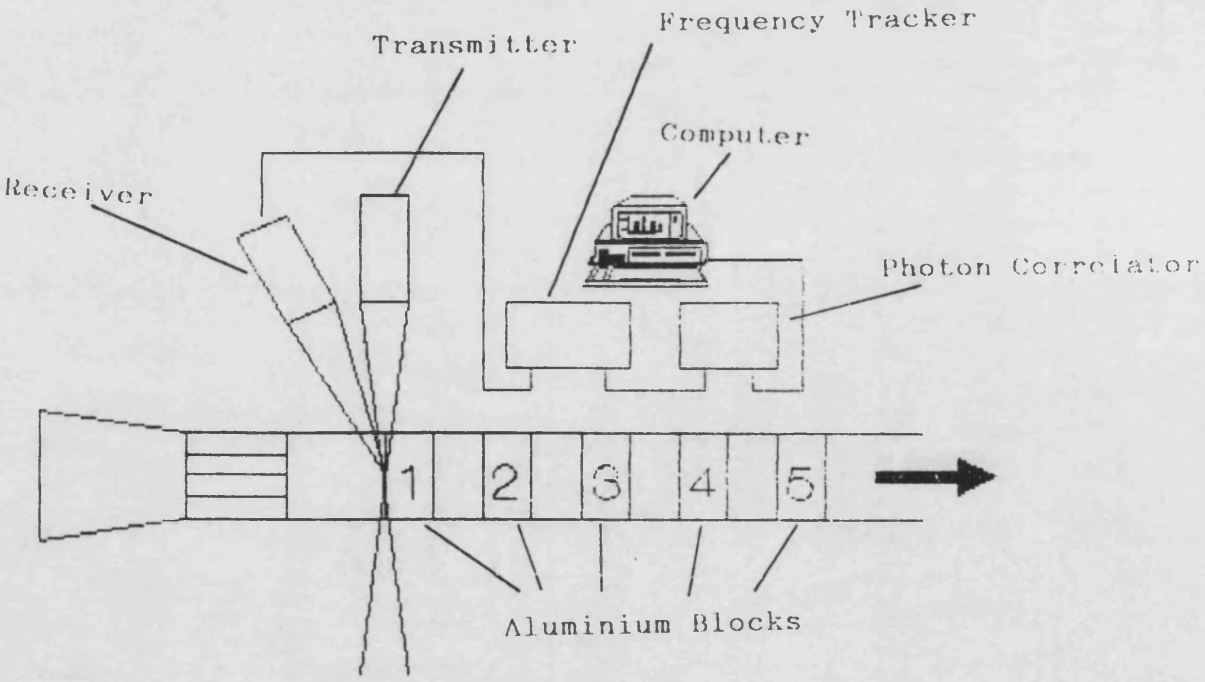

FIGURE 7.7: TEST APPARATUS

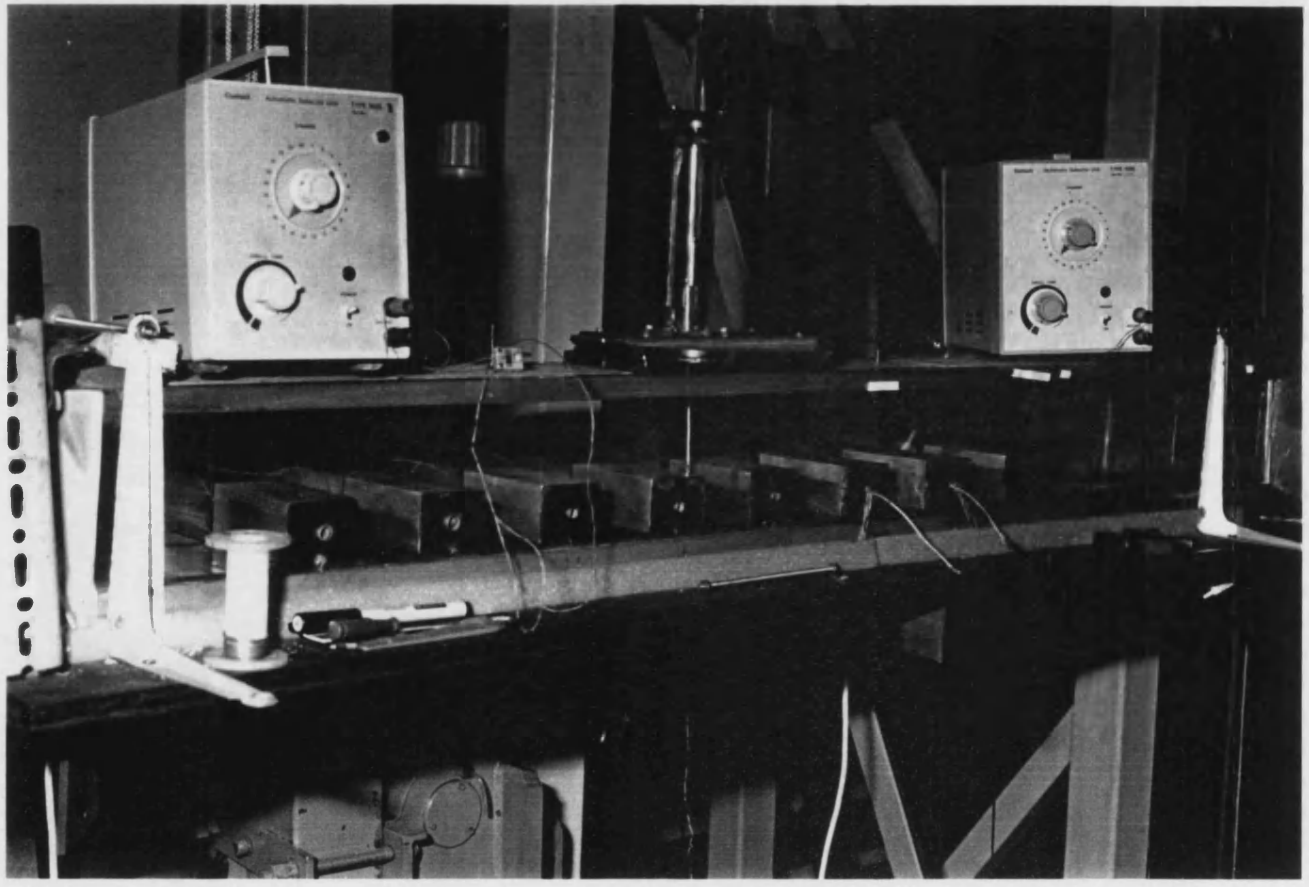

FIGURE 7.8: EXPERIMENTAL TEST SECTION

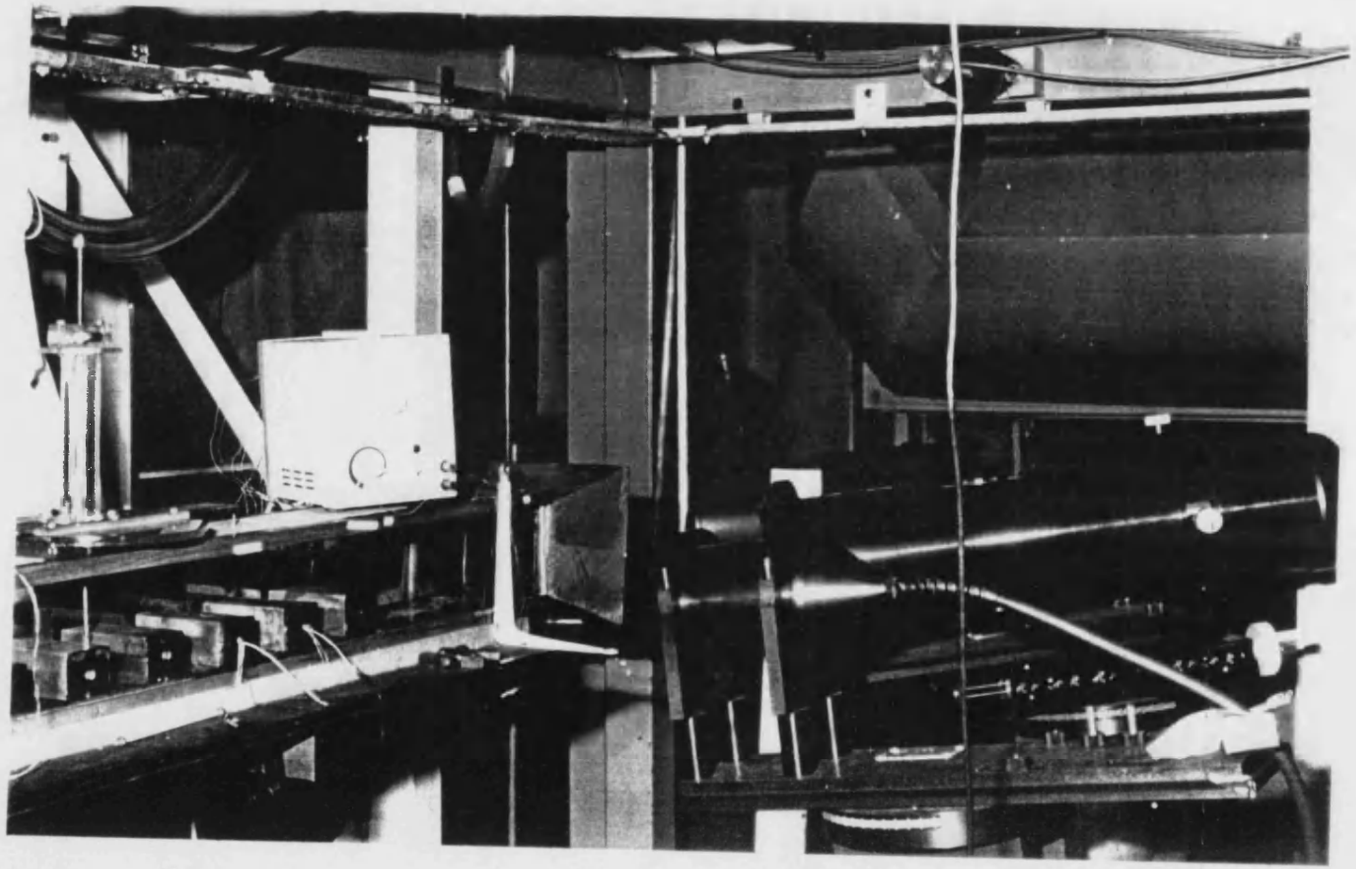

FIGURE 7.9: VIEW OF TEST SECTION TOGETHER WITH LASER TRANSMITTER AND RECEIVER

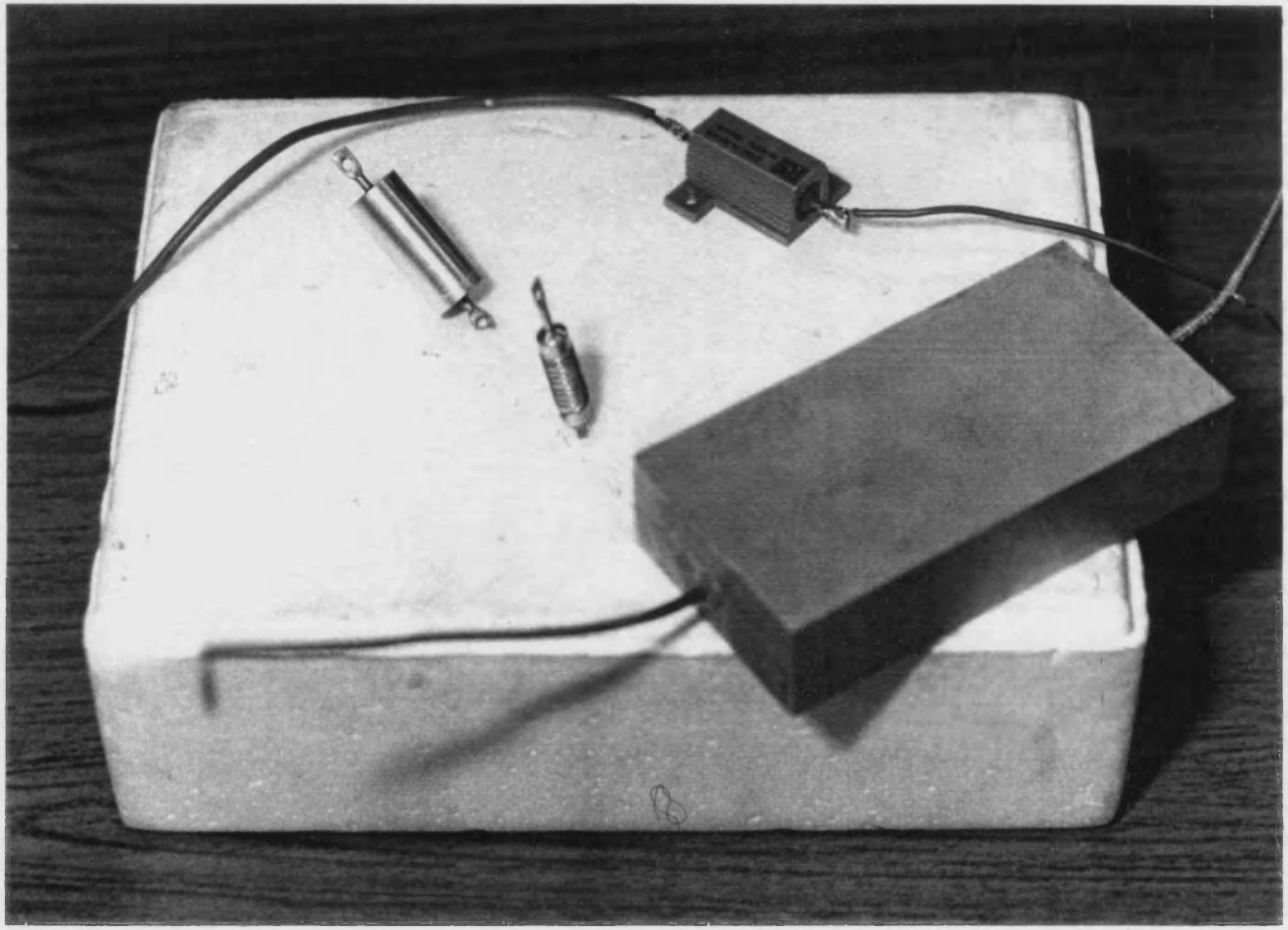

FIGURE 7.10: ALUMINIUM BLOCK USED TOGETHER WITH RESISTOR PACK BEFORE AND AFTER MACHINING

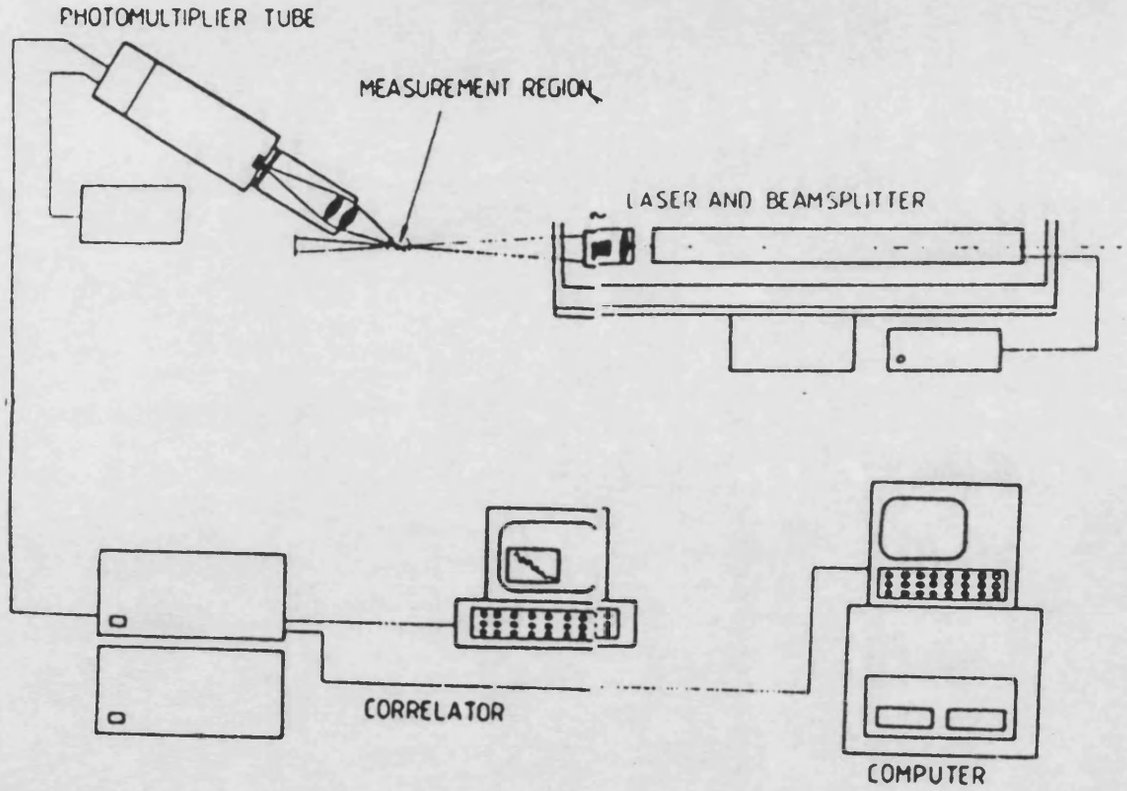

FIGURE 7.11: LASER ANEMOMETER SYSTEM FLOW MEASUREMENTS

FIGURE 7.12: DATA ACQUISITION SYSTEM FOR LDA

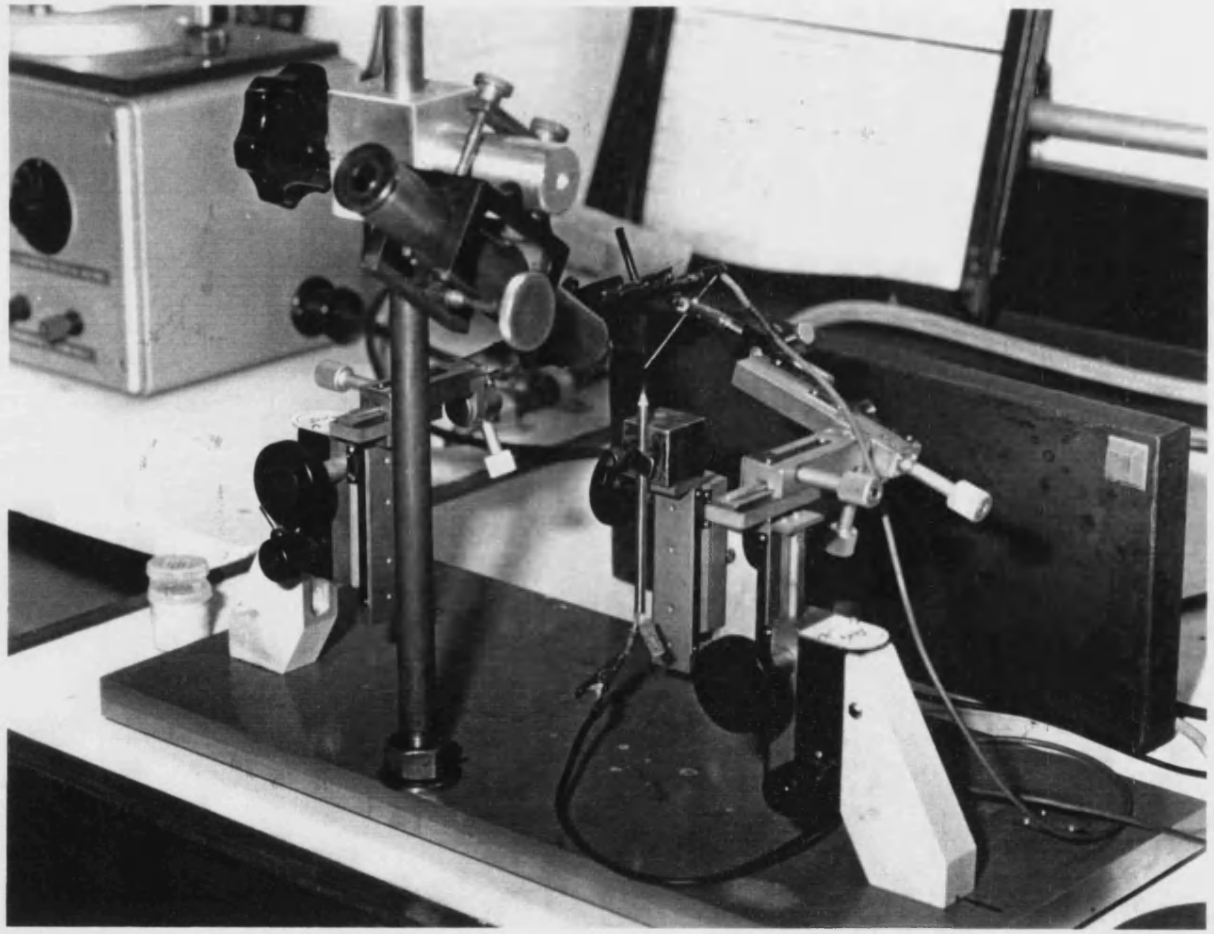

FIGURE 7.13: PURPOSED BUILT MANIPULATOR FOR HOT-WIRE WELDING

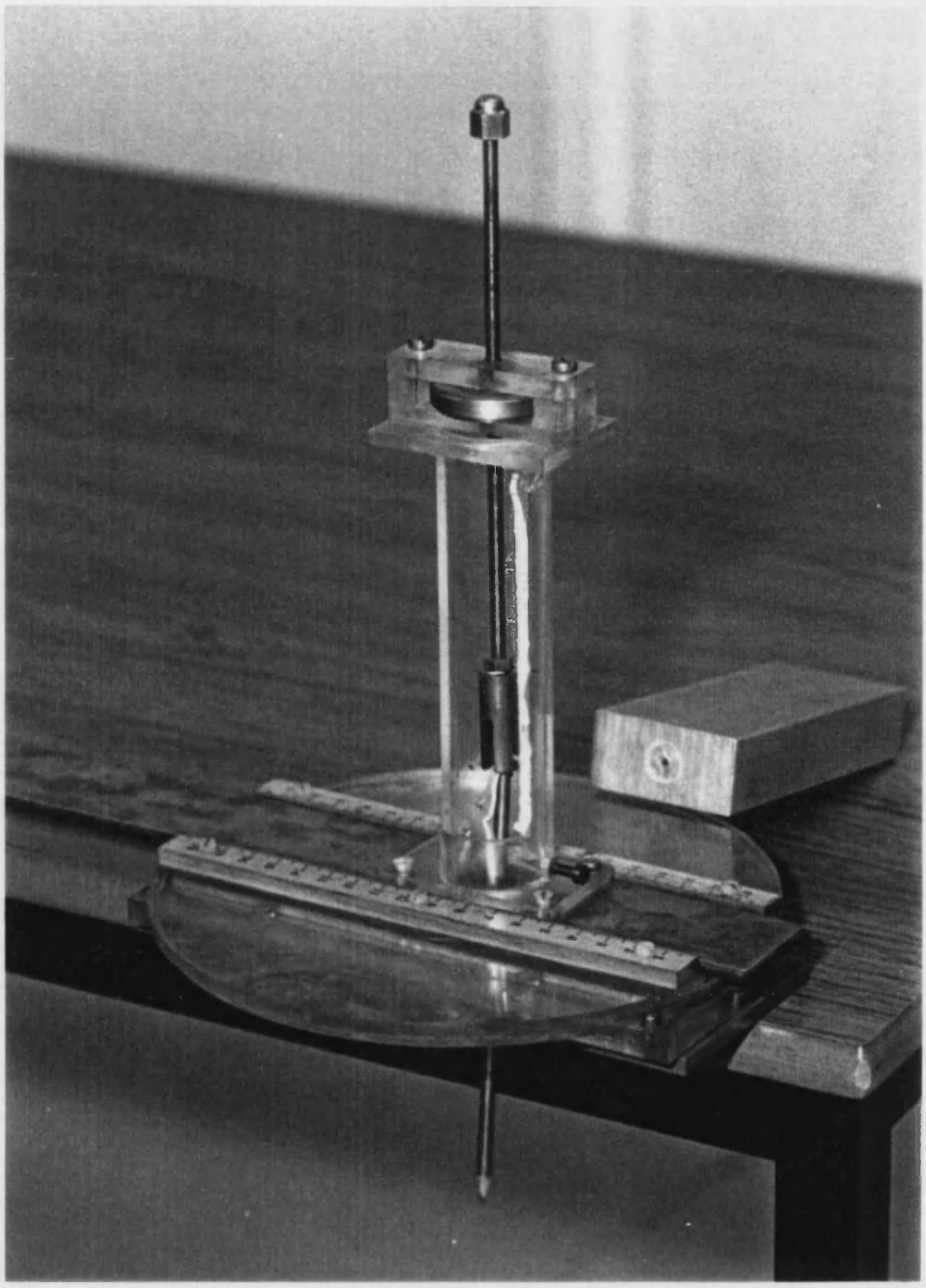

FIGURE 7.14: MANUAL GEAR FOR TRAVERSING THE HOT-WIRE PROBE

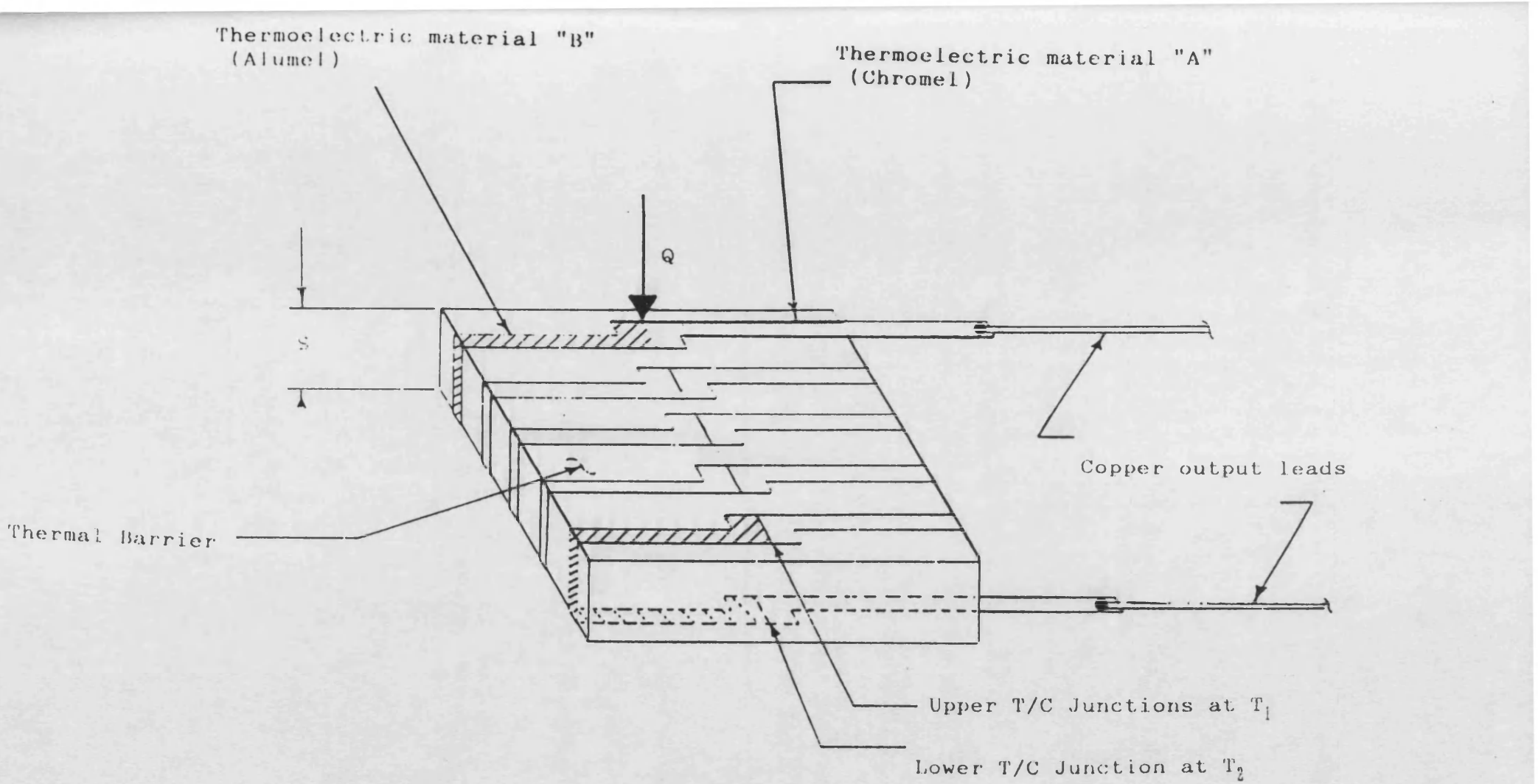

FIGURE 7.15: MICRO–FOIL HEAT FLOW SENSOR

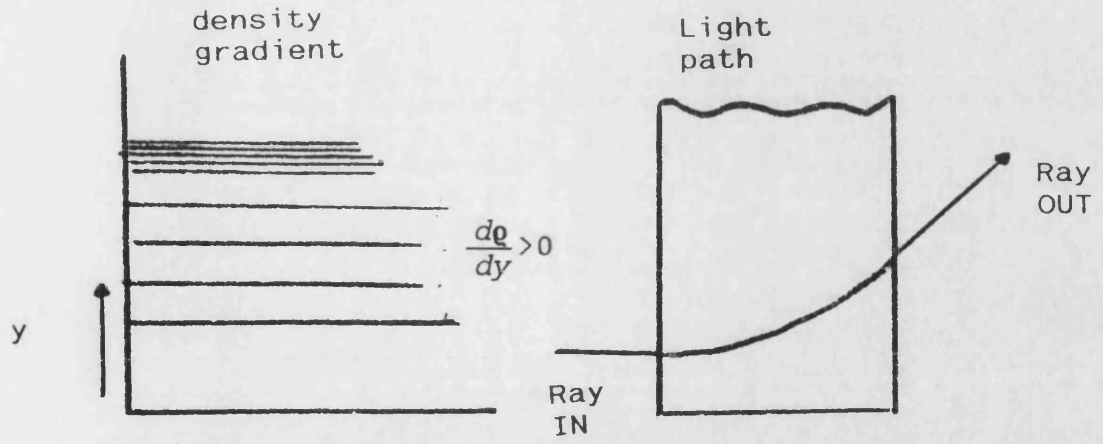

(a)

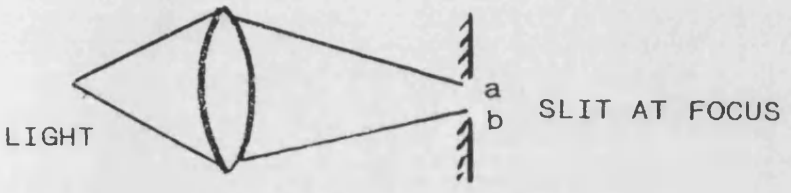

(b)

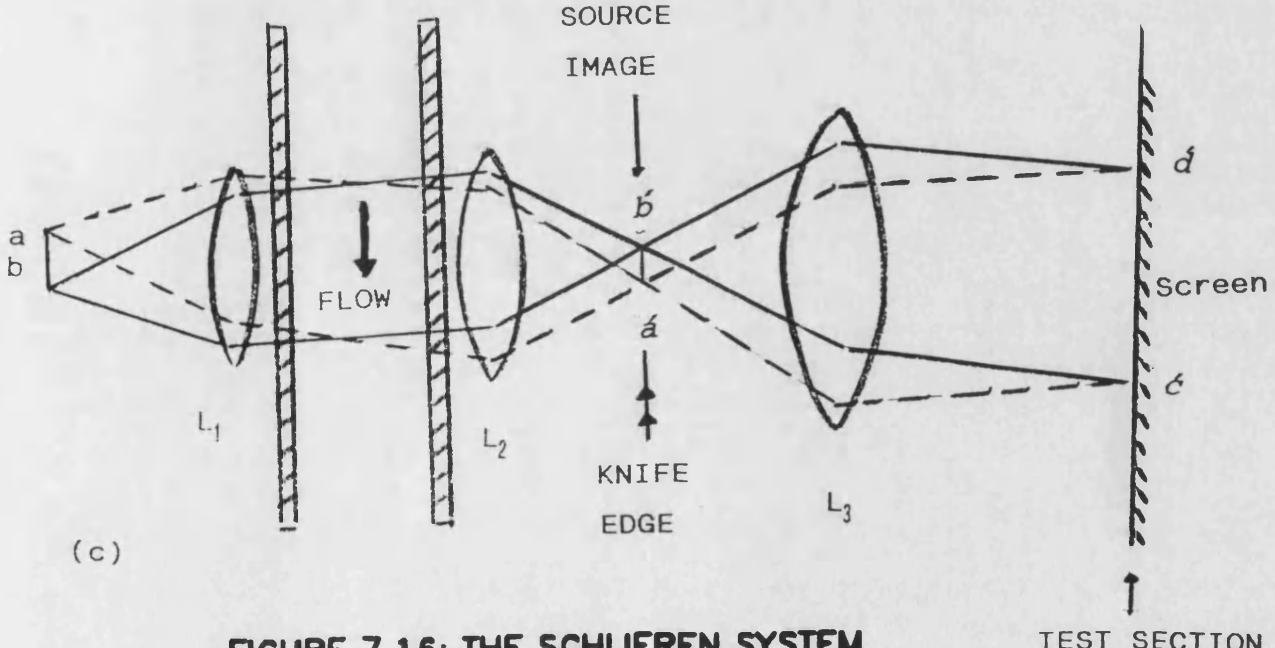

(c)

FIGURE 7.16: THE SCHLIEREN SYSTEM
(a) DENSITY GRADIENT
(b) LINE SOURCE
(c) SYSTEM SET UP

FIGURE 7.17: HAND SKETCH OF THERMAL BOUNDARY LAYER PRODUCED BY SCHLIEREN SUPERIMPOSED ON VELOCITY VECTORS PRODUCED BY LASER OVER SECOND BLOCK

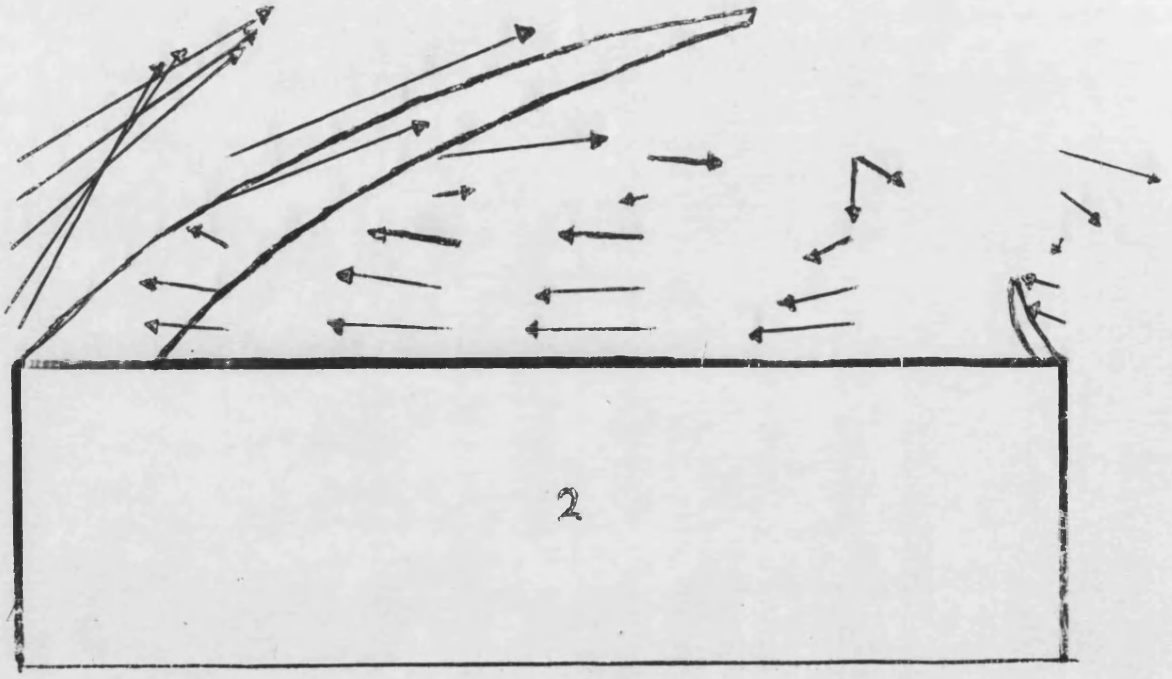

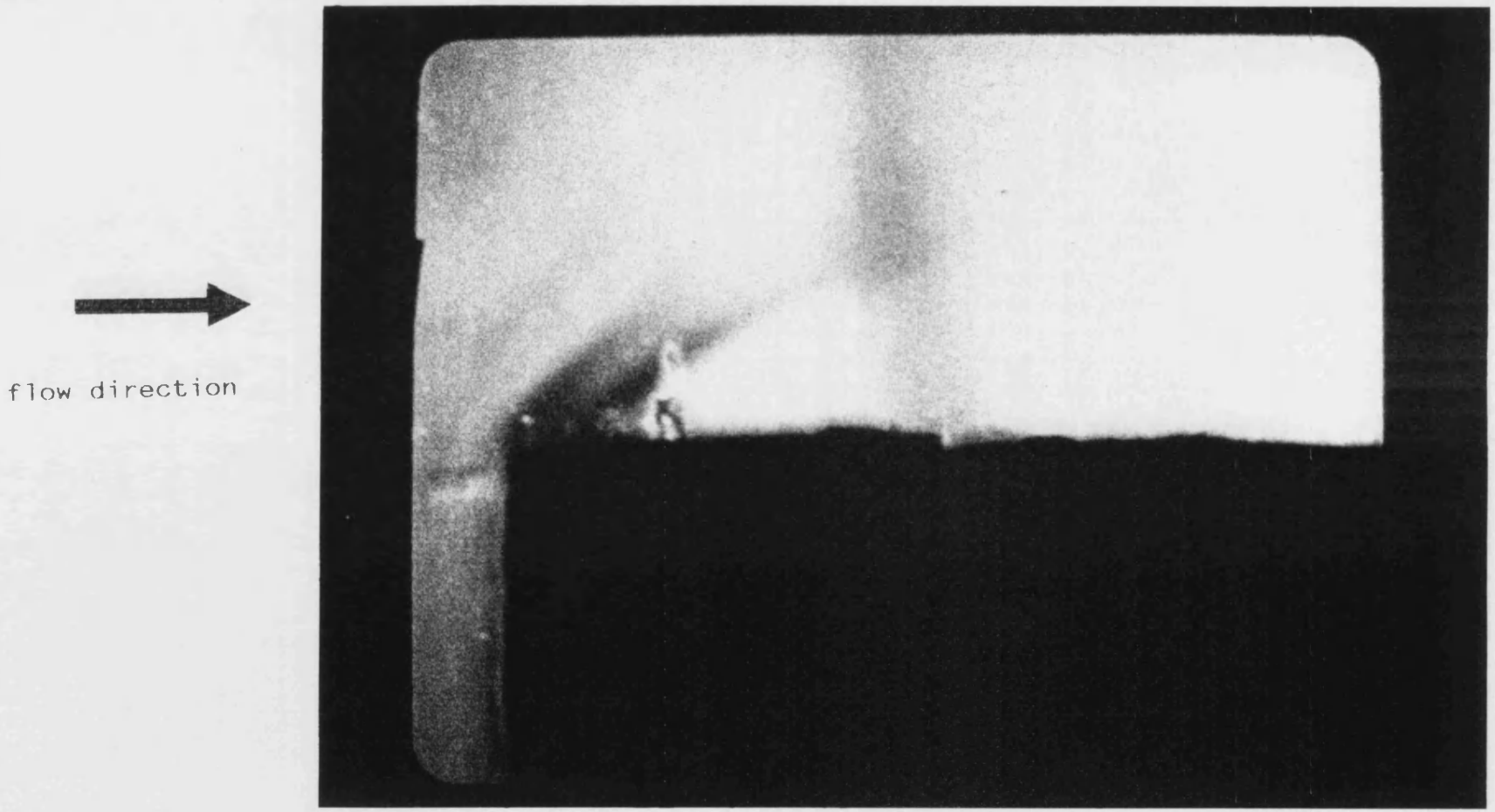

FIGURE 7.18: SCHLIEREN PHOTOGRAPH OF THE THERMAL BOUNDARY LAYER OVER THE SECOND BLOCK

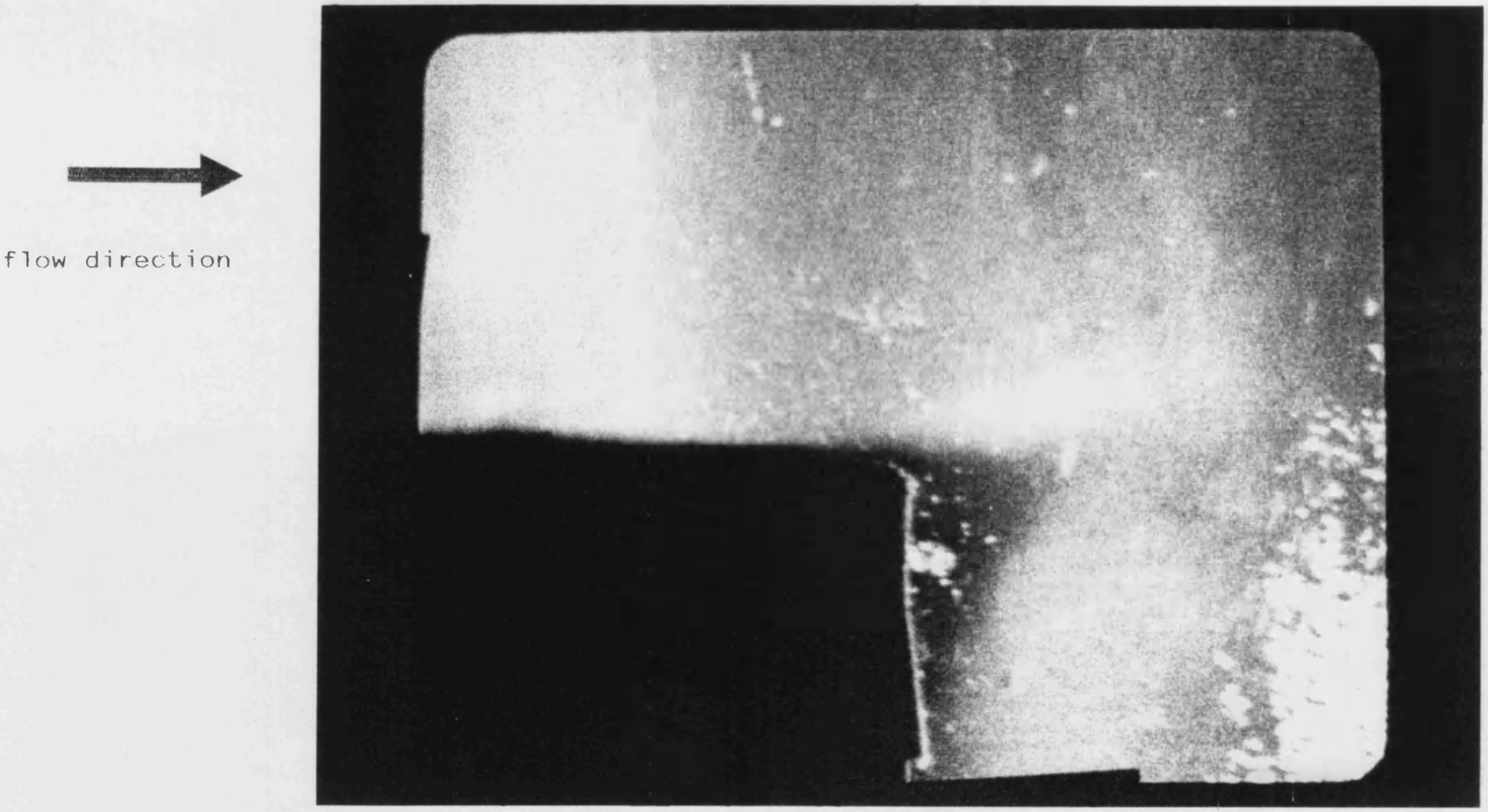

FIGURE 7.19: SCHLIEREN PHOTOGRAPH OF THE THERMAL PATH FROM TRAILING EDGE OF THE SECOND BLOCK

CHAPTER [8]

EXPERIMENTAL INVESTIGATION USING LASER DOPPLER ANEMOMETER

8.1 INTRODUCTION

The experimental investigations described in this Chapter are concerned almost entirely with Laser Doppler Anemometer (LDA) measurements carried out in the test duct. The LDA systems were described in Chapter (7), and the layout of the test rigs was given in the same Chapter. Because of practical considerations, the measurements of velocity profiles and turbulence levels were carried out in two stages.

In the first exploratory stage, the LDA system described in Chapter (7) was used, and the investigation was largely confined to the flow upstream of, and over, the first two elements. Also influenced by industrial practice, air velocities were low (0.7 and 1.24m/s). These LDA measurements broadly confirmed the CFD predictions, and revealed a number of interesting flow phenomena. However because of the limitations of that particular LDA system it proved difficult to obtain consistent measurements in the boundary layer close to the surface.

In the second stage of the investigation the more powerful LDA facility described in Chapter (7) was used. Opportunity

was also taken to increase the velocity of the approaching air (5-10m/s). With this second LDA system it proved possible both to increase the number of points in the measurement grid, and to obtain data in the shear layers extremely close to the solid surfaces.

Before describing these two LDA investigations, the early flow visualisation experiments using smoke, will be briefly described.

8.2 PRELIMINARY SMOKE FLOW VISUALISATION

The smoke tests were carried out at a low approach velocity of 1m/s because it was found that at higher velocities the smoke filaments diffused and the patterns were not clear. Photographs of smoke tests are presented in Figures (8.1) and (8.2). These clearly show an upstream eddy near the tunnel floor and separation on the top surface of the block at an angle of about 45°. There is an indication of a reverse flow on the top surface of the block. A recirculation zone behind the block can also be seen.
Comparison of the smoke visualisation results with graphical output from the CFD package, eg Figure (5.16), confirms the general accuracy of the theoretical predictions. However vector plots, such as Figure (5.16), not only allow flow visualisation, but are quantitative in that they allow the magnitude of the velocities (proportional to vector length) to be readily perceived. In

particular, the vectors show how the flow accelerates as it passes over the block, and reveal the small magnitude of the velocities in the recirculation zones.

8.3 LDA INVESTIGATION: STAGE I (LOW APPROACH VELOCITIES)

8.3.1 PRELIMINARY

The first part of this experimental investigation was taken up with becoming familiar with the LDA system. Also data were produced to reveal the nature of the flow, and the type of boundary layer behaviour to be expected. This was to confirm the suitability of the LDA system for our research program. The following sections are the descriptions of velocity profiles and turbulence intensity obtained by LDA at the low approach velocities of 0.688m/s and 1.24m/s.

The velocity profiles for the velocity of 0.668m/s are discussed in sections 8.3.3-8.3.5. As the profiles for the somewhat higher velocity of 1.24m/s were found to be rather similar, these are more briefly summarised in section 8.3.6.

8.3.2 FLOW APPROACHING FIRST BLOCK

Experimental and theoretical comparison of velocity profiles at various positions along the tunnel center-plane

for two inlet velocities are shown in Figure (8.3). Figure (8.3a) shows the velocity profiles upstream of the first block. This upstream velocity profile is typical of those for a flat plate boundary layer.

Close to the first block (50mm in front of first block) the flow approaching the body is deflected upwards by the build-up of pressure as the fluid impinges on the front face. The boundary layer is influenced by the adverse pressure gradient, which causes the velocities near the floor to be retarded. On the floor immediately in front of the first block the adverse pressure gradient acting on the slower moving fluid in the thin floor boundary layer produces a region of reverse flow. The small recirculating vortex can be seen in the flow visualisation photographs of Figures (8.1a) and (8.2a).

The quantitative agreement between the predicted and the measured flow field is good for these upstream regions, where the average discrepancy between measured and predicted values of mean velocity, for example, is less than 2%.

The acceleration of the flow as it passes over the block is accompanied by a drop in the static pressure the minimum value occurs near the tip, where the acceleration is greatest. Deceleration of the flow at the front face of the block, and its deflection around the top of the obstacle, is caused by a zone of high positive pressure, particularly near the centre of the face where the flow forms a

stagnation region.

The study by Reichardt [63] for two-dimensional turbulent flow past rectangular bluff bodies showed similar flow behaviour in front of the obstacle.

8.3.3 BOUNDARY LAYER DEVELOPMENT OVER FIRST BLOCK (FIG 8.3b)

Velocity profiles were compared over the first block at 30mm from leading edge of the block. There is a good agreement between the predicted and experimental measurements at this position over the block.

The separation region is shown by negative velocity near the block. This separation region is quite weak because of low approach velocity i.e., 0.688m/s.

These regions of complex separated flow show up in the second stage of LDA measurements at the higher approach velocity. They are fully discussed below.

8.3.4 CAVITY FLOW BETWEEN FIRST AND SECOND BLOCKS (FIG 8.3c)

Fluid flow and heat transfer in cavities is an important topic in contemporary heat transfer research. The flow on the top of the block, approaching the cavity between the two blocks has formed into a boundary layer.

A separated shear layer is formed across the open face of

the cavity which reattaches at the leading edge of the downstream block. Some of the fluid in the shear layer enters the reverse flow in the cavity while the remainder of the fluid reforms as a boundary layer on the downstream block. There is a dividing streamline which separates these two flows. This characteristic type of separated forced convection is frequently encountered in engineering applications. The experimental result confirm the theoretical prediction in the middle of the cavity between first and second blocks.

The theoretical predictions in Chapter (6) showed that the thermal conditions of the flow outside the cavity were little affected by the presence of the cavity. This appears to signify, for a cavity of fixed size, that the characteristic of the flow inside the cavity is insensitive to details of the flow outside it. However, the magnitude of the external velocity will obviously influence the level of the internal velocity. In these circumstances, the heat transfer in the cavity becomes a function of the geometry and the velocity of the approaching flow, but is independent of the thickness of the approaching boundary layer.

It might be expected that the size of the cavity would have an effect on heat transfer. The heat transfer coefficient tending to increase with increasing streamwise spacing, due to an increasing interaction between the cavity flow and the main wake flow. However, for the rather limited range of cavity sizes studied in Chapter (6), the predicted data

showed no increase in heat transfer coefficient.
The small deflection of the profiles inside the cavity between the two blocks indicates that there is a region of rather weak recirculation downstream of the first block. However the velocity recirculation is small, and the flow is almost stagnant in this region.

8.3.5 FLOW OVER SECOND BLOCK (FIG 8.3d)

The velocity profiles obtained over and downstream of the second block were found to be generally similar to those over the first. However, it can be seen that relative to the first block the boundary layer thickness has increased.

8.3.6 VELOCITY PROFILES - APPROACH VELOCITY 1.24M/S

To check consistency, all experiments carried out at the approach velocity of 0.688m/s were repeated at the somewhat higher approach velocity of 1.24m/s. The results were found to be quite similar. Again there is a good agreement between these measured and predicted values at different locations in the channel, Figures (8.3e, f, g and h).

8.3.7 U-COMPONENT OF TURBULENCE INTENSITY (FIG 8.4a-8.4b)

For each of the velocity profiles in the investigation discussed above, a corresponding profile of **U**-component turbulence intensity was also measured.
Once again results for an approach velocity of 1.24m/s were, generally, similar to those for a velocity of 0.688m/s. Because of this only the latter results will be shown and commented upon.

Far upstream from the first block where the boundary layer is developing the turbulence intensity is small.
The turbulence intensity is high near the bottom wall of the duct. Away from the wall, in the main stream the turbulence drops significantly. This is similar to the turbulence intensity over a flat plate. The turbulence intensity rises to a maximum in the region of adverse pressure gradient in front of the first block Figure (8.4a).

The turbulence intensity over the first block shown in Figure (8.4b), indicates a low level of turbulence. This is because of the limitations of the LDA system; measurement could only be made at some distance from the upper surface.

8.3.8 CONCLUDING REMARKS ON STAGE I OF THE LDA INVESTIGATION

The measured values of the recirculating velocities in the cavity were somewhat larger than those predicted. After consideration there appeared to be two possible causes of this discrepancy. First, the experiments had revealed that the LDA readings from the recirculating zone were susceptible to errors. To achieve acceptable accuracy, and repeatability, LDA measurements require good and consistent seeding. These requirements were difficult to achieve in the regions between the blocks. Secondly, at high turbulence intensities, and in regions where the space mean of the velocity approached zero, large variations (±10%) could occur in the velocities predicted from the turbulence model.

To overcome these difficulties, it was decided to carry out the remainder of the LDA investigation on a newer and more powerful LDA system, which possessed an improved type of seed generator. The decision was also made to carry out the investigation at higher approach velocities, in the range 5-10m/s.

8.4 LDA INVESTIGATION: STAGE II

8.4.1 FLOW APPROACHING THE FIRST BLOCK

Figure (8.5) shows the **u**-component of the mean velocity profile at three positions upstream of the first block, 10, 20 and 102mm respectively. As was expected, far upstream of the first block, the profile is typical of a flat plate boundary layer. As the flow approaches the first block the profile becomes distorted by the adverse pressure gradient in front of the block.

Very close to the front face of the block there is a small region of recirculation where the velocity becomes negative up to height of 5mm from the wall. The flow then accelerates up the front face of the block rapidly reaching the free stream velocity. This type of flow behaviour close to the front face of the first block confirms the theoretical predictions already described. For example in Chapter (5) Figure (5.9) shows that the velocity is negative close to the block, indicating a small region of recirculating of flow. This is also shown in the vector plot of Figure (5.16). There is a good agreement between prediction and experiment in these regions.

REYNOLDS SHEAR STRESSES

Figure (8.6) shows the Reynolds or turbulent shear stress for two positions upstream of the block. The turbulent shear stress at (**x/H**=-0.1) has a positive maximum value of

0.4 $(m/s)^2$ near the wall, which indicates that the flow is recirculating and travelling away from the wall. Towards the main stream, the shear stress approaches zero. For the case of (**x/H**=-0.2), the shear stress has a negative maximum value of -0.3 $(m/s)^2$ near the wall indicating flow towards the block in the region just upstream of the recirculation zone. Once again the shear stress falls to zero away from the wall, and approaching the main stream.

8.4.2 VELOCITY PROFILES AND TURBULENCE -BLOCKS 1,2,3 AND 5

VELOCITY PROFILES

Figure (8.7) shows the dimensionless velocity profiles over four of the blocks. The measurements were taken at a streamwise location of 40mm from leading edge of each block. With this second LDA system it was now possible to make measurements in the shear layer very much closer to the wall than previously. From Figure (8.7) it can be seen that except for block 1 the profiles are quite similar. The reason for the difference between the velocity profile over the first block and the other profiles is because of flow separation at this block. This is accompanied by a region of strong recirculation close to the upper surface of the first block.

Downstream of block 3, the velocity profiles become fully developed, and are so similar as to make further measurements unnecessary. Because of this, downstream

velocity profiles were measured only on block 3 and 5 Figure (8.7).

It should be noted that predictions from the CFD package confirm these results. Figure (5.14) shows that the velocity profile over the first block is negative near the wall, indicating separation of the flow. Also the vector plot, Figure (5.16), clearly indicates a region of recirculation over the first block. Figure (5.14) also shows that the velocity profiles over the second and third block are almost identical. That the velocity profiles become fully developed after block 3 is clearly shown in Figure (5.15).

TURBULENCE INTENSITY

Figure (8.8) shows the **U**-component of turbulence intensity corresponding to the above velocity profiles. The Figure shows a decrease in turbulence with downstream position. It can also be seen that the highest value of turbulence intensity was measured near the wall of the first block, where the flow changes sign.

VELOCITY PROFILES CLOSE TO THE WALL

Figure (8.9) shows the mean velocity profiles measured very close to the surface of the blocks. It shows that in this near wall region the velocity gradient is large up to a height of 1mm above the wall. In this region velocity fluctuations are relatively small and the stress is dominated by viscous effects. The region is sometimes

referred to as the viscous sub-layer or the laminar sub-layer. Away from the wall, the turbulence intensity is high and turbulent shear stress has the most of effect on the velocity profiles.

Figure (8.9) also shows that after the third block the velocity profiles approach their fully developed form.

8.4.3 MORE DETAILED MEASUREMENTS OVER BLOCK 2 AND 3

(All measurements were recorded at a position 40mm from the leading edge of the block)

NON-DIMENSIONAL VELOCITY PROFILES

The non-dimensional variation of the mean velocity **u(y)** is plotted in Figure (8.10). It is seen to be a typical turbulent velocity profile with a steep increase near the wall and a fairly uniform velocity near the centre. The velocity at the edge of the boundary layer is U_e = 8.0m/s.

TURBULENT SHEAR STRESS

Figure (8.11) shows the turbulent shear stress corresponding to velocity profiles above. As it is expected, at the wall the shear stress is zero, and further from the wall the turbulent shear stress exhibits its maximum at value of 0.7 $(m/s)^2$ at **(y/H=0.25)**. The shear stress and its effect falls to zero at the edge of the boundary layer.

TURBULENCE COMPONENTS

The root-mean-square values of the longitudinal and transverse components of turbulence over block 2 are shown in Figure (8.12). The transverse fluctuation does not vary greatly over the second block at the given position and its average value is about 6 percent that of U_e, but the longitudinal turbulent component exhibits a pronounced maximum of $0.18U_e$ very close to the wall. It is clearly seen from the diagram that both turbulent components decrease to zero at the wall. Figure (8.13) shows similar turbulence measurements over block 3. It can be seen that the root-mean square profiles of the **u** and **v** components are quite similar to those recorded on the second block.

REYNOLDS STRESS

Figure (8.14) shows a plot of the mean value of the product **(-uv)**, which is proportional to the turbulent shearing stress. The value of **(-uv)** falls to zero in the centre of the main stream, for reasons of symmetry. The maximum stress occurs near the wall showing that turbulent friction has its largest value there, and that in this region almost all of the shearing stress is due to turbulence. At the wall, the curve of **(-uv)** decreases to zero, confirming that turbulence dies out near the wall.

CORRELATION COEFFICIENT

For any two points within a turbulent eddy, there may be some correlation between the turbulent velocity components

measured at those points. The correlation coefficient is defined as:-

$$\Psi = \frac{\overline{u'v'}}{\sqrt{\overline{u'^2}} . \sqrt{\overline{v'^2}}} \qquad (8.1)$$

The existence of an apparent shearing stress due to velocity fluctuations always implies a correlation between the turbulent velocity components in two different directions.

Figure (8.15) shows values of the correlation coefficient, Ψ, between the longitudinal and transverse fluctuation at the same relative position over the second and third blocks respectively.

Reichardt [63] carried out measurements in a wind tunnel with a rectangular test section. His profiles of mean velocity and also of fluctuating components are very similar to those produced by the present work. Reichardt's correlation coefficient was -0.45.

ROOT-MEAN-SQUARE FLUCTUATIONS

Typical distributions of root-mean-square components in the turbulent boundary layer over the second block are shown in Figure (8.16). These profiles are similar to those of a flat plate in that they have a maximum value near the wall and fall to zero with increasing distance from the wall. The profiles of the temporal mean of the velocity, **u**, exhibits a shape which is similar to those in a channel or on a flat plate. The variation of the longitudinal

fluctuation, with its pronounced maximum in close proximity of the wall, and the variation of the transverse oscillation closely resemble those obtained in channel and flat plate flows.

Figure (8.17) shows the corresponding set of data for block three which can be seen to be quite similar to that of block two. It may reasonably be assumed that the profiles over other blocks further downstream would also be similar, and that after block three the flow becomes fully developed.

8.5 THE EVALUATION OF FRICTION FACTOR FROM EXPERIMENTAL VELOCITY PROFILES

To specify the flow in the 'wall-region' a velocity scale characteristic of that region is required. This is based on τ_w, the limiting value of the shear stress at the wall, which has the dimensions of density*(velocity)^2. Hence we define $u_\tau=(\tau_w/\rho)^{1/2}$ as our velocity scale. The value of the friction velocity, u_τ, depends on the flow as a whole, but once it is specified, the structure of the flow in the wall region is specified. It has been confirmed experimentally that the turbulence intensity distributions can be scaled on u_τ. For example, the maximum value of u^2 is always about $8u_\tau^2$, Schlichting [66].

Conditions in the wall region are now specified by the

three parameters: the friction velocity u_τ, the distance from the wall **y**, and the kinematic viscosity υ. The velocity profile expressed in dimensionless form as the logarithmic "Law of the Wall", equation (3.37) Chapter (3).

Immediately close to the wall there is the so called viscous sub-layer in which the turbulent fluctuations are relatively small and the dominant shear stress is the viscous one. In this layer the mean velocity is linearly dependent on **y**, and the shear stress is usually assumed constant and equal to its value at the wall.
Equation (3.37) in this region reduces to

$$\frac{u}{u_\tau} = \frac{\tau_w y}{(\mu u_\tau)} = \frac{y u_\tau}{\nu} = y^+ \qquad (8.2)$$

where y^+ denotes yu_τ/υ.

Figure (8.18) shows the typical distribution of u/u_τ versus log y^+. The logarithmic relation holds between a value of y^+ of about 30 and a value in the range of 100 to 1000 depending on the Reynolds number and the external pressure distribution. The range increases with increase of Reynolds number and decreases with increasingly adverse (positive) pressure gradients. Equation 8.3 holds for values of y^+ less than about 30.
Rearranging Equation 8.2 in terms of u/u_e, it follows that

$$\frac{u}{u_e} = \frac{u_\tau}{Ku_e}\ln\left(\frac{y}{\nu}\right) + \frac{u_\tau}{Ku_e}\ln u_\tau + \frac{u_\tau A}{u_e}$$

$$+\frac{u_\tau}{Ku_e}\ln(u_e) - \frac{u_\tau}{Ku_e}\ln(u_e) \qquad \textbf{(8.3)}$$

$$\frac{u}{u_e} = \frac{u_\tau}{Ku_e}\ln\left(\frac{yu_e}{\nu}\right) - \frac{u_\tau}{Ku_e}\ln\left(\frac{u_e}{u_\tau}\right) + \frac{u_\tau A}{u_e} \qquad \textbf{(8.4)}$$

now

$$f = \frac{2\tau_w}{\rho u_e^2} = 2\left(\frac{u_\tau}{u_e}\right)^2 \quad , \quad \sqrt{\frac{f}{2}} = \frac{u_\tau}{u_e}$$

substituting for **f** in Equation (8.4),

$$\frac{u}{u_e} = \frac{\sqrt{f/2}}{k}\ln\left(\frac{u_e y}{\nu}\right) + \sqrt{f}/2\left(A + \frac{1}{k}\ln(\sqrt{f}/2)\right) \qquad \textbf{(8.5)}$$

where **k** and **A** are known constants and $\mathbf{U_e}$ is the velocity at the edge of the boundary layer.

Based on equation (8.5) a chart can be prepared on which is plotted a family of curves of $\mathbf{u/u_e}$ against $\mathbf{\ln(u_e y/\upsilon)}$ for different specified values of $\mathbf{C_f}$, the skin friction factor. A measured velocity profile expressed in the coordinates $\mathbf{u/u_e}$ and $\mathbf{u_e y/\upsilon}$, can now be interpolated onto this chart so that slopes match in the log region. The curve on the chart

whose slope best fits the measured data yields the required value of the friction coefficient **f**. This method of determining C_f is referred to as the Clauser plot method, see Clauser [64].

Figure (8.19) show the Clauser plots for the second, third, forth and fifth blocks respectively. Experimental data were calculated for arbitrarily selected skin friction coefficients and superimposed on the chart. The skin friction coefficient has a value of C_f=0.004 over the second block which agrees with the theoretical predictions.

The skin friction coefficient obtained for the third, forth, and fifth blocks all have roughly the same value of 0.008, which again is in agreement with the theoretical predictions for these blocks.

8.6 CONCLUSIONS

The experimental study described in this Chapter has provided qualitative and quantitative information about the flow around the blocks in a nominally-uniform free stream. Flow visualisation measurements formed part of the investigation, but the major contribution was a comprehensive set of LDA measurements of velocity and turbulence levels of the flow through the test duct.

Observation of the flow obtained by smoke and surface flow visualisation was useful in establishing flow symmetry and qualitative characteristics of the flow. These techniques

revealed an upstream separation zone with eddy dimension about 0.05**H** in the **y** direction. A separation zone on the top surface of about 0.1**H** maximum depth was also shown, as well as regions of reverse flow in between the blocks. The visualisation techniques were helpful in the interpretation of velocity measurements and revealed flow characteristics in regions that were not accessible to the instrument used for velocity measurements.

Velocity measurements in the boundary layer which formed upstream of the first block, showed that the boundary layer thickness on the floor at the position of the block was thin relative to the block height. The boundary layer was approximately two-dimensional apart from close to the tunnel side walls. Except for this thin floor boundary layer, the upstream flow had a uniform velocity distribution.

The flow-field measurements provided a more complete description of the mean velocity distribution around the blocks than in any previously published study.
Some of the most interesting results shown by the velocity components were the strong vertical deflection of the flow near the front face of the block, and the recovery of the flow downstream after the severe distortion imposed by the block. These results were also of great value in assessing predictions of the flow.

The variation of the mean velocity over the second block is seen to be a typical turbulent velocity profile with a steep increase near the wall and a fairly uniform velocity near the centre.

The root-mean-square values of the longitudinal and transverse components are presented, where the transverse fluctuation does not vary greatly over the second block, but the longitudinal turbulent component exhibits a pronounced steep maximum very close to the wall. It is also shown that both turbulent components decreases to zero at the wall. The above statements are also true for the third block.

It is shown that the turbulent shearing stress over the second and third block falls towards zero in the centre of the channel, whereas its maximum occurs near the wall, where the turbulent friction is largest.

A Clauser plot was produced from the experimental data over each block, which showed that the friction coefficient has a value of 0.004 over second block and a constant value of 0.008 over the rest of the blocks.

The above experimental work was compared with the theoretical predictions and in most regions a good agreement was achieved.

FIGURE 8.1: SMOKE TEST FOR LOW APPROACH VELOCITY

a) UPSTREAM OF FIRST BLOCK

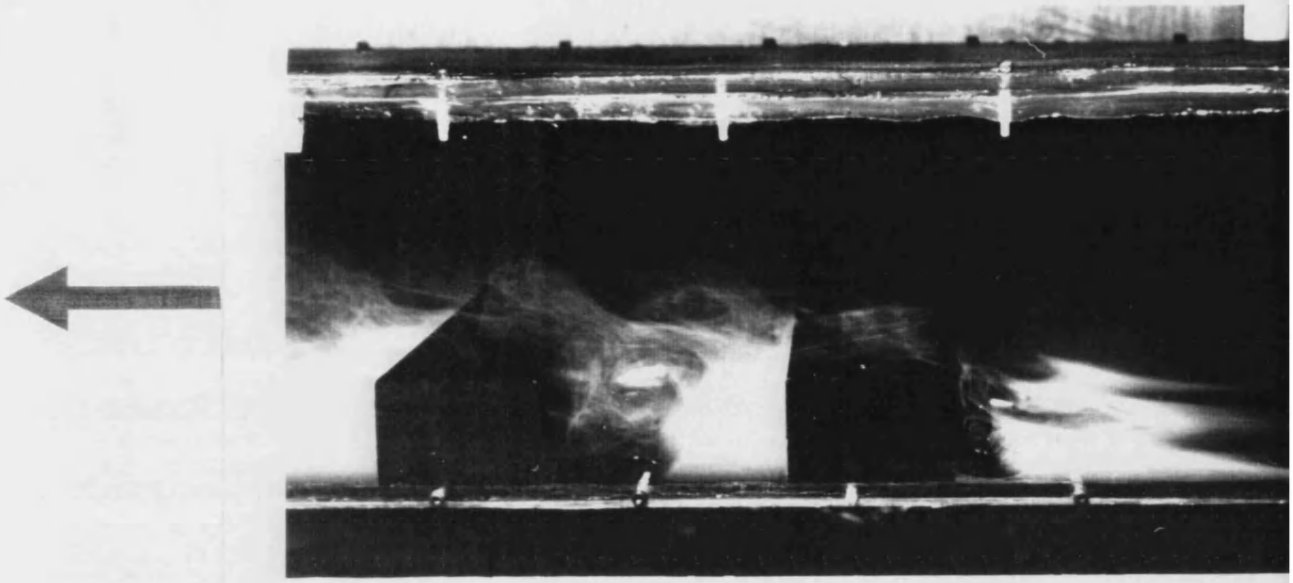

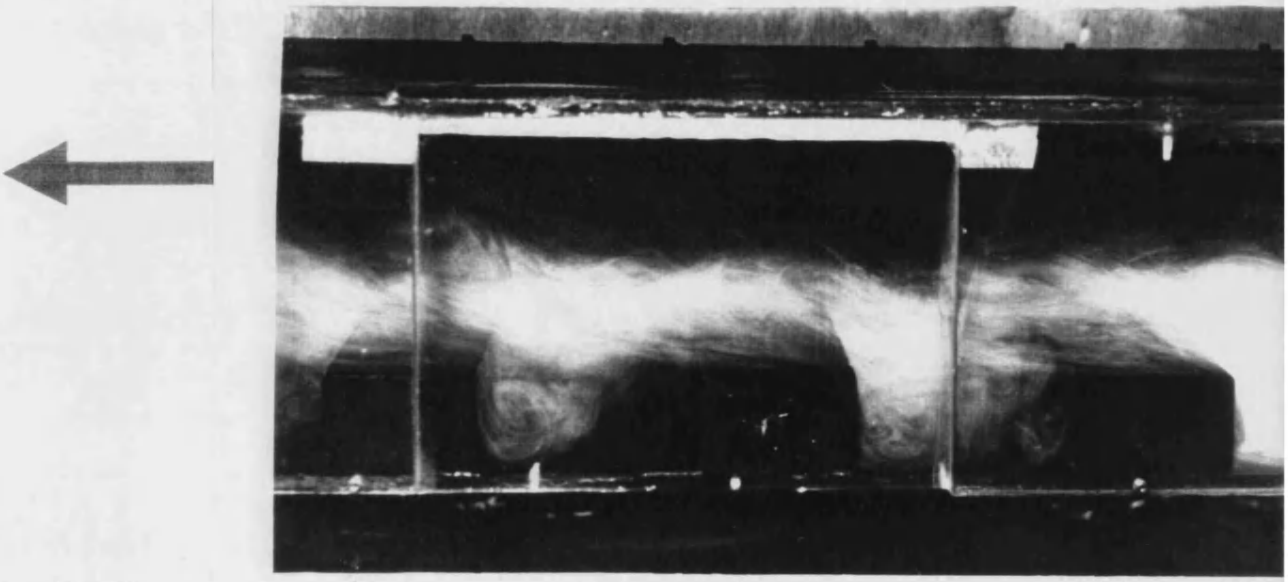

b) OVER FIRST THREE BLOCKS

FIGURE 8.2: SMOKE VISUALISATION OF FLOW

a) UPSTREAM OF OBSTACLE

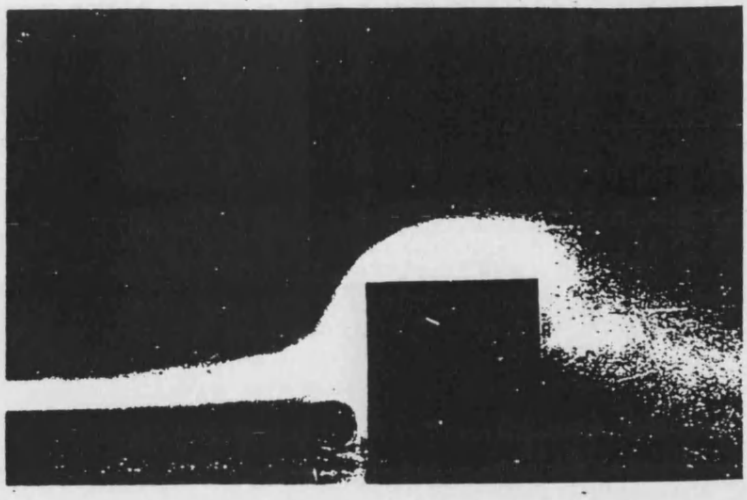

b) SIDE VIEW

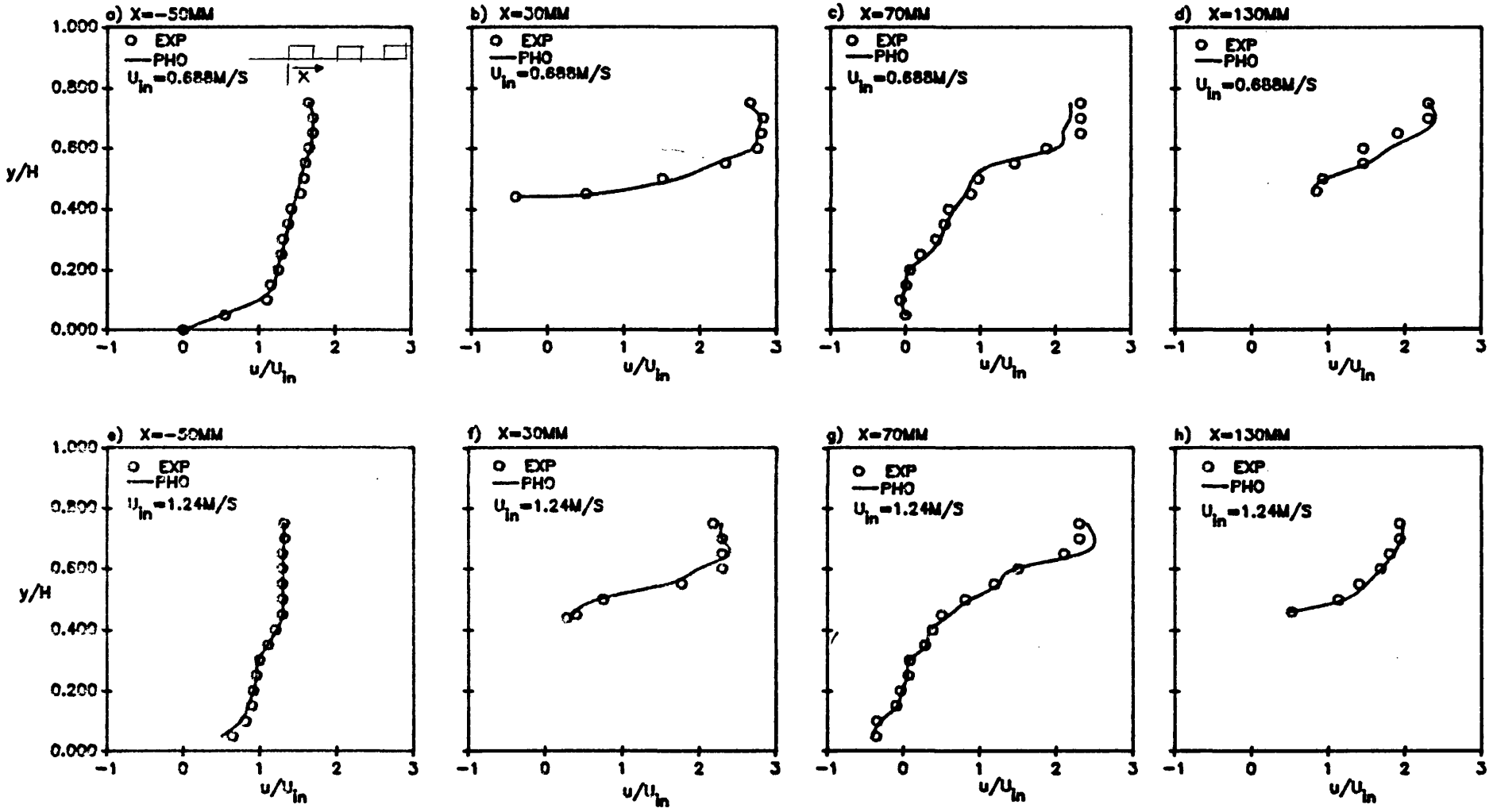

FIGURE 8.3: EXPERIMENTAL AND THEORETICAL COMPARISON OF U-VELOCITY PROFILES

FIGURE 8.4: U-COMPONENT OF TURBULENCE INTENSITY
Uin=0.688M/S

a) UPSTREAM OF THE FIRST BLOCK

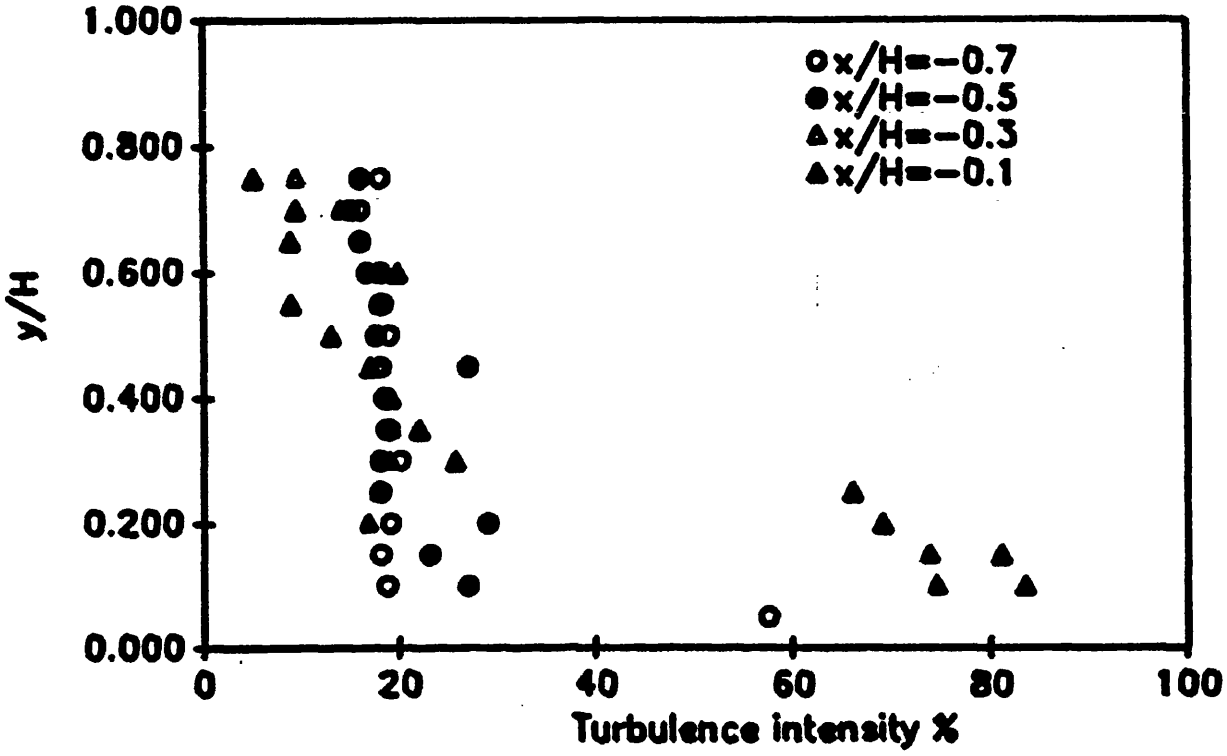

b) OVER THE FIRST BLOCK

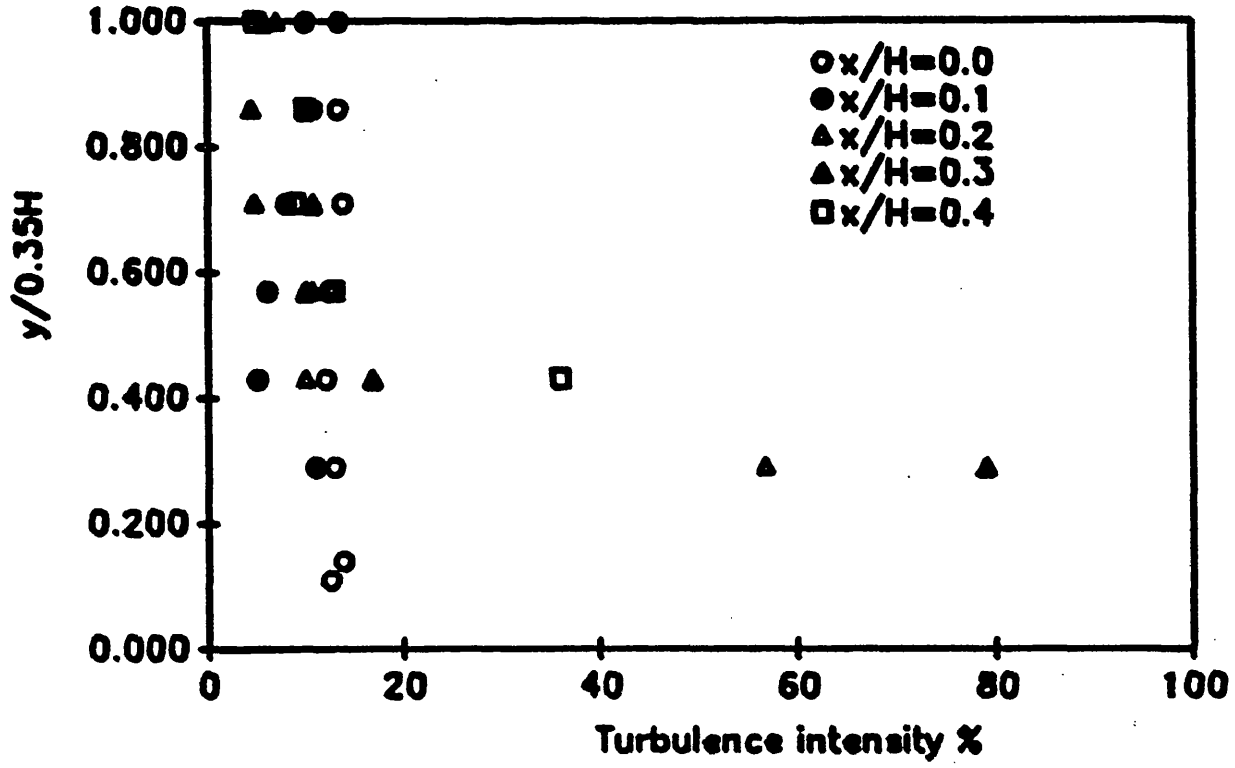

FIGURE 8.5:; U-COMPONENT VELOCITY PROFILE
UPSTREAM OF THE FIRST BLOCK

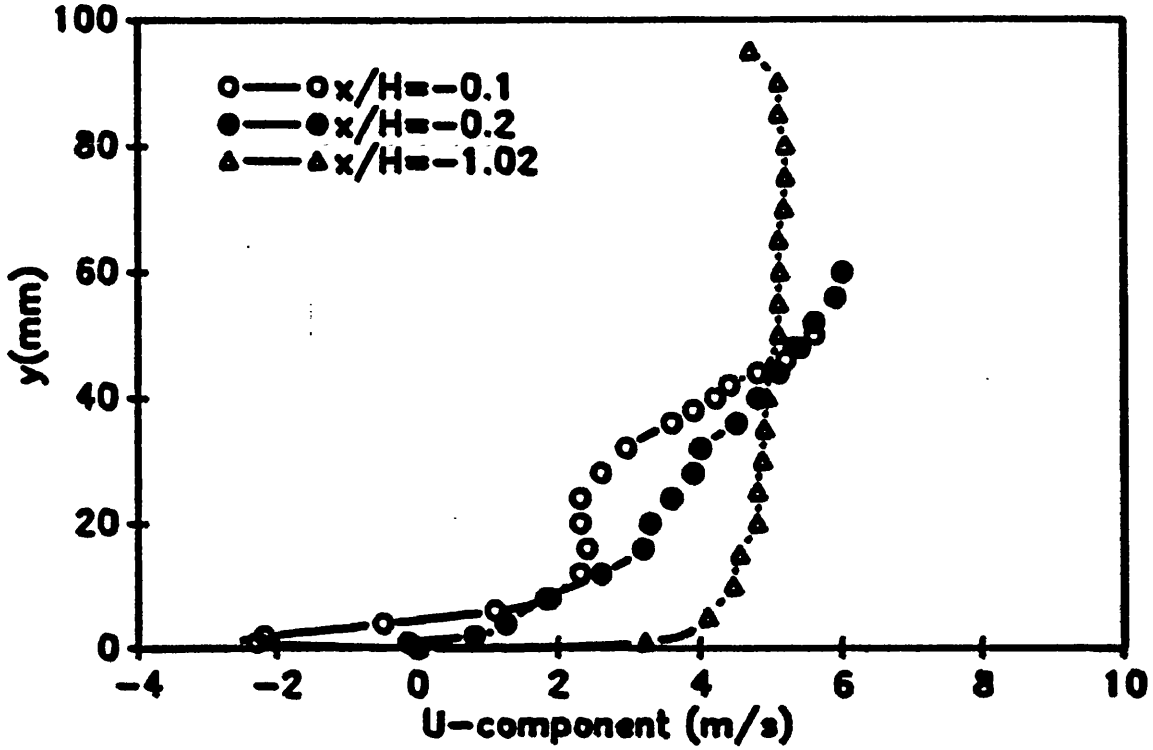

FIGURE 8.6: REYNOLDS SHEAR STRESS
UPSTREAM OF THE FIRST BLOCK

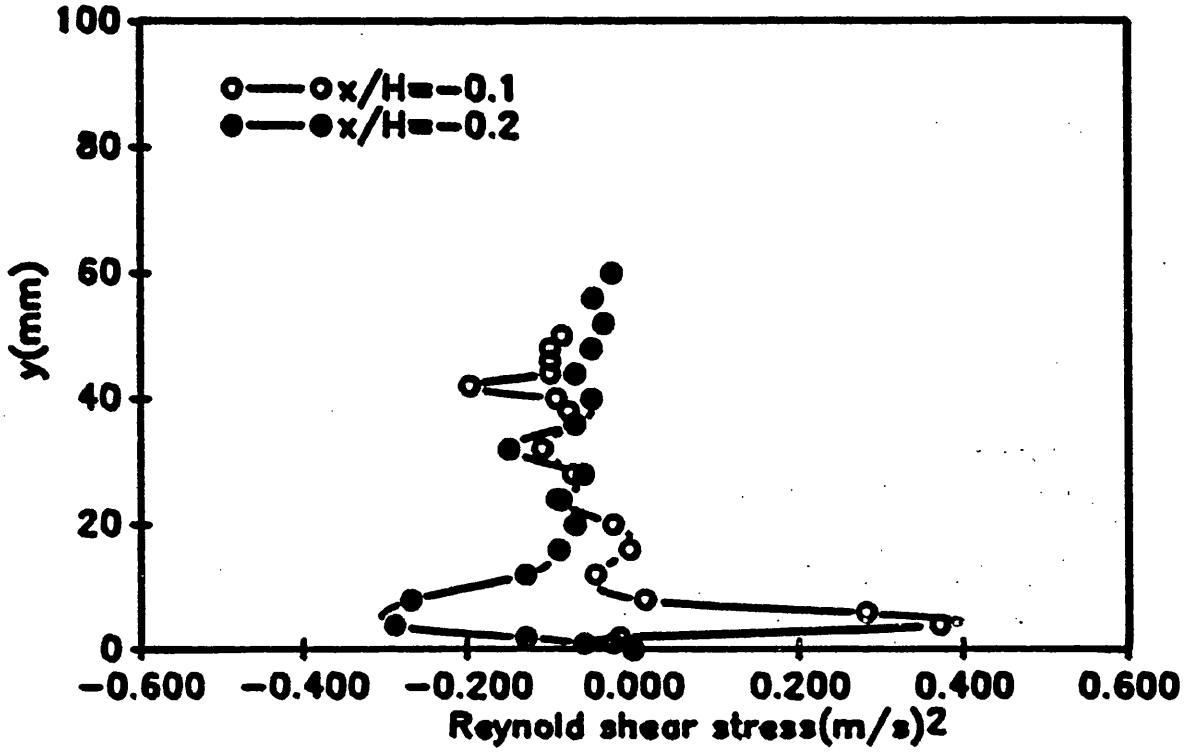

FIGURE 8.7: DIMENSIONLESS VELOCITY PROFILES TAKEN AT 40MM DOWNSTREAM FROM LEADING EDGE OF EACH BLOCK

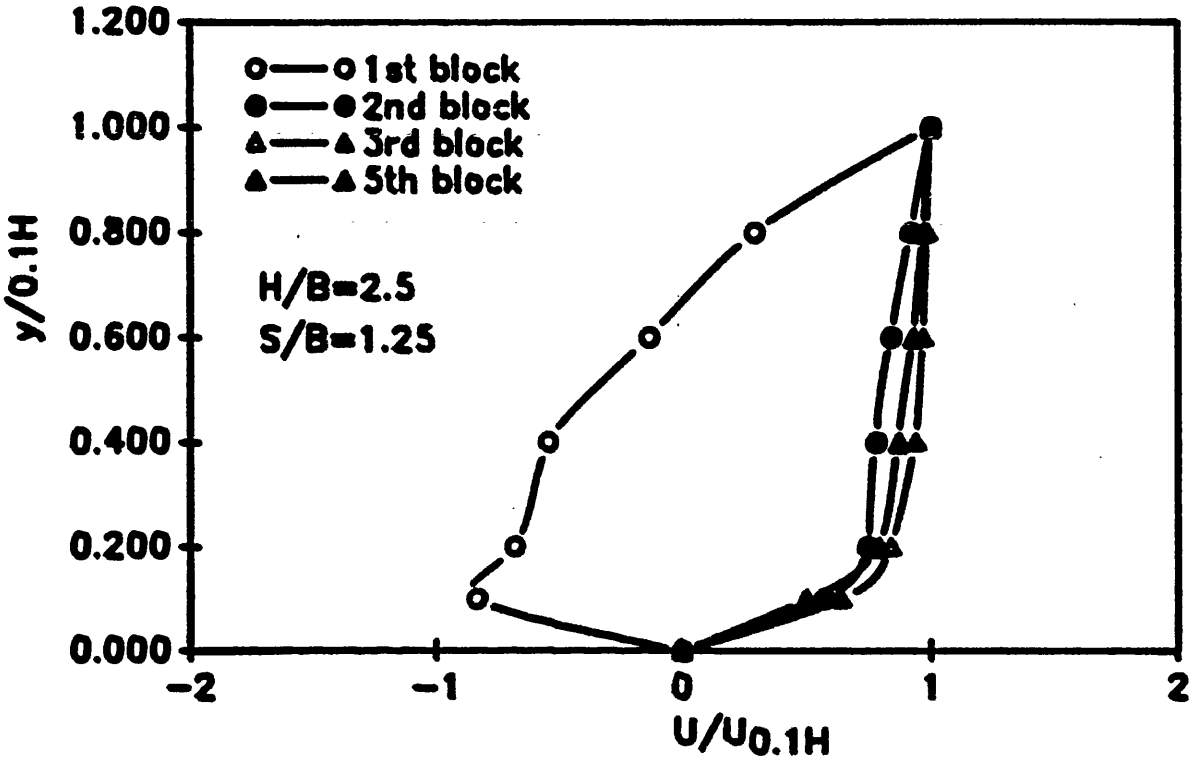

FIGURE 8.8: U-COMPONENT OF TURBULENCE INTENSITY TAKEN AT 40MM DOWNSTREAM FROM LEADING EDGE OF EACH BLOCK

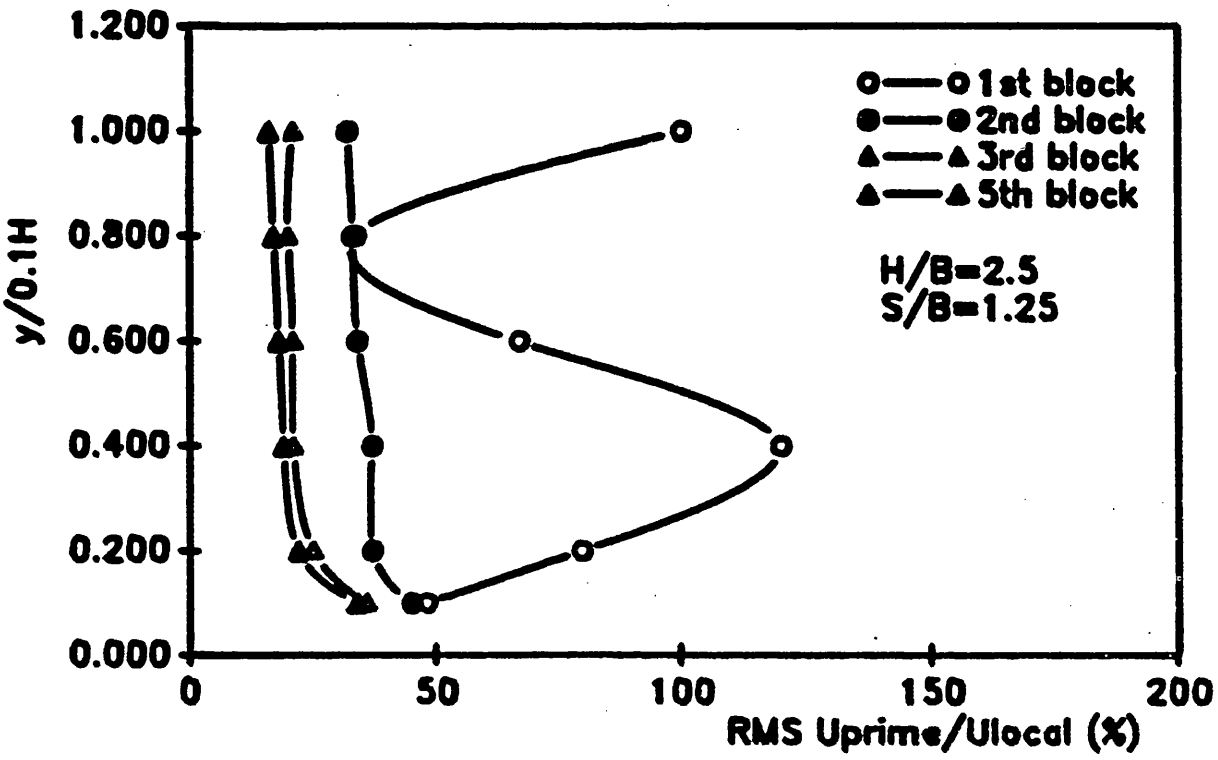

FIGURE 8.9: **MEAN VELOCITY PROFILE OVER THREE BLOCKS**

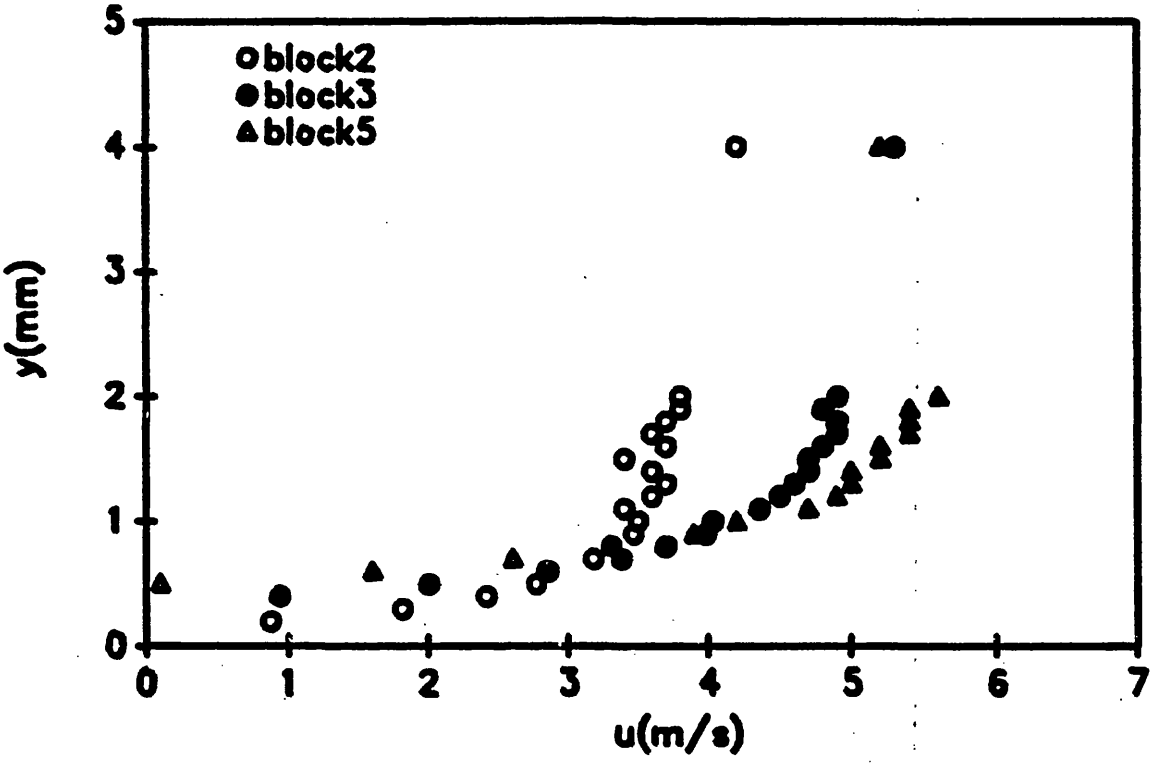

FIGURE 8.10: MEASUREMENT OF MEAN VELOCITY PROFILE u OVER SECOND AND THIRD BLOCK TAKEN AT 40MM FROM LEADING EDGE OF EACH BLOCK

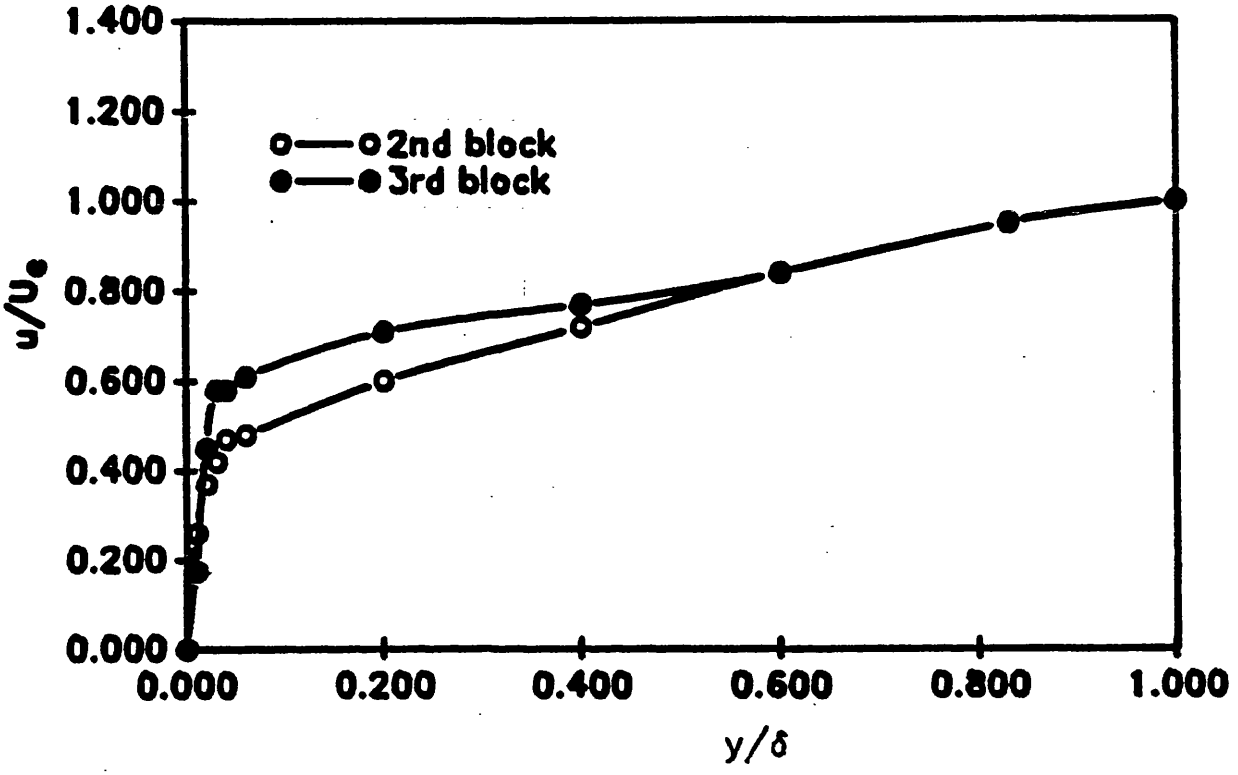

FIGURE 8.11: REYNOLDS SHEAR STRESS OVER SECOND AND THIRD BLOCK TAKEN AT 40MM FROM LEADING EDGE OF EACH BLOCK

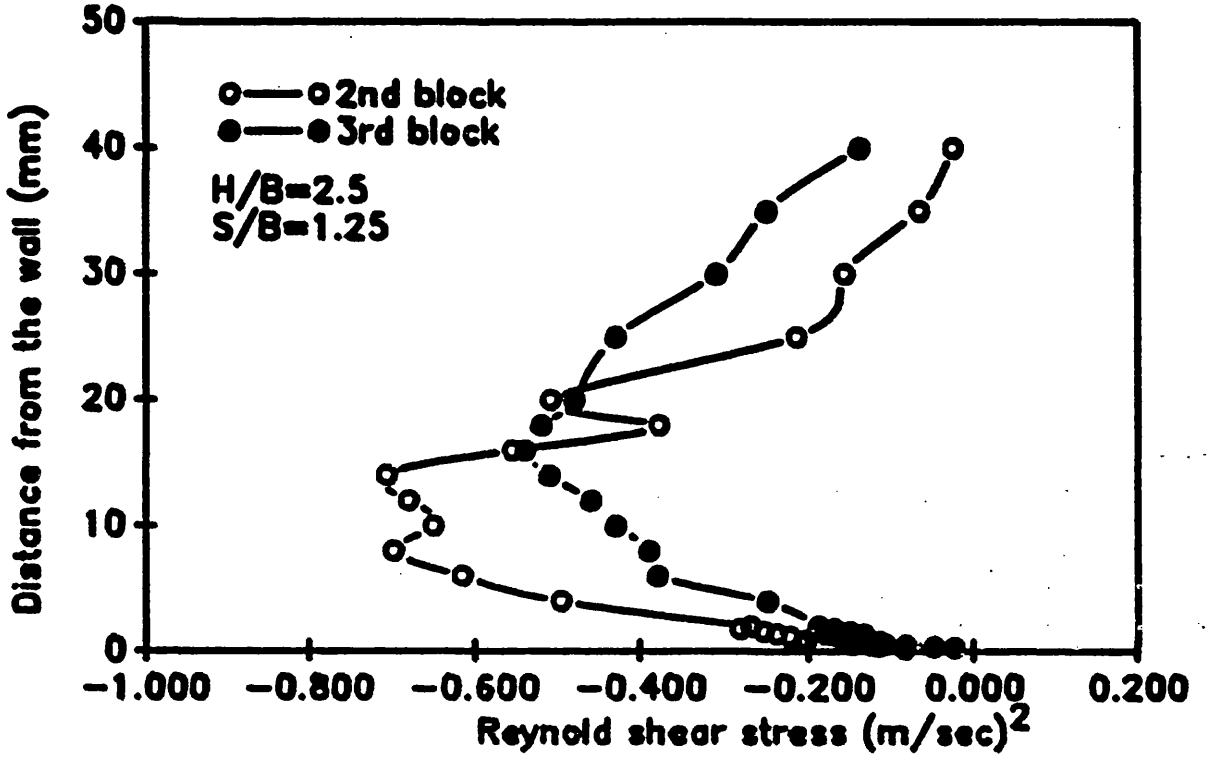

FIGURE 8.12: MEASUREMENT OF FLUCTUATING TURBULENT COMPONENTS OVER SECOND BLOCK AT 40MM FROM LEADING EDGE

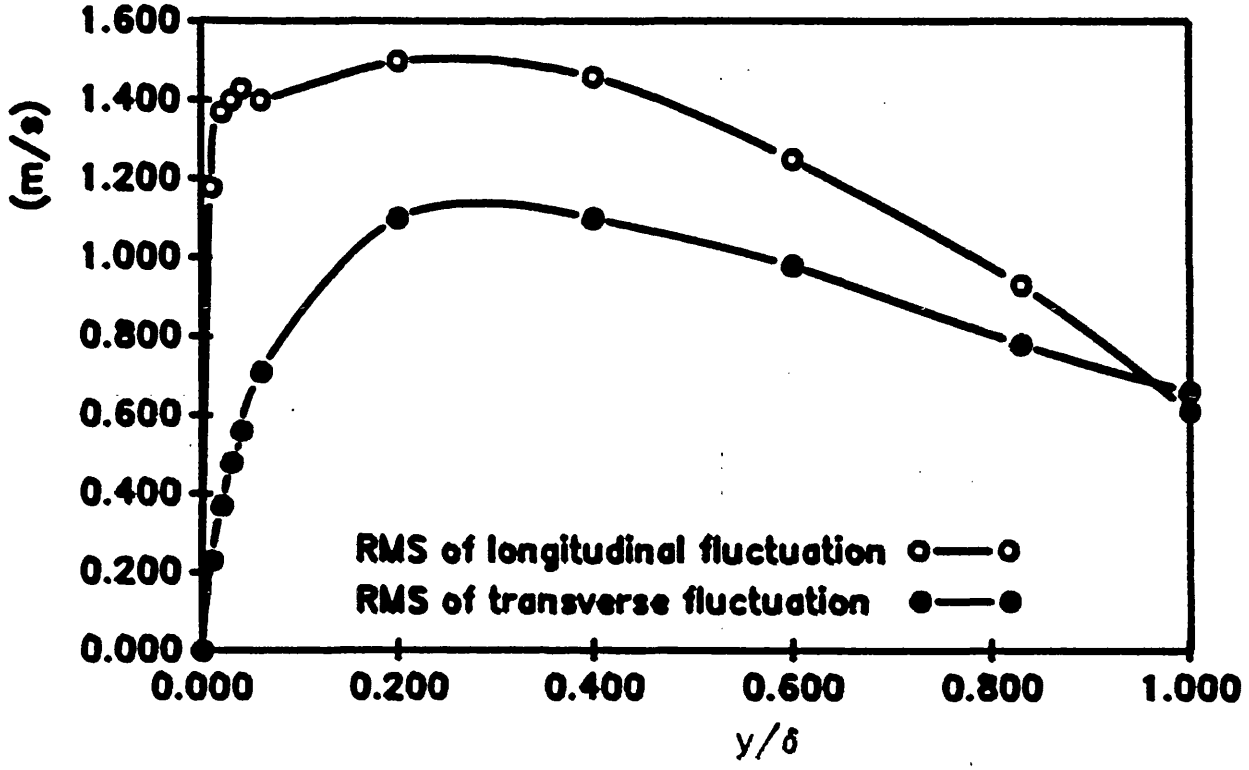

FIGURE 8.13: MEASUREMENT OF FLUCTUATING TURBULENT COMPONENTS OVER THIRD BLOCK AT 40MM FROM LEADING EDGE

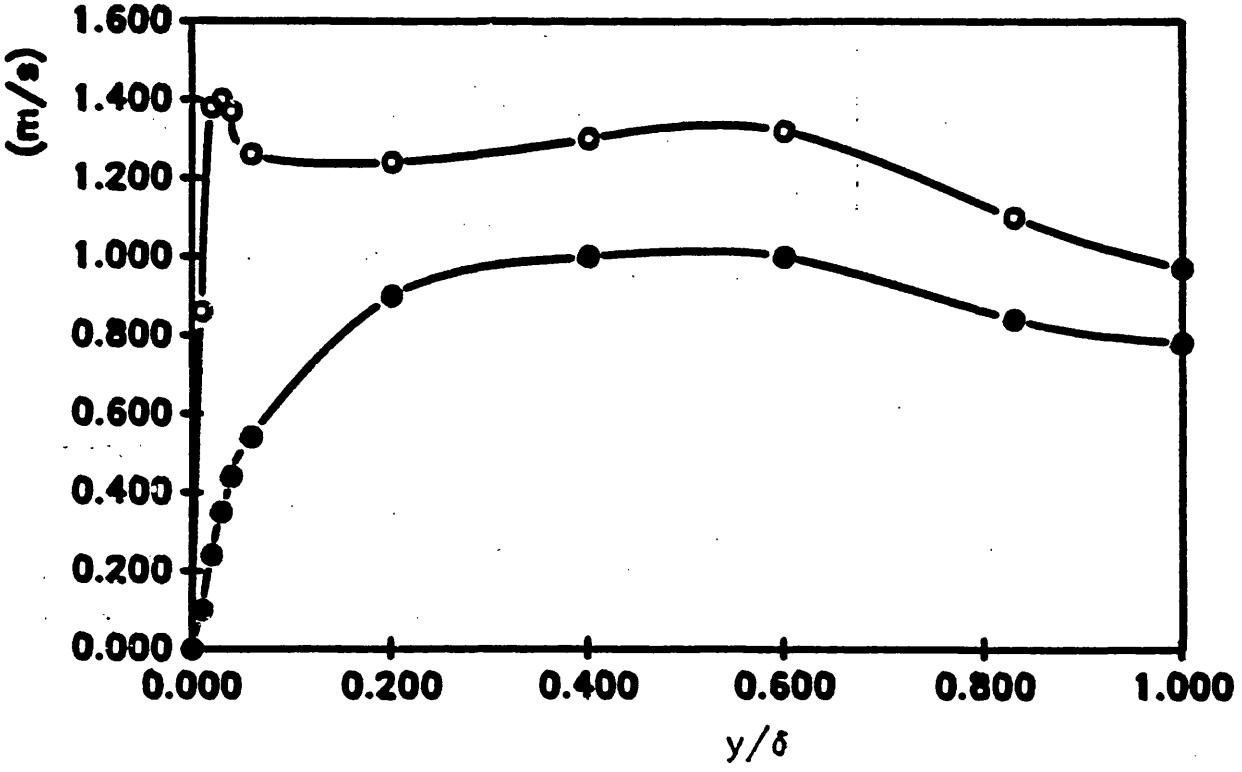

FIGURE 8.14: **MEASUREMENT OF FLUCTUATING COMPONENTS OVER SECOND AND THIRD BLOCK PRODUCT OF u v**

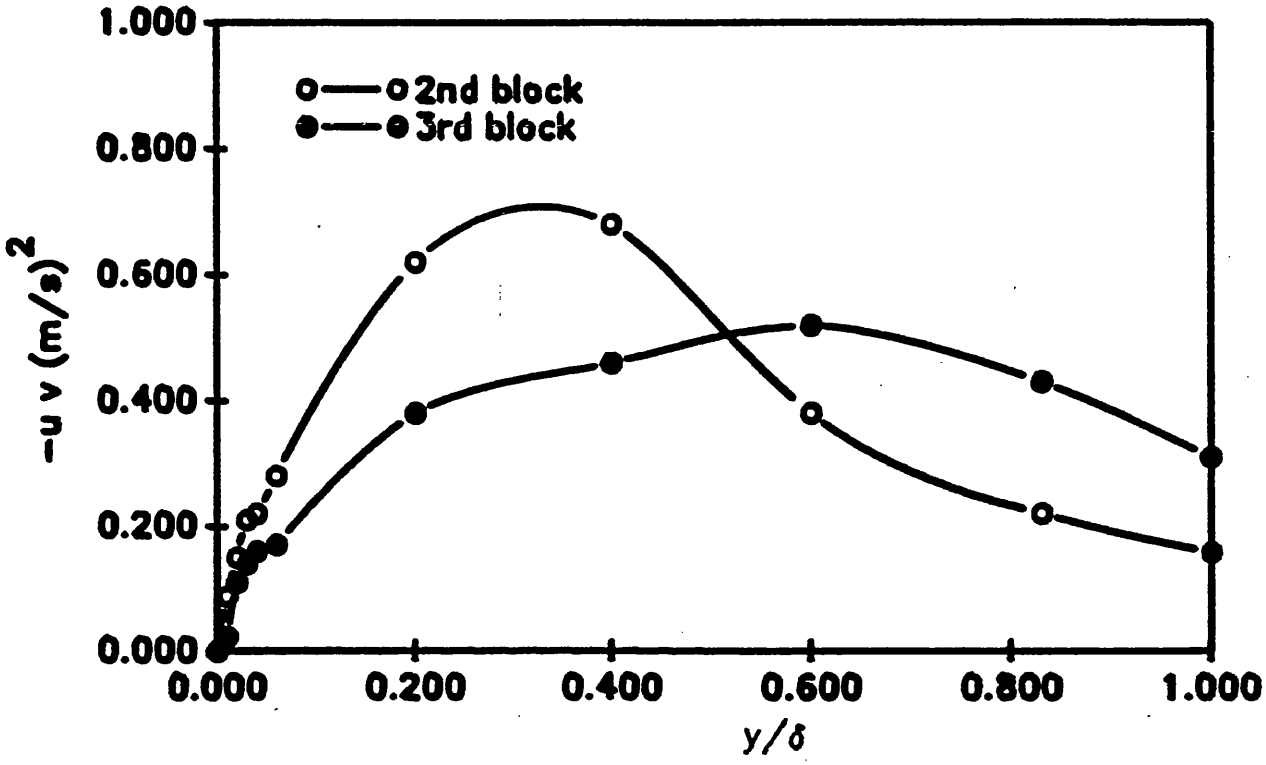

FIGURE 8.15: **CORRELATION COEFFICIENT OVER SECOND AND THIRD BLOCK AT 40MM FROM LEADING EDGE OF EACH BLOCK**

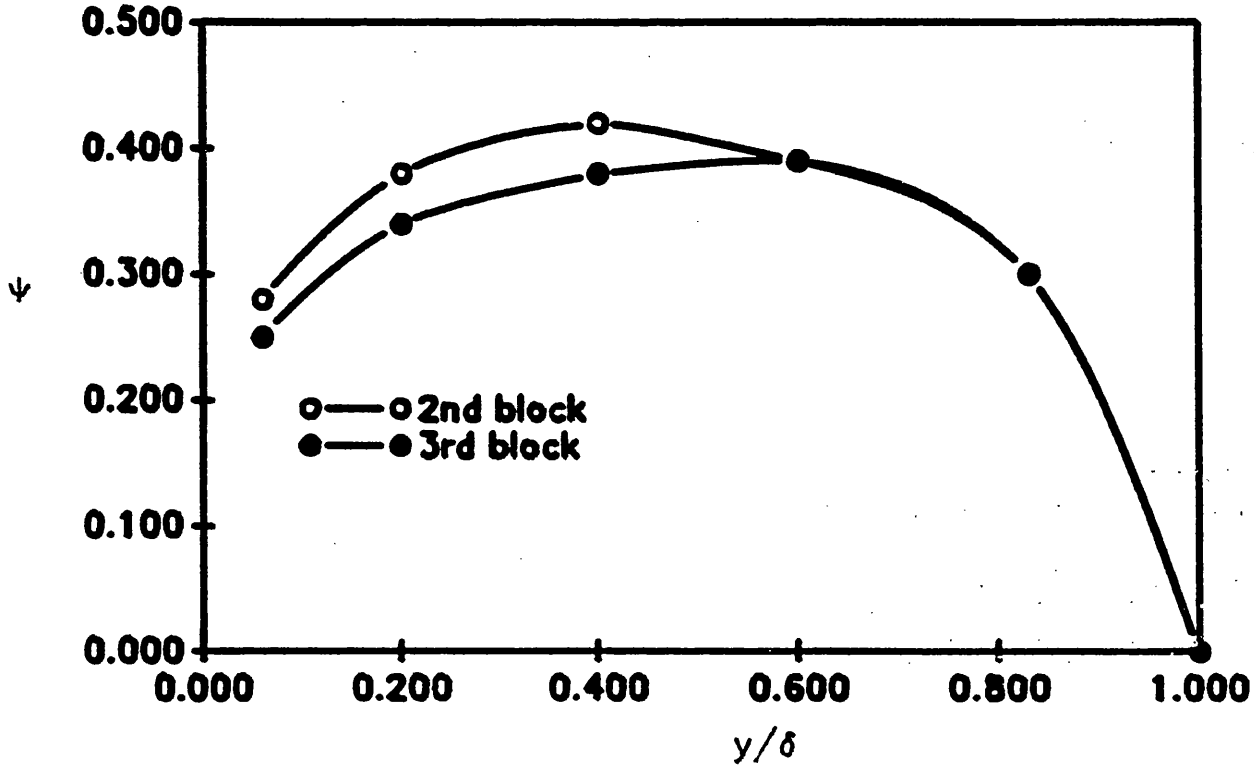

FIGURE 8.16: VARIATION OF THE FLUCTUATING TURBULENT VELOCITY COMPONENTS IN THE BOUNDARY LAYER OVER SECOND BLOCK AT 40MM FROM LEADING EDGE

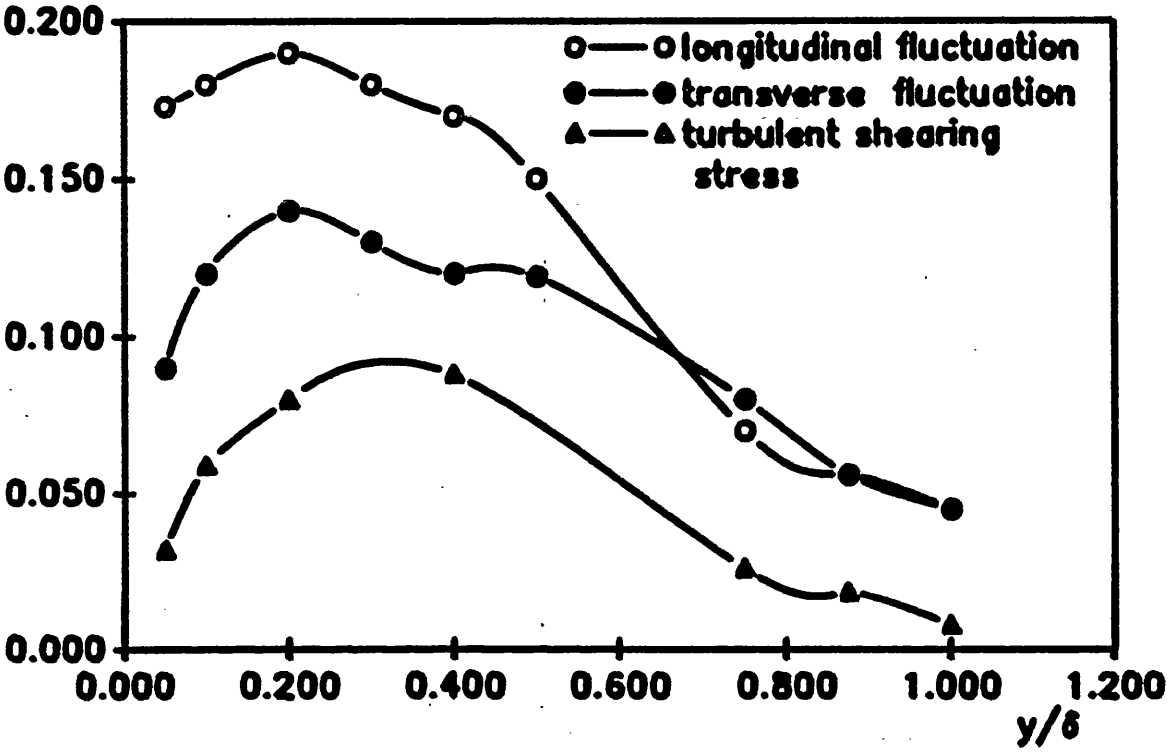

FIGURE 8.17: VARIATION OF THE FLUCTUATING TURBULENT VELOCITY COMPONENTS IN THE BOUNDARY LAYER OVER THIRD BLOCK AT 40MM FROM LEADING EDGE

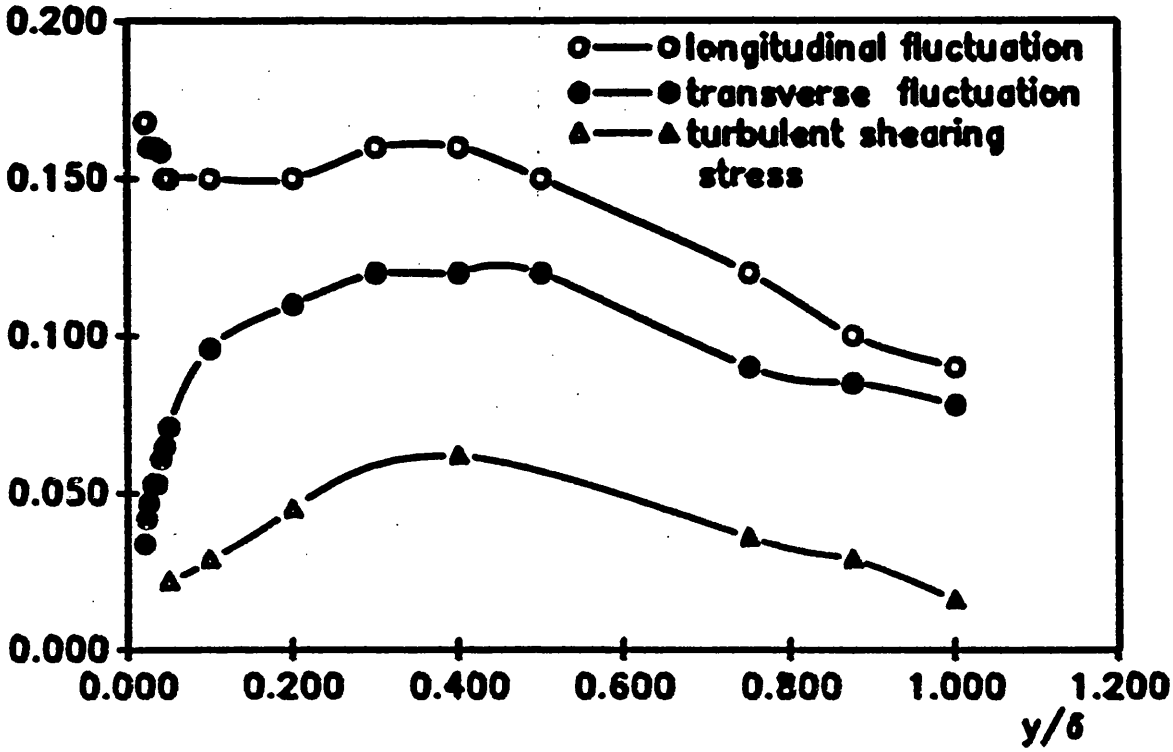

FIGURE 8.18: TYPICAL DISTRIBUTIONS OF u/u_τ AGAINST $\log(u_\tau y/\nu)$ IN THE 'LAW OF THE WALL' REGION OF THE BOUNDARY LAYER OVER THIRD BLOCK

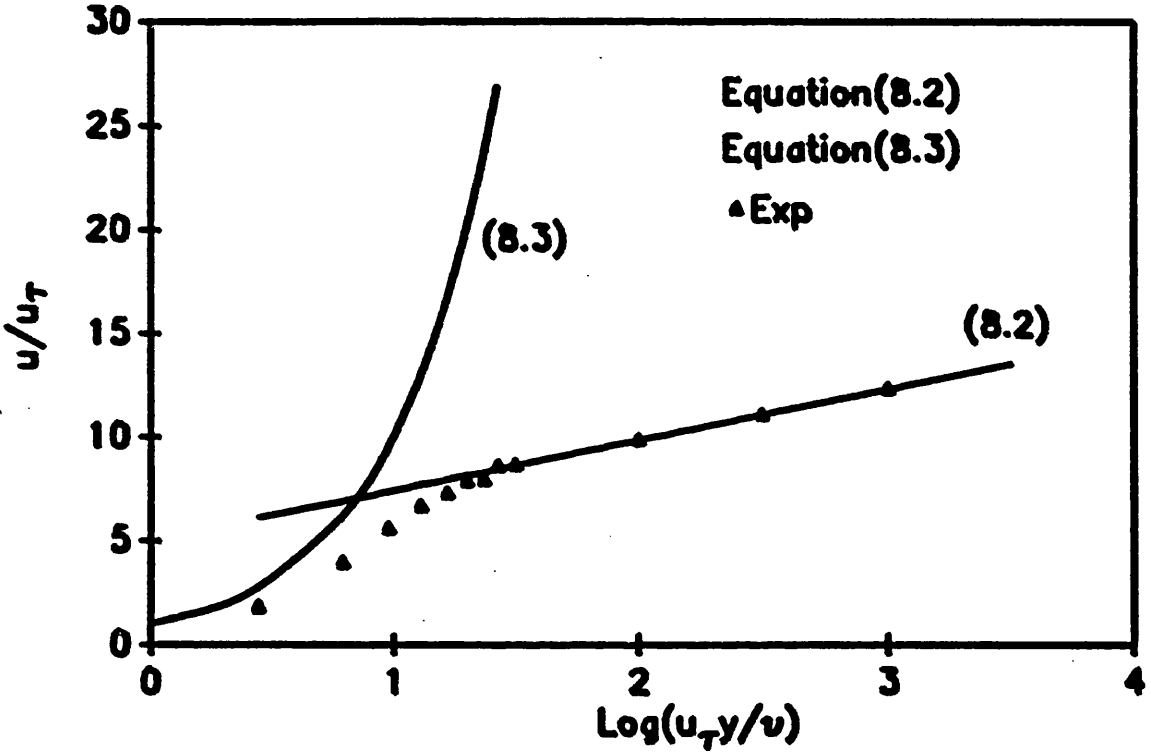

FIGURE 8.19: **CLAUSER PLOTS FOR DETERMINING THE SKIN FRICTION**

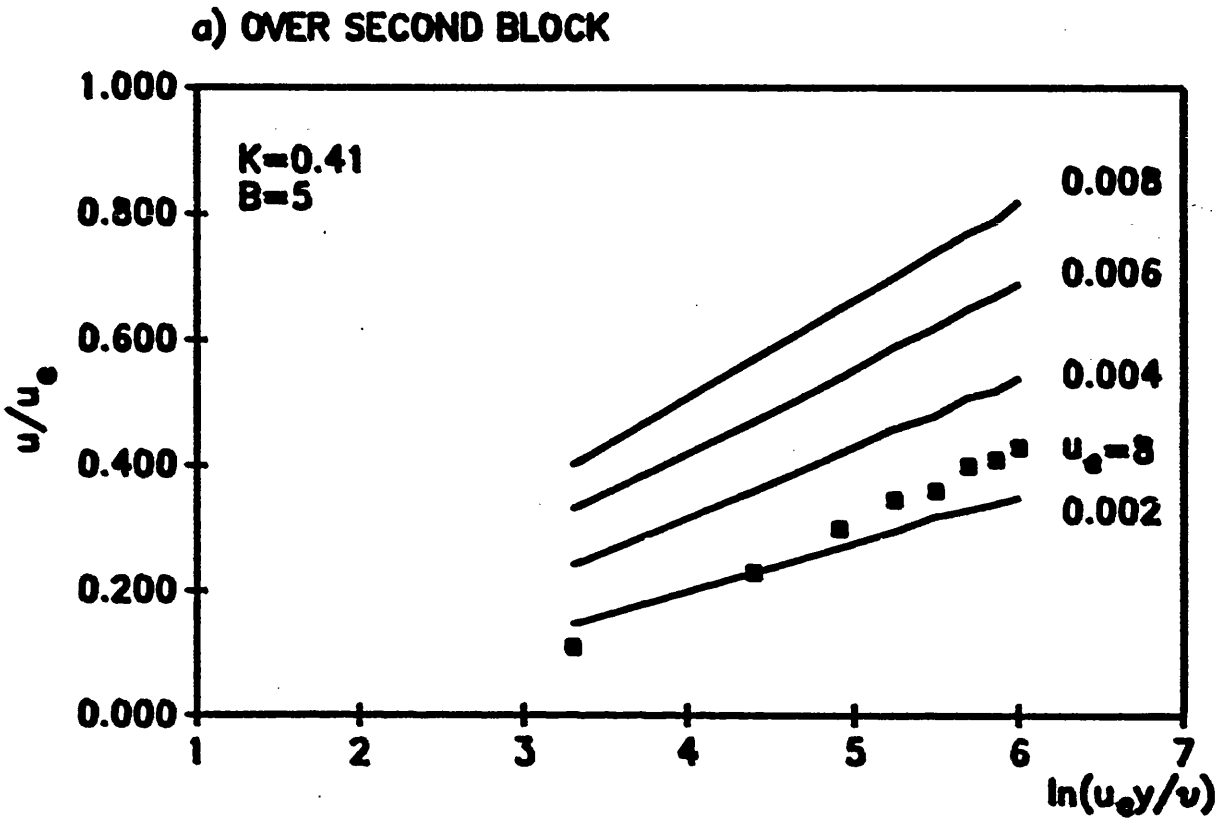

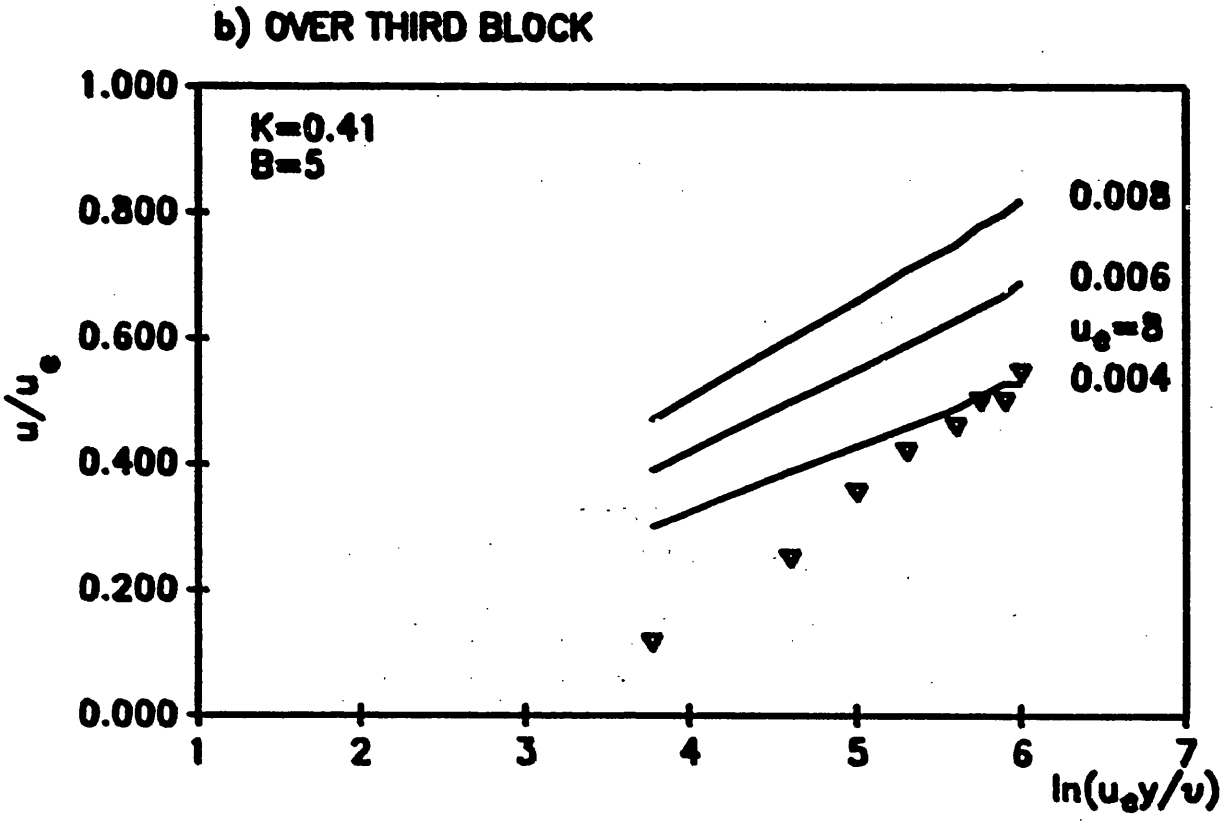

c) OVER FORTH BLOCK

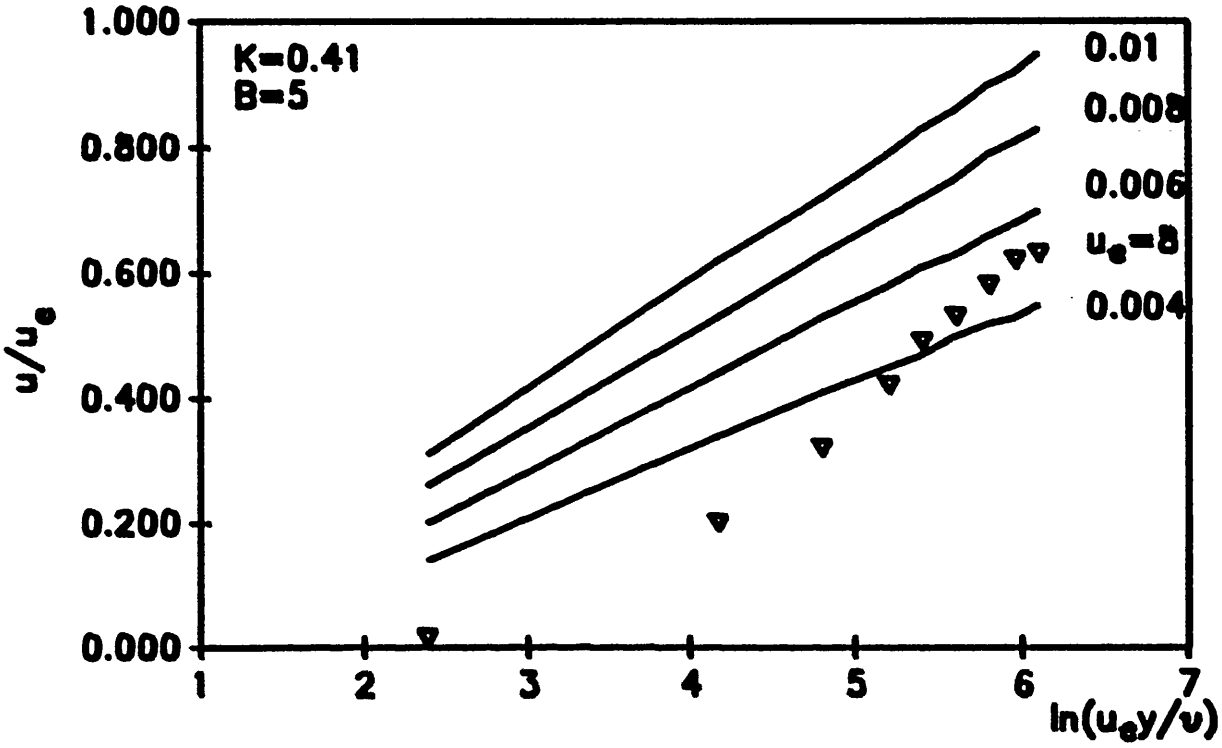

d) OVER FIFTH BLOCK

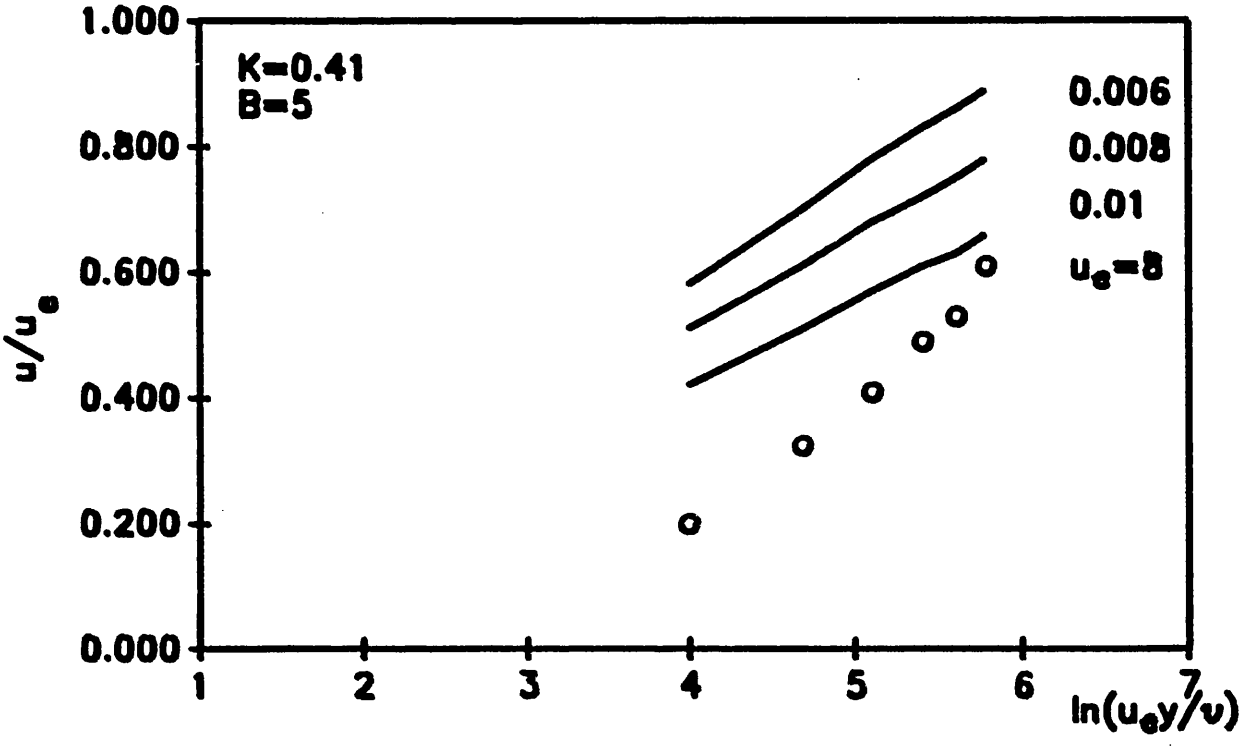

CHAPTER [9]

CONCLUSIONS AND RECOMMENDATIONS FOR FUTURE RESEARCH

The results and conclusions of this investigation into the flow and heat transfer over a rectangular array of heated elements mounted on one wall of an adiabatic channel, may be summarised as follows:

9.1 GENERAL

The existing CFD package was enhanced and developed to simulate the above complex flow. A comprehensive series of runs provided valuable predictive data for heat transfer analysis and thermal design of forced air cooling in electronic circuit packs.

The flow was assumed to be turbulent, and the standard k-ε model of turbulence was employed. The problem was conjugate, such that conduction in the solid was analyzed simultaneously with convection in the fluid.

To allow the same equations to be used throughout the model, the viscosity in the solid regions was set to a very large value. This effectively produced a velocity of zero in these regions so that they acted as solids. Harmonic averaging was employed for the variable enthalpy. To deduce the heat transfer coefficients, and hence the Nusselt number over elements, additional code was developed and

introduced into the "Ground" subroutine. Predictions of heat transfer coefficients from this coding compared well with experimental measurements, and values from the literature.

9.2 TURBULENCE MODEL

It was found that solutions of this complex problem could be obtained with satisfactory economy (20 minutes computing time on a Sun4 Spark station computer for a grid of 180*25 nodes).

The predictions with the standard **k-ε** turbulence model reproduced all the expected qualitative features of the flows, including an upstream eddy adjacent to the base of channel immediately in front of the first block, from which a shear layer originates enclosing a recirculation zone downstream.

It was found, by comparison with experimental measurements of streamwise velocity distribution over the blocks, that regions near the blocks were very closely predicted. This showed that the prediction procedure is able to describe a region of flow with strong pressure gradients and severe flow deflection, provided a suitably fine grid is used.

In general the calculations produced a realistic representation of the flows, and predicted the existence of recirculation zones bounded by shear layers from the edges of the obstacles, mean velocity distributions in

qualitative agreement with the experiments. The predictions, based on finite-difference solutions of the governing momentum and continuity equations coupled with energy equations and a turbulent model, represent the first treatment of conjugate flow. The method is also adaptable to the incorporation of different inlet and boundary conditions and to changes in geometry without fundamental changes to the solution procedure.

9.3 SUGGESTIONS FOR FUTURE WORK

9.3.1 PREDICTION OF TURBULENT WALL FUNCTIONS

The solution procedure for conjugate flows merits particular attention with regard to the turbulence model and the treatment of wall functions. In this investigation the turbulent wall functions applied near the surfaces of the obstacles produced satisfactory results.

The problem starts when it is necessary to locate the near-wall grid nodes very close to the walls in which the logarithmic law wall functions are not valid for distances less than $y^+ = 11.5$. Modification of the wall functions to achieve better modelling of this rather complex flow is likely to be difficult, and result in a loss of the simplicity which is one of their present advantages.

The changes introduced in the wall functions would need to be tested, and again the simpler geometries may prove more suitable for this purpose than those studied in the present work.

9.3.2 EXPERIMENTS

It is necessary to carry out more experiments against which to compare predicted flow patterns and thereby enable improvements in the calculation procedure and turbulence modelling.

Experimental measurements should be directed to provide data on the following regions of particular interest: the boundary of the recirculating flow, e.g., as defined by the surface on which the axial velocity is zero, the flow near the leading and top edges of the obstacle, and the shear layers emanating from these edges.

Experiments made for different geometrical parameters, such as the channel spacing, block spacing, would provide a wide choice of data for testing predictions.

It would also be interesting to extend this work for the three dimensional conditions both theoretically and experimentally since in reality the cooling of electronic components is a three dimensional problem.

REFERENCES

1. Marto, P.J., and Kelleher, N.D., "The Thermal Performance of Air-Cooled Circuit Boards Used in Standard Electronic Package Design," Naval Postgraduate Report No, NPS-59mx74051, May 1974.
2. Bergles, A.E., Chu, R.C., and Seely, J.H., "Survey of Heat Transfer Techniques Applied to Electronic Equipment," ASME paper No.72-WA/HT-39, Presented at the ASME Winter Annual Meeting, New York, N.Y., 1972.
3. Boucher, S.G., and Paradis, L.F., "Experimental Heat Transfer Investigations on Modules Mounting Hybrid Packages," 1973 Electronic Components Conference, Washington, D.C, May14-16, 1973.
4. Aung, W., Bertin, K.I., and Kessler ,T.J., "Natural Convection Cooling of Electronic Cabinets Containing Arrays of Vertical Circuit Cards, "ASME paper No.72-WA/Ht-40, presented at the ASME Winter Annual Meeting, New York, N.Y., November 26-30, 1972.
5. Baker, E., "Liquid Cooling of Microelectronic Devices by Free and Forced Convection, "Microelectronics and Reliability, 11, pp.213-222, 1972.
6. Grakovich, L.P., and Konev, S.V., "Cooling of Electronic Circuits and Instruments, "Heat Transfer Soviet Research, Vol.6, No.3, May-june 1974.
7. Chu, R.C., Seely, J.H., Antonelli, V.W., and Pascuzzo, A.L, 1970, Thermal Design Optimization in Large Digital Computers, TR 00.2039, IBM Corporation Poughkeepse,

N.Y. presented at the 1970 IEEE Computer Group Conf.

8. Bar-Cohen, A., 1985, Thermal Management of Air and Liquid Cooled Multi-chip modules, Presented at the 23d Natl.Heat Transfer Conf., Denver, Colo. Abstract in Heat Transfer in Electronic Equipment-1985, HTD-vol.48, p.3, ASME, New York.
9. Bergles, A.E., 1969. Survey and evaluation of techniques to augment convective heat and mass transfer. prog. Heat mass Transfer, 1, 331-424.
10. Willis, M., Thermal analysis of Air-cooled PCBs, 4parts, Electronic Production, May-August 1983.
11. Cook, D.V., "Cooling Electronics Naturally, "Machine Design, Aug 20, 1970.
12. Chaddock, J.B., "Free Convection Heat Transfer From Vertical Rectangular Fin Arrays, "ASHRAE Journal, Aug.1970.
13. Wise, A.F.E., (1971) Effects due to groups of buildings, phil.trans.roy.soc. a269, 469.
14. Castro, I.P., Jackson, N.A., and Robins, A.G., (1975) The structure and development of a 2m deep simulated suburban boundary layer, C.E.G.B. report R/M/N800.
15. Peterka, J.A. and Cermak, J.E. (1975) Turbulence in building wakes, conf.on wind effects on buildings and structures, Heathrow, london.
16. Tillman, W., (1945) Investigations of some particularities of turbulent boundary layers on plates. British min. of aircraft prod. volkenrode translation MAP-VG-34-45T.

17. Plate, E.J., and Lin, C.W., (1965) The velocity field downstream from a two-dimensional model hill, colorado state univ.report CEP65jP14.
18. Bradshaw, P., and Wong, F., (1972) The reattachment and relaxation of a turbulent shear layer, J.fluid Mech.52,113.
19. Sforza, P.M., and Mons, R.F., (1970) Flow behind a leading edge obstacle, AIAAJ, 8, 2162.
20. Plate, E.J., (1964) The drag on a smooth flat plate with a fence immersed in its turbulent boundary layer, ASME, paper no. 64-Fe-17.
21. Launder.B.E., "An introduction to single-point closure methodology", may 1987, University of Manchester, institute of Science and technology.
22. Leschziner. M.A., "Numerical implementation and performance of Reynolds-stress closures in finite-volume computations of Recirculating and strongly swirling flows", may 1987, University of Manchester, institute of Science and technology.
23. Zebib, A, and Wo, Y, K., A two-dimensional conjugate heat transfer model for forced air cooling of an electronic device, Procs. International electronic packaging conference, Orlando, Florida, pp.135-142, 1985.
24. Caretto, L.S., Gosman, A.D., Patankar, S.V. and Spalding, D.B. (1973), Two calculation procedures for steady three-dimensional flows with recirculation, proc. of third Int. Conference on Numerical Methods in

Fluid Mechanics II 60, Springer-Verlag, Heidelberg.

25. Daly, B.J., and Harlow, F.H., (1970) Transport equations of turbulence, Phys. Fluids, 13, 2634.
26. Gosman, A.D., Pun, W.M., Runchal, A.K., Spalding, D.B. and Wolfshtein, M., (1969) Heat and mass transfer in recirculating flows, Academic press, london.
27. Hanjalic, K., and Launder, B.E., (1972) A Reynolds stress model of turbulence and its application to thin shear flows, J. Fluid Mech., 52, 609.
28. Hinze, J.O., (1959) Turbulence, McGraw-Hill, New York.
29. Jones, W.P., and Launder, B.E., (1973) Prediction of low Reynolds number phenomena with a two-equation model of turbulence. INT. J. Heat Mass Transfer 16, 1119.
30. Kolmogorov, A.N., (1942) Equations of turbulent motions of an incompressible turbulent fluid, Izv. Akad. Nauk SSSR Ser.
31. Launder, B.E., Morse, A.P., Rodi, W., and Spalding, D.B., (1972) The prediction of free shear flows- A comparison of the performance of six turbulence models. Proc. NASA Conf. on free shear flows, Langley.
32. Launder, B.E., Reece, G.J., and Rodi, W., (1975) Progress in the development of a Reynolds stress turbulence closure. J. Fluid Mech., 68, 537.
33. Launder, B.E., and Spalding, D.B., (1972) Mathematical Models of Turbulence, Academic Press, London.
34. Launder, B.E., and Spalding, D.B., (1974) The numerical computation of turbulence flows. Computer method in Appl. Mech. and Eng., 3, 269.

35. Launder, B.E., and Ying, W.M., (1973) Prediction of flow and heat transfer in ducts of square cross-section. Heat and Fluid Flow, 3, 115.

36. Lefeuvre, R., (1973) Laminar and turbulent forced convection processes through in-line tube banks, Ph.D. Thesis, Univ. of London.

37. Matthews, L., and Whitelaw, J.H., (1973) Plane-jet flow over a backward facing step. heat and fluid flow, 3, 133.

38. Ng, K.H., (1971) predictions of turbulent boundary-layer developments using a two-equation model of turbulence, Imperial College, London, Mech. Eng. Dept. report HTS/71/2, Ph.D. Thesis, Univ. of London.

39. Patankar, S.V., and Spalding, D.B., (1970) Heat and Mass transfer in boundary layers, Intertext Books, London, second Edition.

40. Patankar, S.V., and Spalding, D.B., (1972) A calculation Procedure for heat, mass and momentum transfer in three-dimensional parabolic flows, Int.J. Heat Mass Transfer 15, 1787.

41. Prandtl, L., (1925) Bericht Uber Untersuchungen Zur ausgebildeten Turbulenz, ZAMM 5, 136.

42. Roberts, L.W., (1972) Turbulent swirling flows with recirculation, Ph.D. Thesis, Univ. of London.

43. Rodi, W., (1970) basic equations for turbulent flow in Cartesian and cylindrical coordinates, Imperial College, Mech. Eng. Dept. report BL/TN/a/36.

44. Runchal, A.K., (1972) Convergence and accuracy of three

finite difference schemes for a two-dimensional conduction and convection problem, Int. J. Num. Meth. Eng., 4, 541.

45. Spalding, D.B., (1972) A noval finite-difference formulation for differential expressions involving both first and second derivatives, Int. J. Num. Meth. Eng., 4, 551.
46. Tennekes, H., and Lumley, J.L., (1972) A first course in turbulence, MIT Press, Cambridge, Mass.
47. Harlow, F.H., and Nakayama, P.I., Turbulence transport equations, Phys. Fluids 10, 2323-2332 (1967)
48. Patankar, S.V., A numerical method for conduction in composite materials, Flow in irregular geometries and conjugate heat transfer. (1978). Department of Mech Eng, Univ of Minnesota, Minneapolis, Minnesota.
49. Arvizu, D.E., and Moffat, R.J., (1981). Experimental heat transfer from an array of heated cubical elements on an adiabatic channel wall, Report no. HMT-33, Thermosciences Div., Dept. of Mech Eng, Stanford Univ., Stanford, CA.
50. Anderson, A.M., and Moffat, R.J., 1988, "Direct air cooling of electronic components: reducing element temperatures by controlled thermal mixing," submitted for presentation at the ASME Winter Annual Meeting, 1988.
51. Abboud, J., Hardisty, H., The finite element method applied to the thermal analysis of microelectronic packaging, proc. INTERNEPCON, electronic packaging

conf., Brighton, oct. 87, U.K.

52. Hardisty, H., and Abboud, J., 1988. Forced convection cooling of an array of electronic modules using the finite element method to analyse module heat transfer. Proc Instn Mech Engrs Vol 202 No C5. U.K.

53. Sellars, J.R., Tribus, M., and Klein, J.S., 1956, "Heat transfer to laminar flow in a round tube or flat conduit- The graetz problem extended," ASME Trans., Vol. 78,pp.441-448.

54. Hosker, R.P., Jr., 1980. Flow and diffusion near obstacles. ATDL construction 79/10, Oak Ridge, TN 37830.

55. London, A.L., and Shah, R.K., Offset rectangular plate-fin surfaces-heat transfer and flow friction characteristics, I.Engng Power 90, 218-228 (1968).

56. Bryer, D.W. and Pankhurst, R.C, 1971, Pressure-probe methods for determining wind spped and flow direction, H.M.S.O. London

57. Wise, A.F.E., Sexton, D.E. and Lillywhite, M.S., 1965, Air flow round buildings, proc. of Urban Planning Symposium, London, 71.

58. Castro, I.P., 1973, An experimental investigation of the flow around a surface mounted cube in a uniform free stream, C.E.G.B. report R/M/N687.

59. Castro, I.P., and Robins, A.G., 1975, The effect of a thick incident boundary layer on the flow around a small surface mounted cube, C.E.G.B. report R/M/N795.

60. Bradshaw, P., "An introduction to turbulence and its

measurement", Pergamon Press, 1971.

61. Bradbury, L.J.S., and Castro, I.P., 1971 A pulsed-wire technique for velocity measurements in highly turbulent flows, J. Fluid Mech., 49, 657.

62. Durst, F., Melling, A., Whitelaw, J.H., "Principles and practice of laser Doppler Anemometry", Academic press 1976.

63. Reichardt, H., Messungen turbulenter Schwankungen. Naturwissenscaften 404 (1938); see also ZAMM 13, 177-180 (1933) and ZAMM 18, 358-361 (1939).

64. Clauser, F.H., 1954. Turbulent boundary layers in adverse pressure gradients. J. Aeronautical Science, 21, 91.

65. Chen, C.J., and Yoon, Y.W., 1983, "Finite Analytic Numerical Solution Axismmetric Navier-Stokes and energy equations," ASME Journal of Heat Transfer, Vol. 105, pp. 639-645.

66. Schlichting, H., (1968), boundary-layer theory, McGraw-Hill, New York.

APPENDIX [1]

FINITE-DIFFERENCE EQUATIONS

A1.1 DERIVATION OF FULL FINITE-DIFFERENCE EQUATION FOR ϕ_p

Combination of equations (3.18), (3.27) and (3.28), given in section 3.3.3, leads to the following finite difference equation for conservation of ϕ at grid node **p**:

$$A_z\, g_{z_+}\,[(1-F_{z_+})\,\phi_{Z_+}+F_{z_+}\,\phi_p]-A_z\, g_{z_-}[F_{z_-}\,\phi_{Z_-}+(1-F_{z_-})\phi_p]$$

$$+A_y\, g_{y_+}[(1-F_{y_+})\,\phi_{Y_+}+F_{y_+}\,\phi_p]-A_y\, g_{y_-}[F_{y_-}\,\phi_{Y_-}+(1-F_{y_-})\,\phi_p]$$

$$+A_x\, g_{x_+}[(1-f_{x_+})\,\phi_{X_+}+F_{x_+}\,\phi_p]-A_x\, g_{x_-}[F_{x_-}\,\phi_{X_-}+(1-F_{x_-})\,\phi_p]=$$

$$S_U^{\phi}+S_p^{\phi}\,\phi_p \qquad \textbf{(A1.1)}$$

Equation (3.29) is then derived by the following steps: The coefficients of ϕ_p are collected on the left hand side giving an expression as

$$[A_z\, g_{z_+}\,F_{z_+}-A_z\, g_{z_-}(1-F_{z_-})\;A_y\, g_{y_+}\,F_{y_+}-A_y\, g_{y_-}(1-F_{y_-})+A_x\, g_{x_+}\,F_{x_+}$$

$$-A_x\, g_{x_-}(1-F_{x_-})-S_p^{\phi}]\,\phi_p \qquad \textbf{(A1.2)}$$

Adding and subtracting each convective term e.g. $\mathbf{A_z\ g_{z+}}$ - $\mathbf{A_z\ g_{z+}}$ allows one to manipulate the coefficient of ϕ_p into the form

$$[A_z\, g_{z_+} - A_z\, g_{z_-} + A_y\, g_{y_+} - A_y\, g_{y_-} + A_x\, g_{x_+} - A_x\, g_{x_-}]$$

$$+ A_z\, g_{z_+}(F_{z_+}-1) + A_z\, g_{z_-}\, F_{z_-} + A_y\, g_{y_+}\, (F_{y_+}-1) + A_y\, g_{y_-}\, F_y$$

$$+ A_x\, g_{x_+}(F_{x_+}-1) + A_x\, g_{x_-}\, F_{x_-} - S_p^{\phi} \qquad \textbf{(A1.3)}$$

Now, by the continuity equation (3.13) and equations such as (3.19), the term in square brackets is equal zero; thus the total coefficient of ϕ_p is:

$$A_z\, g_{z_+}(F_{z_+}-1) + A_z\, g_{z_-}\, F_{z_-} + A_y\, g_{y_+}(F_{y_+}-1) + A_y\, g_{y_-}\, F_{y_-}$$

$$+ A_x\, g_{x_+}\, (F_{x_+}-1) + A_x\, g_{x_-}\, F_{x_-} - S_p^{\phi} \qquad \textbf{(A1.4)}$$

The other terms in equation (A1.1) can be arranged on the right hand side so that the full finite difference equation becomes

$$[A_z\, g_{z_+}\, (F_{z_+}-1) + A_z\, g_{z_-}\, F_{z_-} + A_y\, g_{y_+}(F_{y_+}-1) + A_y\, g_{y_-}\, F_{y_-} +$$

$$A_x\, g_{x_+}\, (F_{x_+}-1) + A_x\, g_{x_-}\, F_{x_-} - S_p^{\phi}]\, \phi_p =$$

$$A_z\, g_{z_+}\, (F_{z_+}-1)\, \phi_{Z_+} + A_z\, g_{z_-}\, F_{z_-}\, \phi_{Z_-} + A_y\, g_{y_+}\, (F_{y_+}-1)\, \phi_{Y_+} +$$

$$A_y\, g_{y_-}\, F_{y_-}\, \phi_{Y_-} + A_x\, g_{x_+}\, (F_{x_+}-1)\, \Phi_{X_+} + A_x\, g_{x_-}\, F_{x_-}\, \phi_{X_-} + S_U^{\phi}$$

(A1.5)

Equation (A1.5) is identical to equation (3.29).

A1.2 DETAILS OF COEFFICIENTS IN MOMENTUM EQUATIONS

The finite-difference coefficients for the momentum equations differ from the ones derived for the ϕ equation because of different distances between the grid nodes, different cell dimensions and different interpolation practices used to obtain the averaged mass fluxes and transport coefficients for the cell boundaries. Thus, the quantities A_x, g_{x+}, g_{x-}, F_{x+}, F_{x-} etc.
in the coefficient definitions of equations (3.30) must be redefined; the appropriate relations will be given below for the **W**, **V** and **U** components of velocity in turn.

(a) z-MOMENTUM EQUATION

The areas of the cell-faces for the **W**-momentum control volume are:

$$A_x = \Delta^W y \; \Delta^W z$$

$$A_y = \Delta^W z \; \Delta x$$

$$A_z = \Delta^W y \; \Delta x \qquad \text{(A1.6)}$$

where $\Delta^W y$ and $\Delta^W z$ are the dimensions of the cell as shown in Figure (3.2).
The mass fluxes in the **z**-direction are defined as:

$$g_{z_+} = \rho_p \left[W_p f_{z_+}^W + W_{Z_+} (1 - f_{z_+}^W) \right] \qquad \text{(A1.7)}$$

$$g_{z_-} = \rho_{z_-} [W_p f_{z_-}^W + W_{z_-}(1-f_{z_-}^W)] \qquad \text{(A1.8)}$$

where the weighting factors with a non-uniform grid spacing are

$$f_{z_+}^W = \frac{\delta_1^W}{\delta_{z_+}^W} \qquad \text{(A1.9)}$$

$$f_{z_-}^W = \frac{\delta_2^W}{\delta_{z_-}^W} \qquad \text{(A1.10)}$$

in terms of the distances δ^w_1, δ^w_2, δ^w_{z+} and δ^w_{z-} marked on Figure (3.2). For a uniform grid distribution, these factors reduce to unity. The mass fluxes directed laterally are:

$$g_{y+} = 1/4[\rho_{y+} + \rho_{y+z-} + \rho_{z-} + \rho_p]\ 1/2[W_p + W_{y+}] \qquad \text{(A1.11)}$$

$$g_{y-} = 1/4[\rho_{y-} + \rho_{y-z-} + \rho_{z-} + \rho_p]\ 1/2[W_p + W_{y-}] \qquad \text{(A1.12)}$$

$$g_{x+} = 1/4[\rho_{x+} + \rho_{x+z-} + \rho_{z-} + \rho_p]\ 1/2[W_p + W_{x+}] \qquad \text{(A1.13)}$$

$$g_{x-} = 1/4[\rho_{x-} + \rho_{x-z-} + \rho_{z-} + \rho_p]\ 1/2[W_p + W_{x-}] \qquad \text{(A1.14)}$$

Where densities at inter-nodal locations are averaged from values at nearby nodes of the ϕ -grid.

Values for the diffusion coefficients at the cell faces are needed to determine Peclet numbers and, hence, values of $\mathbf{F}_{y+}$ etc by equations (3.24) to (3.26) and analogous equations. For **W**, these coefficients are

$$\Gamma_{z+} = \Gamma_p \qquad \text{(A1.15)}$$

$$\Gamma_{z-} = \Gamma_{z-} \qquad \text{(A1.16)}$$

$$\Gamma_{y+} = 1/4\,[\Gamma_{y+} + \Gamma_{y+z-} + \Gamma_{z-} + \Gamma_p] \qquad \text{(A1.17)}$$

$$\Gamma_{y-} = 1/4\,[\Gamma_{y-} + \Gamma_{y-z-} + \Gamma_{z-} + \Gamma_p] \qquad \text{(A1.18)}$$

$$\Gamma_{x+} = 1/4\,[\Gamma_{x+} + \Gamma_{x+z-} + \Gamma_{z-} + \Gamma_p] \qquad \text{(A1.19)}$$

$$\Gamma_{x-} = 1/4\,[\Gamma_{x-} + \Gamma_{x-z-} + \Gamma_{z-} + \Gamma_p] \qquad \text{(A1.20)}$$

Using appropriate distances between the nodes, the Peclet numbers for the cell faces can be evaluated; for example, for the face through point z_+, of the **W**-cell, it is:

$$Pe_{z+} = g_{z+}\delta^w_{z+}/\Gamma_{z+} \qquad \text{(A1.21)}$$

(b) y-MOMENTUM EQUATION

The areas of the cell-faces for the **V**-momentum control volume in Figure (3.3) are

$$A_x = \Delta^v_y \Delta_z$$

$$A_y = \Delta^v_x \Delta_z$$

$$A_z = \Delta^v_x \Delta^v_y \qquad \text{(A1.22)}$$

Mass fluxes through the cell faces can be written as:

$$g_{x+} = 1/4\,[\rho_p + \rho_{x+} + \rho_{x+y-} + \rho_{y-}]\ 1/2\,[V_p + V_{x+}] \qquad \text{(A1.23)}$$

$$g_{x-} = 1/4\,[\rho_p + \rho_{x-} + \rho_{x-y-} + \rho_{y-}]\ 1/2\,[V_p + V_{x-}] \qquad \text{(A1.24)}$$

$$g_{y+} = \rho_p [V_p f^v_{y+} + V_{y+}\ (1-f^v_{y+})] \qquad \text{(A1.25)}$$

$$g_{y-} = \rho_{y-} [V_p f^v_{y-} + V_{y-}\ (1-f^v_{y-})] \qquad \text{(A1.26)}$$

$$g_{z+} = 1/4\,[\rho_p + \rho_{y-} + \rho_{y-z+} + \rho_{z+}]\ 1/2\,[V_p + V_{z+}] \qquad \text{(A1.27)}$$

$$g_{z-} = 1/4\,[\rho_p + \rho_{y-} + \rho_{y-z-} + \rho_{z-}]\ 1/2\,[V_p + V_{z-}] \qquad \text{(A1.28)}$$

where

$$f^{V}_{y+} = \delta^{V}_{1}/\delta^{V}_{y+} \qquad \text{(A1.29)}$$

$$f^{V}_{y-} = \delta^{V}_{2}/\delta^{V}_{y-} \qquad \text{(A1.30)}$$

The diffusion coefficients for the **V**-momentum equation are

$$\Gamma_{x+} = 1/4[\Gamma_{p} + \Gamma_{x+} + \Gamma_{x+y-} + \Gamma_{y-}] \qquad \text{(A1.31)}$$

$$\Gamma_{x-} = 1/4[\Gamma_{p} + \Gamma_{x-} + \Gamma_{x-y-} + \Gamma_{y-}] \qquad \text{(A1.32)}$$

$$\Gamma_{y+} = \Gamma_{p} \qquad \text{(A1.33)}$$

$$\Gamma_{y-} = \Gamma_{y-} \qquad \text{(A1.34)}$$

$$\Gamma_{z+} = 1/4[\Gamma_{p} + \Gamma_{y-} + \Gamma_{y-z+} + \Gamma_{z+}] \qquad \text{(A1.35)}$$

$$\Gamma_{z-} = 1/4[\Gamma_{p} + \Gamma_{y-} + \Gamma_{y-z-} + \Gamma_{z-}] \qquad \text{(A1.36)}$$

Thus the Peclet number, for the face through point y_+ is

$$Pe_{y+} = g_{y+}\delta^{V}_{y+}/\Gamma_{y+} \qquad \text{(A1.37)}$$

(c) <u>x-MOMENTUM EQUATION</u>

The areas of the cell faces are:

$$A_x = \Delta^{U}_{y}\Delta_z$$

$$A_y = \Delta^{U}_{x}\Delta_z$$

$$A_z = \Delta^{U}_{x}\Delta^{U}_{y} \qquad \text{(A1.38)}$$

where Δ^{U}_{y} and Δ^{U}_{x} are shown in Figure (3.4).

The mass fluxes are defined as:

$$g_{x+} = \rho_{p}[U_{p}f^{U}_{x+} + U_{x+}\ (1-f^{U}_{x+})] \qquad \text{(A1.39)}$$

$$g_{x-} = \rho_{x-}[U_{p}f^{U}_{x-} + U_{x-}\ (1-f^{U}_{x-})] \qquad \text{(A1.40)}$$

$$g_{y+} = 1/4[\rho_p + \rho_{x-} + \rho_{x-y+} + \rho_{y+}]\ 1/2[U_p + U_{y+}] \quad \text{(A1.41)}$$

$$g_{y-} = 1/4[\rho_p + \rho_{x-} + \rho_{x-y-} + \rho_{y-}]\ 1/2[U_p + U_{y-}] \quad \text{(A1.42)}$$

$$g_{z+} = 1/4[\rho_p + \rho_{x-} + \rho_{x-z+} + \rho_{z+}]\ 1/2[U_p + U_{z+}] \quad \text{(A1.43)}$$

$$g_{z-} = 1/4[\rho_p + \rho_{x-} + \rho_{x-z-} + \rho_{z-}]\ 1/2[U_p + U_{z-}] \quad \text{(A1.44)}$$

where

$$f^U_{x+} = \delta^U_1/\delta^U_{x+} \quad \text{(A1.45)}$$

$$f^U_{x-} = \delta^U_2/\delta^U_{x-} \quad \text{(A1.46)}$$

The diffusion coefficients are

$$\Gamma_{x+} = \Gamma_p \quad \text{(A1.47)}$$

$$\Gamma_{x-} = \Gamma_{x-} \quad \text{(A1.48)}$$

$$\Gamma_{y+} = 1/4[\Gamma_p + \Gamma_{x-} + \Gamma_{x-y+} + \Gamma_{y+}] \quad \text{(A1.49)}$$

$$\Gamma_{y-} = 1/4[\Gamma_p + \Gamma_{x-} + \Gamma_{x-y-} + \Gamma_{y-}] \quad \text{(A1.50)}$$

$$\Gamma_{z+} = 1/4[\Gamma_p + \Gamma_{x-} + \Gamma_{x-z+} + \Gamma_{z+}] \quad \text{(A1.51)}$$

$$\Gamma_{z-} = 1/4[\Gamma_p + \Gamma_{x-} + \Gamma_{x-z-} + \Gamma_{z-}] \quad \text{(A1.52)}$$

Finally, the Peclet number through the face through point x_+ is:

$$Pe_{x+} = g_{x+}\delta^U_{x+}/\Gamma_{x+} \quad \text{(A1.53)}$$

A1.3 SOLUTION PROCEDURE

A1.3.1 SOLUTION ALGORITHM FOR VELOCITIES AND PRESSURE

The solution algorithm proceeds as follows. Since the pressure appearing in the finite difference momentum

equations (3.32 to 3.34) are not known beforehand, guessed values denoted by $\mathbf{p}^*$ are first substituted into the momentum equations, which are then solved to yield a field of intermediate velocities $\mathbf{U}^*$, $\mathbf{V}^*$, $\mathbf{W}^*$, which will not in general satisfy the continuity equation (3.13) until the correct pressures are obtained. The preliminary velocities therefore satisfy the equations:

$$C_p^U U_p^* = C_{X_+}^U U_{X_+}^* + C_{X_-}^U U_{X_-}^* + C_{Y_+}^U U_{Y_+}^* + C_{Y_-}^U U_{Y_-}^* + C_{Z_+}^U W_{Z_+}^*$$

$$+ C_{Z_-}^U W_{Z_-}^* + S_U^U + A_x (p_{X_-}^* - p_p^*) \qquad \textbf{(A1.54)}$$

$$C_p^V V_p^* = C_{X_+}^V V_{X_+}^* + C_{X_-}^V V_{X_-}^* + C_{Y_+}^V V_{Y_+}^* + C_{Y_-}^V V_{Y_-}^* + C_{Z_+}^V W_{Z_+}^*$$

$$+ C_{Z_-}^V W_{Z_-}^* + S_U^V + A_y (p_{Y_-}^* - p_p^*) \qquad \textbf{(A1.55)}$$

$$C_p^W W_p^* = C_{X_+}^W W_{X_+}^* + C_{X_-}^W W_{X_-}^* + C_{Y_+}^W W_{Y_+}^* + C_{Y_-}^W W_{Y_-}^* + C_{Z_+}^W W_{Z_+}^*$$

$$+ C_{Z_-}^W W_{Z_-}^* + S_U^W + A_z (p_{Z_-}^* - p_p^*) \qquad \textbf{(A1.56)}$$

The degree to which $\mathbf{U}^*$, $\mathbf{V}^*$ and $\mathbf{W}^*$ do not satisfy the continuity equation is manifested by the existence of a finite mass
imbalance or 'mass source', $\mathbf{M_p}$, at each cell, given by:

$$M_p = A_x (\rho_{x_+} U^*_{X_+} - \rho_{x_-} U^*_p) + A_y (\rho_{y_+} V^*_{Y_+} - \rho_{y_-} V^*_p) + A_z (\rho_{z_+} W^*_{Z_+}$$

$$- \rho_{z_-} W^*_p) \qquad \textbf{(A1.57)}$$

pressure corrections **(p´)** are now made such that the resulting velocity corrections **(U´, V´** and **W´)** will reduce these mass sources to zero,i.e.

$$A_x (\rho_{x_+} U_{X_+} - \rho_{x_-} U_p) + A_y (\rho_{y_+} V_{Y_+} - \rho_{y_-} V_p) + A_z (\rho_{z_+} W_{Z_+} - \rho_{z_-} W_p)$$

$$= -M_p \qquad \textbf{(A1.58)}$$

U´p, V´p and **W´p** are obtained from the linear relations between the velocity and pressure corrections, of the form:

$$U_p = D_p^U (p_{X_-} - p_p) \qquad \textbf{(A1.59)}$$

$$V_p = D_p^V (p_{Y_-} - p_p) \qquad \textbf{(A1.60)}$$

$$W_p = D_p^W (p_{Z_-} - p_p) \qquad \textbf{(A1.61)}$$

where

$$D_p^U = \frac{A_x}{C_p^U} \ , \quad D_p^V = \frac{A_y}{C_p^V} \ , \quad D_p^W = \frac{A_z}{C_p^W} \qquad \textbf{(A1.62)}$$

Equations (A1.59) to (A1.61) requires an approximation to the velocity correction equations, Patankar and Spalding [40].

For **W´p**, for example, equation (3.32) and (A1.56) imply that

$$C_p^W W_p = C_p^W (W_p - W_p^*)$$

$$- C_{X_+}^W (W_{X_+} - W_{X_+}^*) + C_{X_-}^W (W_{X_-} - W_{X_-}^*) + C_{Y_+}^W (W_{Y_+} - W_{Y_+}^*) + C_{Y_-}^W (W_{Y_-} - W_{Y_-}^*)$$

$$+ C_{Z_+}^W (W_{Z_+} - W_{Z_+}^*) + C_{Z_-}^W (W_{Z_-} - W_{Z_-}^*) + A_z (p_{Z_-} - p_p)$$

(A1.63)

equation (A1.63) reduces to equation (A1.61) if only the last term is retained corresponding correction equations can be derived for $\mathbf{U}'_{X+}$, $\mathbf{V}'_{Y+}$ and $\mathbf{W}'_{Z+}$. Substitution of equations (A1.59) to (A1.61) into equation (A1.58) leads to the following finite-difference equation for $\mathbf{p}'\mathbf{p}$:

$$C_p^p p_p = C_{X_+}^p p_{X_+} + C_{X_-}^p p_{X_-} + C_{Y_+}^p p_{Y_+} + C_{Y_-}^p p_{Y_-} + C_{Z_+}^p p_{Z_+} + C_{Z_-}^p p_{Z_-} + S_U^p$$

(A1.64)

where

$$C_{X_+}^p = A_x \rho_{x_+} D_{X_+}^U$$

$$C_{X_-}^p = A_x \rho_{x_-} D_{X_-}^U$$

$$C_{Y_+}^p = A_y \rho_{y_+} D_{Y_+}^V$$

$$C_{Y_-}^p = A_y \rho_{y_-} D_{Y_-}^V$$

$$C_{Z_+}^p = A_z \rho_{z_+} D_{Z_+}^W$$

$$C_{Z_-}^P = A_z \rho_{z_-} D_{Z_-}^W$$

(A1.65)

$$S_U^P = -M_p \qquad \textbf{(A1.66)}$$

and

$$C_p^P = A_x (\rho_{x_+} D_{X_+}^U + \rho_{x_-} D_{X_-}^U) + A_y (\rho_{y_+} D_{Y_+}^V + \rho_{y_-} D_{Y_-}^V) + A_z (\rho_{z_+} D_{Z_+}^W +$$

$$+ \rho_{z_-} D_{Z_-}^W)$$

(A1.67)

$\mathbf{D^U_{X+}}$ and $\mathbf{D^U_{X-}}$ are defined analogously to $\mathbf{D^U p}$ in equation (A1.62), whereas $\mathbf{D^V_{Y+}}$, $\mathbf{D^V_{Y-}}$ and $\mathbf{D^W_{Z+}}$ and $\mathbf{D^W_{Z-}}$ are defined similarly to $\mathbf{D^V p}$ and $\mathbf{D^W p}$ respectively.

Solution of equation (A1.64) yields a $\mathbf{P'}$ field, which is then used to correct the pressure and velocities according to

$$\mathbf{P_p = P^*_p + P'_p} \qquad \textbf{(A1.68)}$$

$$\mathbf{Up = U^*_p + U'_p} \qquad \textbf{(A1.69)}$$

$$\mathbf{Vp = V^*_p + V'_p} \qquad \textbf{(A1.70)}$$

$$\mathbf{Wp = W^*_p + W'_p} \qquad \textbf{(A1.71)}$$

The above sequence describes the solution algorithm for one cycle of the calculations. The complete solution proceeds by the iteration repetition of the following steps.

. First, $\mathbf{U^*}$, $\mathbf{V^*}$ and $\mathbf{W^*}$ are calculated from equation (A1.54) to (A1.56) using $\mathbf{p^{*,s}}$, which may be initial guesses or values from a previous iteration.

- The pressure correction equation (A1.64) is solved, and then the pressure and velocity fields are corrected using equation (A1.68) to (A1.71).
- The general finite difference equation (3.29) is then solved successively for the remaining dependent variables.
- The resulting field of variables is now used as the starting point for the next iteration and this process is repeated until a converged solution is reached.

A1.3.2 SOLUTION OF FINITE DIFFERENCE EQUATIONS

(a) TRI-DIAGONAL MATRIX ALGORITHM

The method employed for solving the equation set for each variable is an alternating-direction version of the tri-diagonal matrix algorithm (TDMA) will be describe in section A1.3.4. In this algorithm, the values of ϕ along a particular grid line are obtained simultaneously by a simple form of Gaussian elimination. The TDMA is well suited to calculation of two-dimensional boundary layer flows, where it leads to rapid and economical computations, Patankar and Spalding [39]. However, in the multi-dimensional finite difference equations of the form of equation (3.29) the value of ϕ at a point is related not only to the values at neighbouring nodes on a particular line, but also to those on adjacent lines. Thus the TDMA cannot give the full solution in one application but it can be used in an iteration fashion as follows. By substituting

the best current estimates for the values of ϕ along the four neighbouring lines, equations for the grid line lender consideration are arranged in a form which can be solved by the TDMA. This is first done for all lines lying in one direction (e.g. the **y**-direction). Then, using this solution as the best estimate, solution along grid lines in a second direction (the **x**-direction) is made.

For example, to solve in the **y**-direction equation (3.29) can be

written as:

$$C_p^{\phi}\,\phi_p^{I} = C_{Y_+}^{\phi}\,\phi_{Y_+}^{I} + C_{Y_-}^{\phi}\,\phi_{Y_-}^{I} + (C_{X_+}^{\phi}\,\phi_{X_+} + C_{X_-}^{\phi}\,\phi_{X_-} + C_{Z_+}^{\phi}\,\phi_{Z_+} + C_{Z_-}^{\phi}\,\phi_{Z_-} + S_U^{\phi}) \qquad \textbf{(A1.72)}$$

where the expression in brackets is taken as known, using the currently available values of ϕ_{x+} , ϕ_{x-} , ϕ_{z+} and ϕ_{z-} along the four neighbouring grid lines. The superscript I denotes values obtained after the first sweep. Having solved equation (A1.72) using the TDMA along all **y**-direction lines, a second sweep is made along all **x**-direction lines to solve an equation of the

form:

$$C_p^{\phi}\,\phi_p^{II} = C_{X_+}^{\phi}\,\phi_{X_+}^{II} + C_{X_-}^{\phi}\,\phi_{X_-}^{II} + (C_{Y_+}^{\phi}\,\phi_{Y_+}^{I} + C_{Y_-}^{\phi}\,\phi_{Y_-}^{I} + C_{Z_+}^{\phi}\,\phi_{Z_+} + C_{Z_-}^{\phi}\,\phi_{Z_-} + S_U^{\phi}) \qquad \textbf{(A1.73)}$$

This completes the double sweep for the calculation of one variable ϕ in one **xy** plane. Since equations (A1.72) and (A1.73) are based on old ϕ'^{s} (the quantities in brackets) one double sweep will not normally provide the correction solution.

Several such double sweeps may therefore be necessary before proceeding to the next step.

So far the solution of the finite difference equations has involved TDMA sweeps in the **x** and **y** directions only. Sweeps could also be performed in third direction, but the finite-difference coefficients of equation (3.29) would have to be available for the entire three-dimensional field.

Since this would require very large computer storage, the TDMA is applied only in the **x**- and **y**-directions, and then a 'block correction' is applied in the **z**-direction. This implies that coefficients need be available only in one **xy** plane at a time.

(b) BLOCK-CORRECTION PROCEDURE

The rationale of the block-correction method is to ensure that the integral conservation equations are satisfied over all **xy** planes of the solution domain. This is achieved by making a uniform adjustment of $\delta\phi_k$ to the ϕ values in each **xy** plane, the $\delta\phi_k'^{s}$ being deduced from the integral balance, which is described below.

Suppose that the application of the TDMA sweeps in the **xy** planes has provided an approximate solution to equation

(3.29), denoted by ϕ_{ijk} where **i**, **j**, **k** denote the position in the **x**, **y**, **z** directions respectively. Next a uniform increment $\delta\phi_k$ is added to each ϕ_{ijk} in **xy** plane of constant **k**, such that the original finite difference equation is satisfied when ϕ is replaced by $\phi_{ijk} + \delta\phi_k$ and summation is performed over all interior nodes, **i** and **j**. This process leads to a set of equations which can be expressed as

$$D_k \ \delta\phi_k = A_k \ \delta\phi_{k+1} + B_k \ \delta\phi_{k-1} + C_k \qquad \textbf{(A1.74)}$$

where

$$A_k = \Sigma_i \Sigma_j \ C^{Z_+}_{ijk} \qquad \textbf{(A1.75)}$$

$$B_k = \Sigma_i \ \Sigma_j \ C^{Z_-}_{ijk} \qquad \textbf{(A1.76)}$$

$$C_k = \Sigma_i \Sigma_j \ (C^{X_+}_{ijk} \Phi_{i+1,jk} + C^{X_-}_{ijk} \Phi_{i-1,jk} + C^{Y_+}_{ijk} \Phi_{i,j+1,k} + C^{Y_-}_{ijk}$$

$$\Phi_{i,j-1,k} + C^{Z_+}_{ijk} \Phi_{ij,k+1} + C^{Z_-}_{ijk} \Phi_{ij,k-1} + B_{ijk}) \qquad \textbf{(A1.77)}$$

and

$$D_k = \Sigma_i \Sigma_j \ (C_{ijk} - C^{X_+}_{ijk} - C^{X_-}_{ijk} - C^{Y_+}_{ijk} - C^{Y_-}_{ijk}) \qquad \textbf{(A1.78)}$$

Equation (A1.74) is of the same form as equation (A1.83), and so can be solved by use of the TDMA.

A1.3.3 NUMERICAL STABILITY, CONVERGENCE CRITERIA AND ACCURACY

(a) NUMERICAL STABILITY

Because of the non-linearities of the partial differential equations and the strong inter-linkages between them, numerical instability may develop leading to divergence of the solution during the computations. The nature of these non-linearities and linkages may be seen from equation (3.12) and Table (3.1) where equations for a variable ϕ incorporate functions of ϕ itself and, via the source term, of other dependent variables in the equation set. These instabilities usually lead to imbalance in conservation of a property ϕ within each control volume and hence over the whole domain, and to oscillation of the calculated values of a variable over successive iterations. Three important factors which may provoke instabilities include poor specification of initial fields, inappropriate choice of under-relaxation factors, and incomplete solution of the equations during iteration. Possible methods of avoiding these instabilities are suggested below.

A simple way to avoid instability arising from poorly specified initial distributions is to provide initial values which are as close as possible to the final solution, this guess might take the form of a previous solution, adjusted if necessary to allow for changed conditions.

Under-relaxation promotes stability by carrying forward

from one iteration to the next a value, ϕ_{new}, which is a weighted mean of the value ϕ, calculated from equation (3.29), and the value ϕ_{old} from the previous iteration. Thus solution, adjusted if necessary to allow for changed conditions. Thus

$$\phi_{new} = \alpha_\phi \phi + (1-\alpha_\phi)\ \phi_{old} \qquad \textbf{(A1.79)}$$

Where α_ϕ is the under-relaxation factor ($|\alpha_\phi|<1$).
In this study α_ϕ was assigned values between 0.1 and 0.7 depending on the variable in question.

The only available method for choosing the most satisfactory factors is that of trial and error, but it is a good practice to limit the maximum value of α_ϕ for the momentum equation to 0.5.

Incomplete solution of the finite difference equations is shown by the existence of unduly large residual sources, defined as the imbalance of terms when the current solution is substituted into the finite difference equations (see section (b) below).
If the variable fields having large residual sources are used in the calculation of other variables, the errors can be magnified thereby causing instability. In this case an increase is required in the number of applications of the TDMA sweeps within the iteration procedure.

(b) CONVERGENCE CRITERIA

The convergence of the iterative procedure is assessed by

examination of the residual sources of the difference equations and the fractional changes in the ϕ's between iterations. The first criterion is based on the residual source of ϕ, R_ϕ, which is defined from equation (3.29) as

$$R_\phi = C_P^\phi \phi_P - \Sigma_n C_n^\phi \phi_n - S_\phi \qquad \textbf{(A1.80)}$$

and should, of course, be zero if the current solution satisfies equation (3.29). The physical meaning of R_ϕ depends on the equation to be solved. In the momentum equation R_ϕ represents an imbalance in conservation of momentum, and for the continuity equation it represents an imbalance in mass conservation. The criterion applied is:

$$\Sigma \mid R_\phi \mid < \lambda_R . R_{\phi_{ref}} \qquad \textbf{(A1.81)}$$

where $R_{\phi ref}$ is some reference value. In this study only the mass conservation imbalance was monitored since this provides a sensitive test for convergence. The reference value used was the incoming mass flow rate and λ_R was 10^{-4}. The second criterion required that the changes of values between two iterations be a small fraction of some reference value, ϕ_{ref} , i.e.

$$[(\phi_{new} - \phi_{old}) / \phi_{ref}]_{max} < \lambda_\phi \qquad \textbf{(A1.82)}$$

where, λ_ϕ is of the order of 10^{-3} and ϕ_{ref} is a representative value for the quantity ϕ in the particular flow situation being studied.

(c) ACCURACY OF SOLUTIONS

Four factors which may influence the accuracy of the predictions may be identified. These are the degree to which the solution satisfies the differential equations, the degree to which it satisfies the finite difference equations, the location of, and conditions imposed at, the boundaries, and the adequacy of the turbulence model.

The first factor results from discretization errors, which are a consequence of representing the continuous distribution of ϕ in terms of values at the grid nodes of finite-difference mesh, and interpolating between them. These errors can be reduced by reducing the spacing between nodes to an acceptable level, preferably by using a non-uniform grid, with nodes concentrated in regions of high gradients. Evidence of the existence or otherwise of discretization errors is obtainable from grid refinement tests, in which the number of grid nodes is systematically increased until changes in the solution become smaller than an acceptable tolerance. Since ϕ_p is evaluated as a weighted mean of the ϕ's at the adjacent nodes, smearing of the profile may occur in a situation where a steep gradient in ϕ occurs. This leads to "false diffusion" which can be minimized by arranging the finite difference grid parallel to the streamlines and by keeping the cell peclet numbers small. The first practice is not feasible in a recirculating flow, and so the latter approach must be used by employing a fine grid mesh in regions where sharp

changes in ϕ are expected.

Concerning the second factor, the extent to which the current solution satisfies the finite difference equations can assessed by ensuring that the residual sources for each variable have been reduced to an acceptable level.

Errors caused by inappropriate location of boundaries or specification of boundary conditions can be detected by adjusting the locations and conditions and determining the sensitivity of the solution to such changes.

If all of the above factors have been eliminated, the adequacy of the turbulence model may then be assessed by comparing the solution with experimental data.

A1.3.4 TRI-DIAGONAL MATRIX ALGORITHM (TDMA)

The TDMA enables the solution of a set of simultaneous, linear, algebraic equations which relate the values of ϕ at adjacent points along a line in the form:

$$\phi_i = A_i \phi_{i+1} + B_i \phi_{i-1} + C_i \qquad \text{(A1.83)}$$

The subscript **i** runs from 1 to **N** and $A_N = B_1 = 0$. The equations (A1.83) can be written in simpler form as

$$\phi_i = A'_i \phi_{i+1} + B'_i \qquad \text{(A1.84)}$$

where the transformed coefficients are now given by recurrence relations as

$$A'_i = A_i/1-B_i\ A'_{i-1} \qquad \text{(A1.85)}$$

$$B'_i = B_i\ B'_{i-1} + C_i/1-B_i\ A'_{i-1} \qquad \text{(A1.86)}$$

The solution is obtained by successive substitution; to start the recurrence process the coefficients are given values:

$A'_1 = 0$ and $B'_1 = 0$.

A1.4 TURBULENCE MODELS

A1.4.1 CLASSIFICATION OF MODELS

Reynolds stress term u_iu_j, which were introduced in section 3.2.2, involve time averages of the products of velocity fluctuations. They represent unknown in the momentum conservation equation (3.7), and additional equations are, therefore, required to enable these Reynolds stresses to be calculated.

The necessary algebraic or differential equation collectively constitute a 'turbulence model'.

The criteria for the choice of a turbulence model include economy of computations, degree of universality, and accuracy. A classification scheme for turbulence models and some examples of their applications are provided by Launder and Spalding [33].

Turbulence models can conveniently be classified according to the number of additional differential equations which they contain. Most zero-, one- and two-equation models represent the Reynolds shear stresses by way of the

turbulent viscosity concept, already introduced in equation (3.8) of section 3.2.2.

Typically, the turbulent viscosity is taken to be proportional to the product of a velocity scale and a length scale characteristics of the local turbulent flow. Zero-equation models employ the mixing length hypothesis, Prandtl [41] in which the length scale is specified by "mixing length" ℓ_m and the velocity scale is of the form $\ell_m|dW/dy|$; the velocity gradient dW/dy is calculated from local mean flow conditions. This model is applicable to simple, two-dimensional boundary layer flows, Patankar and Spalding [39] where ℓ_m is easily prescribed empirically and the predominant mean velocity gradient does not change sign.

In one- and two-equation models, μ_t is related to the kinetic energy of turbulence, $k \equiv 1/2\ u^2_i$,and a length scale ℓ by the expression

$$\mu_t = C_\mu\ \rho\ k^{1/2}\ell \qquad \text{(A1.83)}$$

where C_μ is an empirical coefficient. One-equation models solve a differential transport equation for k (section A1.4.2) but require empirical specification of ℓ. Such a model was used with considerable success by Launder and Ying [35] to predict the fully developed flow in a square duct, but this was one of the few situations (other than a two-dimensional boundary layer) where sufficient knowledge of the length scale distribution was available.

Two-equation models provide a more general approach by

solving transport equations for both **k** and a quantity related to the length scale. In practice, it proves to be more satisfactory to solve for the turbulent dissipation, **ε**, rather than for the dissipation length scale, **ℓ**. The two variables are related, Launder and Spalding [34] by the equation

$$\varepsilon = C_D \, k^{3/2}/\ell \qquad \textbf{(A1.84)}$$

where the constant C_D can be set equal to unity without loss of generality.

By combining equations (A1.83) and (A1.84) the turbulent viscosity can be linked to **k** and ε thus:

$$\mu_t = C_\mu \rho \frac{k^2}{\varepsilon} \qquad \textbf{(A1.85)}$$

Two-equation models are the simplest available means of calculating turbulent stresses in recirculating or separated flows where the length scale distribution cannot be prescribed algebraically. Such models have been applied to wall boundary layers, Ng [38]; Jones and Launder [29], free shear flows, Launder, Mores, Rodi and Spalding [31] and two-dimensional recirculating flows over a backward facing step, Matthews and Whitelaw [37], with swirl Roberts [42] and through in-line tube banks, Le Feuvre [36].

More elaborate turbulence models exist which do not employ the turbulent viscosity concept but solve differential equations for the Reynolds stresses.

In a study of a two-dimensional channel flow, Hanjalic and

Launder [27] solved an equation for one shear stress component in addition to equations for the kinetic energy and dissipation. This model was later extended by replacing the turbulence energy equation by transport equations for the three normal stresses and solving these along with equations for shear stress and dissipation. The resulting five-equation model has been applied to plane jet and wake flows by Launder et al. [32]. Seven equations (six Reynolds stress components and dissipation) are required in the application of the Reynolds stress models to three-dimensional flows. The relative merits of the approaches mentioned above will now be discussed.

In the present study the two-equation **k-ε** turbulence model was employed to predict two-dimensional flows over the aluminium blocks. These flows are characterised by regions of recirculation and an extensive wake.

Zero-and one-equation models are clearly inadequate for such flows because of their reliance on a prescribed length scale distribution, and so a two-equation model was the simplest one which could be accepted. It could be argued that Reynolds stress models should have been used on the grounds that the turbulent viscosity concept is incapable of representing all of the known features of such flows. However, a recent study by Pope and Whitelaw [83] suggests that such an approach may not be profitable at the present state of development of the Reynolds stress models. They investigated the performance of several turbulence models in predicting the shear flows behind axisymmetric bluff

bodies.

A1.4.2 TRANSPORT EQUATIONS FOR TURBULENT KINETIC ENERGY AND DISSIPATION RATE

The exact transport equation for turbulent kinetic energy, first derived by Kolmogorov [30], is obtained via the equation for the turbulent velocity fluctuation u_i. The latter equation can be derived with the help of equation (3.5) by subtracting the time-averaged momentum equation (3.7) from the time-dependent momentum equation (3.2). The result is

$$U_j \frac{du_i}{dx_j} = -u_j \frac{dU_i}{dx_j} - \frac{d}{dx_j}\left(u_i u_j - \overline{u_i u_j}\right) - \frac{1}{\rho}\frac{dp}{dx_i} + \nu \frac{d^2 u_i}{dx_j^2} \qquad \textbf{(A1.86)}$$

where p represents the fluctuating pressure. By multiplying the above equation by u_i, time averaging, and introducing the definition $k \equiv 1/2\ u^2_i$, one obtains the turbulent kinetic energy equation, Launder and Spalding [34]:

$$U_j \frac{dk}{dx_j} = -\overline{u_i u_j}\frac{dU_i}{dx_j} - \frac{d}{dx_j}\left(\frac{\overline{u_j u_i^2}}{2} + \frac{\overline{u_j p}}{\rho} - \nu \frac{dk}{dx_j}\right) - \nu \overline{\left(\frac{du_i}{dx_j}\right)^2} \qquad \textbf{(A1.87)}$$

Introducing the "instantaneous kinetic energy" $k' \equiv 1/2\ u^2_i$ leads to alternative form:

$$U_j \frac{dk}{dx_j} = -\overline{u_i u_j} \frac{dU_i}{dx_j} - \frac{d}{dx_j}\left(\frac{\overline{u_j p}}{\rho} + \overline{u_j k} - \nu \frac{dk}{dx_j}\right) - \epsilon$$

I **II** **III** **IV**

(A1.88)

where

$$\epsilon = \nu \overline{\left(\frac{du_i}{dx_j}\right)^2} \qquad \textbf{(A1.89)}$$

Equation (A1.88) expresses the fact that changes of kinetic energy **(I)** of a small element of fluid occur, Launder and Spalding [33] as a result of an imbalance between **(II)** generation of k by the interaction of shear stresses with mean velocity gradients, **(III)** diffusive transport by pressure fluctuations, velocity fluctuations and molecular diffusion; and **(IV)** destruction of **k** by viscous action. In high Reynolds number flows (i.e. flows for which the effect of molecular viscosity may be neglected), the above equation can be modelled Rodi [43] as

$$\frac{d\rho U_j k}{dx_j} = \frac{d}{dx_j}\left(\frac{\mu_{eff}}{\sigma_k} \frac{dk}{dx_j}\right) + G - \rho\epsilon \qquad \textbf{(A1.90)}$$

where **G** represents term **II** of equation (A1.88). Within the context of a turbulent viscosity model, **G** can be expressed with the aid of equation (3.8) as

$$G = \mu_{eff} \frac{dU_i}{dx_j}\left(\frac{dU_i}{dxj} + \frac{dU_j}{dx_i}\right) \qquad \textbf{(A1.91)}$$

Term **III** of equation (A1.88) has been modelled in equation (A1.90) according to a hypothesis that **k** diffuses along its own gradient, in the manner of many scalar properties.
An exact equation for ε can be derived by a similar procedure to that used above, Harlow and Nakayama [47]; Daly and Harlow [25]. The resulting equation is long and complicated, and it will suffice here to state a modelled form, Launder and Spalding [76]:

$$\frac{d\rho U_j \epsilon}{dx_j} = \frac{d}{dx_j}\left(\frac{\mu_{eff}}{\sigma_\epsilon}\frac{d\epsilon}{dx_j}\right) + \frac{\epsilon}{k}\left(C_1 G - C_2\,\rho\epsilon\right) \qquad \textbf{(A1.92)}$$

The basis of the modelling has been discussed by Rodi [43]. The values of the constants $\sigma_k, \sigma_\varepsilon, C_1$ and C_2 appearing in equations (A1.90) and (A1.92) are given in Chapter (3) section 3.5.3 (Table 3.2).

APPENDIX [2]

PHOENICS PROGRAM STRUCTURES

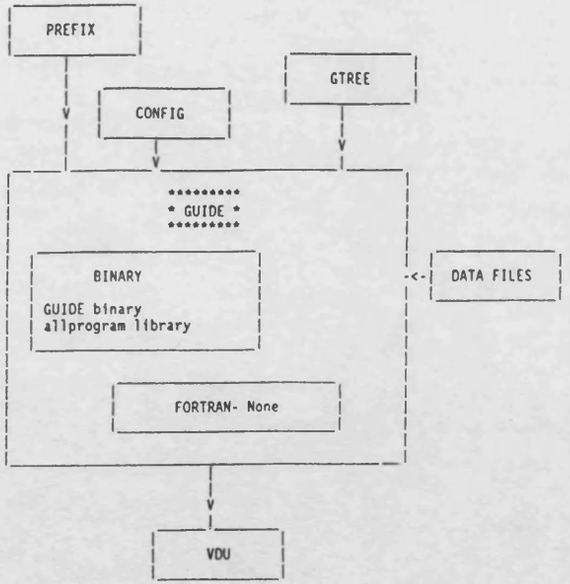

FIGURE 2.1: FLOW DIAGRAM OF GUIDE

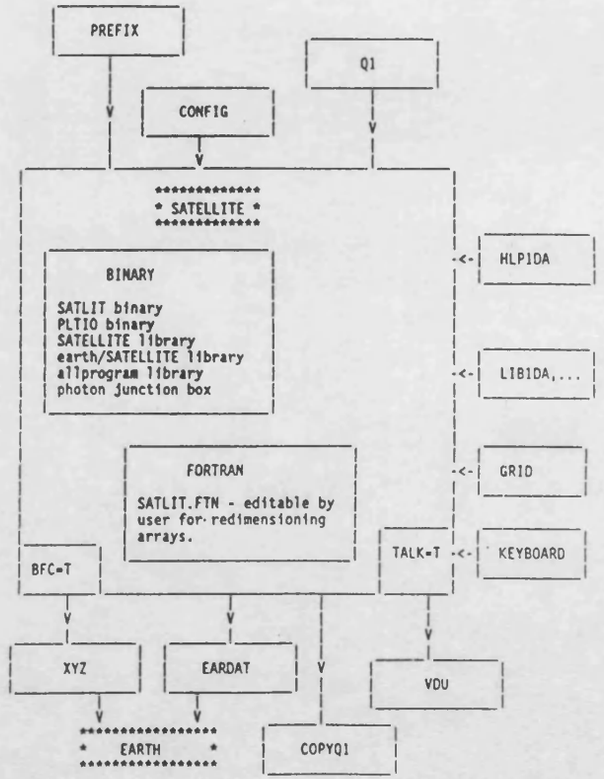

FIGURE 2.2: FLOW DIAGRAM OF SATELLITE

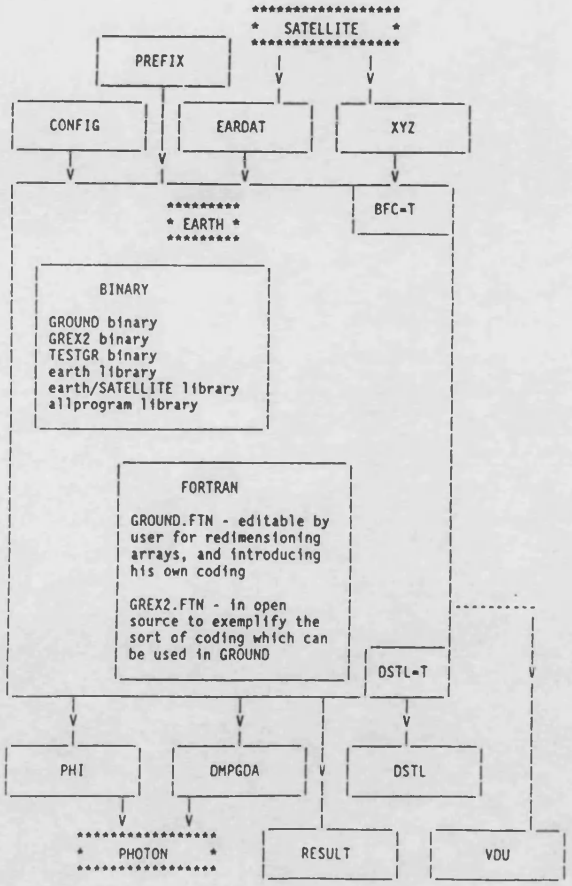

FIGURE 2.3: FLOW DIAGRAM OF EARTH

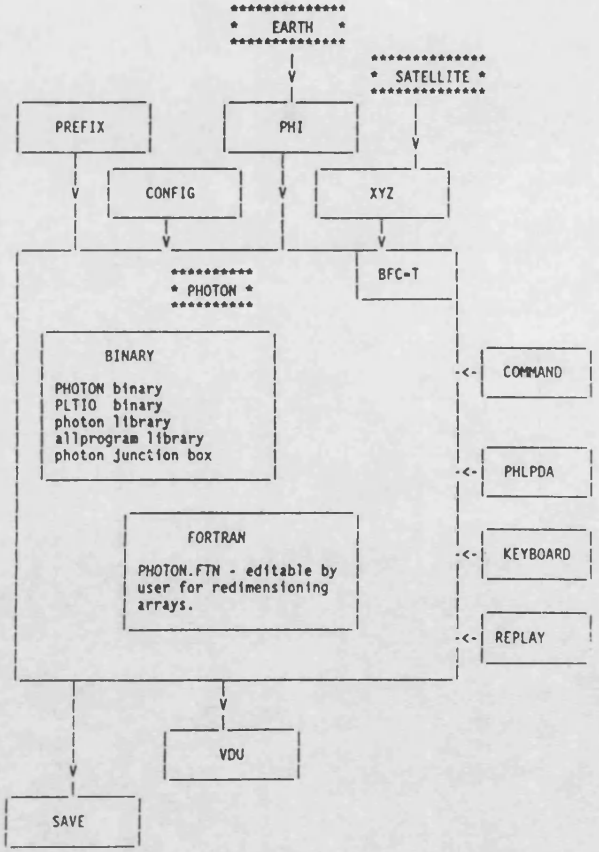

FIGURE 2.4: FLOW DIAGRAM OF PHOTON

a) COMPLETE LISTING OF SATELLITE PROGRAM

```
TALK=T;RUN( 1, 1);VDU=TTY

 ** LOAD(290) FROM THE PHOENICS INPUT LIBRARY

290: ****** TO LOAD CASE: TYPE LOAD(290) ******

**************************************************

    GROUP 1. Run title and other preliminaries

TEXT(CONJUGATE HEAT TRANSFER:K-E MODEL)
     **
     **

     * DECLARE SPECIAL VARIABLES

INTEGER(VARNUM)
INTEGER(NYS,NXS)



REAL(HEIGHT,WIDTH,CLEN,SLEN,REYNO,UIN,TKEIN,EPSIN,GENUT)
REAL(RHOSOL,RHOFLU,CPSOL,CPFLU)
REAL(TMPSOL,TMPFLU,TIN)
REAL(KSOLID,KFLUID,FLUCON,HFREE,HIN)
REAL(DTFL,PIN,PEXIT,RHOIN,RHOOUT,TFREE,UEXIT)

     ** INITIALISATION
     ** Calculation of domain specifications
     ** The properties are at 20c **

HEIGHT=0.1;WIDTH=0.1
RHOSOL=2707;RHOFLU=1.1614;CPSOL=896;CPFLU=1007
    TMPSOL=348.1;TMPFLU=296;TIN=296;TFREE=296
KSOLID=204;KFLUID=0.0263;FLUCON=287.0
HFREE=273*CPFLU

     **INLET CONDITIONS
     *
   PIN=1.013E5
UIN=10
```

```
      ** DOWNSTREAM CONDITIONS
      *
   PEXIT=PIN
   RHOOUT=PEXIT/(FLUCON*TFREE)

**************************************************


    GROUP 2. Transience; time-step specification
    GROUP 3. X-direction grid specification


NX=125;XULAST=1.25

      ** Full length of channel = 1.25

XFRAC(1)=-34;XFRAC(2)=0.008
XFRAC(3)=75;XFRAC(4)=0.008
XFRAC(5)=16;XFRAC(6)=0.008

**************************************************

    GROUP 4. Y-direction grid specification


NY=16;YVLAST=0.16

      ** Full width of channel = 0.05

YFRAC(1)=-10;YFRAC(2)=0.0625
YFRAC(3)=10;YFRAC(4)=0.01
YFRAC(5)=5;YFRAC(6)=0.1

**************************************************

    GROUP 5. Z-direction grid specification
    GROUP 6. Body-fitted coordinates or grid distortion
    GROUP 7. Variables stored, solved & named
    *
SOLVE(P1,U1,V1,H1,RHO1,PRAN)
SOLUTN(P1,Y,Y,Y,N,N,N)
SOLUTN(H1,Y,Y,Y,N,N,Y)
SOLUTN(RHO1,Y,N,N,N,N,N)
SOLUTN(PRAN,Y,N,N,N,N,N)
TURMOD(KEMODL);STORE(ENUT,TMP1);VARNUM=49
    *
```

```
**************************************************

    GROUP 8. Terms (in differential equations) & devices
    DIFCUT=0.0

    * SOLVE FOR H1 AS STATIC ENTHALPY (SOURCE TERMS ACTIVE)
    *
TERMS(H1,N,Y,Y,N,Y,N)
    *

**************************************************

    GROUP 9. Properties of the medium (or media)
    *
    * LAMINAR VISCOSITY (ENUT COMPUTED IN GREX1)
    *
ENUL=1.0E-5
    *
TMP1=GRND2;TMP1A=0.0;TMP1B=1.0/CPFLU

PRNDTL(H1)=-GRND
    *


    * DENSITY FORMULATION (PERFECT GAS LAW)
    *
RHO1=1.0


**************************************************


    GROUP 10. Inter-phase-transfer processes and properties
    GROUP 11. Initialization of variable or porosity fields

      INIADD=F
HIN=CPFLU*273

     ** Calculation of KE (where fric=0.018)...

TKEIN=0.25*UIN*UIN*0.018
    TKEIN=(2/100)*UIN**2
     ** Calculation of EP (where lmix=0.09 x h)...

EPSIN=TKEIN**1.5*0.1643/3.429E-3
    EPSIN=0.1643*TKEIN**2/(0.1*YVLAST)
```

```
      ** Initial values

FIINIT(RHO1)=RHO1
FIINIT(U1)=UIN;FIINIT(P1)=1.3E-4;FIINIT(V1)=0.0
FIINIT(KE)=TKEIN;FIINIT(EP)=EPSIN
FIINIT(PRAN)=KFLUID/CPFLU
FIINIT(H1)=HFREE
FIINIT(TMP1)=273
      RESTRT(ALL)

      ** Initialization of variables in blocked region

     CONPOR(0.0,CELL,1,-NXS,1,-NYS,1,1)

      * INITIALIZATION INSIDE CHIPS*

PATCH(CHIP1,INIVAL,35,39,1,4,1,1,1,1)
COVAL(CHIP1,RHO1,1.0E+2,RHOSOL*CPSOL/CPFLU)
COVAL(CHIP1,PRAN,1.0E+2,KSOLID/CPFLU)
COVAL(CHIP1,U1,FIXVAL,1.0E-10);COVAL(CHIP1,V1,FIXVAL,1.0E-10)

PATCH(CHIP2,INIVAL,45,49,1,4,1,1,1,1)


COVAL(CHIP2,RHO1,1.0E+2,RHOSOL*CPSOL/CPFLU)
COVAL(CHIP2,PRAN,1.0E+2,KSOLID/CPFLU)
COVAL(CHIP2,U1,FIXVAL,1.0E-10);COVAL(CHIP2,V1,FIXVAL,1.0E-10)

PATCH(CHIP3,INIVAL,55,59,1,4,1,1,1,1)
COVAL(CHIP3,RHO1,1.0E+2,RHOSOL*CPSOL/CPFLU)
COVAL(CHIP3,PRAN,1.0E+2,KSOLID/CPFLU)
COVAL(CHIP3,U1,FIXVAL,1.0E-10);COVAL(CHIP3,V1,FIXVAL,1.0E-10)

PATCH(CHIP4,INIVAL,65,69,1,4,1,1,1,1)
COVAL(CHIP4,RHO1,1.0E+2,RHOSOL*CPSOL/CPFLU)
COVAL(CHIP4,PRAN,1.0E+2,KSOLID/CPFLU)
COVAL(CHIP4,U1,FIXVAL,1.0E-10);COVAL(CHIP4,V1,FIXVAL,1.0E-10)

PATCH(CHIP5,INIVAL,75,79,1,4,1,1,1,1)
COVAL(CHIP5,RHO1,1.0E+2,RHOSOL*CPSOL/CPFLU)
COVAL(CHIP5,PRAN,1.0E+2,KSOLID/CPFLU)
COVAL(CHIP5,U1,FIXVAL,1.0E-10);COVAL(CHIP5,V1,FIXVAL,1.0E-10)

PATCH(CHIP6,INIVAL,85,89,1,4,1,1,1,1)
COVAL(CHIP6,RHO1,1.0E+2,RHOSOL*CPSOL/CPFLU)
COVAL(CHIP6,PRAN,1.0E+2,KSOLID/CPFLU)
COVAL(CHIP6,U1,FIXVAL,1.0E-10);COVAL(CHIP6,V1,FIXVAL,1.0E-10)
```

```
PATCH(CHIP7,INIVAL,95,99,1,4,1,1,1,1)
COVAL(CHIP7,RHO1,1.0E+2,RHOSOL*CPSOL/CPFLU)
COVAL(CHIP7,PRAN,1.0E+2,KSOLID/CPFLU)
COVAL(CHIP7,U1,FIXVAL,1.0E-10);COVAL(CHIP7,V1,FIXVAL,1.0E-10)

PATCH(CHIP8,INIVAL,105,109,1,4,1,1,1,1)
COVAL(CHIP8,RHO1,1.0E+2,RHOSOL*CPSOL/CPFLU)
COVAL(CHIP8,PRAN,1.0E+2,KSOLID/CPFLU)
COVAL(CHIP8,U1,FIXVAL,1.0E-10);COVAL(CHIP8,V1,FIXVAL,1.0E-10)


*************************************************************

    GROUP 12. Convection and diffusion adjustments
    GROUP 13. Boundary conditions and special sources

  **  Inlet west-x inflow conditions

PATCH(INLET,WEST,1,1,1,NY,1,1,1,1)
COVAL(INLET,P1,FIXFLU,RHO1*UIN);COVAL(INLET,U1,ONLYMS,UIN)
COVAL(INLET,H1,ONLYMS,HIN)
COVAL(INLET,KE,ONLYMS,TKEIN);COVAL(INLET,EP,ONLYMS,EPSIN)



  **  Exit fixed pressure boundary downstream

PATCH(OUTLET,EAST,NX,NX,1,NY,1,1,1,1)
COVAL(OUTLET,P1,1.0E+05,0.0)
COVAL(OUTLET,H1,ONLYMS,HIN)

  **  WALL BOUNDARY CONDITIONS
      *
  **    N-wall

PATCH(TOPWAL,NWALL,1,NX,NY,NY,1,1,1,1)
COVAL(TOPWAL,U1,GRND2,0.0)
COVAL(TOPWAL,KE,GRND2,GRND2)
COVAL(TOPWAL,EP,GRND2,GRND2)

  **    S1-wall

PATCH(BOTWAL1,SWALL,1,34,1,1,1,1,1,1)
COVAL(BOTWAL1,U1,GRND2,0.0)
COVAL(BOTWAL1,KE,GRND2,GRND2);COVAL(BOTWAL1,EP,GRND2,GRND2)

  **    S2-wall
```

```
PATCH(BOTWAL9,SWALL,110,125,1,1,1,1,1,1)
COVAL(BOTWAL9,U1,GRND2,0.0)
COVAL(BOTWAL9,KE,GRND2,GRND2);COVAL(BOTWAL9,EP,GRND2,GRND2)

PATCH(BOTWAL2,SWALL,40,44,1,1,1,1,1,1)
COVAL(BOTWAL2,U1,GRND2,0.0)
COVAL(BOTWAL2,KE,GRND2,GRND2);COVAL(BOTWAL2,EP,GRND2,GRND2)

PATCH(BOTWAL3,SWALL,50,54,1,1,1,1,1,1)
COVAL(BOTWAL3,U1,GRND2,0.0)
COVAL(BOTWAL3,KE,GRND2,GRND2);COVAL(BOTWAL3,EP,GRND2,GRND2)

PATCH(BOTWAL4,SWALL,60,64,1,1,1,1,1,1)
COVAL(BOTWAL4,U1,GRND2,0.0)
COVAL(BOTWAL4,KE,GRND2,GRND2);COVAL(BOTWAL4,EP,GRND2,GRND2)

PATCH(BOTWAL5,SWALL,70,74,1,1,1,1,1,1)
COVAL(BOTWAL5,U1,GRND2,0.0)
COVAL(BOTWAL5,KE,GRND2,GRND2);COVAL(BOTWAL5,EP,GRND2,GRND2)

PATCH(BOTWAL6,SWALL,80,84,1,1,1,1,1,1)
COVAL(BOTWAL6,U1,GRND2,0.0)
COVAL(BOTWAL6,KE,GRND2,GRND2);COVAL(BOTWAL6,EP,GRND2,GRND2)



PATCH(BOTWAL7,SWALL,90,94,1,1,1,1,1,1)
COVAL(BOTWAL7,U1,GRND2,0.0)
COVAL(BOTWAL7,KE,GRND2,GRND2);COVAL(BOTWAL7,EP,GRND2,GRND2)

PATCH(BOTWAL8,SWALL,100,104,1,1,1,1,1,1)
COVAL(BOTWAL8,U1,GRND2,0.0)
COVAL(BOTWAL8,KE,GRND2,GRND2);COVAL(BOTWAL8,EP,GRND2,GRND2)


     * FLOW SETTINGS FOR CHIPS *

PATCH(CHIP1BC,CELL,35,39,1,4,1,1,1,1)
COVAL(CHIP1BC,U1,FIXVAL,1.0E-10);COVAL(CHIP1BC,V1,FIXVAL,1.0E-10)


PATCH(CHIP2BC,CELL,45,49,1,4,1,1,1,1)
COVAL(CHIP2BC,U1,FIXVAL,1.0E-10);COVAL(CHIP2BC,V1,FIXVAL,1.0E-10)

PATCH(CHIP3BC,CELL,55,59,1,4,1,1,1,1)
COVAL(CHIP3BC,U1,FIXVAL,1.0E-10);COVAL(CHIP3BC,V1,FIXVAL,1.0E-10)
```

```
PATCH(CHIP4BC,CELL,65,69,1,4,1,1,1,1)
COVAL(CHIP4BC,U1,FIXVAL,1.0E-10);COVAL(CHIP4BC,V1,FIXVAL,1.0E-10)

PATCH(CHIP5BC,CELL,75,79,1,4,1,1,1,1)
COVAL(CHIP5BC,U1,FIXVAL,1.0E-10);COVAL(CHIP5BC,V1,FIXVAL,1.0E-10)

PATCH(CHIP6BC,CELL,85,89,1,4,1,1,1,1)
COVAL(CHIP6BC,U1,FIXVAL,1.0E-10);COVAL(CHIP6BC,V1,FIXVAL,1.0E-10)

PATCH(CHIP7BC,CELL,95,99,1,4,1,1,1,1)
COVAL(CHIP7BC,U1,FIXVAL,1.0E-10);COVAL(CHIP7BC,V1,FIXVAL,1.0E-10)

PATCH(CHIP8BC,CELL,105,109,1,4,1,1,1,1)
COVAL(CHIP8BC,U1,FIXVAL,1.0E-10);COVAL(CHIP8BC,V1,FIXVAL,1.0E-10)



    * BOUNDARY LAYERS ON CHIPS SURFACES *



STORE(GENR)

PATCH(CH1UP,EWALL,34,34,1,4,1,1,1,1)
COVAL(CH1UP,V1,GRND2,0.0)
COVAL(CH1UP,KE,GRND2,GRND2)
COVAL(CH1UP,EP,GRND2,GRND2)

PATCH(CH1TOP,SWALL,35,39,5,5,1,1,1,1)
COVAL(CH1TOP,U1,GRND3,0.0)
COVAL(CH1TOP,EP,GRND3,GRND3)

PATCH(CH1DOW,WWALL,40,40,1,4,1,1,1,1)
COVAL(CH1DOW,V1,GRND2,0.0)
COVAL(CH1DOW,KE,GRND2,GRND2)
COVAL(CH1DOW,EP,GRND2,GRND2)

PATCH(CH2UP,EWALL,44,44,1,4,1,1,1,LSTEP)
COVAL(CH2UP,V1,GRND2,0.0)
COVAL(CH2UP,H1,GRND2,298.5*CPFLU)
COVAL(CH2UP,KE,GRND2,GRND2)
COVAL(CH2UP,EP,GRND2,GRND2)
```

```
PATCH(CH2TOP,SWALL,45,49,5,5,1,1,1,LSTEP)
COVAL(CH2TOP,U1,GRND3,0.0)
COVAL(CH2TOP,H1,GRND2,298.5*CPFLU)
COVAL(CH2TOP,EP,GRND3,GRND3)

PATCH(CH2DOW,WWALL,50,50,1,4,1,1,1,LSTEP)
COVAL(CH2DOW,V1,GRND2,0.0)
COVAL(CH2DOW,H1,GRND2,298.5*CPFLU)
COVAL(CH2DOW,KE,GRND2,GRND2)
COVAL(CH2DOW,EP,GRND2,GRND2)

PATCH(CH3UP,EWALL,54,54,1,4,1,1,1,1)
COVAL(CH3UP,V1,GRND2,0.0)
COVAL(CH3UP,H1,GRND2,301.9*CPFLU)
COVAL(CH3UP,KE,GRND2,GRND2);COVAL(CH3UP,EP,GRND2,GRND2)

PATCH(CH3TOP,SWALL,55,59,5,5,1,1,1,1);COVAL(CH3TOP,U1,GRND3,0.0)
COVAL(CH3TOP,EP,GRND3,GRND3)
COVAL(CH3TOP,H1,GRND2,301.9*CPFLU)

PATCH(CH3DOW,WWALL,60,60,1,4,1,1,1,1);COVAL(CH3DOW,V1,GRND2,0.0)
COVAL(CH3DOW,KE,GRND2,GRND2);COVAL(CH3DOW,EP,GRND2,GRND2)


COVAL(CH3DOW,H1,GRND2,301.9*CPFLU)

PATCH(CH4UP,EWALL,64,64,1,4,1,1,1,1);COVAL(CH4UP,V1,GRND2,0.0)
COVAL(CH4UP,KE,GRND2,GRND2);COVAL(CH4UP,EP,GRND2,GRND2)

PATCH(CH4TOP,SWALL,65,69,5,5,1,1,1,1);COVAL(CH4TOP,U1,GRND3,0.0)
COVAL(CH4TOP,EP,GRND3,GRND3)

PATCH(CH4DOW,WWALL,70,70,1,4,1,1,1,1);COVAL(CH4DOW,V1,GRND2,0.0)
COVAL(CH4DOW,KE,GRND2,GRND2);COVAL(CH4DOW,EP,GRND2,GRND2)

PATCH(CH5UP,EWALL,74,74,1,4,1,1,1,1);COVAL(CH5UP,V1,GRND2,0.0)
COVAL(CH5UP,KE,GRND2,GRND2);COVAL(CH5UP,EP,GRND2,GRND2)

PATCH(CH5TOP,SWALL,75,79,5,5,1,1,1,1);COVAL(CH5TOP,U1,GRND3,0.0)
COVAL(CH5TOP,EP,GRND3,GRND3)

PATCH(CH5DOW,WWALL,80,80,1,4,1,1,1,1);COVAL(CH5DOW,V1,GRND2,0.0)
COVAL(CH5DOW,KE,GRND2,GRND2);COVAL(CH5DOW,EP,GRND2,GRND2)

PATCH(CH6UP,EWALL,84,84,1,4,1,1,1,1);COVAL(CH6UP,V1,GRND2,0.0)
COVAL(CH6UP,KE,GRND2,GRND2);COVAL(CH6UP,EP,GRND2,GRND2)
```

```
PATCH(CH6TOP,SWALL,85,89,5,5,1,1,1,1);COVAL(CH6TOP,U1,GRND3,0.0)
COVAL(CH6TOP,EP,GRND3,GRND3)

PATCH(CH6DOW,WWALL,90,90,1,4,1,1,1,1);COVAL(CH6DOW,V1,GRND2,0.0)
COVAL(CH6DOW,KE,GRND2,GRND2);COVAL(CH6DOW,EP,GRND2,GRND2)

PATCH(CH7UP,EWALL,94,94,1,4,1,1,1,1);COVAL(CH7UP,V1,GRND2,0.0)
COVAL(CH7UP,KE,GRND2,GRND2);COVAL(CH7UP,EP,GRND2,GRND2)

PATCH(CH7TOP,SWALL,95,99,5,5,1,1,1,1);COVAL(CH7TOP,U1,GRND3,0.0)
COVAL(CH7TOP,EP,GRND3,GRND3)

PATCH(CH7DOW,WWALL,100,100,1,4,1,1,1,1);COVAL(CH7DOW,V1,GRND2,0.0)
COVAL(CH7DOW,KE,GRND2,GRND2);COVAL(CH7DOW,EP,GRND2,GRND2)

PATCH(CH8UP,EWALL,104,104,1,4,1,1,1,1);COVAL(CH8UP,V1,GRND2,0.0)
COVAL(CH8UP,KE,GRND2,GRND2);COVAL(CH8UP,EP,GRND2,GRND2)

PATCH(CH8TOP,SWALL,105,109,5,5,1,1,1,1);COVAL(CH8TOP,U1,GRND3,0.0)
COVAL(CH8TOP,EP,GRND3,GRND3)

PATCH(CH8DOW,WWALL,110,110,1,4,1,1,1,1);COVAL(CH8DOW,V1,GRND2,0.0)


COVAL(CH8DOW,KE,GRND2,GRND2);COVAL(CH8DOW,EP,GRND2,GRND2)




    * TEMPERATURE SOURCE *

PATCH(BOTSIDE1,SOUTH,35,39,1,1,1,1,1,1)
COVAL(BOTSIDE1,H1,FIXFLU,6750)

PATCH(BOTSIDE2,SOUTH,45,49,1,1,1,1,1,1)
COVAL(BOTSIDE2,H1,FIXFLU,6750)

COVAL(BOTSIDE3,SOUTH,55,59,1,1,1,1,1,1)
COVAL(BOTSIDE3,H1,FIXFLU,6750)

PATCH(BOTSIDE4,SOUTH,65,69,1,1,1,1,1,1)
COVAL(BOTSIDE4,H1,FIXFLU,6750)

PATCH(BOTSIDE5,SOUTH,75,79,1,1,1,1,1,1)
COVAL(BOTSIDE5,H1,FIXFLU,6750)
```

```
PATCH(BOTSIDE6,SOUTH,85,89,1,1,1,1,1,1)
COVAL(BOTSIDE6,H1,FIXFLU,6750)

PATCH(BOTSIDE7,SOUTH,95,99,1,1,1,1,1,1)
COVAL(BOTSIDE7,H1,FIXFLU,6750)

PATCH(BOTSIDE8,SOUTH,105,109,1,1,1,1,1,1)
COVAL(BOTSIDE8,H1,FIXFLU,6750)


PATCH(COLD,CELL,1,NX,NY,NY,1,1,1,1)
COVAL(COLD,H1,FIXVAL,273*CPFLU)


**********************************************************

    GROUP 14. Downstream pressure for PARAB=.TRUE.
    GROUP 15. Termination of sweeps

RESREF(P1)=0.001*10
RESREF(U1)=10*RESREF(P1);RESREF(V1)=RESREF(U1)
RESREF(KE)=TKEIN*RESREF(P1);RESREF(EP)=EPSIN*RESREF(P1)


LSWEEP=3
   RESTRT(ALL)

**********************************************************

    GROUP 16. Termination of iterations
    GROUP 17. Under-relaxation devices

RELAX(P1,LINRLX,0.5)
DTFL=0.3
RELAX(U1,FALSDT,DTFL)
RELAX(V1,FALSDT,DTFL)
RELAX(KE,FALSDT,DTFL)
RELAX(EP,FALSDT,DTFL)
RELAX(H1,FALSDT,DTFL)
     RELAX(RHO1,LINRLX,0.5)


**********************************************************

    GROUP 18. Limits on variables or increments to them
    GROUP 19. Data communicated by satellite to GROUND
```

```
USEGRD=T
        USEGRD=F

       * ACTIVATE VARIABLE EXCHANGE COEFFICIENTS *

IG(1)=VARNUM
LG(1)=T
LSG3=T
1SG5=2*3*5*7


     ** The GROUND variables used to normalise output :

*****************************************************************

    GROUP 20. Preliminary print-out

ECHO=T

*****************************************************************

    GROUP 21. Print-out of variables



OUTPUT(P1,Y,N,N,N,N,N)
OUTPUT(RHO1,Y,N,N,N,N,N)


*****************************************************************

    GROUP 22. Monitor print-out

1YMON=10;IXMON=80
NPLT=1;NPRMON=5
TSTSWP=20


*****************************************************************

    GROUP 23. Field print-out and plot control

NXPRIN=1;NYPRIN=1
ITABL=3
IPLTL=LSWEEP
ABSIZ=0.6;ORSIZ=0.6
PATCH(MAP,CONTUR,1,NX,1,NY,1,1,1,1)
```

```
PLOT(MAP,P1,0.0,10.0);PLOT(MAP,U1,0.0,10.0)
PLOT(MAP,V1,0.0,10.0);PLOT(MAP,KE,0.0,10.0)
PLOT(MAP,EP,0.0,10.0)
PLOT(MAP,TMP1,0.0,10.0)
PLOT(MAP,H1,0.0,10.0)

 LIBREF=290
 **END OF LIBRARY CASE 290
STOP
```

b) COMPLETE LISTING OF GROUND SUBROUTINE

```
C*****************************************************************
C
C
C--- GROUP 1. Run title and other preliminaries
C
    1 GO TO (1001,1002),ISC
 1001 CONTINUE
       CALL MAKE(DYV2D)
       CALL MAKE(DXU2D)
       CALL MAKE(EASP1)
       CALL MAKE(EASP2)
C       CALL MAKE(GRSP1)
C       CALL MAKE(GRSP2)
      RETURN
 1002 CONTINUE
      RETURN
C*****************************************************************
C
C--- GROUP 2. Transience; time-step specification
C
    2 CONTINUE
      RETURN
C*****************************************************************


C   * -------------------- SECTION  7 ----------------------------
C    For PRNDTL( ).LE.GRND--- laminar PRANDTL nos., or diffusivity.
C
C-----NONUNIFORM FIELD FOR PRANDTL NUMBER
C     ----------------------------------
C
C     SET VIA STORED VARIABLE PRAN
C
      IF(INDVAR.EQ.H1) THEN
C
           IF(LGPRN(1).AND.LG(1)) THEN
           WRITE(6,*) 'GROUND CHAP. 9, SEC. 7 FOR PRANDTL NUMBER.'
           WRITE(*,*) 'GROUND CHAP. 9, SEC. 7 FOR PRANDTL NUMBER.'
           LGPRN(1)=.FALSE.
         ENDIF
C
         IF(LG(1)) CALL FNO(LAMPR,IG(1))
C
      ENDIF
C
C-----END OF USER CODING
C
      RETURN
```

```
C-------------------- SECTION  3 ------------- coefficient = GRND2
      IF (ISWEEP.EQ.LSWEEP) THEN
C      IF (NPATCH(1:3).EQ.'CH2'.AND.INDVAR.EQ.H1) THEN
      IF (NPATCH(1:2).EQ.'CH'.AND.INDVAR.EQ.H1) THEN
         LOCO=LOF(CO)
         IF(RHO1.LE.GRND)LODEN=LOF(AUX(DEN1))
         LOVEL=LOF(LD7)
         GCP=1007
         GTC=0.0263
         IF (NPATCH.EQ.'CH2UP'.OR.NPATCH.EQ.'CH2DOW')THEN
C         IF (NPATCH.EQ.'CHUP1' .OR.NPATCH.EQ.'CHDOW1') THEN
         LODEL=LOF(DXU2D)
         ELSE
         LODEL=LOF(DYV2D)
         END IF
C         IF (NPATCH.EQ.'CHUP2' .OR.NPATCH.EQ.'CHDOW2') THEN
C         LODEL=LOF(DXU2D)
C         ELSE
C         LODEL=LOF(DYV2D)
C         END IF
          LOHTC=LOF(EASP1)
          LONU=LOF(EASP2)
C         LOHTC=LOF(GRSP1)


C         LONU=LOF(GRSP2)

         DO 1335 IX=IXF,IXL
         DO 1334 IY=IYF,IYL
            ICELL=IY+(IX-1)*NY

              IF(RHO1.GT.0.0) THEN
                GRHO=RHO1
              ELSE
                GRHO=F(LODEN+ICELL)
              END IF
C  Calculate heat transfer coefficient from stanton number

           F(LOHTC+ICELL)=GRHO*F(LOVEL+ICELL)*GCP*F(LOCO+ICELL)
           WRITE(*,*)GRHO,GCP
           WRITE(*,*)F(LOVEL+ICELL),F(LOCO+ICELL),F(LOHTC+ICELL),IX,IY
C  Calculate Nusselt Number
            F(LONU+ICELL)=F(LOHTC+ICELL)*(F(LODEL+ICELL)/2)/GTC
            WRITE(*,*)F(LONU+ICELL),(F(LODEL+ICELL)/2),GTC,IX,IY
1334  CONTINUE
1335  CONTINUE

C   Store Q1-defined printout control parameters into local arguments
```

```
C   Store Q1-defined printout control parameters into local arguments
       JXPRF=IXPRF
       JXPRL=IXPRL
       JYPRF=IYPRF
       JYPRL=IYPRL
C   Reset printout control parameters for the specific wall-patch
       IXPRF=IXF
       IXPRL=IXL
       IYPRF=IYF
       IYPRL=IYL

       WRITE(14,'("HEAT TRANSFER CO FOR PATCH=",A8)')NPATCH
       CALL PRN('HTC ',EASP1)
C       CALL PRN('HTC ',GRSP1)
       WRITE(14,'("NUSSELT NUMBER FOR PATCH=",A8)')NPATCH
       CALL PRN('NUS ',EASP2)
C       CALL PRN('NUS ',GRSP2)
C       WRITE(14,'("VELOCITY=",A8)')NPATCH
C       CALL PRN('VEL ',L07)
C       WRITE(14,'("STAN=",A8)')NPATCH
C       CALL PRN('CO ',CO)
C       WRITE(14,'("DEN=",A8)')NPATCH
C       CALL PRN('RHO1 ',DEN)


C   RESET THE PRINTOUT CONTROL PARAMETERS TO Q1-SET VALUES
       IXPRF=JXPRF
       IXPRL=JXPRL
       IYPRF=JYPRF
       IYPRL=JYPRL
      END IF
      END IF
       RETURN
  133 CONTINUE
C-------------------- SECTION  4 ------------- coefficient = GRND3
      RETURN
  134 CONTINUE
C-------------------- SECTION  5 ------------- coefficient = GRND4
      RETURN
  135 CONTINUE
C-------------------- SECTION  6 ------------- coefficient = GRND5
      RETURN
  136 CONTINUE
C-------------------- SECTION  7 ------------- coefficient = GRND6
      RETURN
  137 CONTINUE
C-------------------- SECTION  8 ------------- coefficient = GRND7
      RETURN
```

```
C-----------------------------------GRND2 coefficient for enthalpy et
C
C-----ORIGINAL SETTINGS FOR CHAM CONSTANT PRANDTL NUMBER CODE
C     ------------------------------------------------------
C
C      IF(GRN(-ABS(PRNDTL(INDVAR))).OR.LEZ(PRT(INDVAR))) GO TO 1391
C      CALL SUB2R(SL,PRNDTL(INDVAR),ST,PRT(INDVAR))
C
      CALL SUB2R(SL,0.71,ST,PRT(INDVAR))
C
C     In this section, the Stanton number is deduced from
C     the following formula, ie.,
C     St=s/(Prt*(1.0+P*s**0.5)), where Prt is the turbulent
C     Prandtl number, and where the sublayer-resistance function
C     is given by the formula deduced by Launder and
C     Spalding (1974), ie.,
C     Pm=9.0*(Prl/Prt-1.0)*(Prt/Prl)**0.25
C     where Prl is the laminar Prandtl number.
      PRLT=SL/ST
      PJAY=9.0*(PRLT-1.0)*PRLT**(-0.25)
      CALL FNPAXY(EASP9,PV07)
      CALL FNSTAN(CO,EASP10,EASP9,1.0/ST,1.0/SL,HEIGHT,PJAY)
      CALL FNXYPA(PVSTAN,CO)


C
C-----ORIGINAL CHAM CODE FOR CONSTANT PRANDTL NUMBER CASES ONLY
C     ------------------------------------------------------
C
C 1305     IF(GRN(-ABS(PRNDTL(INDVAR))).OR.LEZ(PRT(INDVAR))) GO TO 1391
C          CALL SUB2R(SL,PRNDTL(INDVAR),ST,PRT(INDVAR))
C
 1305     CONTINUE
          CALL SUB2R(SL,0.71,ST,PRT(INDVAR))
C
          IF(QNE(ST,1.0)) CALL FN25(CO,1.0/ST)
C     The laminar-resistance-function-modified Stanton number, is
C     set to,
C     St = 1/(Prt/s + Prt*Pm*vel/(cmucd**0.25*k**0.5))
C     where s is the skin-friction factor.
          IF(ISC.EQ.5) GO TO 99
          IF(QEQ(ST,SL).AND.LEZ(HEIGHT)) GO TO 1304
      PRLT=SL/ST
      PJAY=9.0*(PRLT-1.0)*PRLT**(-0.25)
      CALL FNSTAN(CO,EASP8,EASP9,1.0/ST,1.0/SL,HEIGHT,PJAY)
 1304 CALL FNXYPA(PVSTAN,CO)
      CALL TQCAL
      GO TO 99
```

```
C
C------EXTRA WALL FUNCTION CODING AS PER CHAM/PER/88/2
C
      WALL=.FALSE.
      DO 10021 I=1,NUMREG
         CALL GETPAT(I,IDUM,TYPE,IX1,IX2,IY1,IY2,IZ1,IZ2,IT1,IT2)
10021 IF(QGE(TYPE,17.0).AND.QLE(TYPE,22.0)) GO TO 10022
      GO TO 10023
10022 WALL=.TRUE.
      CALL GEWFUN
10023 CONTINUE
C
      RETURN
C*****************************************************************
C
C--- GROUP 2. Transience; time-step specification
C
    2 CONTINUE
C   * Set DT if TLAST has been made .LE.GRND in satellite
      RETURN
C*****************************************************************
C
C--- GROUP 3. X-direction grid specification


C
C-----INSERT CODING AS PER CHAM/PER/88/2
C
          IF(NPAT.EQ.'KESO') CALL GEKESO(VIST,LEN1)
C
C     Momentum source caused by lateral gravity
C     in 2-phase flow                                          GXLATG
          IF(NPAT.EQ.'LATG') CALL GXLATG
C
C---- Tentative length-scale source for two-fluid
C     turbulence model                                         GXLESO
          IF(NPAT.EQ.'LESO') CALL GXLESO('SOUTH')
C
C---- The following call to                                    GXNEPA
C     allows the "values" used in
C     a COVAL command to be chosen as the "neighbour-values" of
C     the cell in specified space, time or "variable-space"
C     directions. The condition for the call is that the PATCH
C     name should begin with the characters NE.
          IF(NPAT(1:2).EQ.'NE') CALL GXNEPA(NPAT)
C
C---- The following call to                                    GXPOLR
C     fixes the u- and v-velocities at the circumferential boundary
```

```
C
C GROUP 19  SECTION 7  FINISH OF SWEEP.
  197 CONTINUE
C
C----WALL RELATED TERMS OUTPUT AS PER CHAM/PER/88/2
C    (FOR GROUP 23 !)
C
      IF(ISWEEP.EQ.LSWEEP) THEN
      IF(MOD(ISG5,2).EQ.0) CALL PRNPAT('SKIN    ',3)
      IF(MOD(ISG5,3).EQ.0) CALL PRNPAT('STANTON ',4)
      IF(MOD(ISG5,5).EQ.0) CALL PRNPAT('STRESS  ',5)
      IF(MOD(ISG5,7).EQ.0) CALL PRNPAT('HEAT.FLX',6)
      ENDIF
C
      RETURN
C
C GROUP 19  SECTION 8  FINISH OF TIME STEP.
  198 CONTINUE
      RETURN
C*****************************************************************
C
C--- GROUP 20. Preliminary print-out
C
```

c) COMPLETE LISTING OF GREX2 SUBROUTINE

```
C------------------------------------------ additional declarations
      EQUIVALENCE (IZ,IZSTEP)
C
C-----INSERT COMMON AS CHAM/PER/88/2
C
      COMMON/LWFUN/WALL,LWFIL(202)
      LOGICAL WALL,LWFIL
C
      COMMON/RAKEEP/RADIAT
      LOGICAL RADIAT,SOR
      LOGICAL EQZ,NEZ,LTZ,GTZ,GEZ,LEZ,GRN
      LOGICAL QEQ,QNE,QGT,QLT,QGE,QLE
C
C
C--------------------------------- GO TO the group indicated by IGR
C
          IF(IGR.EQ.19) GO TO 19
          IF(IGR.EQ.13) GO TO 13
      GO TO (1,2,3,4,5,6,24,8,9,10,11,12,13,14,24,24,24,24,19,20,24,
     124,24,24),IGR
C*****************************************************************
C
C---- GROUP 1. Run title and other preliminaries


C
C-----INSERT INITIALISING CALL TO GEWFUN AS DOCUMENTED IN
C     PHOENICS JOURNAL NO. 1 PAGE 90
C
C     WRITE(*,*) 'GREX2 CALLING GEWFUN - GR 1 SEC 1'
C
      CALL GEWFUN
C
C---------------------------------  Turbulence-model constants
      CALL SUB4R(CMU,0.5478,CD,0.1643,CMUCD,0.09,C1E,1.44)
      CALL SUB3R(C2E,1.92,AK,0.435,EWAL,9.0)
      CALL GXSQUR(0,PARAB,NX,NY,NZ,0)
C
C---------------------------------  Radiation initializations
      RADIAT=GTZ((RSG23+RSG26))
          IF(RADIAT) CALL GXRADI(CARTES,NX,NY,NZ,TEMP1,DEN1,RHO1)
C---------------------------------- CALL MODIFY (inactive)
C         IF(LSG3) CALL MODIFY
C
C---------------------------------- identification of GREX2 to vdu
      LUPRST=LUPR1
      LUPR1=LUPR3
      CALL WRIT40('GREX2 OF 25.07.87 HAS BEEN CALLED       ')
```

```
C
C---- Wall functions                                              GXWFUN
C
C-----REPLACE GXWFUN CALL WITH CALL TO GEWFUN AS DOCUMENTED IN
C     PHOENICS JOURNAL NO. 1 PAGE 90 (GENERALISED WALL FUNCTIONS)
C
C     IF(WALLTY) CALL GXWFUN(PRNDTL(INDVAR),PRT(INDVAR),FIXVAL)
C
      IF(WALLTY) CALL GEWFUN
C
C---- Velocity resolutes at a curved inlet boundary          GXBFC
          IF(NPAT(1:3).EQ.'BFC') CALL GXBFC(NX,NY,NZ)
C
      RETURN
C*****************************************************************
C
C--- GROUP 14. Downstream pressure for PARAB=.TRUE.
C
   14 CONTINUE
      RETURN
C*****************************************************************
C   * Make changes for these groups only in group 19.
C--- GROUP 15. Termination of sweeps


C
C-----INSERT CALL TO GEWFUN AS PER CHAM/PER/88/2
C     PAGE 13
C
      IF(WALL) CALL GEWFUN
C
      RETURN
C
C   * ----------GROUP 19  SECTION 5 ---- FINISH OF ITERATION.
C---- Compute velocities from potential differences.
  195     IF(LSG10.AND.ISWEEP.NE.1) CALL GXPOTV(NZ,DZG,
     1NPOR,EPOR,HPOR)
C
C---- Allow for compressibility in a potential flow
          IF(LSG10.AND.LSG9.AND.ISWEEP.NE.1) CALL GXPOTC
     1(EPOR,NPOR,HPOR,CINT(ISG10),PHINT(ISG10),NZ)
      RETURN
C
C GROUP 19  SECTION 6  FINISH OF IZ SLAB
C---- Reset the nominal porosities
  196     IF(ISG11.GE.IZ)
     1    CALL GXPORA(EPOR,EASP3,RSG11,RSG12,SETPOR,2)
          IF(ISG12.GE.IZ)
```

APPENDIX [3]

TABULATED DATA

x=0.0 (mm)							
y (mm)	U (m/s)	U RMS (m/s)	V (m/s)	V RMS (m/s)	Total Velocity (m/s)	Flow Angle Deg	Shear Stress $(m/s)^2$
1	4.3	1.2	0.8	0.99	4.3	11.1	-0.62
2	4.9	1.3	0.4	0.9	4.9	4.6	-0.57
4	5.6	1.3	0.1	0.8	5.6	1.37	-0.48
6	6.1	1.1	0.06	0.78	6.1	0.57	-0.37
8	6.5	1.1	-0.01	0.74	6.5	-0.06	-0.31
10	6.7	1.0	-0.04	0.76	6.7	-0.3	-0.27
x=10 (mm)							
1	5.2	1.3	-0.18	0.447	5.2	-1.95	-0.12
2	5.5	1.2	-0.13	0.6	5.5	-1.9	-0.18
4	5.8	1.2	-0.07	0.7	5.8	-1.25	-0.32
6	6.3	1.1	-0.09	0.7	6.3	-0.65	-0.29
8	6.6	1.1	-0.08	0.7	6.6	-0.77	-0.25
10	6.8	1.0	-0.04	0.7	6.8	-0.64	-0.26
x=20 (mm)							
1	4.7	1.3	-0.1	0.33	4.7	-1.2	-0.11
2	5.4	1.2	-0.12	0.56	5.4	-1.27	-0.16
4	5.8	1.2	-0.14	0.68	5.8	-1.4	-0.24
6	6.2	1.1	-0.12	0.69	6.2	-1.1	-0.28
8	6.5	1.1	-0.1	0.7	6.5	-1.2	-0.25
10	6.8	1.1	-0.14	0.7	6.8	-1.12	-0.27
x=30 (mm)							
1	4.1	1.3	-0.07	0.27	4.1	-1.0	-0.11
2	5.4	1.2	-0.1	0.5	5.4	-1.1	-0.15
4	5.9	1.2	-0.16	0.64	5.9	-1.5	-0.2
6	6.3	1.1	-0.16	0.71	6.3	-1.5	-0.24
8	6.6	1.1	-0.14	0.71	6.6	-1.2	-0.27
10	6.9	1.1	-0.16	0.67	6.9	-1.3	-0.26

Experimental data over fifth block Uin=5.0(m/s).

x=40 (mm)							
y (mm)	U (m/s)	U RMS (m/s)	V (m/s)	V RMS (m/s)	Total Velocity (m/s)	Flow Angle Deg	Shear Stress $(m/s)^2$
1	3.46	1.2	-0.04	0.2	3.5	-0.73	-0.078
2	5.4	1.2	-0.08	0.49	5.4	-0.88	-0.12
4	5.9	1.1	-0.12	0.65	5.9	-1.2	-0.23
6	6.3	1.1	-0.15	0.68	6.3	-1.4	-0.28
8	6.6	1.1	-0.12	0.7	6.6	-1.1	-w28
10	6.8	1.1	-0.1	0.71	6.8	-0.8	-0.23
x=50 (mm)							
1	2.6	1.0	-0.06	0.1	2.6	-1.4	-0.03
2	5.1	1.2	-0.05	0.45	5.1	-0.63	-0.14
4	5.9	1.1	-0.09	0.6	5.9	-0.9	-0.2
6	6.2	1.1	-0.12	0.7	6.2	-1.1	-0.28
8	6.6	1.1	-0.13	0.69	6.6	-1.1	-0.23
10	6.9	1.1	-0.14	0.68	6.9	-1.2	-0.22

Experimental data over fifth block Uin=5.0(m/s).

	x=0 (mm)	x=10 (mm)	x=20 (mm)	x=30 (mm)	x=40 (mm)	x=50 (mm)
y (mm)	U (m/s)	U (m/s)	U (m/s)	U (m/s)	U (m/s)	U (m/s)
1	3.4	2.9	2.7	2.7	2.7	2.8
2	4.0	3.9	3.9	3.9	3.9	3.9
3	4.4	4.4	4.4	4.4	4.5	4.4
4	4.7	4.8	4.8	4.8	4.8	4.8
5	5.0	5.1	5.1	5.1	5.2	5.2
6	5.3	5.3	5.3	5.4	5.4	5.4
7	5.5	5.6	5.6	5.6	5.7	5.7
8	5.8	5.8	5.8	5.8	5.9	5.9
9	6.0	6.0	6.0	6.1	6.1	6.1
10	6.2	6.2	6.2	6.3	6.3	6.3
20	7.2	7.2	7.2	7.2	7.2	7.2
30	8.8	8.8	8.8	8.8	8.8	8.8

Computational data over fifth block Uin=5.0 (m/s).

Fifth block						
x (mm)	C_f	St	τ (m/s)^2	q (w/m^2)	h (w/m^{2}c)	Nu
10	0.0083	0.012	0.07	743	34	0.65
20	0.00845	0.012	0.063	555	33	0.62
30	0.0085	0.012	0.061	494	32	0.61
40	0.0085	0.012	0.06	466	32	0.61
50	0.00845	0.012	0.063	469	33	0.62
Sixth block						
x (mm)	C_f	St	τ (m/s)^2	q (w/m^2)	h (w/m^{2}c)	Nu
10	0.0082	0.012	0.074	741	34.6	0.66
20	0.0085	0.012	0.067	552	33	0.63
30	0.00845	0.012	0.065	490	32.8	0.62
40	0.0085	0.012	0.064	464	32.6	0.62
50	0.0084	0.012	0.66	468	33	0.63

Computational data over Fifth and Sixth block Uin=5.0 (m/s).

	x=10 (mm)	x=20 (mm)	x=30 (mm)	x=40 (mm)	x=50 (mm)
y (mm)	T (deg c)	T (deg c)	T (deg c)	T (deg c)	T (deg c)
1	40.4	45	46.6	47.3	47.4
2	26.3	28.2	29.4	30.2	30.5
3	23.2	24.1	25	25.6	26.1
4	21.3	21.7	22.3	22.7	23.1
5	19.9	20	20.3	20.7	21.0
6	18.6	18.7	18.8	19.1	19.3
7	17.4	17.5	17.6	17.7	17.9
8	16.4	16.4	16.5	16.6	16.7
9	15.4	15.5	15.5	15.6	15.7
10	12.5	12.6	12.6	12.7	12.7
20	6.5	6.6	6.8	6.9	7.0
30	2.1	2.1	2.3	2.4	2.5

Computational data over fifth block Uin=5.0 (m/s).

Technique	Scheme	Description
A Conduction Cooling	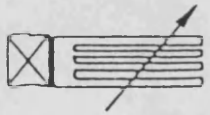	
A1 Fins		Heat transfer by conduction to the fins which are cooled by convection and/or radiation.
A2 Heat Pipe	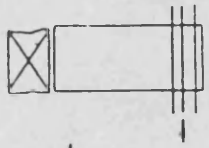	Heat transfer by conduction to the heat pipe (evaporator). The condenser end of the pipe is cooled by convection or radiation.
B Air Cooling		
B1 Natural Convection		Device is cooled by natural convection of air.
B2 Forced Convection		Device is cooled by forced convection of air.
C Liquid Cooling		
C1 Liquid Forced Convection	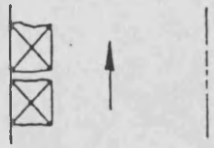	Devices mounted in a channel, in which a liquid is forced to flow. The liquid is then cooled in an air or liquid-cooled heat exchanger.
C2 Vapor Space Condenser	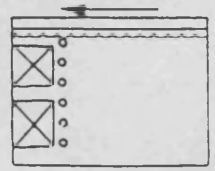	Devices are submerged in a boiling liquid. Heat is rejected to an air or water-cooled condenser. The condenser is usually finned.
C3 Submerged Condenser	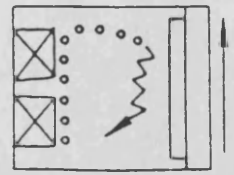	Devices are mounted in an enclosure which is filled with a dielectric fluid, and cooled by an air-cooled or water-cooled heat exchanger. Internal and/or external fins are used.

FIGURE 1.3: ELECTRONIC DEVICE COOLING TECHNIQUES